

# Lawrence Berkeley National Laboratory

## LBL Publications

### Title

DECOVALEX-2023 Task G: SAFENET Final Report

### Permalink

<https://escholarship.org/uc/item/0gg9m6z0>

### Authors

Faybishenko, Boris

Kolditz, Olaf

McDermott, Christopher

et al.

### Publication Date

2024-06-15

### Copyright Information

This work is made available under the terms of a Creative Commons Attribution License, available at <https://creativecommons.org/licenses/by/4.0/>

Peer reviewed

# DECOVALEX-2023

## Task G: SAFENET

### Final Report

Olaf Kolditz, Christopher McDermott, Jeoung Seok Yoon

With contributions from:

Hejuan Liu, Pengzhi Pan (CAS), Son Nguyen (CNSC), Saeha Kwon (KAERI),  
Jung-Wook Park, Chan-Hee Park (KIGAM), Li Zhuang (KICT),  
Teklu Hadgu, Yifeng Wang (SNL), Mengsu Hu, Tsubasa Sasaki,  
Jonny Rutqvist and Jens Birkholzer (LBNL), Mostafa Mollaali,  
Wenqing Wang (UFZ), Gonçalo Cunha, Steven Benbow,  
Claire Watson, Alex Bond, Neil Chittenden (UoE, Quintessa)

June 2024



## Disclaimer

This document was prepared as an account of the international research project DECOVALEX-2023 comprising participants from industry, government and academia, with funding organizations—Andra, BASE, BGE, BGR, CAS, CNSC, COVRA, U.S. DOE, Enresa, ENSI, JAEA, KAERI, NWSMO, NWS, SÚRAO, SSM and Taipower. The statements made in the report are, however, solely those of the authors and do not necessarily reflect those of the Funding Organizations. While this document is believed to contain correct information, neither the United States Government nor any agency thereof, nor the Regents of the University of California, nor any of their employees, makes any warranty, express or implied, or assumes any legal responsibility for the accuracy, completeness, or usefulness of any information, apparatus, product, or process disclosed, or represents that its use would not infringe privately owned rights. Reference herein to any specific commercial product, process, or service by its trade name, trademark, manufacturer, or otherwise does not necessarily constitute or imply its endorsement, recommendation, or favoring by the United States Government or any agency thereof or the Regents of the University of California. The views and opinions of the authors expressed herein do not necessarily state or reflect those of the United States Government, any agency thereof, or the Regents of the University of California.

This technical document does not consider contractual limitations or obligations under the Standard Contract for Disposal of Spent Nuclear Fuel and/or High-Level Radioactive Waste (Standard Contract) (10 CFR Part 961).

To the extent discussions or recommendations in this document conflict with the provisions of the Standard Contract, the Standard Contract governs the obligations of the parties, and this presentation in no manner supersedes, overrides, or amends the Standard Contract.

No inferences should be drawn from this document regarding future actions by DOE, which are limited by the terms of the Standard Contract and Congressional appropriations for the Department to fulfill its obligations under the Nuclear Waste Policy Act, including licensing and constructing a spent nuclear fuel repository.

## Copyright

This publication has been composed under the direction of editors at Lawrence Berkeley National Laboratory under Contract No. DE-AC02-05CH11231 with the U.S. Department of Energy, Quintessa Limited, Birchwood Park, Warrington WA3 6GA, UK. The U.S. Government retains a non-exclusive, irrevocable, worldwide license to publish or reproduce this published report or allow others to do so for U.S. Government purposes.

*Writers for each chapter are responsible for copyright permissions (if applicable) for graphics within their chapter.*

# DECOVALEX-2023

## Task G Final Report



### **Main Authors:**

Olaf Kolditz<sup>1</sup>, Christopher McDermott<sup>2</sup>, Jeoung Seok Yoon<sup>3</sup>

<sup>1</sup>Helmholtz Centre for Environmental Research, Technische Universität Dresden

<sup>2</sup>University of Edinburgh

<sup>3</sup>DynaFrax

### **Contributing Authors (alphabetical by organisation):**

Hejuan Liu, Pengzhi Pan (CAS), Son Nguyen (CNSC),  
Saeha Kwon (KAERI), Jung-Wook Park, Chan-Hee Park (KIGAM), Li Zhuang (KICT),  
Teklu Hadgu, Yifeng Wang (SNL), Mengsu Hu, Tsubasa Sasaki, Jonny Rutqvist and Jens Birkholzer (LBNL),  
Mostafa Mollaali, Wenqing Wang (UFZ),  
Gonçalo Cunha, Steven Benbow, Claire Watson, Alex Bond, Neil Chittenden (UoE, Quintessa)

Reviewed by AE Bond

June 2024

LBNL-2001628

## Preface

The DECOVALEX Project is an ongoing international research collaboration established in 1992 to advance the understanding and modeling of coupled Thermal (T), Hydrological (H), Mechanical (M), and Chemical (C) processes in geological systems. DECOVALEX was initially motivated by recognising that predicting these coupled effects is essential to the performance and safety assessment of geologic disposal systems for radioactive waste and spent nuclear fuel. Later, it was realized that these processes also play a critical role in other subsurface engineering activities, such as subsurface CO<sub>2</sub> storage, enhanced geothermal systems, and unconventional oil and gas production through hydraulic fracturing. Research teams from many countries (e.g., Canada, China, Czech Republic, Finland, France, Germany, Japan, Netherlands, Republic of Korea, Spain, Sweden, Switzerland, Taiwan, United Kingdom, and the United States) various institutions have participated in the DECOVALEX Project over the years, providing a wide range of perspectives and solutions to these complex problems. These institutions represent radioactive waste management organizations, national research institutes, regulatory agencies, universities, and industry and consulting groups.

At the core of the collaborative work within DECOVALEX is the collaborative analysis and comparative modeling of state-of-the-art field and laboratory experiments. DECOVALEX engages model comparison in a broad and comprehensive sense, including the modelers' interpretation of experimental data, selection of boundary conditions, rock and fluid properties, etc., and their choice of coupling schemes and simulators. This recent phase of DECOVALEX has expanded the work scope to include the modelers being challenged to gain an understanding of the representation coupled processes in generic 'whole system' or 'performance assessment' models. In-depth and detailed discussions among the teams yield insight into the coupled THMC processes and stimulate the development of modeling capabilities and measurement methods. This would have been impossible if only one or two groups had studied the data.

Since the project initiation, DECOVALEX has been organized in several four-year phases, each featuring several modeling tasks of importance to radioactive waste disposal and other geoscience applications. Seven project phases were successfully concluded between 1992 and 2019, the results of which have been summarized in several overview publications (e.g., Tsang et al., 2009; Birkholzer et al., 2018; Birkholzer et al., 2019, Birkholzer et al., 2024). The most recent phase, DECOVALEX-2023, started in 2020 and ended in 2023. Seven tasks were conducted in DECOVALEX-2023, as follows:

- **Task A: HGFrac** – Thermal- and gas- induced fracturing of the Callovo-Oxfordian Clay, France
- **Task B: MAGIC** – Migration of gas in compacted clay
- **Task C: FE Experiment** – Thermal-hydro-mechanical (THM) modelling of the FE experiment at Mont Terri, Switzerland
- **Task D: Horonobe EBS Experiment** - THM modelling of the Horonobe EBS experiment at the Horonobe URL, Japan
- **Task E: BATS** – THM modeling for the Brine Availability Test in Salt (BATS) at the WIPP, New Mexico, USA
- **Task F: Performance Assessment** – Comparative generic performance assessment models in crystalline and salt formations
- **Task G: SAFENET** – Laboratory-scale HM and TM analyses of single fractures

The DECOVALEX Project would not have been possible without the support and engagement of the participating organizations who jointly support the coordination of the project within a given project phase, propose and coordinate modeling tasks, including the necessary experimental data, and deploy their research team (or teams) working on a selection of the tasks conducted in the project. The partner organizations in DECOVALEX-2023 were:

- Andra, National Radioactive Waste Management Agency, *France*
- BASE, Federal Office for the Safety of Nuclear Waste Management, *Germany*
- BGE, Federal Company for Radioactive Waste Disposal, *Germany*
- BGR, Federal Institute for Geosciences and Natural Resources, *Germany*
- CAS, Chinese Academy of Sciences, *China*
- CNSC, Canadian Nuclear Safety Commission, *Canada*
- COVRA, Central Organisation for Radioactive Waste, *Netherlands*
- DOE, Department of Energy, *USA*
- Enresa, National Radioactive Waste Management Agency, *Spain*
- ENSI, Swiss Federal Nuclear Safety Inspectorate, *Switzerland*
- JAEA, Japan Atomic Energy Agency, *Japan*
- KAERI, Korea Atomic Energy Research Institute, *Republic of Korea*
- NWMO, Nuclear Waste Management Organization, *Canada*
- NWS, Nuclear Waste Services, *United Kingdom*
- SSM, Swedish Radiation Safety Authority, *Sweden*
- SÚRAO, Radioactive Waste Repository Authority, *Czech Republic*
- Taipower, Taiwan Power Company, *Taiwan*

We are extremely grateful to these organizations for their financial and technical support of DECOVALEX-2019.

*Jens Birkholzer (Chairman of the DECOVALEX project) and Alex Bond (Technical Coordinator of the DECOVALEX Project).*

*Berkeley, California, USA, October 2024*

**References:**

- Birkholzer, J.T., Bond, A.E., Hudson, J.A., Jing, L., Tsang, C.-F., Shao, H., Kolditz, O. (2018): DECOVALEX-2015 - An International Collaboration for Advancing the Understanding and Modeling of Coupled Thermo-Hydro-Mechanical-Chemical (THMC) Processes in Geological Systems, *Environmental Earth Sciences*, 77(14). <https://doi.org/10.1007/s12665-018-7697-7>
- Birkholzer, J.T., Tsang, C.-F., Bond, A.E., Hudson, J.A., Jing, L., and Stephansson, O. (2019): 25 Years of DECOVALEX - Scientific Advances and Lessons Learned from an International Research Collaboration in Coupled Subsurface Processes, *Invited Review, International Journal and Rock Mechanics and Mining Sciences*, 122. <https://doi.org/10.1016/j.ijrmms.2019.03.015>
- Birkholzer, J.T., Bond, A.E. and Tsang, C.-F. (2024). The DECOVALEX international collaboration on modeling of coupled subsurface processes and its contribution to confidence building in radioactive waste disposal. *Hydrogeology Journal*, <https://doi.org/10.1007/s10040-024-02799-7>
- Tsang, C.-F., Stephansson, O., Jing, L., and Kautsky, F. (2009): DECOVALEX Project: from 1992 to 2007. *Environmental Geology*, 57(6). <https://doi.org/10.1007/s00254-008-1625-1>

## Summary

### Task objectives and scientific interest

DECOVALEX Task G deals with fracture mechanics at several scales using a combined approach of experimental work, related model development, benchmarking and experimental analysis<sup>1</sup>. Fig. 0.1 provides a graphical abstract for Task G. The experimental basis for the related mechanical (M), hydro-mechanical (HM), and thermo-mechanical (TM) processes comes from the rock mechanics laboratories of Universities of Freiberg (TUBAF) and Edinburgh, as well as the Korea Institute of Civil Engineering and Building Technology (KICT). The experimental work in the rock laboratories is closely linked to the underground research laboratories (URLs) Reiche Zeche (Germany), KURT (Korea), and Mont Terri (Switzerland). The scientific key questions are related to fracture permeability evolution under THM conditions, anisotropy effects on fracturing processes, and thermal fracture slip, which are being addressed in specific steps of the task. A large variety of numerical methods have been developed and applied for experimental analysis, ranging from continuum to discontinuum approaches. A detailed comparison of mechanical and hydro-mechanical processes is given in the section 3 via the benchmarking exercises. As a result of DECOVALEX-2023 Task G we further improved our understanding and predictability of fracturing processes under THM conditions. This was based on robust numerical simulation methods and in-depth experimental analysis.

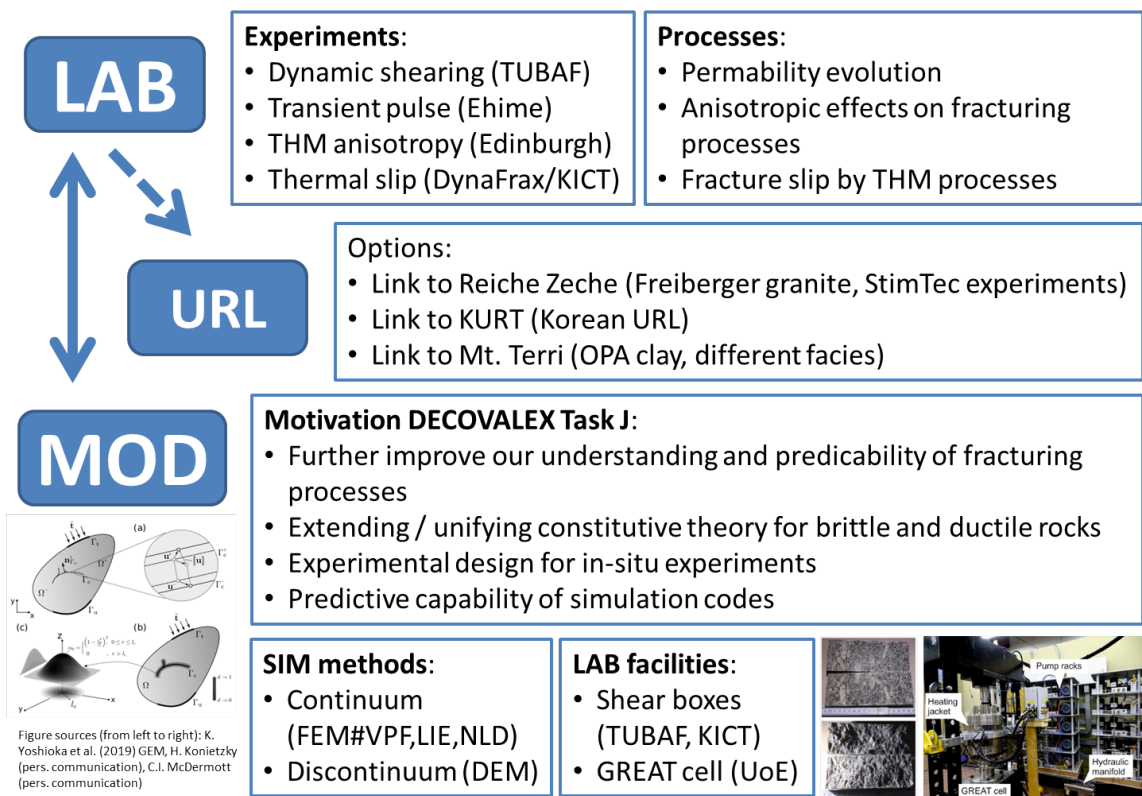


Figure 0.1: Graphical abstract fo Task G

<sup>1</sup><https://decovallex.org/D-2023/task-g.html>

## Experimental data

Several laboratory experiments have provided important data for Task G. These are essentially experiments to investigate M, HM and TM processes.

- As part of the GeomInt project (Kolditz et al., 2021) the Freiberg Experiments (Rock mechanics lab of the University of Mining Technology Freiberg, TUBAF) different kinds of direct shear tests have been conducted to investigate shear characteristics of fractures in crystalline rocks, namely Constant Normal Load (CNL) and Constant Normal Stiffness (CNS) tests (Frühwirt, Pötschke, and Konietzky, 2021). A detailed description can be found in section 4. The experimental analysis has been conducted by the TUBAF, CNCS (Nguyen et al., 2024), and CAS teams, see section 4.
- The GREAT cell at the University of Edinburgh offers a unique capability to load hydraulically connected fractures in larger rock samples (200 mm diameter and height) under a controlled triaxial stress field (McDermott et al., 2018). It also allows for the alteration of the polyaxial stress field during the experiment, enabling the investigation of the impact of normal and shear stress on fracture permeability (section 5.1). The GREAT cell experiments have served to develop a new set of benchmarks for M and HM fracture mechanics (section 3.5). Various sample types have been investigated, including synthetic samples (section 5.2), as well as greywacke and Freiberg granite.
- The rock mechanics lab at the Korean Institute of Civil Engineering and Building Technology used a true-triaxial testing equipment with a 1.1 MN load capacity in each axis and 150°C heating to investigate the thermoshearing behavior of granite fractures, specifically thermally induced fracture slip and shear dilation. During the experiments, acoustic emission (AE) was measured to estimate the related energy release during thermal fracturing. Pocheon granite was used in all experiments (section 6).

## Analysis approaches

Numerical methods were used to analyse experimental data from three rock mechanics labs in Germany, UK, and Korea (section 2.2), including both continuum and discontinuum methods. Prior to experimental analyses, an extensive verification study was conducted for different fracture types and processes, such as plane and rough fractures, as well as fracture networks (section 3).

## Key learning points

This text summarises key learning points regarding the developed methodology, benchmarking procedure, and analysis of experimental results.

- Methodology: In section 2, a range of numerical methods has been developed and tested to describe coupled HM and TM fracture processes. It is essential to have a sound theoretical foundation and cross-verification of numerical methods and codes to build confidence in the performance of more realistic fracture models. The comprehensive methodology has further improved the reliability of HM and TM modelling of fracture mechanics in brittle rocks.



- **Benchmarking:** Section 3 discusses benchmarking. A systematic benchmarking procedure has been implemented to quantitatively evaluate and compare different numerical algorithms for mechanical, hydro-mechanical, and thermo-mechanical coupled fracture mechanics. The procedure is crucial for efficient code verification. Simplified solutions for mechanics can be utilized as envelopes for more complex fracture geometries, such as rough fractures. Reproducing process-specific benchmarks should always be a prerequisite for more complex studies.
- **Experimental analysis:** The experimental analysis (sections 4, 5, 6) shows that, based on the developed methodology and verification of numerical tools in a cross-referenced fashion, novel HM and TM experiments' results could be better understood and reproduced numerically with sufficient accuracy representing main process characteristic. It is important to note that fracture roughness plays a key role in rock matrix damage and fracture shear processes and fracture propagation, which in turn affects stress-dependent permeabilities. Joint roughness coefficients (JRC) and joint compressive strength (JCS) are important parameters for these processes. According to experimental observations, damage occurred not only to the fracture asperities but also propagated into the rock matrix in the form of microcracks and localized macrocracks.
- **Additional work is needed to enhance modelling capabilities for THM fracture processes, which was not accomplished in the current iteration of SAFENET. Furthermore, there is a need to comprehend fracture processes across different scales, which is part of the planned future work.**

### **Areas for future work**

The SAFENET (Safety Assessment of Fluid Flow, Shear, Thermal and Reaction Processes within Crystalline Rock Fracture NETWORKS) task will be continued in DECOVALEX 2027 (section 7). The main focus is to extend the knowledge from DECOVALEX-2023 towards the analysis of field experiments, such as the STIMTEC experiments in the Teaching and Research Mine "Reiche Zeche" in Freiberg.

## Contents

<b>1</b>	<b>Introduction</b>	<b>13</b>
1.1	Benchmark exercises (BE)	14
1.1.1	Concept	14
1.1.2	Benchmarking GREAT cell experiments	14
1.2	Experimental analysis (EA)	16
	References	16
<b>2</b>	<b>Methods</b>	<b>17</b>
2.1	Governing equations	17
2.2	Numerical methods	18
2.2.1	Variational Phase Field–Finite Element Method (VPF–FEM)	18
2.2.2	Hybrid Cellular Automata–(x) Finite Element Method (hCA–FEM/xFEM)	19
2.2.3	Lower Dimensional Interface Elements–Finite Element Method (LIE–FEM)	20
2.2.4	Contact Modeling with Embedded Fracture Model–Finite Element Method (CMEFM–FEM)	21
2.2.5	Embedded Thin Elastic Layer–Finite Element Method (ETEL–FEM)	22
2.2.6	Grain Based Model–Distinct Element Method (GBM–DEM)	23
2.2.7	Bonded Particle Model–Distinct Element Method (BPM–DEM)	24
2.2.8	Integral Finite Difference Method–Distinct Element Method (IFDM–DEM)	24
2.2.9	NMM - Numerical Manifold Method	25
2.3	Characterisation of Laboratory Scale Fractures	27
2.3.1	Context and Task Overview	27
2.3.2	Fracture Roughness Characterisation (PhD support work)	27
2.3.3	Kriging	32
2.3.4	Representative Elementary Volume (REV)	34
2.3.5	Extrapolation	39
2.3.6	Application of Spatial continuity to Finite Element Method models meshes	39
2.3.7	Future work	42
	References	43
<b>3</b>	<b>Benchmarking</b>	<b>44</b>
3.1	Plane fractures	44

3.1.1	Benchmark 1: Static fracture aperture under a constant pressure . . . . .	44
3.1.2	Benchmark 2: Propagating fracture in the toughness dominated regime . . . . .	46
3.1.3	Benchmark 3: Static straight fracture under constant pressure with differential in-situ stress . . . . .	48
3.1.4	Benchmark 4: Static inclined fracture under constant pressure with differential in-situ stress . . . . .	48
3.1.5	Mesh studies . . . . .	49
3.1.6	Domain size study . . . . .	52
3.2	Fracture slip under mechanical loading (M processes) . . . . .	55
3.2.1	Preparation of rough fracture surface data set . . . . .	55
3.2.2	Benchmark 5: Static rough fracture under differential in-situ stress . . . . .	55
3.3	Fracture slip under mechanical and thermal loading (TM processes) . . . . .	61
3.4	Fracture networks . . . . .	67
3.4.1	Benchmarking study . . . . .	67
3.4.2	Fracture networks - Damage processes . . . . .	69
3.5	GREAT cell benchmarks . . . . .	75
3.5.1	Intact samples (M1) . . . . .	75
3.5.2	Fractured samples (M3a & M3b) . . . . .	78
3.5.3	Pressurized samples (HM3a & HM3b) . . . . .	81
3.5.4	Hydraulic Fracturing (HM4): Variational phase-field method (OGS and CAS Teams) . . . . .	84
	References . . . . .	89
<b>4</b>	<b>Freiberg experiments (M processes)</b>	<b>91</b>
4.1	Experimental facility . . . . .	91
4.2	Experimental procedure and results . . . . .	91
4.3	Experimental data . . . . .	92
4.4	Fracture geometry . . . . .	93
4.5	Data access . . . . .	93
4.6	Simulation results . . . . .	94
4.6.1	CAS team . . . . .	94
4.6.2	CNSC team . . . . .	95
	References . . . . .	98

<b>5</b>	<b>GREAT (Geo-Reservoir Experimental Analogue Technology) cell experiments (M and HM processes)</b>	<b>99</b>
5.1	Experimental facility and programme . . . . .	99
5.2	Experimental analysis of synthetic samples . . . . .	105
5.2.1	Overview . . . . .	105
5.2.2	Intact sample - Model set-up (M1) . . . . .	105
5.2.3	Intact sample - Analysis (M1) (McDermott et al., 2018) . . . . .	108
5.2.4	Partially fractured sample (M2) . . . . .	111
5.2.5	Partially fractured sample (HM2) . . . . .	115
5.2.6	Fully fractured sample (M3) . . . . .	121
5.3	Fully fractured sample (HM3) . . . . .	123
	References . . . . .	126
<b>6</b>	<b>KICT experiments (M and TM processes)</b>	<b>127</b>
6.1	Experimental concept and procedure . . . . .	127
6.2	Experimental setup and monitoring data . . . . .	127
6.3	Characterization of test specimen . . . . .	129
6.4	Experimental results and analysis . . . . .	131
6.4.1	Temperature evolution and distribution . . . . .	131
6.4.2	Thermally induced fracture slip and shear dilation . . . . .	132
6.4.3	Discrepancy between the measurements by the transducers and the DIC analysis . . . . .	134
6.4.4	Fracture surface change . . . . .	134
6.4.5	Acoustic emission (AE) characteristics . . . . .	136
6.5	Test case modelling of KICT thermoslip experiment . . . . .	139
6.5.1	PFC modelling by the SSM/DynaFrax team . . . . .	139
6.5.2	FLAC3D modelling by the LBNL team . . . . .	141
6.5.3	COMSOL modelling by the CNSC team . . . . .	143
6.5.4	3DEC modelling by the KIGAM team . . . . .	145
6.5.5	TOUGH-3DEC modelling by the KAERI team . . . . .	149
6.5.6	Summary . . . . .	150
	References . . . . .	151
<b>7</b>	<b>Outlook to SAFENET-2: THM Fracture Mechanics - From Lab to Field Scale</b>	<b>153</b>
	References . . . . .	155

<b>8</b>	<b>Planned and Completed Publications</b>	<b>156</b>
<b>9</b>	<b>Acknowledgements</b>	<b>158</b>
<b>A</b>	<b>List of symbols</b>	<b>159</b>
<b>B</b>	<b>Details of numerical methods</b>	<b>161</b>
B.1	Lower-dimensional interface element (LIE) method . . . . .	161
B.2	Fundamentals of NMM (LBNL) . . . . .	162
B.3	Fundamentals of FLAC3D (LBNL) . . . . .	166
	References . . . . .	170

## 1 Introduction

Understanding of shear reactivation of pre-existing discontinuities for brittle host rocks is an area of considerable interest for radioactive waste disposal. In particular, the potential for existing features to undergo shear displacements and consequent changes in permeability as the result of coupled thermal, mechanical, hydrogeological and chemical effects can all have significant impacts on repository safety functions (e.g., creating permeable pathways or, for very large displacements, mechanical damage of waste packages and engineered barriers).

The structure and contents of Task G under DECOVALEX-2023 is (see Fig. 1.1 for Task G structure):

- Step 1: Mechanical (M) results derived from constant normal load (CNL) direct shear tests and constant normal stiffness (CNS) direct shear tests, as well as high-resolution fracture surface scans (TUBAF), established a starting point for fracture characterisation.
- Step 2: Investigate hydro-mechanical (HM) results obtained with the GREAT cell (University of Edinburgh) with a focus on fundamental shear processes under complex 3D stress states.
- Step 3: Investigate and model thermo-mechanical (TM) results obtained from tri-axial tests conducted at KICT with a focus on shear processes triggered by thermal stresses.
- Step 4: Combining and upscaling near-field approaches for THM analysis.

The emphasis of this task was at the laboratory scale, using well-designed experiments to link micro-scale THM(C) effects acting on fracture surfaces and asperity contacts with emergent fracture properties such as permeability.

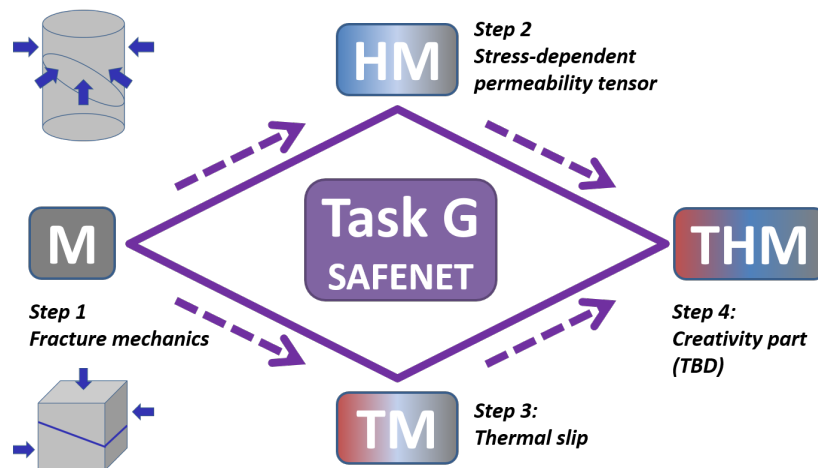


Figure 1.1: DECOVALEX 2023 Task G structure

Within the Task Steps the following modelling exercises have been conducted with increasing complexity:

- Benchmark exercises (BE) (section 3 and section 1.1.2)
- Experimental analysis (EA) (section 1.2)

## 1.1 Benchmark exercises (BE)

### 1.1.1 Concept

The illustration below shows the general concept of benchmarking exercises for cubic and cylindrical rock samples as motivated by the KICT triaxial (Fig. 1.2) and GREAT cell polyaxial (Fig. 1.3) tests, respectively. The basic idea is to systematically increase the complexity of the coupled processes in order to better understand the associated effects on fracture processes (e.g. shear, propagation, permeability). Within SAFENET, only part of this has been addressed, and the benchmarking concept is valid for ongoing research activities.

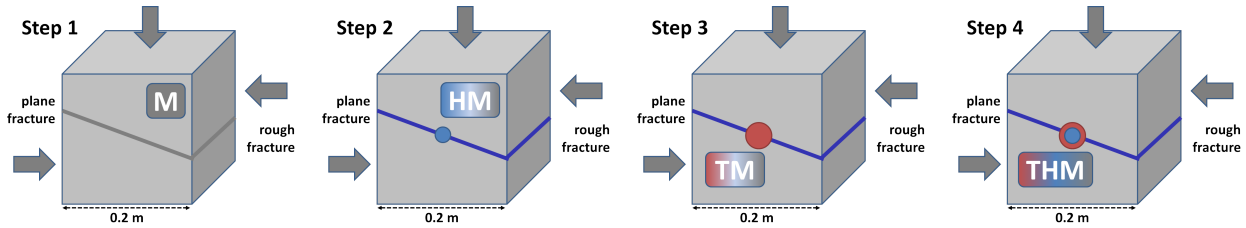


Figure 1.2: Geometric cases (cubes) for KICT experiments by processes: M > HM > TM > THM

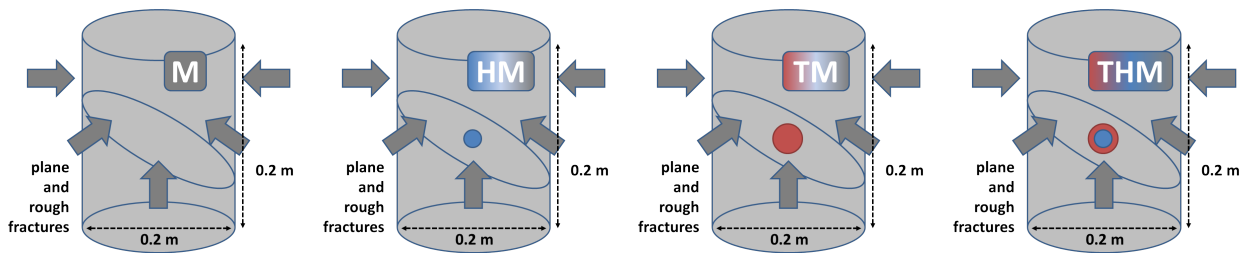


Figure 1.3: Geometric cases (cylinders) for GREAT cell experiments by processes: M > HM > TM > THM

The first benchmarking exercises have been further simplified by representing plane, coarse fractures and simple fracture networks in simple strain models:

- Plane fracture (section 3.1),
- Rough fractures under mechanical load (M processes) (section 3.2),
- Rough fracture under mechanical and thermal loading (TM processes) (section 3.3),
- Fracture networks (section 3.4).

### 1.1.2 Benchmarking GREAT cell experiments

As a prerequisite to the model analyses of the GREAT cell experiments (see sec. 5), we conduct a thorough benchmarking exercise to provide a sound basis of model capabilities and accuracies (e.g. required discretization for comparable accuracy). The benchmark exercises represent simplified variants of the GREAT cell experiments covering general features (e.g. fracture pattern and coupled processes).

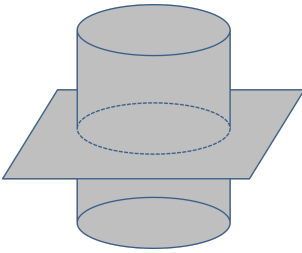


Figure 1.4: Benchmarking concept of 2D horizontal cross-sections (plane-strain)

The benchmark exercises have been conducted in 2D (plane strain). For this purpose we consider a horizontal section through the rock samples tested in the GREAT cell (Figure 1.4). The main characteristics of the HM fracture mechanics can be studied in a 2D plane-strain fashion. The 2D option is easier to model and is intended to encourage more modelers to participate in the benchmark exercises. The benchmarking concept is based on a stepwise increase in complexity, including mechanical (M) and hydromechanical (HM) exercises (Figure 1.5). The base case (M1) represents the mechanical response of the rock sample due to rotating boundary conditions. M3 considers two different fractured samples. HM2 and HM3 are hydromechanical extensions due to point and line fluid injections respectively. The HM4 case allows for fracture propagation.

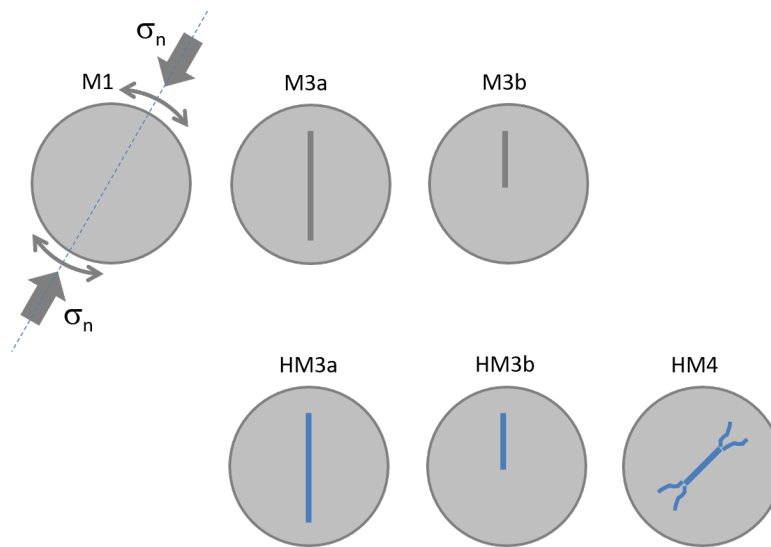


Figure 1.5: Benchmarking idea for 2D plane-strain conditions; upper figures represent M processes, lower figures represent HM processes

The benchmark exercises are briefly summarized below:

#### M-Process

- M1: Mechanical response of an intact sample to polyaxial stress boundary conditions
- M3a: Mechanical response of a fractured sample to polyaxial stress boundary conditions (two-wing fracture)
- M3b: Mechanical response of a half-fractured sample to polyaxial stress boundary conditions (one-wing fracture)

#### HM-Process

- HM3a: M1 plus fluid injection in a static fracture (HM process with line injection)
- HM3b: M1 plus fluid injection in a static half-fracture (HM process with line injection)
- HM4: M3a plus fluid injection in a dynamic fracture (HM process with line injection and fracture propagation)



## 1.2 Experimental analysis (EA)

A summary of the experimental facilities used for for Task G is given in Tab. 1.1. Experimental methodology and results are described in more detail in the relevant step descriptions.

- Step 1: Freiberg CNL/CNS experiments (Frühwirt, Pötschke, and Konietzky, 2021) (section 4)
- Step 2: GREAT cell experiments (McDermott et al., 2018) (section 5)
- Step 3: KICT experiments (Sun et al., 2023) (section 6)

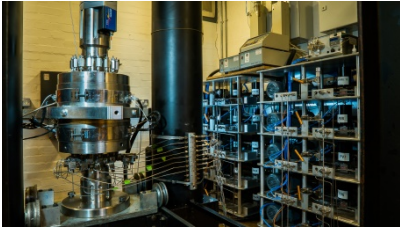
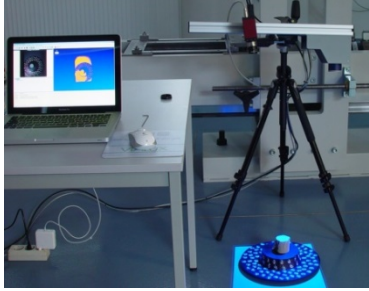

Task J Experimental Facilities		
University of Edinburgh	TU BA Freiberg	KICT
		
GREAT cell for polyaxial (including true-triaxial) THMC testing	3D surface and body scanner (max. 30μm resolution)	True-triaxial THM testing, High-resolution X-ray μCT, AE monitoring system

Table 1.1: Overview of experimental work in Task G

## References

- Frühwirt, Thomas, Daniel Pötschke, and Heinz Konietzky (2021). "Simulation of direct shear tests using a forces on fracture surfaces (FFS) approach". In: *Environmental Earth Sciences* 80.8. Cited by: 5; All Open Access, Hybrid Gold Open Access. DOI: [10.1007/s12665-021-09606-6](https://doi.org/10.1007/s12665-021-09606-6). URL: <https://www.scopus.com/inward/record.uri?eid=2-s2.0-85104006276&doi=10.1007%2fs12665-021-09606-6&partnerID=40&md5=38352a2edca39a24d14e93ed56c3fad>.
- McDermott, C.I. et al. (2018). "New Experimental Equipment Recreating Geo-Reservoir Conditions in Large, Fractured, Porous Samples to Investigate Coupled Thermal, Hydraulic and Polyaxial Stress Processes". In: *Scientific Reports* 8.1. Cited by: 6; All Open Access, Gold Open Access, Green Open Access. DOI: [10.1038/s41598-018-32753-z](https://doi.org/10.1038/s41598-018-32753-z). URL: <https://www.scopus.com/inward/record.uri?eid=2-s2.0-85054070649&doi=10.1038%2fs41598-018-32753-z&partnerID=40&md5=dbe9cf549a76065fee706766d0597676>.
- Sun, C. et al. (2023). "Thermally induced shear reactivation of critically-stressed smooth and rough granite fractures". In: *IOP Conference Series: Earth and Environmental Science* 1124.1. DOI: [10.1088/1755-1315/1124/1/012119](https://doi.org/10.1088/1755-1315/1124/1/012119). URL: <https://www.scopus.com/inward/record.uri?eid=2-s2.0-85146558465&doi=10.1088%2f1755-1315%2f1124%2f1%2f012119&partnerID=40&md5=b0a8c674baeb8d07dfe817c5c220b3f0>.

## 2 Methods

SAFENET focuses on the hydro-mechanical (HM) and thermo-mechanical (TM) responses of a fractured rock under various controlled stress magnitudes and orientations. In Section 2.1, we summarize the governing equations for poro-elastic and thermo-elastic deformation, fluid flow in porous media as well as in fractures. Plasticity effects are included in the constitutive relationships. These are the underlying governing equations for the SAFENET Task. Furthermore, we briefly introduce the various numerical methods that were involved in this project in Section 2.2.1.

To achieve SAFENET’s scientific goal of better understanding fracture initiation and evolution in crystalline rocks under hydro-mechanical and thermo-mechanical loading, a systematic experimental and modeling program was organized and completed under Task G of DECOVALEX 2023. Three experimental programs were carried out in Freiberg, Seoul and Edinburgh to study mechanical and thermo-mechanical shear and stress-dependent permeability changes in fractured crystalline rocks. For numerical analyses, the modeling teams offer a wide range of continuum mechanics and discontinuous methods for the numerical modeling of fracture mechanics processes (see Sec. 2.2). Details of the numerical methods are described in Mollaali et al., 2023, only a short overview is given here (Sec. 2.2, Tab. 2.1).

### 2.1 Governing equations

The basic framework of SAFENET is the theory of porous media: a combination of mixing theory with the concept of volume fractions and continuum mechanics. The thermo-hydro-mechanical (THM) model is considered: as local correspondences of the balance equations for energy (2.1), mass (2.2) and momentum (2.3) and under constitutive assumptions and continuity requirements, a system of coupled partial differential equations follows:

$$\text{T: } (\varrho c_p)^{\text{eff}} \frac{d_S T}{dt} + (\varrho_{\text{FR}} c_{pF}) \text{grad } T \cdot \tilde{\mathbf{w}}_{\text{FS}} - \lambda^{\text{eff}} \text{div}[\text{grad } T] = Q_T \quad (2.1)$$

$$\text{with } \tilde{\mathbf{w}}_{\text{FS}} = -\frac{\mathbf{k}}{\mu_{\text{FR}}} [\text{grad } p - \varrho_{\text{FR}} \mathbf{g}]$$

$$\begin{aligned} \text{H: } & \varrho_{\text{FR}} [\phi \beta_{pF} + (\alpha_B - \phi) \beta_{pS}] \frac{d_S p}{dt} - \varrho_{\text{FR}} [\phi_F \beta_{TF} + (\alpha_B - \phi) \beta_T^S] \frac{d_S T}{dt} \\ & + \varrho_{\text{FR}} \alpha_B \text{div} \frac{d_S \mathbf{u}}{dt} + \text{div}(\varrho_{\text{FR}} \tilde{\mathbf{w}}_{\text{FS}}) = Q_H \end{aligned} \quad (2.2)$$

$$\text{M: } \text{div}[\boldsymbol{\sigma}_S^E - \alpha_B p \mathbf{I}] + \varrho^{\text{eff}} \mathbf{g} = \mathbf{0} \quad \text{with} \quad \boldsymbol{\sigma}_S^E = \mathbb{C} : (\boldsymbol{\varepsilon} - \boldsymbol{\varepsilon}_p - \alpha_T^S \mathbf{I} \Delta T) \quad (2.3)$$

Here,  $\frac{d_S(*)}{dt}$  refers to the material time derivative related to the solid phase. The indices F, S stand for fluid (pore fluid) or solid (solid skeleton) and R denotes intrinsic quantities of a phase (e.g. the real density), which are not averaged over the mixture volume in the sense of the equivalent continua. The list of symbols is compiled in the Appendix A. The above equations apply to the porous medium. For fractured media, the description in the discontinuities is added, which is based on the balancing of the same variables, but is formulated e.g. for the low-dimensional continuum (fracture displacement, fracture flow etc.), see Appendix B.1 as an example for the Lower-Interface-Method (FEM-LIE).

## 2.2 Numerical methods

There exists several approaches for the numerical modeling of hydro–mechanical responses in fractured rock. Generally, they can be classified into two types of general approach, *sharp fracture approaches* (xFEM and etc.) and *diffuse fracture approaches* (phase-field models). In this study, eight teams collaborate to simulate and predict the hydro–mechanical reaction of fractured rock using different numerical methods and computing packages, Table 2.1.

Table 2.1: Numerical methods and codes

Team	Numerical methods	Codes	Section
UFZ	VPF-FEM	OpenGeoSys-6	(2.2.1)
CAS	hCA-FEM/xFEM	CASRock	(2.2.2)
TUBAF	LIE-FEM	OpenGeoSys-6	(2.2.3)
CNSC	ETEL-FEM	COMSOL	(2.2.5)
RWM/Q/UoE	CMEFM-FEM	COMSOL / OpenGeoSys-5	(2.2.4)
KIGAM	GBM-DEM	3DEC	(2.2.6)
SSM/DynaFrax	BPM-DEM	PFC	(2.2.7)
KAERI	IFDM-DEM	TOUGH/3DEC	(2.2.8)
DOE/LBNL	NMM	NMM	(B.2)
DOE/LBNL	FEM	FLAC3D	(B.3)
DOE/SNL	FEM	COMSOL	(2.2.5)

### 2.2.1 VPF-FEM

**Numerical method.** Variational phase-field for fracture models have become one of the most extensively used methods to simulate fracture propagation for a number of applications such as brittle (Bourdin, Francfort, and Marigo, 2000; Miehe, Hofacker, and Welschinger, 2010; Mesgarnejad, Bourdin, and Khonsari, 2015), ductile (Ambati, Gerasimov, and De Lorenzis, 2015; Kuhn, Noll, and Müller, 2016; Alessi et al., 2018; Yin and Kaliske, 2020), dynamic (Bourdin, Larsen, and Richardson, 2011; Borden et al., 2012; Li et al., 2016; Nguyen and Wu, 2018), fatigue (Seiler et al., 2018; Carrara et al., 2020), interface () desiccation (Maurini et al., 2013; Ca-juhi, Sanavia, and De Lorenzis, 2018), environment assisted Martínez-Pañeda, Golahmar, and Niordson, 2018; Schuler, Ilgen, and Newell, 2020; Cui, Ma, and Martínez-Pañeda, 2021, and hydraulic fracturing (Bourdin, Chukwudozie, and Yoshioka, 2012; Wheeler, Wick, and Wollner, 2014; Heider and Markert, 2017; Santillán, Juanes, and Cueto-Felgueroso, 2017; Choo and Sun, 2018; Mollaali, Ziaei-Rad, and Shen, 2019). Their popularity stems from their ability to represent the complex evolution of any number of fractures without confining their propagation to any specific grid.

**Mathematical model.** Griffith’s criterion was reformulated by Francfort and Marigo Francfort and Marigo, 1998 as the minimization of total energy, which is the sum of potential and fracture surface energy defined as:

$$\mathcal{F}(u, \Gamma) := \int_{\Omega \setminus \Gamma} W(\mathbf{u}) \, d\Omega + \int_{\Gamma} G_c \, d\Gamma, \quad (2.4)$$

the strain energy density and fracture toughness are represented by  $W(\mathbf{u})$  and  $G_c$ , respectively. Evaluating the crack surface energy for non-trivial crack geometry is challenging since it includes the surface integral

over an evolving discrete crack set  $\Gamma$ . To address this issue, the variational phase-field approach presented in Bourdin, Francfort, and Marigo, 2000 follows the approximation of Ambrosio and Tortorelli, 1992 via  $\Gamma$ -convergence Braides, 1998. The energy functional is regularized (Bourdin, Francfort, and Marigo, 2000) by introducing a scalar phase-field variable,  $v : \Omega \mapsto [0, 1]$  and a regularization length parameter  $\ell > 0$ ,

$$\mathcal{F}_\ell := \int_{\Omega} v^2 W(\mathbf{u}) \, d\Omega + \int_{\Omega} \frac{G_c}{4c_n} \left( \frac{(1-v)^n}{\ell} + \ell |\nabla v|^2 \right) \, d\Omega. \quad (2.5)$$

The work done by fluid pressure,  $\int_{\Gamma} p_f \llbracket \mathbf{u} \cdot \mathbf{n} \rrbracket \, d\Gamma$ , can be added to the total energy function, where  $p_f$  is the “net” pressure defined as the surplus pressure above the minimum stress and  $\mathbf{n}$  is the normal vector to  $\Gamma$ . The amount of jump over  $\Gamma$  might be approximated as (Bourdin, Chukwudozie, and Yoshioka, 2012; Chukwudozie, Bourdin, and Yoshioka, 2019):

$$\int_{\Gamma} \llbracket \mathbf{u} \cdot \mathbf{n} \rrbracket \, d\Gamma \approx \int_{\Omega} \mathbf{u} \cdot \nabla v \, d\Omega.$$

Because the toughness-dominated hydraulic fracturing regime takes no pressure loss in the crack into account, our total energy is as follows:

$$\mathcal{E}_\ell := \int_{\Omega} v^2 W(\mathbf{u}) \, d\Omega + \int_{\Omega} \frac{G_c}{4c_n} \left( \frac{(1-v)^n}{\ell} + \ell |\nabla v|^2 \right) \, d\Omega + p_f \int_{\Omega} \mathbf{u} \cdot \nabla v \, d\Omega. \quad (2.6)$$

Therefore we minimize (2.6) with the mass balance constrain as follows:

$$(\mathbf{u}_i, v_i; p_f) = \operatorname{argmin} \left\{ \mathcal{E}_\ell(\mathbf{u}, v; p) : \mathbf{u} \in \mathcal{U}(t_i), v \in \mathcal{V}(t_i, v_{i-1}), Q_i = \int_{\Omega} \mathbf{u} \cdot \nabla v \, d\Omega \right\}. \quad (2.7)$$

**Computing package.** The current model is implemented in an open-source code, OpenGeoSys (Bilke et al., 2019). OpenGeoSys (OGS) is an open-source scientific project that aims to develop numerical methods for simulating thermo-hydro-mechanical-chemical (THMC) processes in porous and fractured media. More information concerning the code and simulation examples are freely available at <https://www.opengeosys.org/>.

### 2.2.2 hCA-FEM/xFEM

**Numerical method.** Cellular automata uses a local updating rule to solve the state variables. According to cellular automata localization theory, only the states of the cell itself and its neighbours contribute to the state of the cell. We can develop the updating rule for displacement, temperature and fluid pressure using local equilibrium conditions, in which the local stiffness is taken from the element stiffness of FEM/xFEM (Feng, Pan, and Zhou, 2006; Pan et al., 2013). The hybrid cellular automata scheme avoids the solution of large linear equations and the complexity herein. To represent the fracture, interface elements or Goodman elements, internal interfaces or internal boundaries, and weak elements, are implemented .

In this study, the fluid flow and mechanical processes are sequentially coupled. The fluid mass balance and momentum balance equations are expressed in Section 2.1. The equations can be solved via spatial and temporal discretization. Instead of using traditional numerical methods, the cellular automata technique is used for the solution of displacement and fluid pressure on the spatial scale by developing the local updating rule

according to the local equilibrium conditions,

$$\mathbf{K}_{ij}\Delta\mathbf{H}_j = \Delta Q_i, \quad (2.8)$$

where  $\mathbf{K}_{ij}$  is the local nodal stiffness matrix, which is summation of stiffness of cell elements related to the cell node.  $\Delta\mathbf{H}_j$  is the incremental value of physical variable;  $\Delta Q_i$  is the incremental value of source term. When the incremental value of physical variable is obtained, the incremental value of source term at its neighbour cell nodes can be solved. The neighbour cell nodes will follow the same rule and the global calculation is divided into the iterations of cells one by one. On the temporal scale, an explicit finite difference scheme is used. The equation of the time derivative of specified physical variable as a column vector is listed below,

$$\left\{\frac{\partial\mathbf{H}}{\partial t}\right\}_t = \frac{1}{\Delta t}(\mathbf{H}_t - \mathbf{H}_{t-\Delta t}) + o(\Delta t), \quad (2.9)$$

where  $o(\Delta t)$  is an error item and

$$\left\{\frac{\partial\mathbf{H}}{\partial t}\right\} = \left\{\left(\frac{\partial\mathbf{H}_1}{\partial t}\right) \quad \left(\frac{\partial\mathbf{H}_2}{\partial t}\right) \cdots \left(\frac{\partial\mathbf{H}_n}{\partial t}\right)\right\}^T, \quad (2.10)$$

weak elements approach are chosen for fracture representation (Papachristos et al., 2017). For a weak element, the stiffness of the element depends on the size of the element and a simple formula is used for selecting the appropriate Young's modulus for the element, i.e.,

$$\frac{1}{E_f} = \frac{1}{E_r} + \frac{1}{(k_n \times b)}, \quad (2.11)$$

where  $E_f$  and  $E_r$  are Young's modulus of fracture and rock matrix element, respectively.  $k_n$  is the normal stiffness of fracture and  $b$  is the mean size of fracture element, which can be defined as the square root of fracture element area.

**Computing package.** The model is based on a self-developed software, CASRock, which is based on cellular automata, FEM and xFEM (Pan, Feng, and Hudson, 2009; Pan, Feng, and Zhou, 2012; Pan et al., 2016; Pan, Yan, and Feng, 2012). CASRock is a versatile software that can be used to simulate rock failure processes, tunnel excavation, multi-field coupling, dynamic load effects, and more. Further information about the software can be found at [www.casrock.cn](http://www.casrock.cn).

### 2.2.3 LIE-FEM

**Numerical method.** A diverse range of methods exists to capture fractures in porous media as embedded lower-dimensional continua (Flemisch et al., 2017; Hattori et al., 2017; Nishiyama et al., 2014; Lecampion, 2009; Vinci, Renner, and Steeb, 2014; Berre, Doster, and Keilegavlen, 2019; Schmidt and Steeb, 2019). This lower-dimensional representation is often achieved by integrating over one spatial dimension—usually the fracture thickness—subject to a set of assumptions, such as parallel-plate flow. The lower-dimensional interface element (LIE) method has been developed to enhance the capability of simulating hydraulic fracturing and shearing (Watanabe et al., 2012; Yoshioka et al., 2019). Several constitutive formulations for the hydraulic and mechanical behaviour of the discrete interface are available, such as elasto-plasticity or cohesive-zone models.

**Mathematical model.** A coupled hydraulic-mechanical problem is solved on a domain  $\Omega = \Omega^+ \cup \Omega^-$  separated into the two indicated parts by a sharp interface  $\Gamma$  representing the fracture. The weak form of the mechanical problem reads

$$\int_{\Omega \setminus \Gamma} [\boldsymbol{\sigma} : \nabla \mathbf{v} - \rho \mathbf{g} \cdot \mathbf{v}] \, d\Omega - \int_{\Gamma} \boldsymbol{\tau}_{\Gamma} \cdot [[\mathbf{v}]]_{\Gamma} \, d\Gamma = \int_{\partial\Omega} \boldsymbol{\tau} \cdot \mathbf{v} \, d\Gamma, \quad (2.12)$$

where an enriched Bubnov-Galerkin test function  $\mathbf{v}$  of the same space as the solid displacement itself was introduced, consisting of a continuous (standard) part  $\mathbf{v}_c$  and a Heaviside enrichment  $H(\mathbf{x})\mathbf{a}_{\Gamma}$  in the form

$$\mathbf{v} = \mathbf{v}_c + H(\mathbf{x})\mathbf{a}_{\Gamma}, \quad (2.13)$$

with the Heaviside function  $H(\mathbf{x}) = \pm 0.5 \, \forall \mathbf{x} \in \Omega^{\pm}$  distinguishing the domains separated by the fracture.

Note that  $\boldsymbol{\sigma}$  and  $\mathbf{t}_{\Gamma}$  are the total stresses and tractions, respectively, in a HM formulation of a fluid-saturated porous medium in the sense of the effective stress principle:

$$\boldsymbol{\sigma} = \boldsymbol{\sigma}' - \alpha p_p \mathbf{I} \quad \text{with} \quad d\boldsymbol{\sigma}' = \mathcal{C}_e : d\boldsymbol{\varepsilon}_e \quad (2.14)$$

$$\boldsymbol{\tau}_{\Gamma} = \boldsymbol{\tau}'_{\Gamma} - p_p \mathbf{n}_{\Gamma} \quad \text{with} \quad d\boldsymbol{\tau}'_{\Gamma} = \mathbf{K}^f d\mathbf{w}^e. \quad (2.15)$$

The weak form for matrix flow based on a standard scalar test function  $\bar{v}$  reads

$$\int_{\Omega} \bar{v} [S p'_S + \alpha \nabla \cdot \mathbf{u}'_S - \delta_{\Gamma}(\mathbf{x}) \tilde{q}_F] - \mathbf{q}_p \cdot \nabla \bar{v} \, d\Omega = \int_{\partial\Omega} \bar{v} q_n \, d\Gamma, \quad (2.16)$$

with the Darcy velocity  $\mathbf{q}_p$ . The fluid exchange  $\tilde{q}_F$  is active only at fractures where the following weak form is used:

$$\int_{\Gamma} \bar{v}_{\Gamma} [b'_S + b S^f p'_S + b \tilde{q}_F] - b \mathbf{q}_p^{\Gamma} \cdot \nabla_{\Gamma} \bar{v}_{\Gamma} \, d\Gamma = \int_{\partial\Gamma} \bar{v}_{\Gamma} q_n^{\Gamma} \, dl. \quad (2.17)$$

The mass exchange between fractures and matrix remains implicit as the current implementation assumes local mass exchange processes between matrix and fracture to be sufficiently fast to ensure pressure continuity between both compartments.

**Computing package.** The present model is implemented in the scientific open-source finite element software OpenGeoSys (Bilke et al., 2019; Nagel et al., 2013).

#### 2.2.4 CMEFM-FEM

**Numerical method.** The RWM/Quintessa/UoE team applied a full contact representation of the embedded fracture using the COMSOL Multiphysics® Structural Mechanics module (AB, 2020), with an internal boundary load applied to either side of the fracture to represent the fluid pressure. This approach allows the possibility of representing opening, friction, separation, and other complex non-linear behaviours at the fracture surface, though only the zero friction case is considered in the benchmark. The remainder of the domain is modelled

as an elastic rock medium.

**Mathematical model.** The main equation for solving the system is standard solid mechanics solving for displacement. Full details of this approach are in the COMSOL Multiphysics® Structural Mechanics module User Guide (AB, 2020).

The contact boundary pair(s) representing the fracture is used to introduce contact forces when in contact; when there is a gap, there is no contact and thus no contact force. By its nature, this method can be highly non-linear and therefore can be difficult to solve. For this benchmark model, a penalty factor formulation is used which describes a spring stiffness of two connecting boundaries in contact, defining the contact stress, which allows some (potentially nonphysical) penetration as the contacts are forced together. The contact stress is governed by:

$$T_n = \begin{cases} -P_n g_n + T_0 & \text{if } g_n \leq \frac{T_0}{P_n} \\ 0 & \text{otherwise.} \end{cases} \quad (2.18)$$

Here,  $T_n$  and  $T_0$  are the contact stress and contact stress at zero gap;  $g_n$  is the gap; and  $P_n$  is the penalty factor that is tuned to give the required contact elasticity.

**Computing package.** COMSOL Multiphysics® using the Structural Mechanics module which is a commercial application for simulation and coupled process modelling using the finite element method.

### 2.2.5 ETEL-FEM

**Numerical method.** The finite element method, implemented in the commercial software COMSOL Multiphysics® (AB, 2020), was used to numerically solve the governing equations of the mathematical model. Solid serendipity elements are used to represent the intact rock, with cubic shape functions for the mechanical behaviour, and linear shape functions for the flow behaviour. The fracture is represented as an interface with springs shear and normal directions that connect adjacent solid elements. The normal and shear stresses across the fracture are proportional to the relative shear and normal displacements through the spring constants.

**Mathematical model.** The mathematical model was developed from the theory of poro-mechanics (Nguyen, 2021), with the governing equations in Section 2.1.

**Computing package.** The model was implemented in the COMSOL Multiphysics® package. COMSOL solves partial differential equations using the finite element method. The Structural Mechanics and Darcy's flow modules of COMSOL were used in this work. For more information: [www.comsol.com](http://www.comsol.com).

### 2.2.6 GBM-DEM

**Numerical method.** In a grain-based model (GBM), the microstructure of a rock-like material is represented as a group of angular particles. Particles can be rigid or deformable (elastic or inelastic), while interfaces are treated as boundary conditions between particles. The interaction of the particles (blocks) and their interfaces (contacts) is calculated using a distinct element method (DEM) (Ghazvinian, Diederichs, and Quey, 2014; Lan, Martin, and Hu, 2010; Li, Bahrani, et al., 2020; Wang et al., 2021).

**Mathematical model.** The calculation in the DEM alternates between the application of a force-displacement law at all contacts and Newton's second law for all blocks. At each timestep, the integration of the law of motion provides the new block positions resulting from the known forces acting on the blocks. The contact forces are then updated from the force-displacement law and known displacements. The elastic force increments at contact are calculated as

$$\Delta \mathbf{F}^n = -k_n \Delta \mathbf{u}^n A_c \quad (2.19)$$

$$\Delta \mathbf{F}^s = -k_s \Delta \mathbf{u}^s A_c. \quad (2.20)$$

where  $\mathbf{F}^n$  is the contact normal force,  $\mathbf{F}^s$  are the contact shear force vectors,  $k_n$  is the contact normal stiffness,  $k_s$  is the contact shear stiffness,  $\mathbf{u}^n$  is the contact normal displacement,  $\mathbf{u}^s$  are the contact shear displacement vectors, and  $A_c$  is the area of the sub-contact.

The contact model approximates linear representation of stiffness and yield limit, considering the displacement-weakening as a result of loss in frictional, cohesive, and tensile strength at the onset of failure. If the maximum limit for normal force or shear force is exceeded, the onset of failure is identified at the sub-contact, and the new contact forces are corrected.

The hydro-mechanical simulation is performed by sequentially alternating mechanical calculation and fluid calculation. The fluid flow inside the fracture (zero-strength contacts or failed contacts) is approximated by two-dimensional horizontal flow within parallel walls separated by a hydraulic aperture. The hydraulic aperture is updated by the elastic opening,  $\mathbf{u}_e^n$ , due to the change in effective normal stress, and the plastic opening,  $\mathbf{u}_p^n$ , due to slip-induced dilation:

$$\Delta \mathbf{u}_p^n = \Delta \sigma'_n / k_n \quad (2.21)$$

$$\Delta \mathbf{u}_p^n = \mathbf{u}_p^s \tan \psi, \quad (2.22)$$

where  $\sigma'_n$  is the effective normal stress,  $\mathbf{u}_p^s$  is the plastic shear displacement, and  $\psi$  is the dilation angle.

The flow rate per unit width of the fractures is characterized by the cubic law (Witherspoon et al., 1980). The fracture pressures are calculated and stored in the flow elements corresponding to the grid points of blocks. After the flow rate calculations, the pressures are updated taking into account the net flow into the flow element and possible changes in flow element volume due to the incremental motion of the surrounding blocks:



$$\Delta p_f = K^f Q \frac{\Delta t}{V} - K^f \frac{\Delta V}{V_m}, \quad (2.23)$$

where  $K^f$  is the bulk modulus of the fluid,  $Q$  is the sum of flow rates into the flow element from all surrounding contacts,  $\Delta t$  is the timestep,  $V$  is the flow element volume, and  $V_m$  is the average flow element volume of the previous and current timesteps.

**Computing package.** The above approach is implemented into the commercial code 3DEC (Itasca Consulting Group, Inc., 2017), a three-dimensional DEM code.

### 2.2.7 BPM-DEM

**Numerical method.** In the bonded particle model (BPM), a material is simulated as an aggregate of rigid particles (2D: disks, 3D: spheres) bonded at their contact points with finite stiffness and strength (Potyondy and Cundall, 2004).

**Mathematical model.** In BPM, Newton’s second law of motion ( $F=ma$ ) is applied to individual particles to determine their accelerations and subsequent movements based on the net forces acting on them. The contact model within BPM governs these interactions, accounting for normal and tangential forces that arise when particles come into contact. These forces include elastic and plastic deformation, friction, and potential bonding or breakage between particles. Failure of the bond is governed by the Mohr Coulomb failure criterion. A fracture (discontinuity) is simulated by smooth joint contact model. The smooth joint model allows for the representation of pre-existing cracks and joints by defining a smooth surface along which particles can slide and separate. This model adjusts the contact forces and moments based on the relative displacement and rotation of particles across the joint, ensuring realistic simulation of fracture propagation and interaction. In a bonded state, the interface exhibits linear elastic behavior. When the strength limit is exceeded, causing the bond to break, the unbonded interface becomes linear elastic and frictional with dilation. In the latter state, Coulomb sliding occurs, where slip is controlled by imposing a Coulomb limit on the shear force.

**Computing package.** The modelling concept and mathematical formulation are implemented in the commercial code Particle Flow Code 2D/3D (PFC2D/3D) (Itasca Consulting Group, Inc., 2008), using FISH programming.

### 2.2.8 IFDM-DEM

**Numerical method.** The integral finite difference method (IFDM) for thermal-hydraulic analysis (Pruess, Oldenburg, and Moridis, 2012) is coupled with the distinct element method for discontinuum mechanical analysis (Itasca Consulting Group, Inc., 2020), to describe the thermal-hydraulic-mechanical analysis of fractured rock mass (Kwon et al., 2021). The discontinuum model consists of tetrahedral meshes and discontinuity faces, and the discontinuities are assumed as elements with aperture-size width for the thermal-hydraulic analysis in IFDM. IFDM and DEM exchange and reflect the thermal, hydraulic, and mechanical parameters in each time step of IFDM.

**Mathematical model.** The mechanical analysis is based on the interactions between blocks due to the movements and rotations in DEM module. The interactions are calculated by Newton's second law on each face of blocks and the force–displacement law on each contact between blocks (Equations (2.19) and (2.20)). The contacts between blocks represent the discontinuities, and the detailed mechanical models can be applied on each contact. In this study, the linear normal and shear deformation models are assumed with the shear and tensile failure. When the normal and shear stresses reach the tensile and shear strength of the discontinuity, the normal and shear stress yield and induce the plastic displacement. Both elastic and plastic displacements in the normal direction on discontinuities accompany the hydraulic aperture change, and the shear displacement also can induce the dilation of aperture based on the dilation angle, which is the parameter regarding the discontinuity roughness. The permeabilities of discontinuities are updated based on the hydraulic aperture change and the cubic law (Witherspoon et al., 1980). The updated permeability field in every mechanical simulation is transferred to IFDM module for hydraulic analysis.

IFDM module constructs the elements and connections data for hydraulic analysis. The discontinuity elements have appropriate hydraulic properties equivalently calculated or updated from the mechanical analysis. The fluid flow in IFDM module is based on the mass balance equation between two adjacent elements. The mass balance equation includes the multiphase and multicomponent fluid flow (Pruess, Oldenburg, and Moridis, 2012).

$$\frac{d}{dt} \int_{\Omega} M^i d\Omega = \int_{\partial\Omega} \mathbf{j}^i \cdot \mathbf{n} d\Gamma + \int_{\Omega} q^i d\Omega, \quad (2.24)$$

where,  $\Omega$  is the volume of an arbitrary domain,  $\partial\Omega$  is the closed surface of the domain with the normal vector  $\mathbf{n}$ ,  $M$  is the mass per volume,  $\mathbf{j}$  is the mass flux,  $q$  is the mass source/sink, and  $i$  denotes each component. The mass flux consists of individual phase fluxes calculated by Darcy's law.

$$\mathbf{j}^{\beta} = \rho^{\beta} \mathbf{q}_p^{\beta} \quad (2.25)$$

where,  $\mathbf{j}^{\beta}$  is the mass flux of phase  $\beta$ ,  $\rho^{\beta}$  is the density of phase  $\beta$ ,  $\mathbf{q}_p^{\beta}$  is the Darcy velocity in phase  $\beta$ . According to the mass balance equation, the pore pressures on whole elements are updated, and the pore pressure data is transferred to DEM module to be reflected for the mechanical analysis in every hydraulic time step.

**Computing package.** The model in this study is implemented in TOUGH2, a numerical simulator for multi dimensional, multiphase, multicomponent fluid flows and heat transfer (Pruess, Oldenburg, and Moridis, 2012), and 3DEC, a block-based three-dimensional distinct element method (Itasca Consulting Group, Inc., 2020). Additional TOUGH–3DEC linking algorithms for the coupled processes are developed in FISH, FORTRAN, and MATLAB (Kwon et al., 2021).

### 2.2.9 NMM - Numerical Manifold Method

**Numerical method.** The numerical manifold method (NMM), based on the theory of mathematical manifolds (Hu, Wang, and Rutqvist, 2015; Hu and Rutqvist, 2020; Hu et al., 2024), is a promising method for analyzing both continuous and discontinuous media. In the past three decades, NMM has been developed and success-

fully applied to various problems. NMM has been applied for analyzing crack growth, hydraulic fracturing, coupled flow and mechanics processes in fractured media, and grouting of fractures around tunnels. Previously, we have developed comprehensive model capabilities to simulate dynamic frictional contacts and deformation that are coupled with fluid flow, heat transfer and chemical reaction based on the numerical manifold method. The modeling capabilities involve different governing equations, constitutive relationships, couplings of thermal-hydro-mechanical-chemical (THMC) processes, and approaches for addressing intersections and shearing of interfaces at different scales. These modeling capabilities have been applied for analyzing coupled processes in porous, fractured, and granular systems at different scales. Numerical Manifold Method (NMM) using independent meshes for interpolation and integration of continuous and discontinuous state variables of the multifield problem (Shi, 1992). More details of the NMM methods can be found in the Appendix B.2.

## 2.3 Characterisation of Laboratory Scale Fractures

*Gonçalo Cunha, Steven Benbow, Claire Watson, Alex Bond*

### 2.3.1 Context and Task Overview

Understanding of shear reactivation of pre-existing discontinuities for brittle host rocks is an area of considerable interest for radioactive waste disposal. In particular, the potential for existing features to undergo shear displacements and related changes in permeability as the result of coupled thermal, mechanical, hydraulic and chemical effects can all have significant impacts on repository safety functions (e.g., by creating permeable pathways or, for very large displacements, mechanical damage of waste packages). Safety Implications of Fluid Flow, ShEar, Thermal and Reaction Processes within Crystalline Rock Fracture NETWORKS (SAFENET – Task G) is designed to investigate these processes using highly constrained and state of the art laboratory experiments. In many respects this task continues the work from DECOVALEX-2015, in which NWS participated (Bond et al., 2016; Bond et al., 2017; Chittenden et al., 2016-08-03; McDermott et al., 2015).

### 2.3.2 Fracture Roughness Characterisation (PhD support work)

As outlined in the previous annual reports (Bond et al., 2023) including explicit representations of fracture surfaces and apertures in physical models is fraught with issues, even in 2D, so there is considerable interest in linking the available understanding of fracture topography with effective hydro-mechanical properties at different spatial scales. This element of work is focused on looking at describing fracture topography in a way that it is useful to interpreting effective fracture properties, and their evolution with the intention of supporting the work discussed in the preceding sections. This work has been conducted as a component of a part funded NWS PhD at the University of Edinburgh.

Min et al., 2016 summarises many methods to quantify roughness; however none of these methods takes into account the directionality or 2D spatial distribution of the roughness. Zimmerman and Main, 2004 introduce the concept of utilising the semi-variogram to describe fracture roughness but don't apply it.

In the ongoing UoE PhD work, a variogram analysis approach to each of the fracture face in order to understand the distribution of variability of roughness (fracture face topography) as a function of unit of distance (lag) and direction. With this information available, it should be possible to recreate the original fracture to very good detail from an upscaled (using up to 94% fewer points) version of the original fracture face using a kriging method for each face. Following this, aperture models can be created as a function of the “matchedness” of the two faces which in turn would allow THMC numerical modelling to be performed on a less computationally expensive model as opposed to using the original dense dataset. This method also allows the statistical properties of the fracture aperture to be characterised to be used in more indirect methods of physical modelling, e.g. through definitions of centiles of aperture, contact ratios, etc. This may be helpful to characterise the properties of a fracture surface below the scale of homogenisation for a given model, and hence support the appropriate parameterisation for the processes in question. Much of the work presented in Bond et al., 2023 is repeated here, because the variogram nomenclature is quite specialist and so it is helpful to include, to aid the reader.

**Data Acquisition** In a dataset exhibiting any spatial correlation, two data points closer together are more likely to have similar values than two points further apart. We can use this principle to analyse all points within a certain distance for their variability. This data collection will allow the construction of geostatistical tools to analyse our dataset such as h-scatterplots and semi-variograms. This process is then repeated for other separation distances (lags) and for other directions, if any anisotropy within the data has been found to exist. Because a vector, by definition, possesses a direction and magnitude (lag), vectors can be useful to acquire the type of data in question. If one was to draw a vector between two points, for all data pairs aligned in a particular direction for a particular lag ( $h$ ), one could create a table of tail and head values of that particular vector, for instance if  $lag = 1$  in the South-North direction (Figure 2.1a). In addition, if we are interested in the vector  $45^\circ$  (SE-NW) and  $lag = \sqrt{2}$ , this exercise would resemble Figure 2.1b).

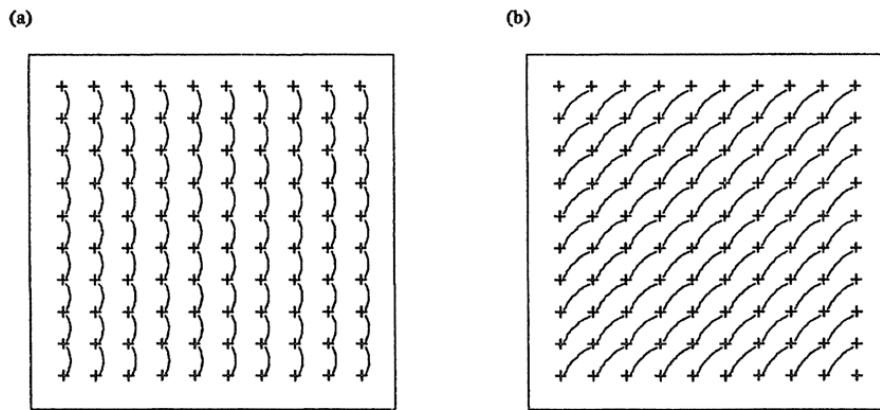


Figure 2.1: h-Scatterplot data acquisition examples. Example a) shows the data acquisition for an h-Scatterplot in the South-North direction for lag = 1. Similarly, b) shows the data acquisition for an h-Scatterplot in the Southwest-Northeast direction for a lag of  $\sqrt{2}$ , (Isaaks and Srivastava, 1989).

If the data are not regularly spaced as in the previous case (but instead scattered), the data points have to be grouped into bins, otherwise the probabilities of finding significant amount of point pairs in exactly a certain direction and lag would become too small and the data sample would have too few points, if any. A cone of investigation is used which is composed by the direction of the vector (angle), the angle tolerance (angle amount added to either side of the vector direction), bandwidth (maximum distance measured perpendicular to the vector direction) and lag tolerance (distance measured in either direction along the vector’s direction which in conjunction with the bandwidth and angle tolerance thresholds forms the bin’s limits); shown in Figure 2.2.

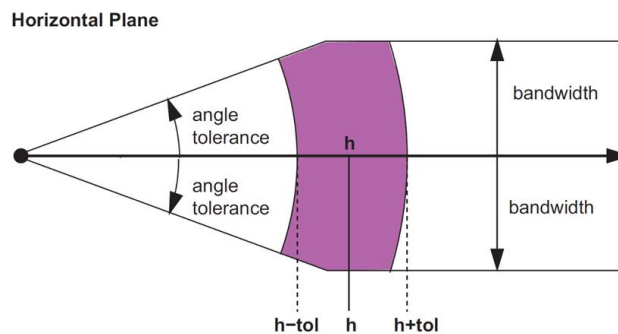


Figure 2.2: Illustration of the cone of investigation for scattered data:  $h=lag$ ,  $h-tol/h+tol = lag\ tolerance$ , angle tolerance and bandwidth, (Pyrzcz and Deutsch, 2014 - 2014).

The parameters chosen vary with the dataset statistics including the mean distance between points for the lag. If the data has no anisotropy, an angle tolerance can be set to 90° or above which renders an omnidirectional variogram. Angle tolerance and bandwidth depend on short scale average point distance, clustering, point density and overall spatial distribution of the data points. Lag tolerance is generally ½ lag in that direction. Number of lags is generally chosen to be equal to ½ the total distance times the lag distance in that direction. This is on account of the fact that distance lags greater than ½ the space containing the data in one particular direction don't permit the data in the middle of that space to be used.

**Variograms** A variogram is a mathematical tool to analyse spatial discontinuity, as opposed to the spatial continuity of the co-variance function (equation 2.27). In effect, there is no reason not to use the latter to describe the spatial continuity, nevertheless, the variogram (or semi-variogram) has been used more widely and frequently. The variogram is the graphical representation of the average squared difference between a property value pair for all measurement locations within a specific lag distance over all lag distances (equation 2.26). The semi-variogram is half the average value, hence “semi”. A semi-variogram is said to be omnidirectional if no distinction between the vector direction is made, i.e. all point pairs in the data set, within that lag distance for all directions, are measured. Conversely, a semi-variogram is said to be directional when only the vectors along an arbitrary direction for that specific lag are considered, within the bounds of the angle tolerances and other buffers explained in detail in section 2.3.2.

$$\gamma(h) = \frac{1}{2N(h)} \sum_{i=1}^{N(h)} (z(x_i) - z(x_i + h))^2 \quad (2.26)$$

$$C(h) = \frac{1}{2N(h)} \sum_{i=1}^{N(h)} \left( (z(x_i) - \overline{z(x_i)}) * (z(x_i + h) - \overline{z(x_i + h)}) \right)^2 \quad (2.27)$$

where  $x_i$  is the location  $x$  with index  $i$ ,  $x_i + h$  is the location  $x$  with index  $i$  plus the current lag distance,  $z$  depicts the attribute (elevation in this case) of the point location in parenthesis. The overbar indicates the mean.

**Semi-variogram analysis** Semi-variogram analysis assumes intrinsic stationarity of the dataset, that is, there is no observable trend; in other words, the data has a constant mean and the variation is caused by the random process (residual). This means that the spatial correlation of  $Z$  (any variable, in this case elevation) depends only on the separation distance (lag,  $h$ ) and direction and not on the location. In this way we are not only dealing with one data pair but we increase the number of pairs, for a given lag distance. If the dataset is isotropic, meaning the semi-variance of the dataset is independent of the direction it is measured, then only one semi-variogram is needed to describe the spatial distribution of the data, otherwise two are necessary for a 2D variable or three for a 3D variable. If the data has a trend the intrinsic hypothesis is violated, i.e. the stationarity is not held or the mean depends on the spatial location, then detrending is necessary and the variogram analysis must be done on the residuals (Bivand, Gómez-Rubio, and Pebesma, 2013 - 2013; Vieira et al., 2010). The simplest and often easiest way to accomplish this is to fit a trend surface by least squares and subtracting it from the original data, resulting in a new dataset (variable) called residuals.

**Example Case Study** To illustrate the process, a greywacke fracture from Cloburn Quarry (in Scotland) was analysed - the top surface scan is shown in Figure 2.3.

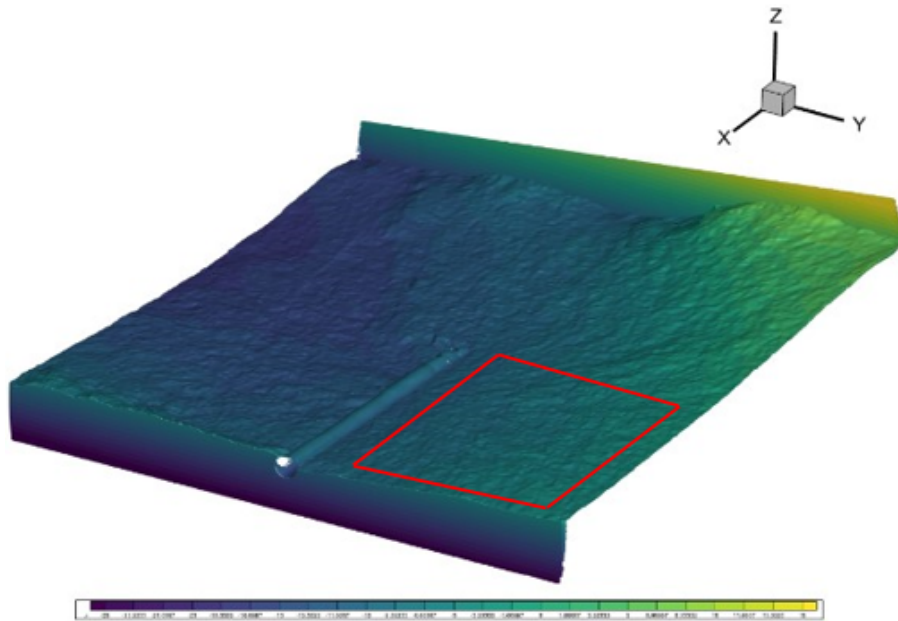


Figure 2.3: Dataset: Matched greywacke top and bottom surfaces. The red square depicts a sub-dataset used for the study.

Due to the number of points in the whole dataset, a subset of the whole dataset (within the 4th quadrant illustrated by the red square) has been retrieved and used for the analysis, henceforth referred to as the “dataset”. The “walls” at each end of the x-axis are simply artefacts of the scanner used to analyse the surface of the rock, whereas the cylinder in the centre is a borehole used to inject fluids through the fracture for other experiments prior to the scanning. Figure 2.4 shows the top fracture (henceforth referred to solely as the “fracture”) map in absolute values as retrieved by the scanner. It is immediately obvious from the colour scale that the fracture has a South-North upward trend, i.e. the values along this direction tend to gradually increase. The variogram map of Figure 2.4 has been calculated with lag = 5 mm (the choice on 5 mm in this case was made to enhance clarity in the shown variogram map). The presented normalised variogram map (Figure 2.5) gives a visual representation of the likelihood that two points on Figure 2.4 with a relative offset from one another will have different values (hence the domain on the variogram map is twice the size of the profiled surface). The map clearly shows a high degree of continuity approximately  $N85^{\circ}E$  whereas there is a strong discontinuity approximately  $N5^{\circ}W$ . This is highly indicative of a substantial trend in the profiling data and hence the data need to be corrected further.

The presence of a trend can be easily verified by the absence of a stable sill (Vieira et al., 2010). As we can see in Figure 2.6 top, the semi-variogram fulfils this requirement, hence the data has a strong trend in the  $0^{\circ}$  direction. In the same figure bottom, the trend is much weaker, if present. This cannot be fully corroborated because the semi-variogram doesn’t reach the theoretical sill. For this reason, the trend needs to be quantified and removed. To accomplish this, a plane is fitted through the data and each point is subtracted the z-value of the plane at the same x, y location, providing us with a residual de-trended dataset (Figure 2.7). The variogram map can again be calculated for this new dataset (Figure 2.8) giving us new directions of maximum and minimum spatial continuity in red, compared to the ones from the original trended dataset in green.

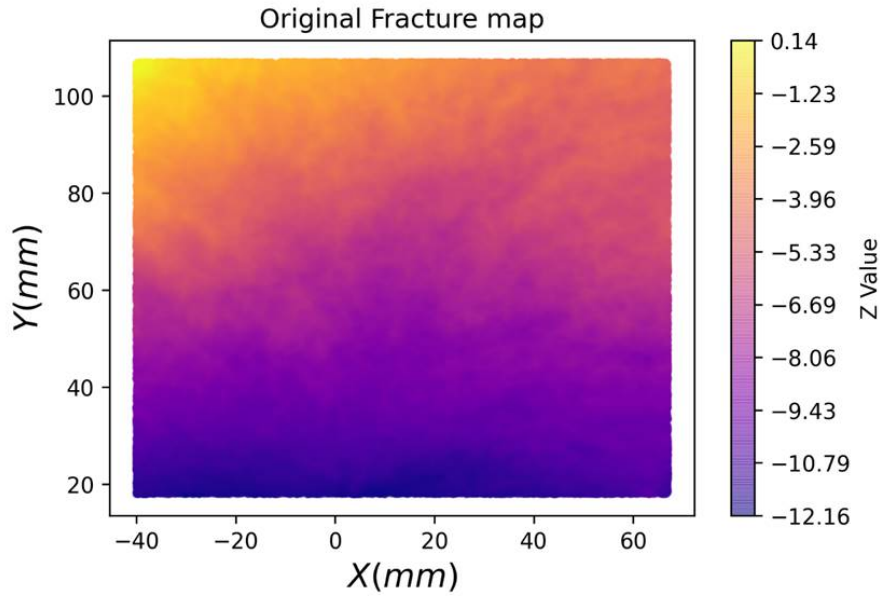


Figure 2.4: Fracture map of the greywacke top surface original data for the red square area only (Quadrant 4). X, Y and Z values are in mm.

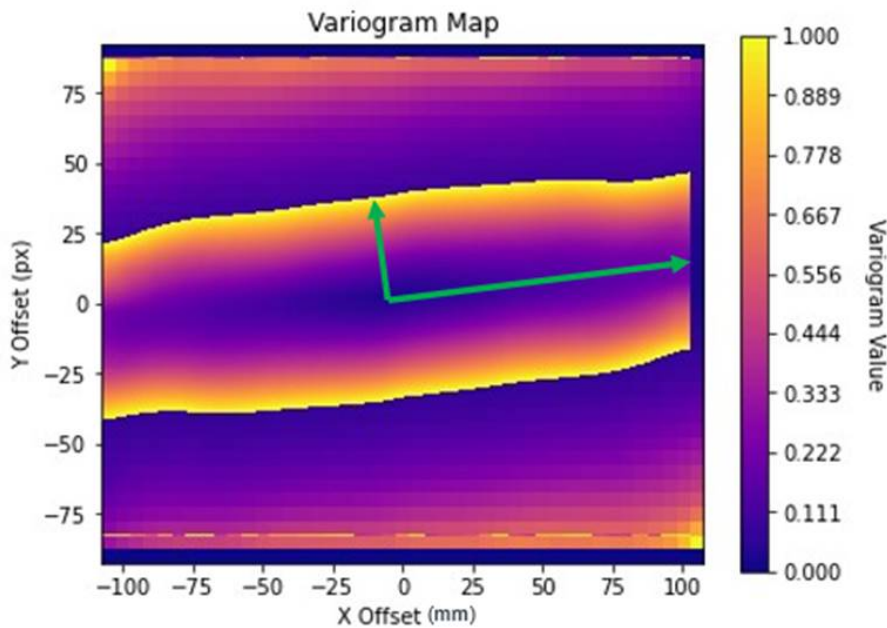


Figure 2.5: Variogram map of Figure 2.4 using normalised data and lag = 5 mm. X and Y values are in mm.

**Example Upscaling** Upscaling the high-resolution profile data is necessary for future numerical modelling and comparison of the results of effective parameterisation for different treatment of explicit variability (scale of homogenisation). An example is given here upscaling the original data to reduce the number of data points, to create the basis for kriging the fracture and comparing back to the original data. The chosen methodology for the upscaling was to sub-divide the fracture into many square bounding boxes (BBs). The number of BBs depends on the scale used: scale 1 uses BBs with sides equal to the average minimum distance between points whereas all subsequent scales use BBs with double the side length, until there's too few BBs to continue. The data points inside each BB are then fitted to a bilinear plane, similar to the process of removing the trend from



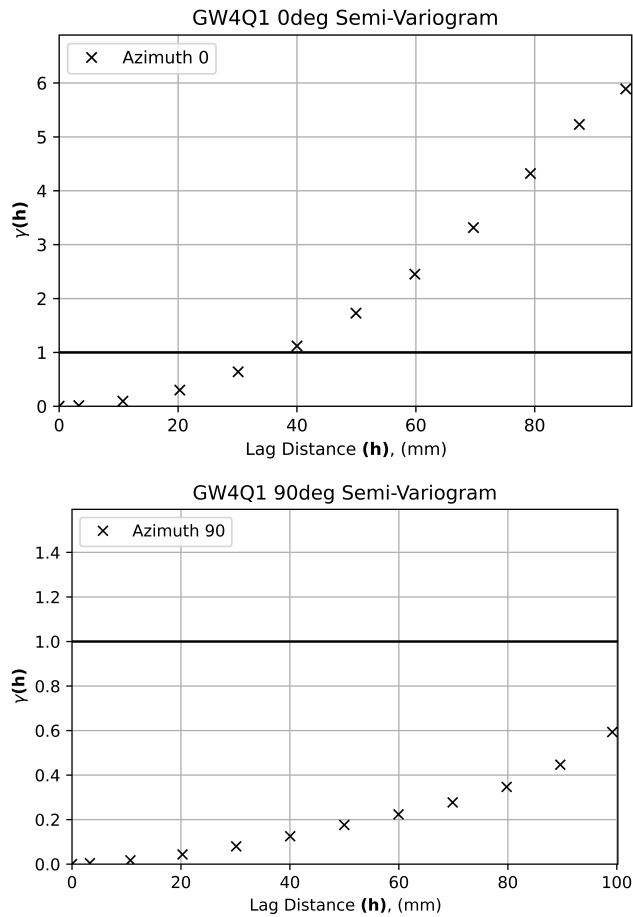


Figure 2.6: Semi-variograms for  $0^\circ$  orientation (top) and  $90^\circ$  (bottom), note the change in y-axis scale between the two graphs.

the original dataset (see Figure 2.7 top corner). The elevation-value of the centre of the BB is taken as the representative value. This approach tends to mitigate problems of taking simple averages within a BB where the number of data points is few or spatially clustered within a BB. Furthermore, in this technique, only the plane's central point is retained which changes the data's nature from unstructured to structured, reducing the number of points and simplifying the data structure. Results of upscaling are shown in Figure 2.9. An early example kriged structure using the upscaled points is shown in Figure 2.10. The data clearly retain the general structure, but the range of data has increased through the process.

As outlined in the previous sections, creating numerical models based on explicit representations of fracture surfaces and apertures is computationally expensive and time consuming hence there is considerable interest in understanding the best method to upscale the topography whilst conserving the statistics of the initial fracture topography and apertures. The method discussed here also allows for interpolation and extrapolation, up to certain limits, which in turn allows for a better control over the density of the model: even further to the raw data if required.

### 2.3.3 Kriging

The normalized (from Figure 2.7) residuals (Figure 2.11a) and the kriging results (Figure 2.11b), using the scale 2 upscaled points from Figure 2.9, are shown below.

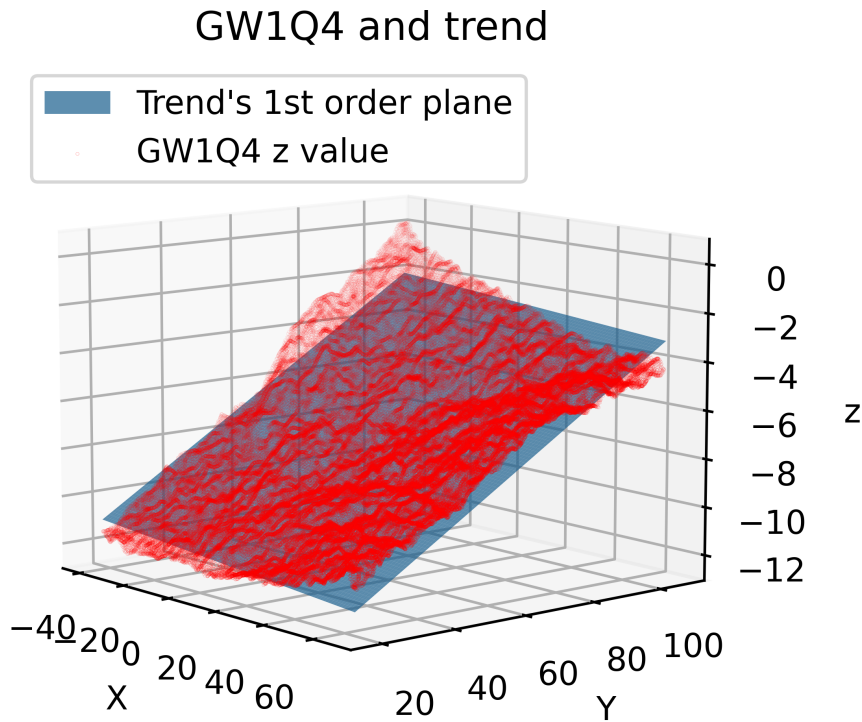


Figure 2.7: Fracture map of residuals after trend has been subtracted (inset top-left). X and Y values are in mm.

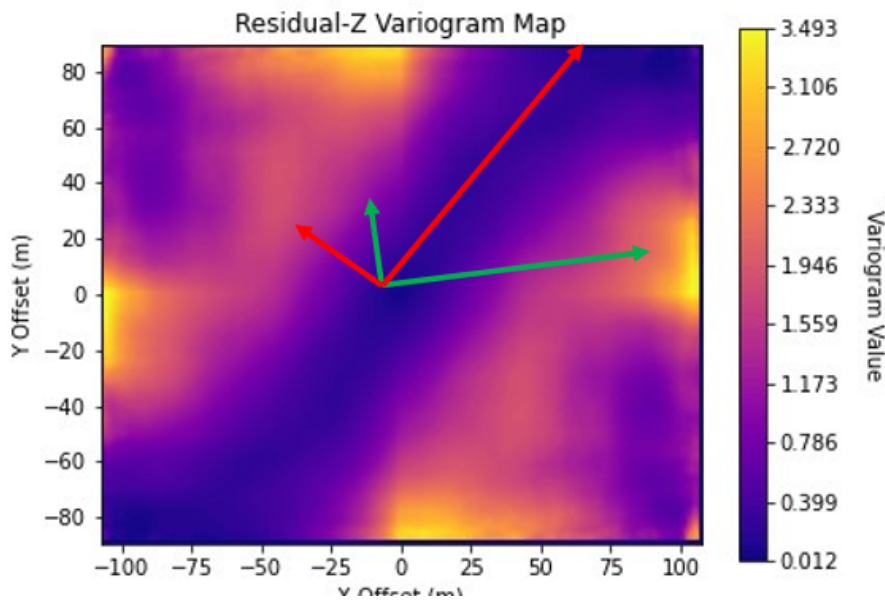


Figure 2.8: Variogram map of Figure 2.7 using raw data and lag = 1 mm. X and Y values are in mm. Red arrows are the interpreted minor and major directions of spatial continuity whilst the green ones refer to the trended data from Figure 2.5.

The number of points reduces from 138,771 to 38,092 points using the scale 2 upscaled points from Figure 2.9 with a x-density and y-density of 1 mm between each upscaled data point. This is one of the advantages of this method which is to reduce the amount of elements to compute in the couple processes numerical model's mesh by reducing the number of points. The distributions of both aperture surfaces are shown in

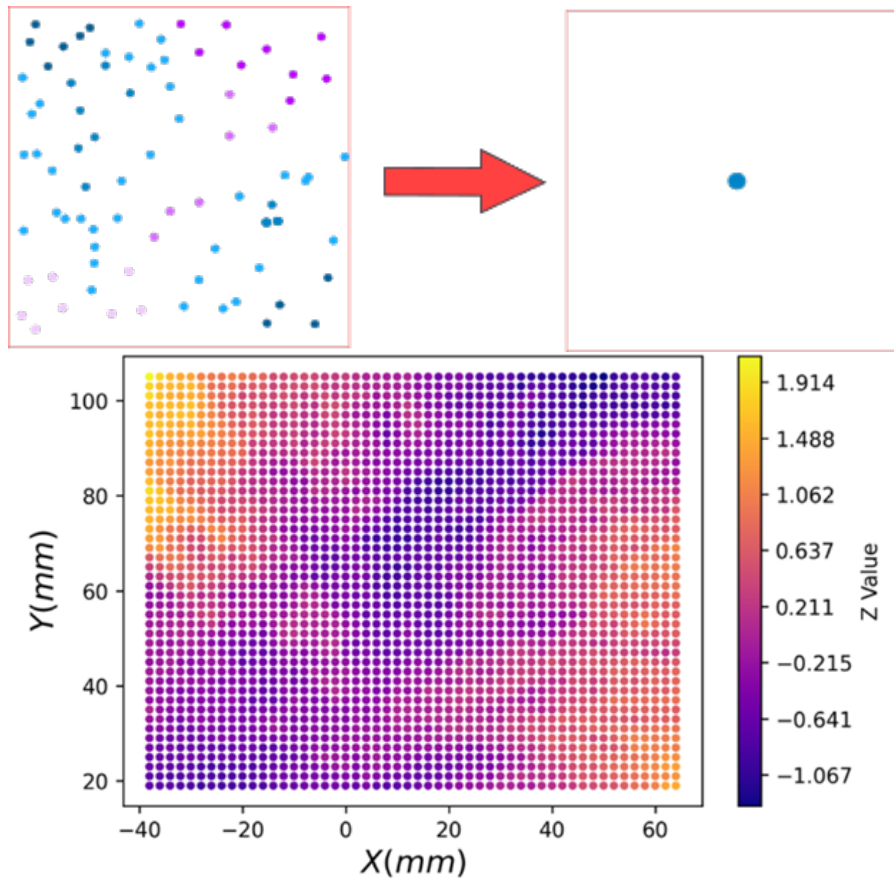


Figure 2.9: Upscaling technique illustration using a plane fitting in each bounding box and taking the bounding box central point's z-value.

Figure 2.12. The distribution for the normalised GW1Q4 Residuals shows a perfect normal distribution because that is the fundamental variability structure assumed, whereas the kriged surface has variability re-introduced as an intrinsic consequence of the kriging process.

The difference (error) between original normalised residuals (Figure 2.11a) and kriged results (Figure 2.11b) can be seen below in Figure 2.13.

With a maximum absolute error of 0.3 mm and a coefficient of determination of nearly 1, and no structure in the residuals, the surfaces are here demonstrated to be extremely similar. What is left is to confirm is how the method can be used to support modelling and any limitations of the method.

#### 2.3.4 Representative Elementary Volume (REV)

The upscaling process itself raises the question of how far can the data be upscaled before it loses its statistical meaning. This occurs when the sample points become too far apart for the scale being analysed or the reconstruction's error becomes too big. Whilst performing the variogram (spatial continuity) analysis on each upscaling scale, it became noticeable that, apart from the obvious loss in detail as the scale increases, there was a point where semi-variograms could not accurately be modelled without significant uncertainty. This loss of resolution was equally noticeable on the variogram map as the available data points' number became gradually smaller. This behaviour provides a notional 'Representative Elementary Volume' (REV) of the aper-

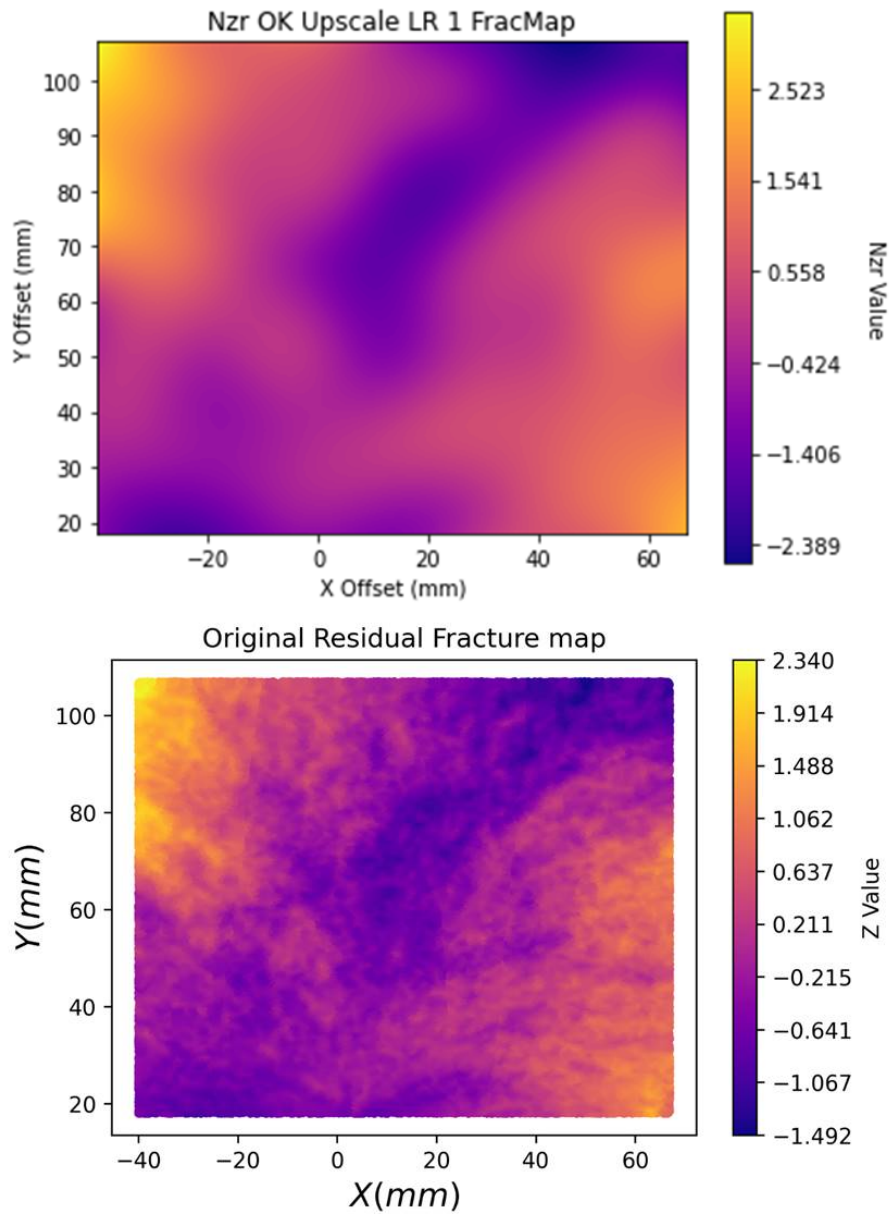


Figure 2.10: Comparison of a kriged dataset (top) based on the upscaled surface data compared with the original high-resolution dataset (bottom).

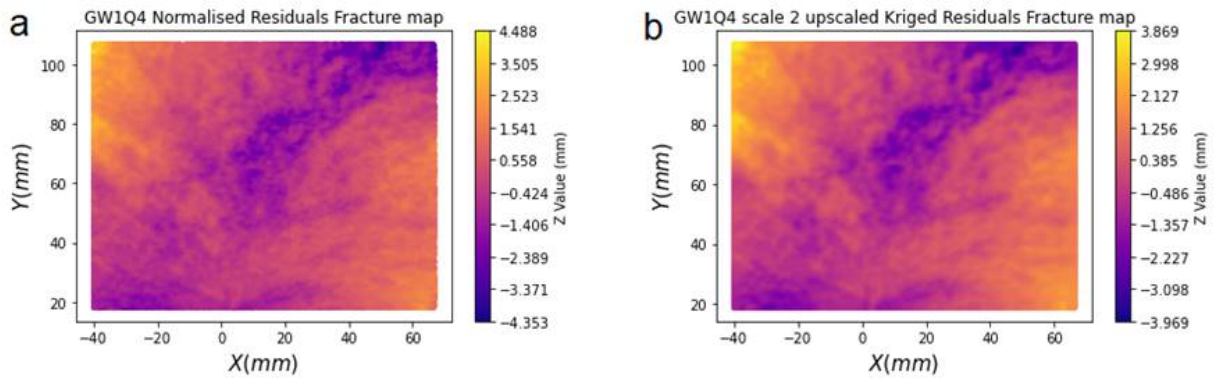


Figure 2.11: a) Normalised original data's residuals and b) Kriging results (using Figure 2.9 base points).

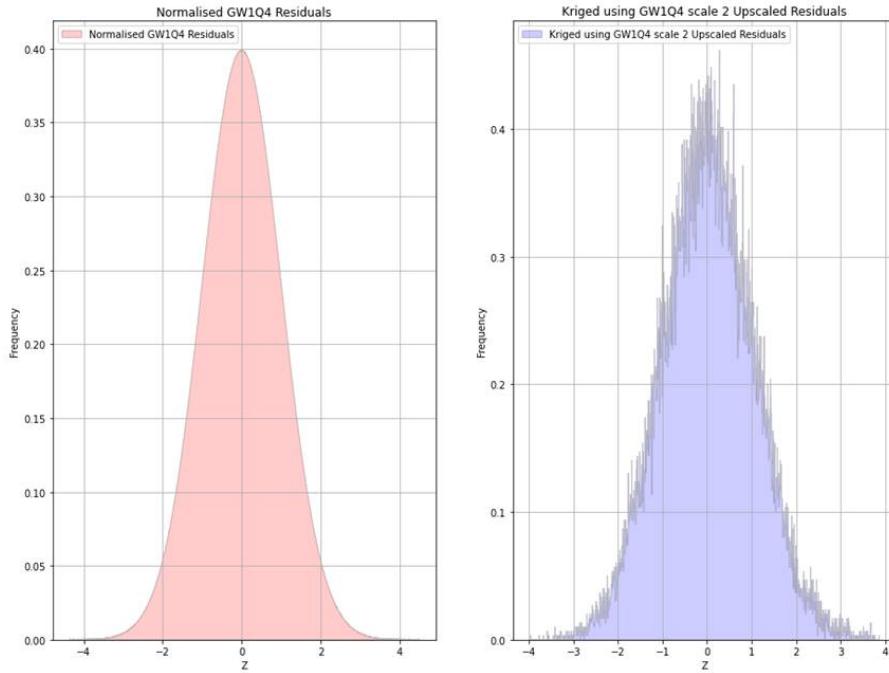


Figure 2.12: Frequency distribution of the normalised GW1Q4 residual fracture points (related to Figure 2.11a) and the frequency distribution of the kriged surface using GW1Q4 scale 2 upscaled residual points (related to Figure 2.11b).

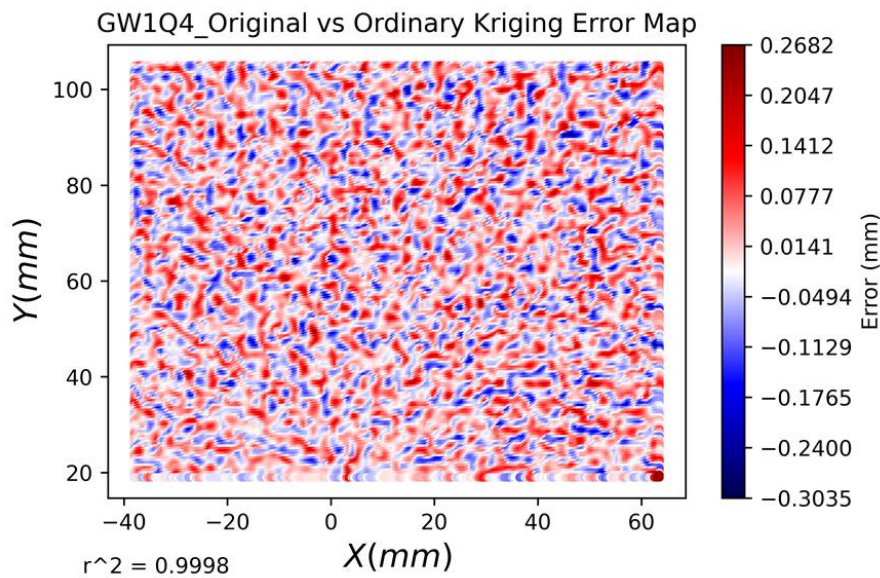


Figure 2.13: Difference (error) between original normalised fracture aperture and kriged fracture aperture using upscaled scale 2 points.

ture distribution of the fracture (the spatial scale above which the effective heterogeneity of a system can be homogenised, for a given purpose (Drugan and Willis, 1996)). To estimate the REV, the top and bottom surfaces of the fracture were matched as closely as possible taking care not to overlap or cross, which would result in a “negative aperture” and the difference was calculated, providing an estimated aperture distribution. Figure 2.14a shows the normalised fracture aperture surface resulting from this matching and Figure 2.14b its respective variogram map. Figure 2.15 shows the semi-variograms for the major (of  $67.5^\circ$ ) and minor ( $157.5^\circ$ ) continuity directions.

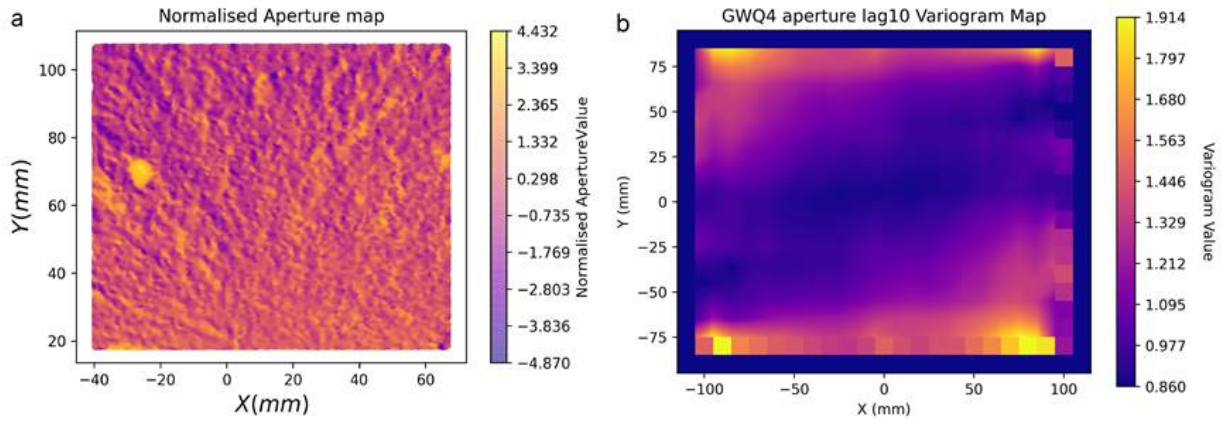


Figure 2.14: Normalised Greywacke Quadrant 4 (GWQ4): a) Aperture map; b) Log10 Aperture Variogram Map.

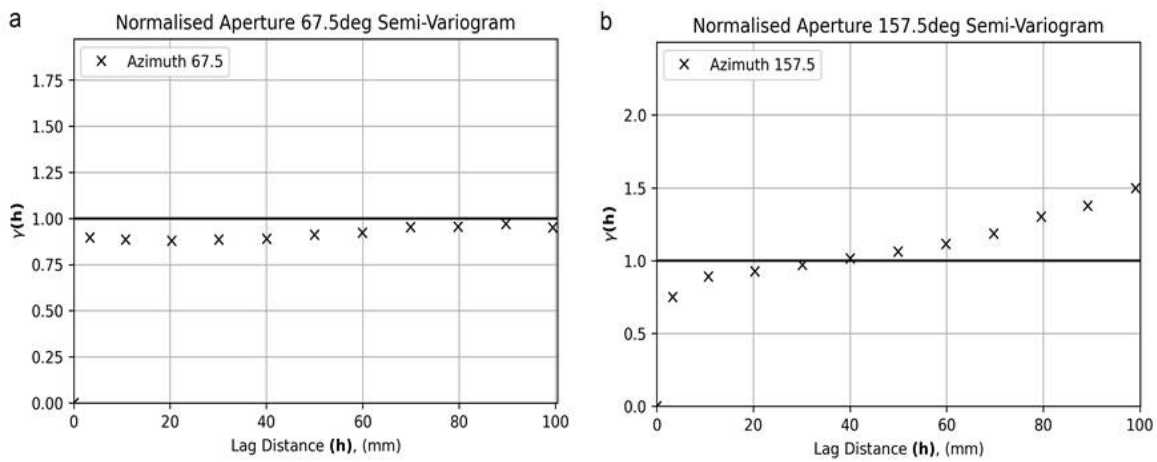


Figure 2.15: Normalised Greywacke Quadrant 4 (GWQ4): a) Aperture semi-variogram for  $67.5^\circ$  direction; b) Aperture semi-variogram for  $157.5^\circ$  direction.

After upscaling, the number of points available obviously reduces which leads to weaker estimations of the spatial continuity directions and semi-variances along those vectors, as we can see in both examples for scale 9 and scale 19 upscaling factors (Figure 2.16 & Figure 2.17 and Figure 2.18 & Figure 2.19, respectively).

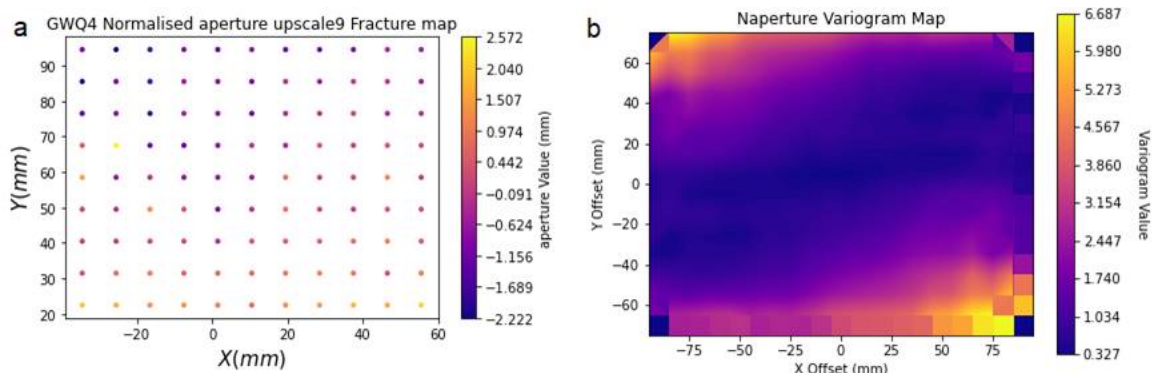


Figure 2.16: Normalised Greywacke Quadrant 4 (GWQ4) Upscale 9: a) Aperture map; b) Aperture Variogram Map

When the fracture is upscaled too far, the statistics are not representative, thus the semi-variograms and variogram maps start having gaps and the semi-variograms have very few points, which will prove insufficient for an accurate semi-variogram modelling. This is interpreted as beyond the REV of the fracture: for the purposes

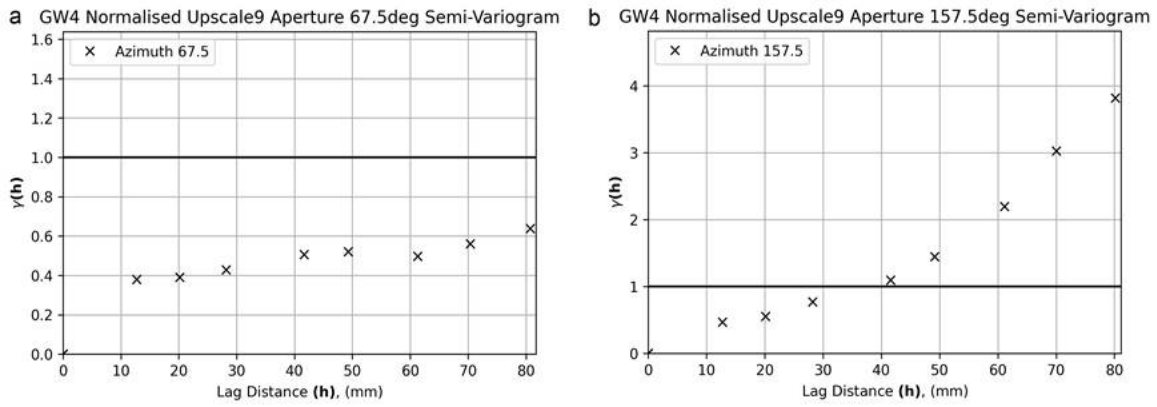


Figure 2.17: Normalised Greywacke Quadrant 4 (GWQ4) Upscale 9: a) Aperture semi-variogram for 67.5° direction; b) Aperture semi-variogram for 157.5° direction.

of the surface variability the REV will then be an upscaling level above where these ‘gaps’ are observed.

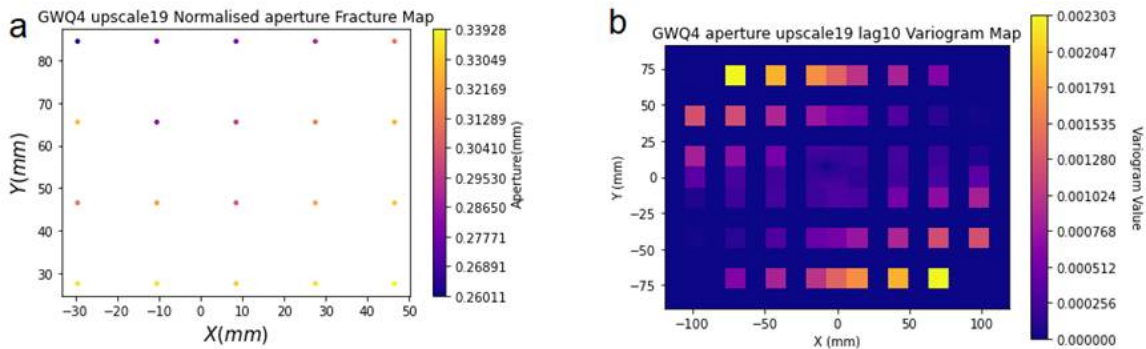


Figure 2.18: Normalised Greywacke Quadrant 4 (GWQ4) Upscale 19: a) Aperture map; b) Aperture Variogram Map

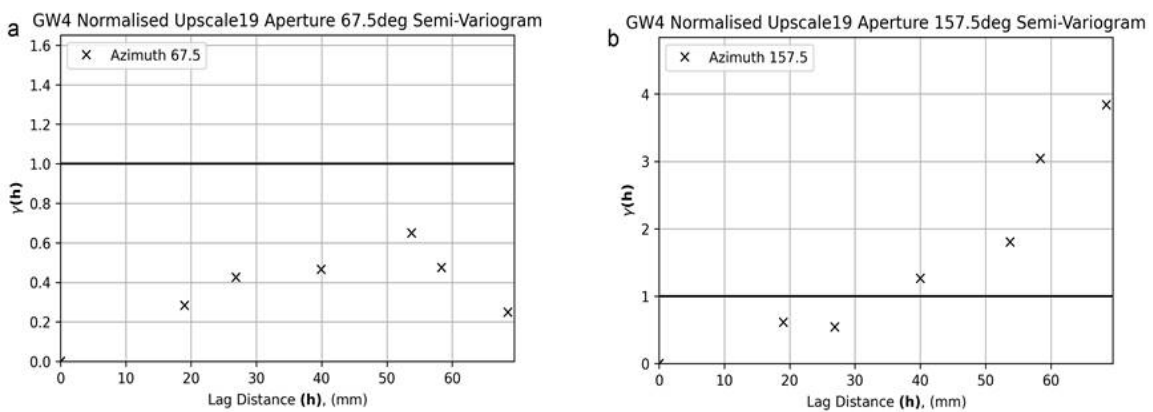


Figure 2.19: Normalised Greywacke Quadrant 4 (GWQ4) Upscale 19: a) Aperture semi-variogram for 67.5° direction; b) Aperture semi-variogram for 157.5° direction.

The variogram maps suffer a lot more detail loss from scale 9 to 19 than from scale 1 to 9. This is due to the gaps between the points being smaller than the lag used for the analysis, leaving gaps in the variogram map in scale 19. At this scale, identifying the directions is much harder whereas for scale 9 the difference is almost indistinguishable. The semi-variograms however lose structure, especially for the major continuity direction in this case, even from scale 1 to 9 but even more so in scale 19 where it is quite difficult to see the structure and use the experimental semi-variogram to model the continuous variogram. The choice of which scale represents

the data's 'REV' is subjective and dependent on application, but in this particular case, scale 9 seems to be a good compromise depending on the desired model's points density and accuracy. It is suspected the loss of detail will depend on the nature of the initial dataset itself (absolute number of data points, clustering, areal extension, the upscaling method, etc.) or the parametrisation chosen for the analysis including the lags in the x- and y-directions. More work will need to be done to have a more robust idea of the implication of the data upscaling has in on the spatial continuity results and how that affects the 'REV' of the data.

### 2.3.5 Extrapolation

It is also of interest to have the ability to scale up fractures' descriptions and their characteristics to where there isn't available data (extrapolation), without simply assuming that the part of the fracture measured is representative of other parts of the fracture. With the use of spatial continuity statistics, albeit still statistical extrapolation in the literal sense, the directional and separation distances variabilities of the dataset can be used to predict the asperities heights or aperture spacings of fractures to a larger scale, rather than using traditionally more simplistic statistics. With the two (major and minor) directions of spatial continuity and respective vector ranges, an ellipse of correlation can be drawn. This ellipse is in effect the limit up to which a point has any influence or correlation to any other point in its vicinity. In other words, the point at the centre of the ellipse has no correlation or influence outside this ellipse of correlation. This means that the ellipse limits the area up to which extrapolation can be estimated, which in turn depends on the data itself. The more data that are available for the spatial continuity analysis and the wider those data are distributed, the better the chances of "extending" the ranges of the correlation vectors and thus the limit to which extrapolation can be estimated. However, this will ultimately depend on the variance of the data as the lag distance increases and is, of course, directly related to the nature of the data. Figure 2.20 shows the upscaled aperture field inside the red polygon and between the red and the blue polygons the extrapolation using the spatial continuity of the aperture field. This extrapolation is limited by the ranges and directions of the spatial continuity analysis, i.e. the ellipse of correlation drawn by the two major and minor continuity vectors' directions and ranges.

### 2.3.6 Application of Spatial continuity to Finite Element Method models meshes

The amount of datapoints in fracture scans, and consequently in derived aperture fields, are often too many to use as nodes in FEM coupled THMC models' meshes. There is therefore the need to create a mesh encompassing the dataset and upscale the datapoints onto the mesh: first natural instinct is to average the points, which disregards the spatial continuity of the data which may have implications on the models' results. This is similar to the exercise of upscaling the aperture distribution into a grid from Figure 2.9.

Depending on the spatial continuity of the data, points within the element that do not share correlation will not be used in the prediction. Conversely, if the correlation ellipse reaches outside the element, points outside the element may be used in the prediction calculation. Four Hydro-Mechanical models were created using the fracture aperture field of a Freiberg gneiss using a combination of the two upscaling methods (arithmetic averaging and kriging) and two mesh element sizes, which rendered a coarse model (32x32 elements) and a fine model (64x64 elements). Both the coarse and the fine models have fringes on either side: 2 elements in the coarse and 4 in the fine models. This was added to equalise the fluid pressures along the boundary, which has proven beneficial in avoiding overpressures and artefacts in the model and hence erroneous results.



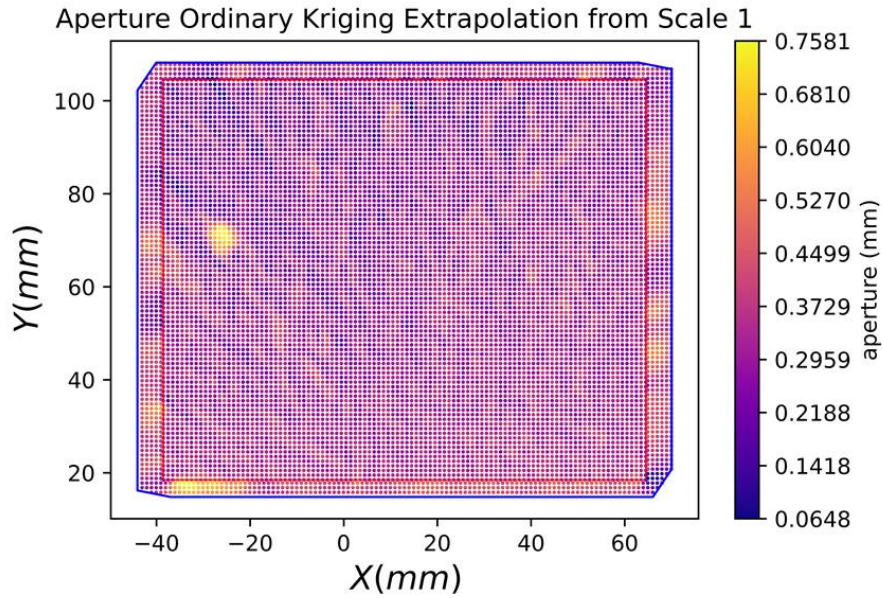


Figure 2.20: Within red square: Greywacke Quadrant 4 (GWQ4) Upscale 1 Aperture field. Between red square and blue polygon: extrapolation using spatial continuity analysis.

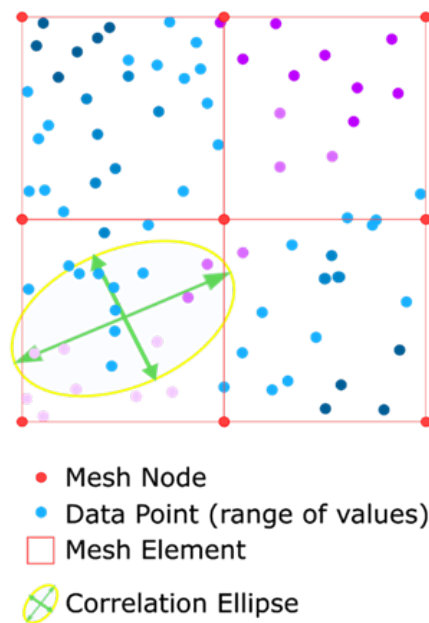


Figure 2.21: Predict the value at the centre of the model's element using kriging and the spatial continuity of the data, which uses only the points that are statistically correlated to each other.

This exercise of comparing the two models is analogous to using creating a model of the raw data and one of the upscaled data and then comparing the results. The code used for the simulation was the OGS-5 code from McDermott et al., 2015 where the aperture field is used to calculate the permeability field based on the normal stress acting on the fracture and then performing a flow simulation. The code allows for the application of normal stress on the fracture plane, calculated from experimental conditions at different time steps, which alters the aperture and permeability fields rendering mass flow results and a flow channel map.

The models seem to perform similarly when the mesh is fine enough. However, with the coarse mesh, the krig-

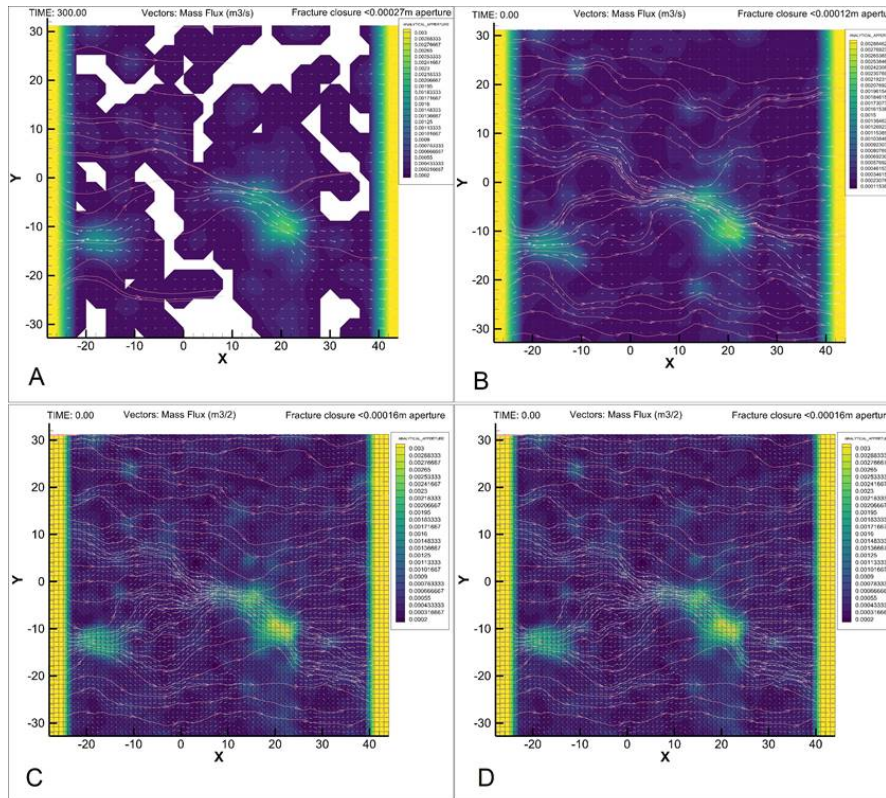


Figure 2.22: Model comparison: The top row shows the coarse model (32x32 elements) and the bottom row the fine model (64x64 elements) – The 2 and 4 fringes’ elements in either side (coarse and fine models respectively) are not accounted for. Left and right columns display the averaging method (arithmetic averaging and kriging, respectively). The colour map represents the hydraulic aperture, the white vectors the fluid velocity and the pink arrows the fluid flow lines. The models are blanked where the fracture is deemed in contact across the two faces.

ing element averaging method performs much better than the normal element arithmetic averaging method. The differences in the aperture threshold for fracture closure are due to the fact the each model has different minimum values of aperture in the aperture field. There would need to be further investigation on the relationship between the spatial continuity and the element size and what controls the threshold of when one method is more beneficial than the other.

**Single fracture Hydro-Mechanical OGS-5 code enhancement** The OGS-5 code mentioned above cannot cope with experimental conditions that cause the fluid pressure to exceed the normal stress at the element level: it has a control that causes the fluid pressure to be equal to the normal stress. This is to avoid element opening without bounds. An edited code was created to correct for this shortfall in order to model the greywacke fracture with the experimental conditions published in Fraser-Harris et al., 2020. The original code uses a loop to check for the number of elements in contact between two consecutive iterations. If the number of contacts does not change between two consecutive iterations, a trigger is turned on causing the code to exit the loop into the primary loop that in turn checks if the error is within a specified error threshold. The experimental conditions of the greywacke experiment cause the fluid pressure at the element level to rise above the applied normal stress. The old code’s coping mechanism is to set the element’s fluid pressure to zero to avoid opening without bounds, which causes artefacts. The new code turns off this mechanism and limits the element opening by setting the fluid pressure to 5% that of the normal stress. It then uses an average hydraulic

aperture control between iterations, alongside the number of contacts control from the old code. A note on the average hydraulic aperture comparison between two consecutive iterations: because that value is a float, the comparison is done through a function up to a defined threshold of within 5 decimal places, whereas the number of contacts control is an integer it does not need this extra function.

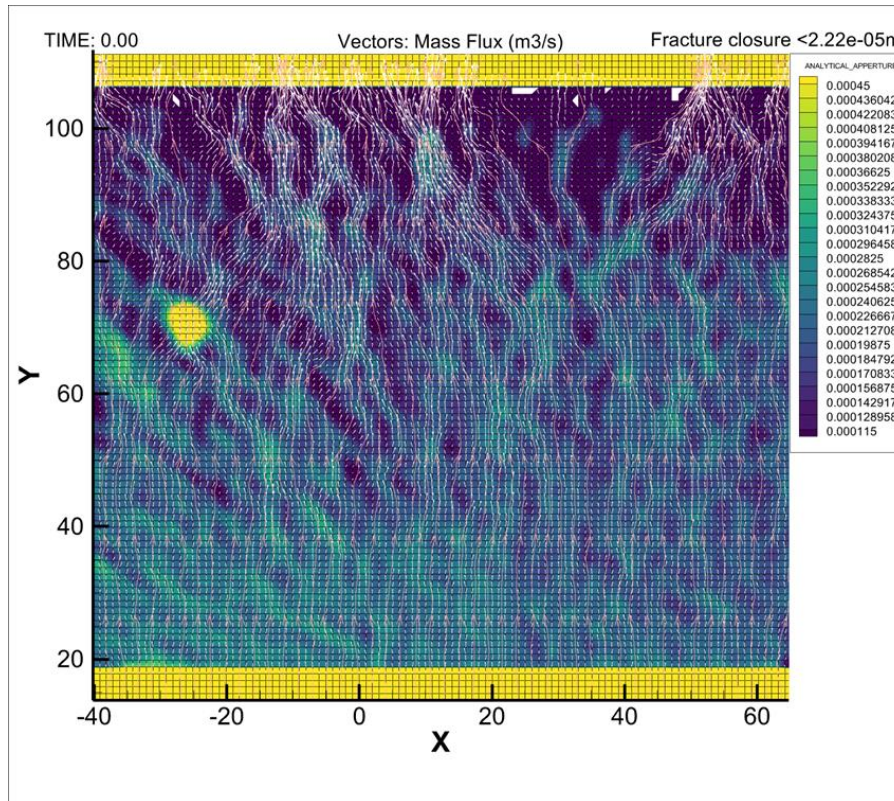


Figure 2.23: Greywacke Quadrant 4 Hydro-Mechanical model . The colour map represents the hydraulic aperture, the white vectors the fluid velocity and the pink arrows the fluid flow lines. The models are blanked where the fracture is deemed in contact across the two faces.

Figure 2.23 shows the results of time step 0 seconds which clearly demonstrates the fluid pathways (channels) forming during compression. Because the new code allows for element expansion, it also shows that the higher fluid pressure at the inlet and lower at the outlet causes higher and lower hydraulic aperture at the inlet and outlet, respectively, a sort of “trend” in the hydraulic aperture field alluding to the spatial continuity analysis section of the greywacke quadrant 4 rough surface.

### 2.3.7 Future work

The spatial continuity analysis process has proven successful in identifying the spatial continuity directions and the variability of the data along those two vectors. Similarly, this analysis was used in the kriging process which was also successful in interpolating the values at unknown locations with minimal errors. Additionally, this information can be used to extrapolate the data outside the known values up to the limits of the major and minor continuity directions' respective ranges. The immediate way forward is to now apply this knowledge to hydro-mechanical flow simulations and compare the results with similar models derived from the raw data to understand if there are significant deviations, and how those deviations manifest with different levels of refinement. It is possible that this method of characterising a fracture surfaces and its aperture distribution

will be preferable when it comes to computation resources and times because it will give the opportunity to understand the consequences of using de-refined fracture representations and selecting appropriate spatial scales for representation. It will now be possible to make the comparison between the experimental results in both the greywacke and the Freiberg gneiss experiments and the models. This will be the last exercise of the PhD due to time constraints. A suggested way forward is to find a mechanism to calculate the aperture distribution of the fracture after shear displacements with the caveat that that shear displacement doesn't occur in a trivial orientation but in the major and minor continuity directions identified in the spatial continuity analysis of the fracture roughness. It is our interpretation from the spatial distribution of the fracture roughness and the spatial continuity directions that similar amounts of shear displacement in each of the minor and major continuity directions will render results inversely proportionally to the ranges in those same directions.

## References

- Bivand, Roger., Virgilio. Gómez-Rubio, and Edzer J. Pebesma (2013 - 2013). *Applied spatial data analysis with R* Roger S. Bivand, Edzer Pebesma, Virgilio Gómez-Rubio. eng. Second edition. Use R! New York, NY: Springer. ISBN: 1461476186.
- Bond, A. et al. (2023). *Coupled Processes, Project: Participation in DECOVALEX-2023 Tasks, Second Annual Report, Quintessa Report for RWM QRS21612G-R2 v1.1*. Henley-on-Thames, UK. Tech. rep. Quintessa Limited.
- Bond, Alexander E. et al. (2016). "Development of approaches for modelling coupled thermal-hydraulic-mechanical-chemical processes in single granite fracture experiments". eng. In: *Environmental earth sciences* 75.19, pp. 1-. ISSN: 1866-6280.
- Bond, Alexander E. et al. (2017). "A synthesis of approaches for modelling coupled thermal-hydraulic-mechanical-chemical processes in a single novaculite fracture experiment". eng. In: *Environmental earth sciences* 76.1, pp. 1-. ISSN: 1866-6280.
- Chittenden, Neil et al. (2016-08-03). "Evaluating the importance of different coupled thermal, hydraulic, mechanical, and chemical process simulations during fluid flow experiments in fractured novaculite and fractured granite". eng. In:
- Drugan, W.J. and J.R. Willis (1996). "A micromechanics-based nonlocal constitutive equation and estimates of representative volume element size for elastic composites". eng. In: *Journal of the mechanics and physics of solids* 44.4, pp. 497-524. ISSN: 0022-5096.
- Fraser-Harris, A.P. et al. (2020). "Experimental Investigation of Hydraulic Fracturing and Stress Sensitivity of Fracture Permeability Under Changing Polyaxial Stress Conditions". In: *Journal of Geophysical Research: Solid Earth* 125.12. Cited by: 10; All Open Access, Green Open Access. DOI: [10.1029/2020JB020044](https://doi.org/10.1029/2020JB020044). URL: <https://www.scopus.com/inward/record.uri?eid=2-s2.0-85098225724&doi=10.1029%2f2020JB020044&partnerID=40&md5=705e37470080c4eaf99398d33dfa22d>.
- Isaaks, Edward H. and R. Mohan. Srivastava (1989). *Applied geostatistics / Edward H. Isaaks, R. Mohan Srivastava*. eng. New York ; Oxford University Press. ISBN: 0195050126.
- McDermott, Christopher et al. (2015). "Application of hybrid numerical and analytical solutions for the simulation of coupled thermal, hydraulic, mechanical and chemical processes during fluid flow through a fractured rock". eng. In: *Environmental earth sciences* 74.12, pp. 7837-7854. ISSN: 1866-6280.
- Min, Wang et al. (2016). "Influence of surface roughness on nonlinear flow behaviors in 3D self-affine rough fractures; lattice Boltzmann simulations". eng. In: *Advances in water resources* 96, pp. 373-388. ISSN: 0309-1708.
- Pyrz, Michael J. and Clayton V. Deutsch (2014 - 2014). *Geostatistical reservoir modeling / Michael J. Pyrcz, Clayton V. Deutsch*. eng. Second edition. New York: Oxford University Press. ISBN: 0-19-935883-4.
- Vieira, Sidney Rosa et al. (2010). "Detrending non stationary data for geostatistical applications". por. In: *Bragantia* 69.suppl, pp. 01-08. ISSN: 1678-4499.
- Zimmerman, Robert and Ian Main (2004). "Chapter 7 Hydromechanical Behavior of Fractured Rocks". eng. In: *International Geophysics*. Vol. 89. Elsevier Science & Technology, pp. 363-421. ISBN: 0123053552.

### 3 Benchmarking

This section offers an outline of the benchmarking studies undertaken in Task G, with emphasis on fracture mechanics involving M, HM, and TM processes. Benchmarks have been introduced for both plane and rough fractures, as well as for fracture networks. Relevant publications (in preparation, see sec. 8) contain further information. The section is structured as follows:

- Plane fractures (classical benchmarks), sec. 3.1
- Rough fractures, sec. 3.2
- Fracture networks, sec. 3.4

#### 3.1 Plane fractures

This section contains a set of benchmarks to verify the hydro-mechanical process in various simulation packages. First, the fracture aperture with Sneddon's solution (static - Sneddon and Lowengrub, 1969a) was compared. Second, the model was verified with plane-strain hydraulic fracture propagation in a toughness dominated regime based on Sneddon's solution (Sneddon and Lowengrub, 1969a). To account for the infinite boundaries in Sneddon's closed-form solution, a large finite domain was considered. Third, a benchmark was conducted with a domain size that is more realistic for laboratory experiments while applying differential stresses at the boundaries. Fourth, the third benchmark was repeated with an inclined fracture. Lastly, mesh and domain studies were performed. Figure 3.1 summarizes the overviews of benchmarks. Table 3.1 lists the material properties.

Table 3.1: Rock parameters of granite used in the direct shear tests (Frühwirt, Pötschke, and Konietzky, 2021)

Name	Symbol	Value	Unit
Young's modulus	$E$	$49.75 \times 10^9$	Pa
Fracture toughness <sup>†</sup>	$K_I$	$0.95 \times 10^6$	Pa · m <sup>1/2</sup>
Poisson's ratio	$\nu$	0.26	-
Compressive strength	$\sigma_c$	$120.54 \times 10^6$	Pa
Tensile strength	$\sigma_t$	$7.02 \times 10^6$	Pa
Friction angle (Mohr)	$\phi$	52.5	°
Basic Friction angle (Mohr)	$\phi_b$	30	°
Cohesion	$c$	$22.5 \times 10^6$	Pa

$${}^\dagger G_c = K_I^2(1 - \nu^2)/E$$

##### 3.1.1 Benchmark 1: Static fracture aperture under a constant pressure

A line fracture  $[-a_0, a_0] \times \{0\}$  ( $a_0 = 0.1\text{m}$ ) with no external loading and an internal fluid pressure of  $p = 1$  MPa was applied on the fracture surfaces and the fracture aperture was compared with the analytical solution (Sneddon and Lowengrub, 1969b, p. 29) for the fracture half-opening:

$$u(x, 0) = \frac{2pa_0}{E'} \sqrt{1 - (x/a_0)^2}, \quad (3.1)$$

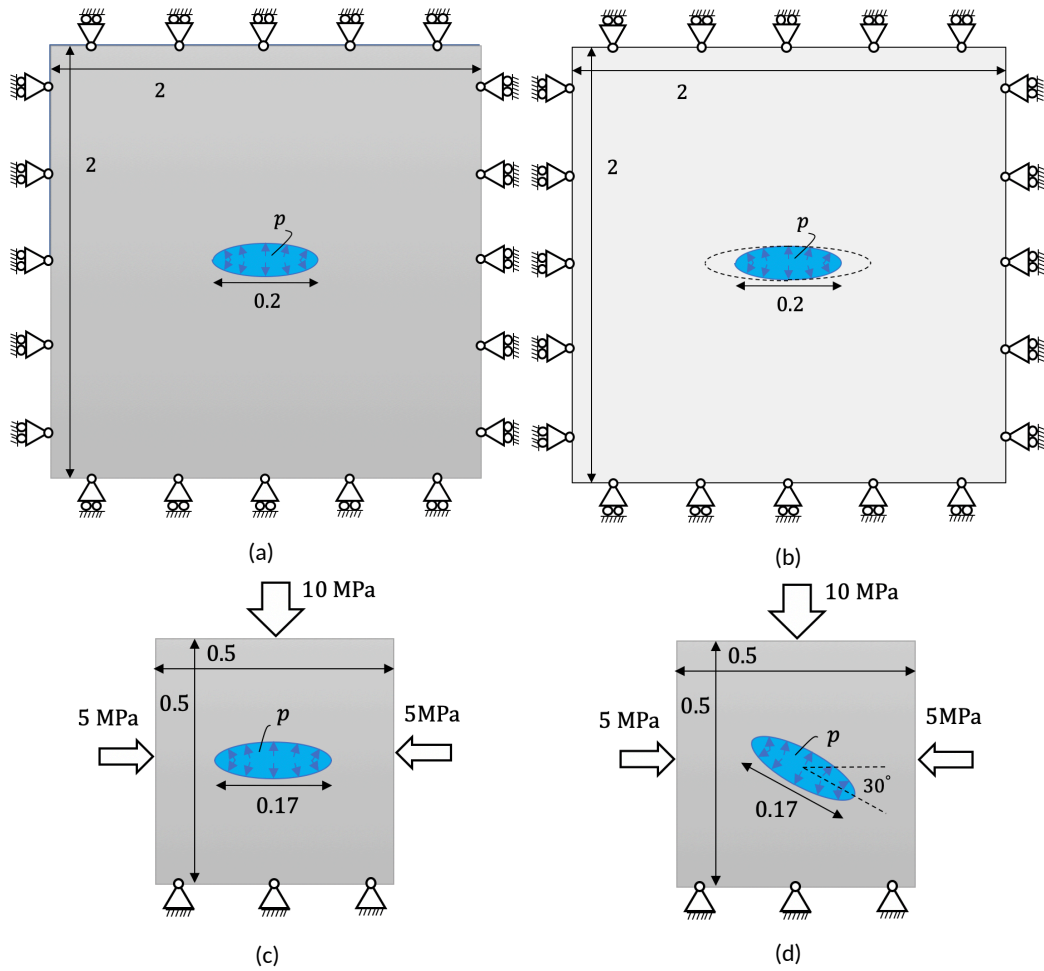


Figure 3.1: Benchmarks overview. (a) *benchmark 1*: static horizontal fracture under a constant pressure, (b) *benchmark 2*: propagating horizontal fracture in the toughness dominated regime, (c) *benchmark 3*: static horizontal fracture under a constant pressure with differential in-situ stress and (d) *benchmark 4*: static inclined fracture under a constant pressure with differential in-situ stress. The unit of domain size is meter [m].

where  $u$  is the displacement  $E'$  is the plane strain Young's modulus ( $E' = E/(1 - \nu^2)$ ) with  $\nu$  is Poisson's ratio,  $p$  is the fluid pressure inside the fracture. To account for the infinite boundaries in the closed-form solution, a large finite domain was considered:  $[-10a_o, 10a_o] \times [-10a_o, 10a_o]$  (Figure 3.1). The effective element size,  $h$ , is  $1 \times 10^{-3}$  m.

Computed fracture half-aperture and error profiles from different numerical methods are compared against the analytical solution (Eq. (3.1)) in Figure 3.2. The errors are computed as a relative error from the closed form solution. The error profiles demonstrate that the aperture in the middle of the fracture is in good agreement with the close form solution, however near the fracture tip, most numerical solutions are highly inaccurate.

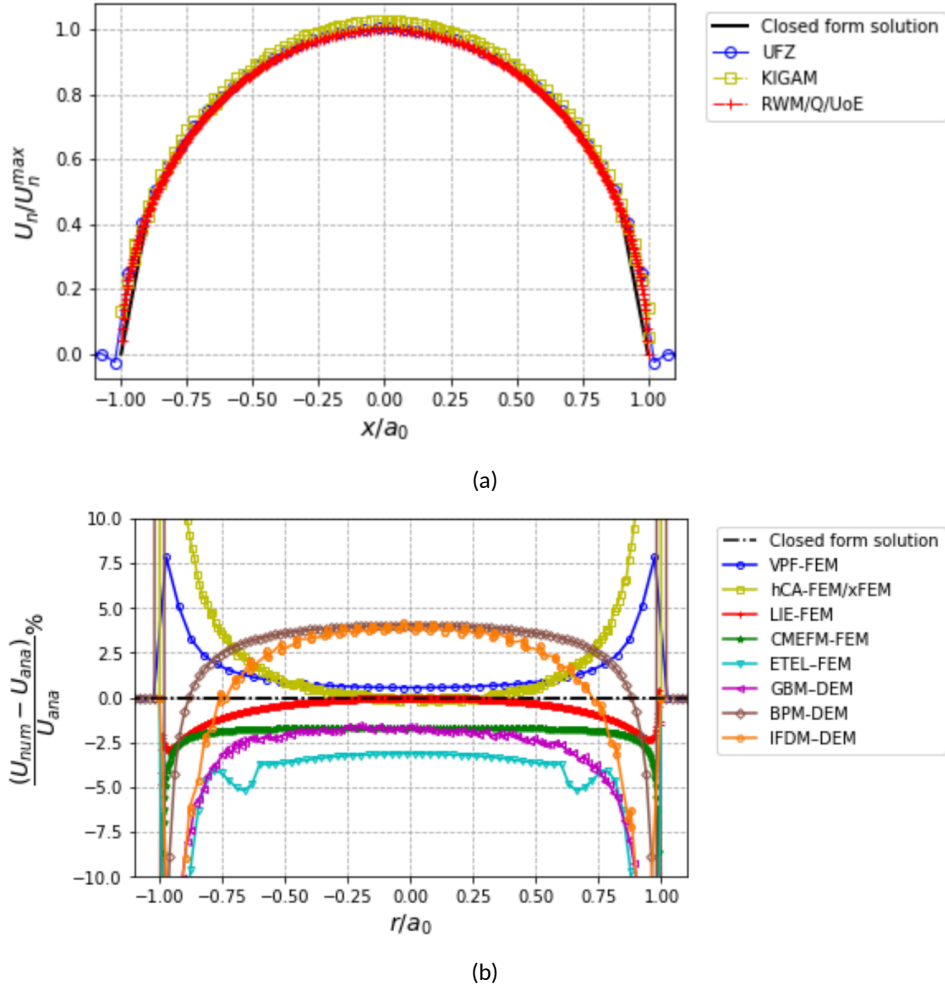


Figure 3.2: (a) Fracture half-aperture profiles and (b) error from different numerical methods compared against the closed-form solution.

### 3.1.2 Benchmark 2: Propagating fracture in the toughness dominated regime

Under the toughness dominated regime without leak-off, the energy dissipation by the fluid viscosity is negligible compared with the energy released for the fracture surface creation (Detournay, 2016). Therefore, in this regime, the pressure loss within the fracture could be neglected and the pressure and the length evolution were derived using Eq.(3.1) (Ji, Settari, and Sullivan, 2009; Dean and Schmidt, 2009; Bourdin, Chukwudozie,

and Yoshioka, 2012). From Eq.(3.1), the work of the pressure force is given as

$$\mathcal{W}(R) = \frac{2p^2 a^2}{E'}. \quad (3.2)$$

Applying Clapeyron's theorem, the elastic energy is

$$\mathcal{E}(R) = -\frac{\pi p^2 a^2}{E'}, \quad (3.3)$$

and the energy release rate with respect to the crack length  $a_0$  propagating along the initial inclination is

$$G(R) = -\frac{\partial \mathcal{E}}{\partial (2a)} = \frac{\pi p^2 a}{E'}. \quad (3.4)$$

According to Griffith's criterion (Griffith, 1920), in a quasi-static volume control setting<sup>2</sup>, the fracture propagates when  $G = G_c$  and the critical volume for crack propagation is  $V_c := \sqrt{\frac{4\pi G_c a^3}{E'}}$ . The corresponding pressure and the fracture length evolution are:

$$p(V) = \begin{cases} \frac{E'V}{2\pi a_0^2} & \text{for } V < V_c \\ \left[ \frac{2E'G_c^2}{\pi V} \right]^{\frac{1}{3}} & \text{for } V \geq V_c, \end{cases} \quad (3.5)$$

$$a(V) = \begin{cases} a_0 & V < V_c \\ \left[ \frac{E'V^2}{4\pi G_c} \right]^{\frac{1}{3}} & V \geq V_c. \end{cases} \quad (3.6)$$

The normalized pressure  $p_f/p_c$  and the normalized crack length/ $a_0$  are plotted against the normalized volume  $V/V_c$  in Figs 3.3. While VPF-FEM slightly overestimates the peak pressure, LIE-FEM slightly underestimates it. As the crack grows, both converge to the closed-form solution curve.

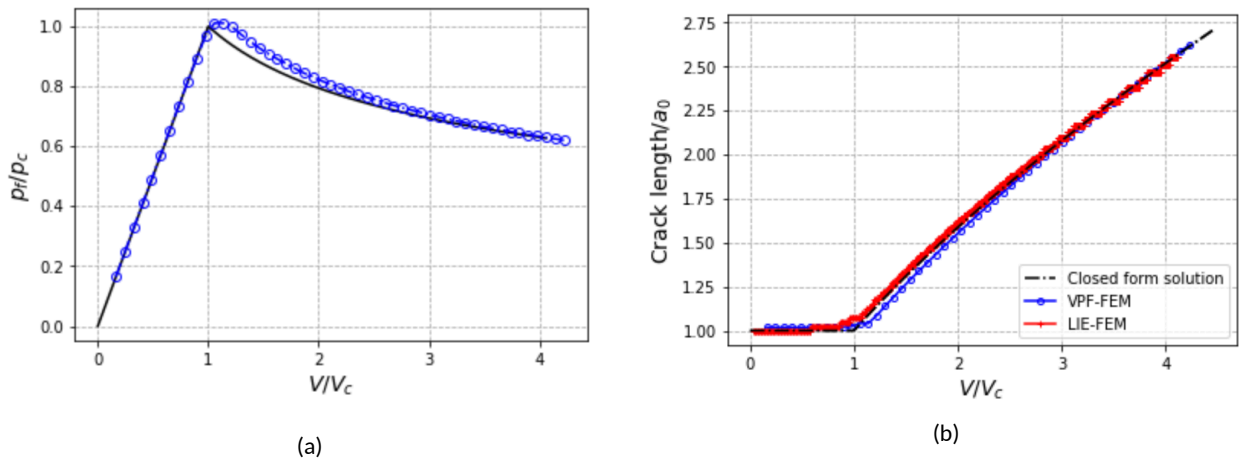


Figure 3.3: (a) Pressure and (b) fracture length evolution against injected volume

<sup>2</sup>The fracture propagation is always unstable with pressure control.



### 3.1.3 Benchmark 3: Static straight fracture under constant pressure with differential in-situ stress

To compare our results with laboratory experiments, a static benchmark was conducted with horizontal fracture and a sample size of  $0.5 \text{ m} \times 0.5 \text{ m}$ . The total length of fracture is  $0.17 \text{ m}$ . The fluid pressure within the fracture gives  $p = 12 \text{ MPa}$ . The material properties are listed in Table 3.1.

Figure 3.4 shows the aperture profiles for the Granite specimen with a plane horizontal fracture. While good agreement was achieved between numerical results and the analytical solution in Section 3.1.1, there is a  $2 \mu\text{m}$  discrepancy between different numerical results in this case for the aperture profiles. It is important to note that the previous benchmark (Section 3.1.1) used a large computational domain to mimic an infinite domain. In contrast, this benchmark employed a laboratory-scale sample with boundaries close to the fracture, which might influence the results. Additionally, applying in-situ stress at the boundaries could be another reason for this discrepancy.

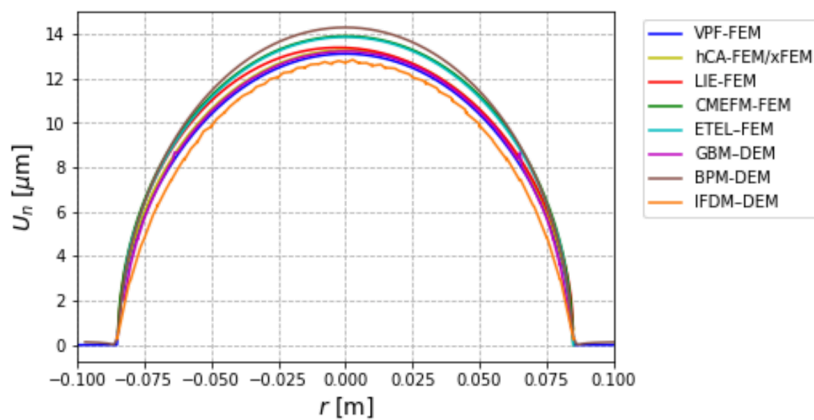


Figure 3.4: Aperture profile for the Granite specimen with a plane horizontal fracture.

### 3.1.4 Benchmark 4: Static inclined fracture under constant pressure with differential in-situ stress

To account for the effect of inclination, the benchmark 3 is replicated with an inclined fracture. The fracture is inclined by  $30^\circ$  to horizontal. The remaining material and geometrical properties are identical to those of benchmark 3.

Figure 3.5 shows the aperture profiles for the granite specimen with an inclined fracture. In comparison to horizontal fracture in Benchmark 3, the fracture inclination dominated the discrepancies between the results of different approaches. All methods exhibit a parabolic trend with peak apertures near the center. VPF-FEM shows the highest peak ( $\sim 23 \mu\text{m}$ ), while IFDM-DEM shows a lower peak ( $\sim 20 \mu\text{m}$ ). IFDM-DEM deviates slightly from other models.

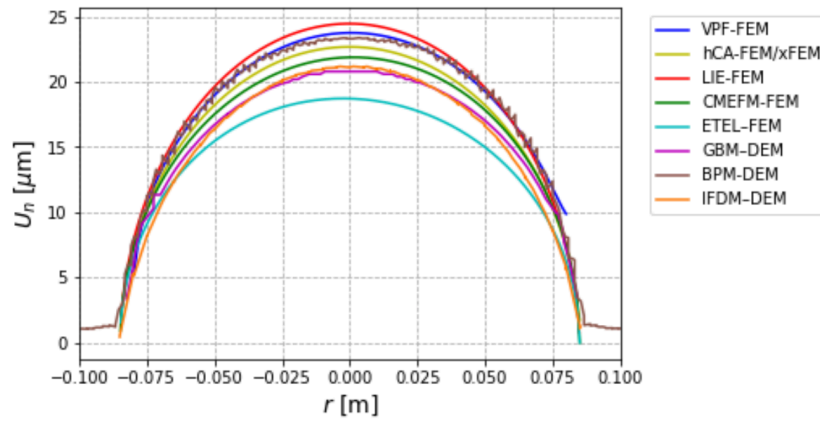


Figure 3.5: Aperture profiles for the Granite specimen with a plane inclined  $30^\circ$  fracture.

### 3.1.5 Mesh studies

This section investigates the numerical aspects of discretization effects such as mesh size and orientation.

**Mesh size effect** We studied a mesh sensitivity by analyzing the convergence of the aperture profile for different mesh discretizations. We repeated benchmark 1 with varying mesh sizes,  $h = 0.001, 0.003, 0.006,$  and  $0.01$  m, where  $h$  is mesh size (Figure 3.7). As a sample, mesh discretization for the mesh study is shown in Figure 3.6 for VPF-FEM. The central region, which is our region of interest for demonstrating fracture behavior, consists of structured quadrilateral elements with a mesh size of  $h = 0.01$ , while the surrounding area is discretized using an unstructured mesh with  $h = 0.1$ . As can be seen in Figure 3.7b, for hCA-FEM/xFEM, the results converge when  $h = 0.003$ m, arriving at a slightly higher profile than the closed-form solution. The higher profile in the hCA-FEM/xFEM results may be due to differences in material representation in the numerical model. While the analytical solution does not account for fracture stiffness, the hCA-FEM/xFEM method might involve material properties that result in a higher fracture aperture.

Figure 3.7c shows the results of BPM-DEM approach. We see with the increase of the mesh density, the calculated fracture aperture keeps increasing until converges at slightly higher values than the closed-form solution. By contrast, the results of CMEFM-FEM approach are quite close to the analytical solution. This may be attributed by: (i) the use of contact stress instead of contact force that somehow alleviates the sensitivity of penalty spring on the mesh sizes, (ii) the advantages of combining FEM interpolation for continuum mechanics and contact calculation for discontinuum mechanics, and (iii) well-constrained penalty springs. Figure 3.8 shows similar yet magnified patterns of convergence of the maximum aperture calculated by these different approaches.

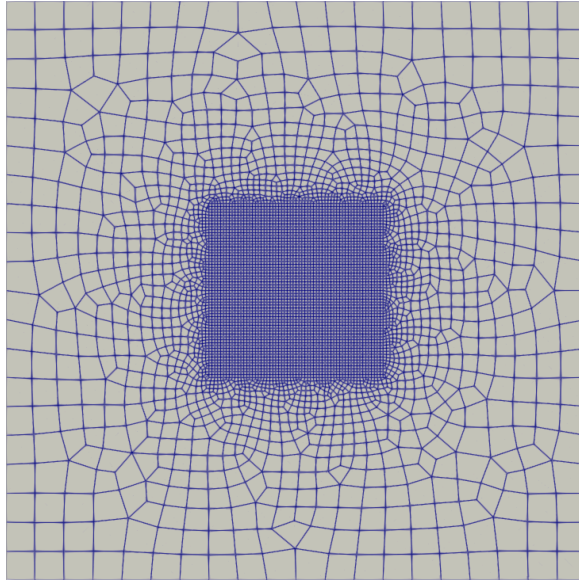


Figure 3.6: Mesh discretization for the mesh study using VPF-FEM: the middle square has structured quadrilateral elements with a mesh size  $h = 0.01$ , and outside of that, there is an unstructured mesh with mesh size  $h = 0.1$ .

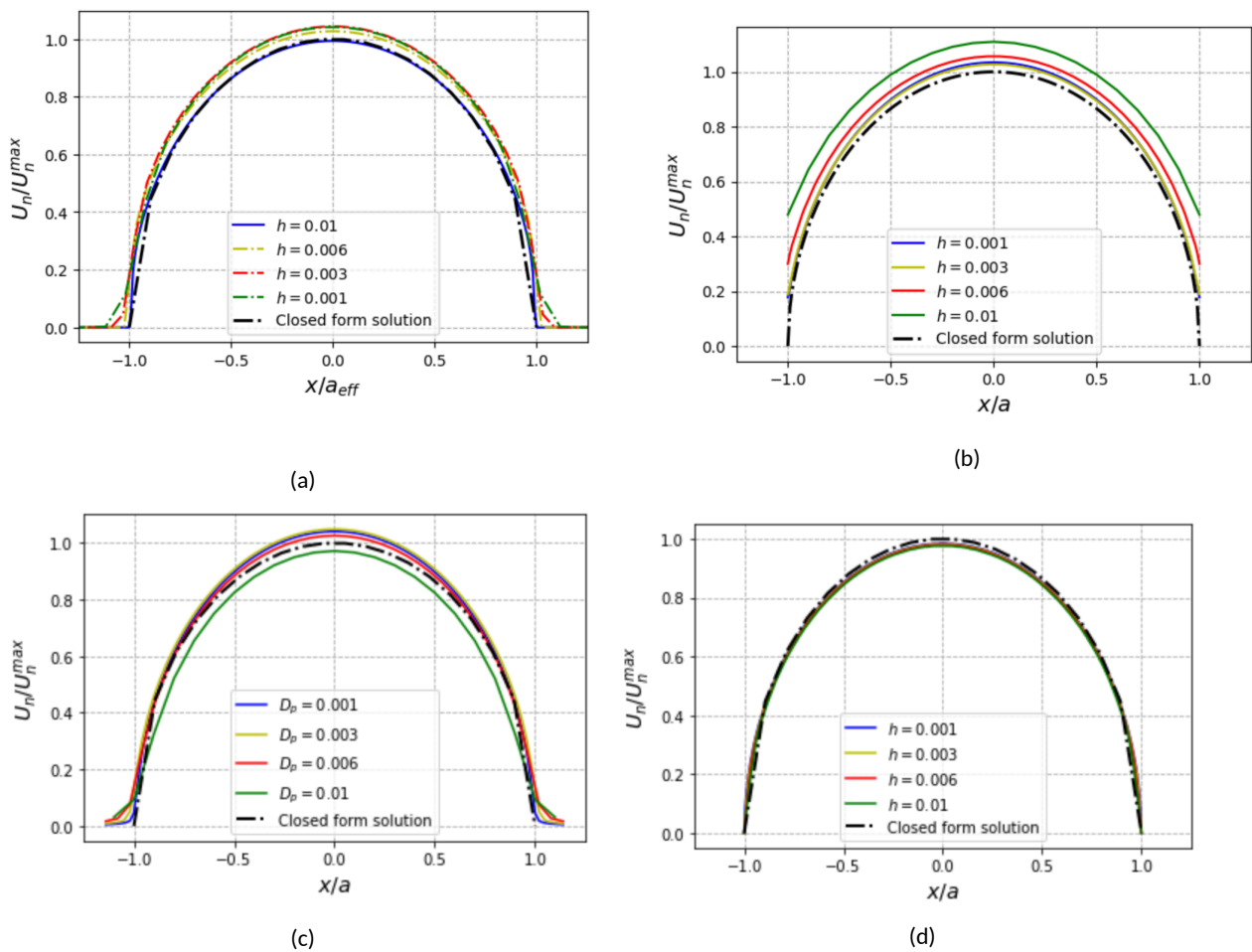


Figure 3.7: Fracture aperture profiles of (a) VPF-FEM, (b) hCA-FEM/xFEM, (c) BPM-DEM and (d) CMEFM-FEM with different mesh sizes compared against the analytical solution.

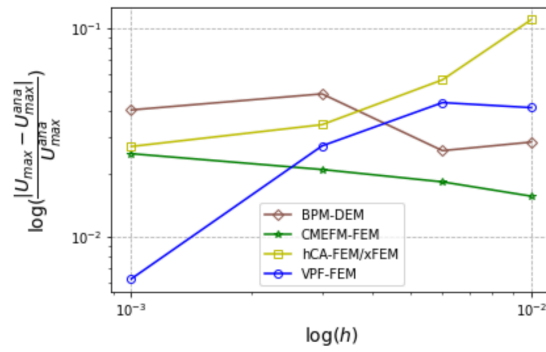


Figure 3.8: Convergence curve for the error of maximum aperture with different mesh sizes for benchmark 1.

**Mesh alignment with inclined fracture in VPF-FEM** One of the advantages of the VPF-FEM is that explicitly mesh the fracture does not need and allowing fractures to propagate along pre-defined mesh elements. To see the effect of the alignment of mesh and fracture on fracture aperture, benchmark 4 was repeated with two different mesh inclinations (Figure 3.9) to see the impact of the alignment of mesh and fracture on fracture aperture. The fracture aperture is computed based on the line integral of the gradient of the phase field variable (Bourdin, Chukwudozie, and Yoshioka, 2012; Yoshioka, Naumov, and Kolditz, 2020).

Figure 3.10 shows the aperture profiles from the VPF-FEM for the granite specimen with an inclined fracture. The aperture profile oscillates with the non-aligned mesh while the profile is smooth with the aligned (Figure 3.9a). The computation of aperture is inaccurate in the vicinity of the fracture tip because the crack's normal direction is improperly identified from the gradient of the phase field variable.

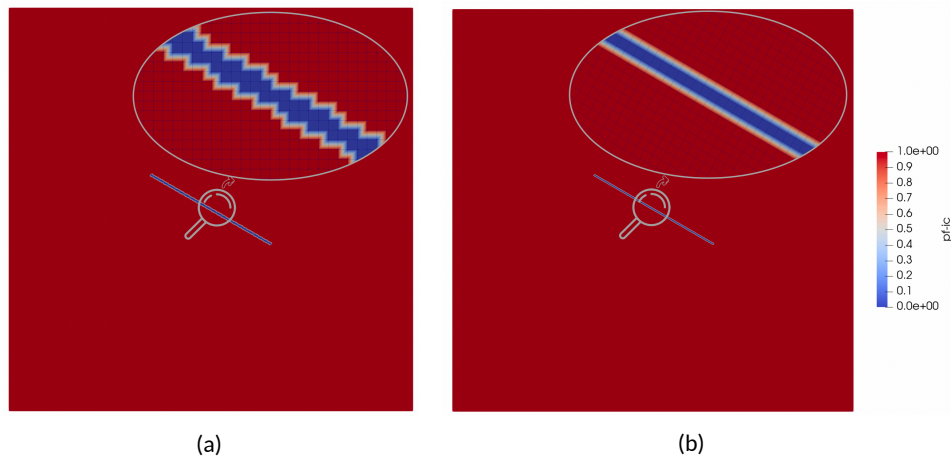


Figure 3.9: Initial phase field profile (a) not aligned mesh with inclined fracture and (b) aligned mesh with inclined fracture in VPF-FEM approach.

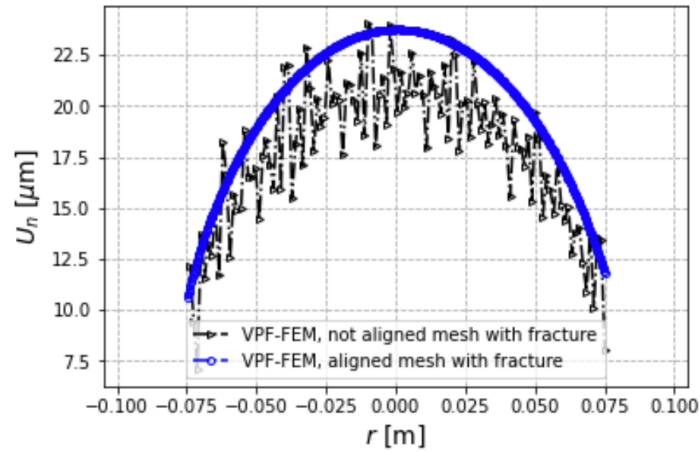


Figure 3.10: Aperture profiles for the Granite specimen with a plane inclined  $30^\circ$  fracture using VPF-FEM approach.

### 3.1.6 Domain size study

To investigate the effect of domain size and boundaries, a series of examples were performed with the same material and geometrical parameters, fracture size, and boundary conditions as benchmark 3 but with different domain sizes. Four distinct computational domain sizes (m) were used:  $\Omega = [-0.125, 0.125] \times [-0.125, 0.125]$ ,  $\Omega = [-0.25, 0.25] \times [-0.25, 0.25]$ ,  $\Omega = [-0.5, 0.5] \times [-0.5, 0.5]$ , and  $\Omega = [-0.75, 0.75] \times [-0.75, 0.75]$  (Figure 3.11).

Figure 3.12 shows the results of using different domain sizes by different approaches. Despite the differences in the results which are similar to Figure 3.7, all the models show results converge when the domain size reaches or exceeds  $\Omega = [-0.5, 0.5] \times [-0.5, 0.5]$ . A notable difference between different teams is when the domain size  $\Omega = [-0.25, 0.25] \times [-0.25, 0.25]$ . Differently from other FEM and DEM approaches, the results calculated by IFDM-DEM show that when the domain size reaches  $\Omega = [-0.25, 0.25] \times [-0.25, 0.25]$ , the boundaries do not have an impact on the fracture aperture. Closer examination of the results of  $\Omega = [-0.25, 0.25] \times [-0.25, 0.25]$  reveals good agreement of the results by different approaches. Even though the width converges by increasing the domain size for each team, there is still a relatively significant difference between the calculated width in different team results. This difference could be due to (i) the lack of resolution for the region near the thin fracture for finite elements and (ii) the sensitivity to penalty springs.

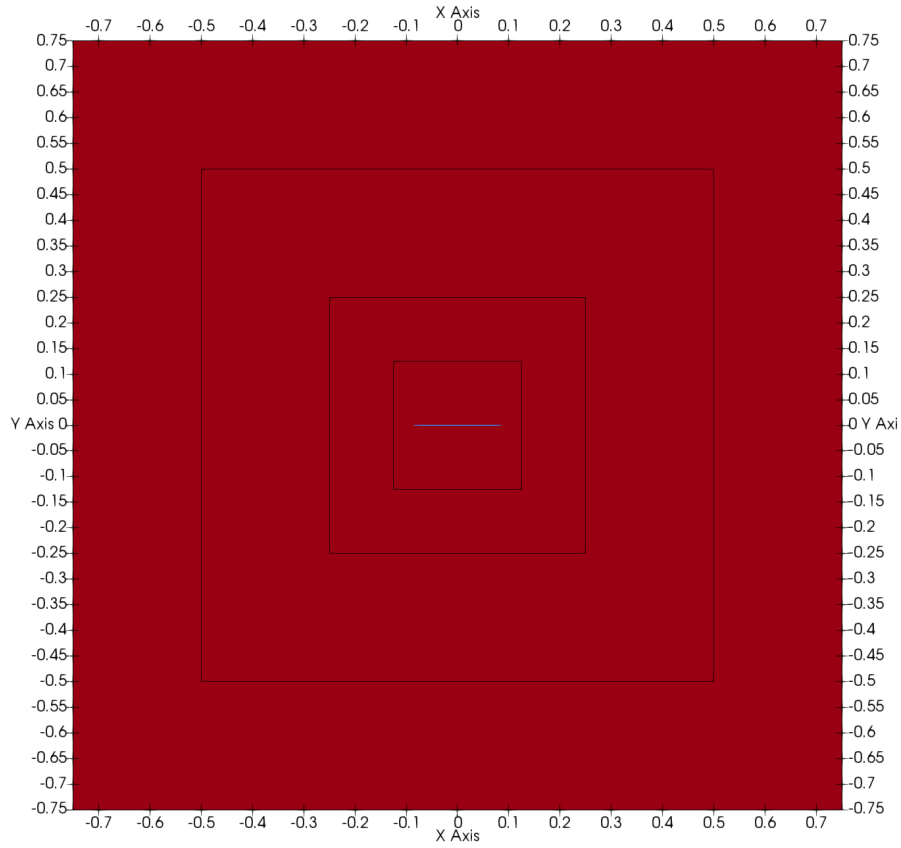


Figure 3.11: Domain size study for benchmark 3:  $\Omega = [-0.125, 0.125] \times [-0.125, 0.125]$ ,  $\Omega = [-0.25, 0.25] \times [-0.25, 0.25]$ ,  $\Omega = [-0.5, 0.5] \times [-0.5, 0.5]$ , and  $\Omega = [-0.75, 0.75] \times [-0.75, 0.75]$ . The unit of domain sizes is meter [m].

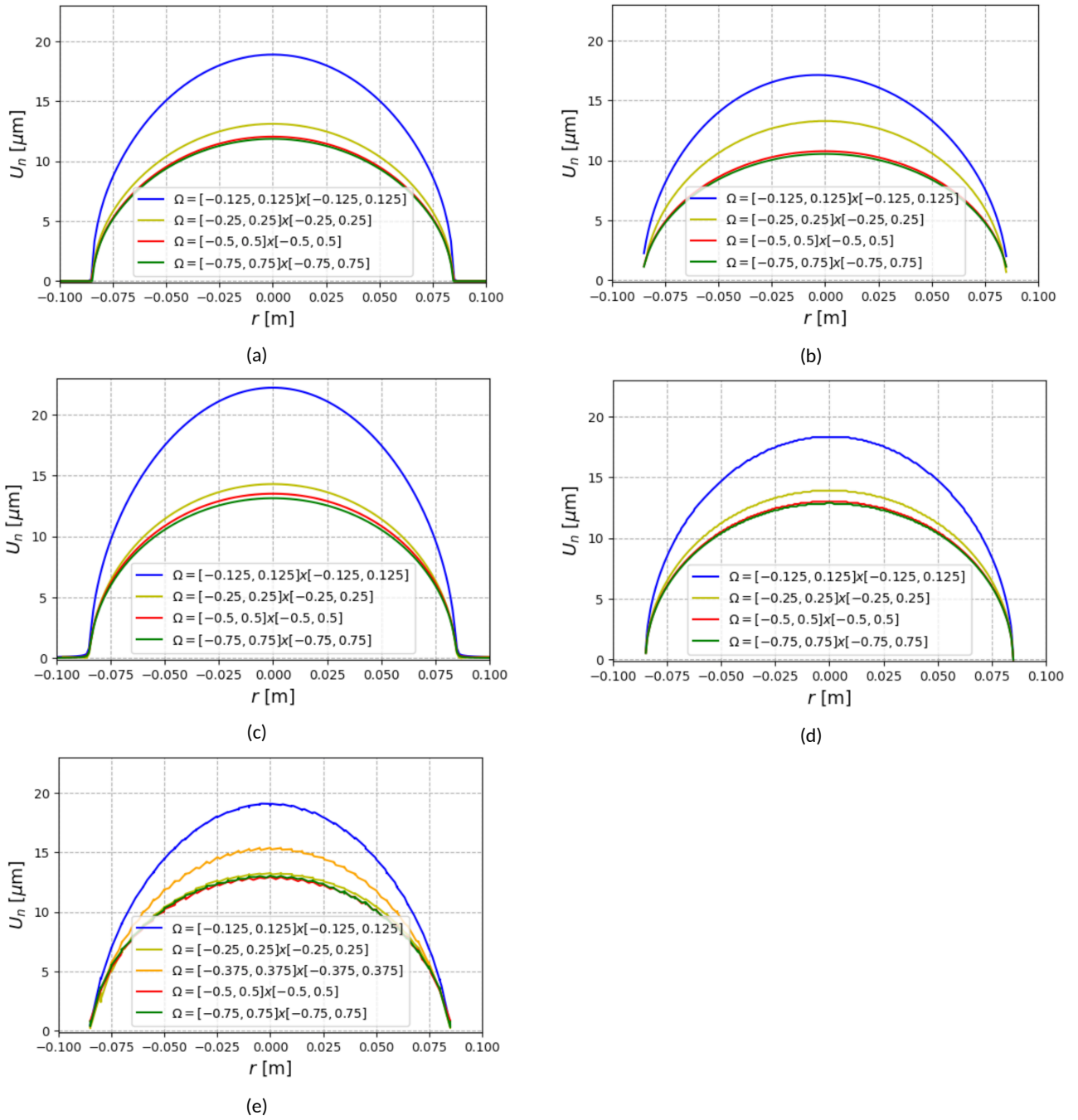


Figure 3.12: Aperture profiles of (a) VPF-FEM, (b) hCA-FEM/xFEM, (c) BPM-DEM, (d) CMEFM-FEM, and (e) IFDM-DEM for the Granite specimen with a plane horizontal fracture with different domain sizes.

### 3.2 Fracture slip under mechanical loading (M processes)

The rough fracture slip benchmark exercise involves simulating an inclined fracture with roughness under differential biaxial stress conditions. The primary objective of this benchmark was to guide the research teams into developing methodologies to incorporate roughness into their respective numerical models. Furthermore, the exercise aimed at observing and analyzing how the slip profile of a rough fracture differs from that of a straight fracture under the influence of varying stress conditions. The participating teams include CAS, CNSC, LBNL, KIGAM, Quintessa/UoE/RWM, and SSM/DynaFrax.

#### 3.2.1 Preparation of rough fracture surface data set

In preparation for rough fracture modeling, the dataset was derived from a fracture specimen of Freiberg granite, specifically tested for direct shear behavior. The fracture surface was laser scanned and the surface data were plotted into four different resolutions (Figure 3.13). Each set of scanned data provided a unique perspective on the fracture surface, enabling flexibility for research teams to choose the dataset that best suited their numerical models and mesh resolution requirements. Three line profile traces were extracted from a single fracture surface for 2D fracture modeling (Figure 3.14).

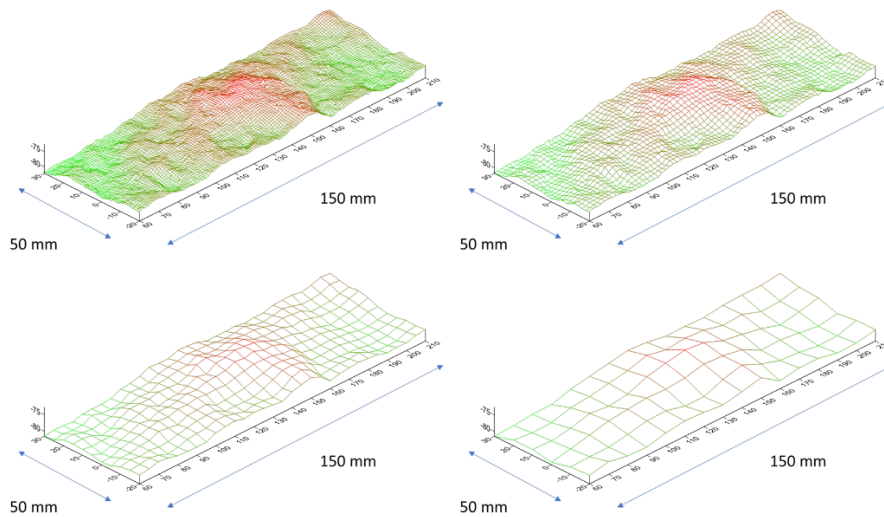


Figure 3.13: Freiberg granite fracture surface scan data in four different mesh resolution.

#### 3.2.2 Benchmark 5: Static rough fracture under differential in-situ stress

The CAS team introduced their rough fracture model as shown in Figure 3.15, depicting a 45-degree inclined fracture with roughness subjected to biaxial stress conditions—5 MPa horizontally and 10 MPa vertically. The team conducted a thorough analysis by comparing slip profiles between a planar fracture and a fracture with roughness. The results of the comparison revealed that the slip profile of the rough fracture deviates from the expected parabolic slip profile. Additionally, the CAS team performed stress analysis, as depicted in the accompanying figure (Figure 3.16). The distributions of major and minor principal stresses highlighted substantial stress concentrations at the two fracture tips.

The SSM/DynaFrax team investigated the effect of fracture roughness on slip distribution, as illustrated in



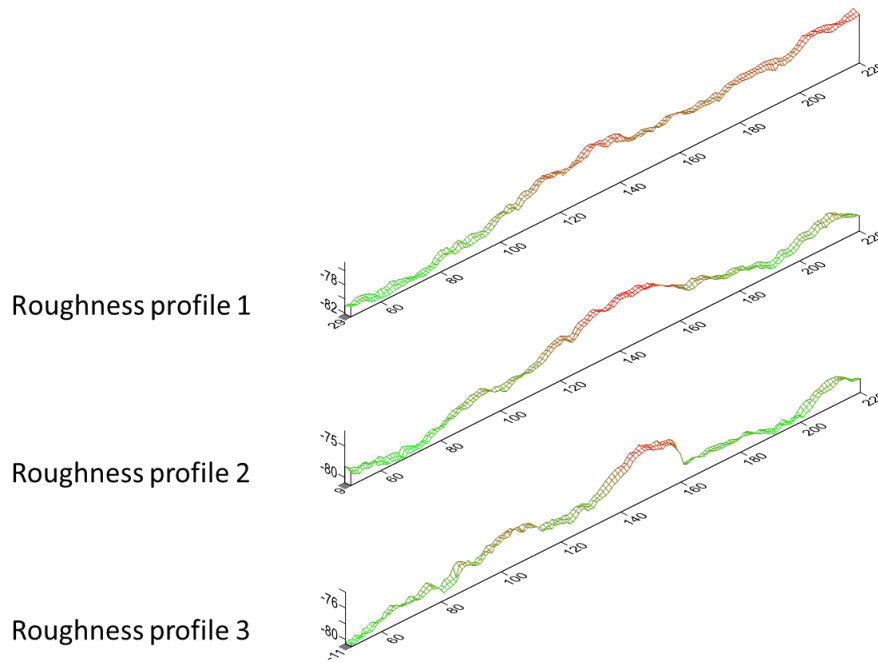


Figure 3.14: Three traces (roughness profiles) taken from the fracture surface scan data.

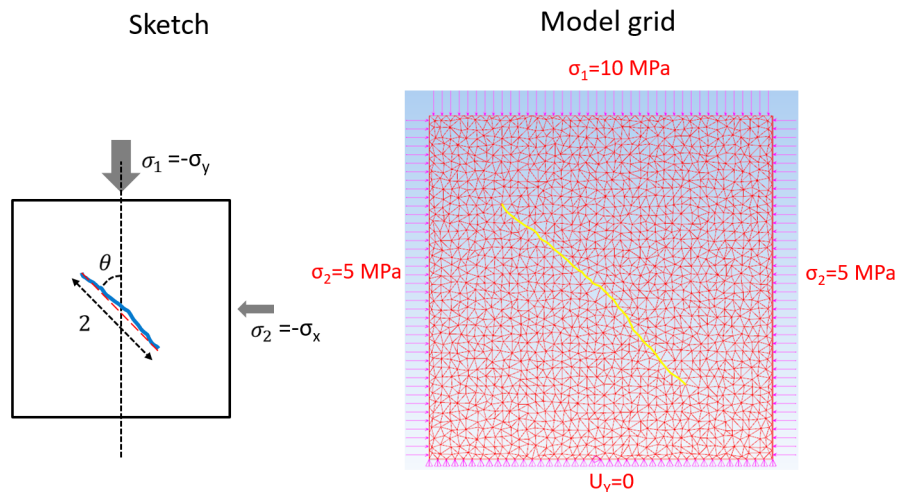


Figure 3.15: 2D rough fracture slip analysis (CAS).

Figure 3.17. The model features a 45-degree inclined fracture with roughness under biaxial stress conditions—5 MPa horizontally and 10 MPa vertically. The team compared slip profiles between a planar fracture and a fracture with roughness. The result demonstrated a notable deviation in the slip profile of the rough fracture from the anticipated parabolic slip profile, with the location of maximum slip offsetting from the fracture center. Moreover, the results showed variations in slip estimates along the fracture trace, with some parts exhibiting lower slip than the parabolic profile and others displaying significantly larger slip. The occurrence of substantial slip aligned with changes in roughness along the fracture trace. In addition to PFC modeling, the SSM/DynaFrax team employed BEM-based FRACOD2D modeling, with results showing a similarity to the PFC model results (Figure 3.18).

The research teams addressed concerns related to the length of the fracture in comparison to the model size (Figure 3.19). The issue arose from the initial benchmark exercise, where the ratio of the model's side length to

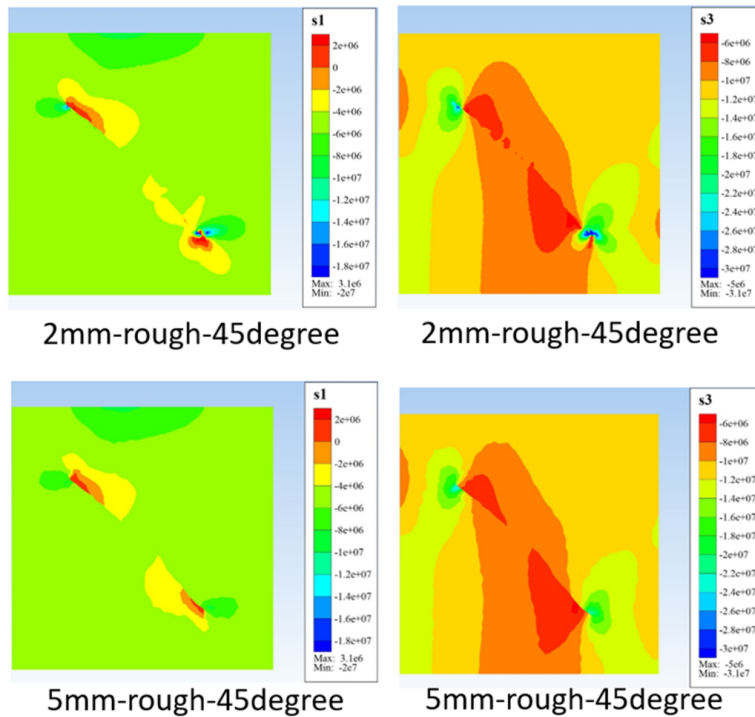


Figure 3.16: Distribution of max and min principal stresses around the 45 deg inclined rough fracture under shear slip (CAS).

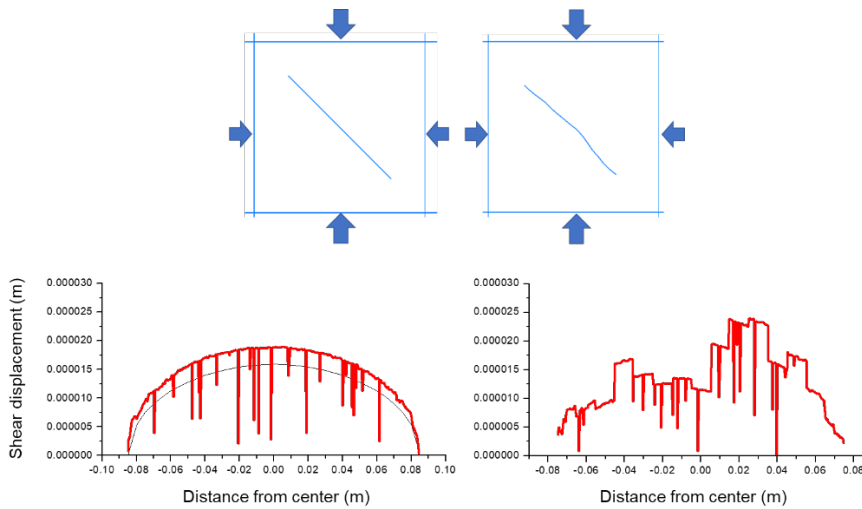


Figure 3.17: Slip profiles of planar and rough fractures modelled by smooth joint contact model (SSM/DynaFrac).

the fracture's full length was set at 1.17. This configuration resulted in challenges, particularly with the fracture tip proximity to the stress boundary, prompting discussions among the teams. To mitigate this, there was consensus to adjust the model size to 0.5 m, ensuring that the ratio of the model size (side length) to the fracture length remains above 2. This adjustment was necessary to maintain a favourable scenario where stress concentrations at the fracture tip are sufficiently distant from the boundary, as illustrated in the accompanying figure.

The CAS team introduced a new model with a reduced size of 0.5 m, featuring rough fractures at different inclination angles—30 and 60 degrees. Comparative analysis of slip profiles showed significant deviations from the parabolic profile for both rough fractures, with the maximum slip offset from the fracture centre,

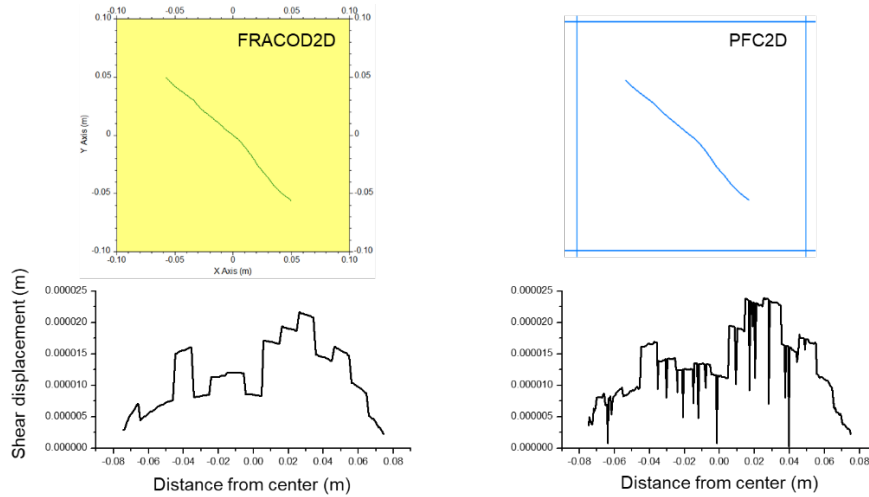


Figure 3.18: Slip profiles of rough fracture simulated by FRACOD2D and PFC2D (SSM/DynaFrax).

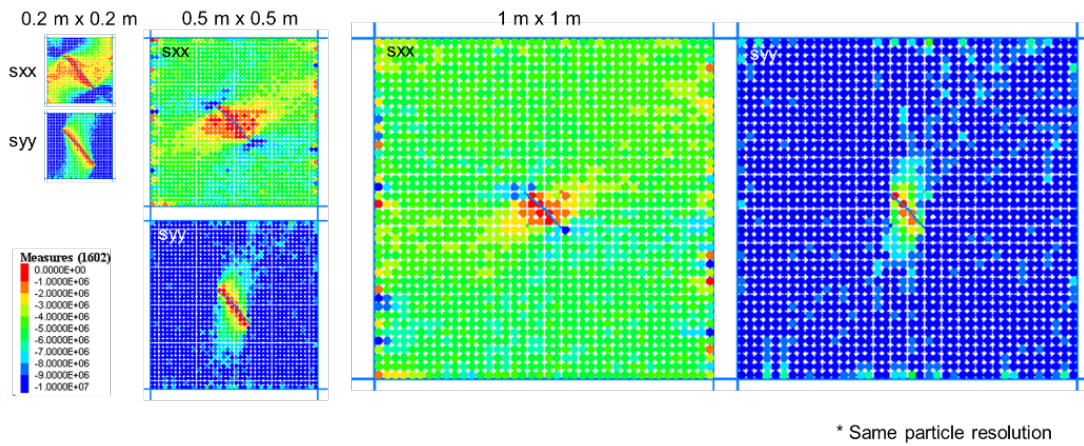


Figure 3.19: Distribution of stresses around a 45 deg inclined fracture under shear in different model size and fracture length ratios (SSM/DynaFrax).

as shown in Figure 3.20. Additionally, the CAS team explored the impact of small cracks, presenting results that highlight the substantial influence these scattered fractures have on the deformation of the main fracture (Figure 3.21).

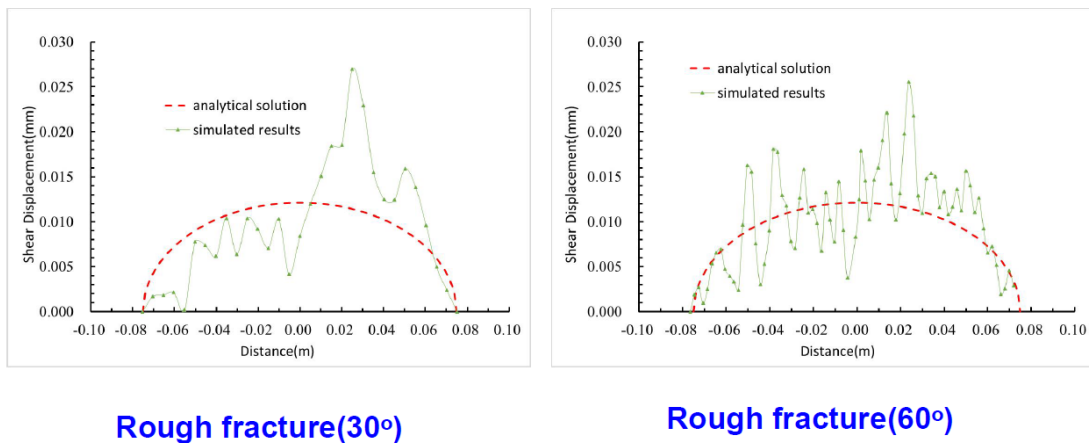


Figure 3.20: Comparison of rough fracture slip profiles with different orientations (CAS).

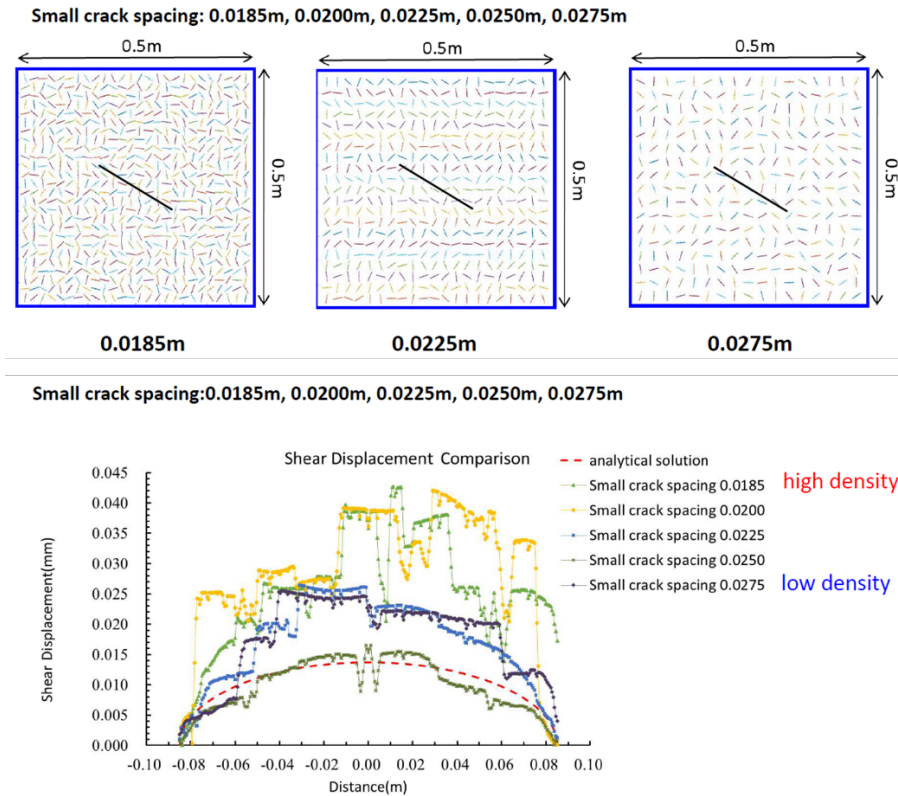


Figure 3.21: Effect of presence of small cracks and their spacings on slip profiles of the main fracture (CAS).

The CNSC team presented their approach to the rough fracture slip model. The fracture was represented by a zero-thickness interface with shear and normal stiffness. The normal stiffness was set equivalent to the rock matrix in compression and zero in tension, while the shear stiffness was set to zero for a smooth fracture. In the case of a rough fracture, the joint profiles were used to incorporate shear stiffness. The rock matrix properties were defined with an elastic modulus ( $E$ ) of 50 GPa and a Poisson's ratio ( $\nu$ ) of 0.26. For the elastoplastic rock matrix case, a nonlocal plastic model with the Drucker-Prager criterion was employed. The implementation was carried out using COMSOL® Multiphysics. The results showed that rough fracture slip profiles consistently exhibited maximum slip offset from the fracture centre, and this trend became more pronounced with increased fracture roughness, as illustrated in Figure 3.22.

The LBNL team used NMM and presented slip profile of a rough fracture. The slip profile of the rough fracture demonstrated that the maximum slip occurred at a location offset from the fracture centre, consistent with the observations in similar studies (Figure 3.23). This reiterated the common behaviour seen in rough fractures and reinforced the understanding that the slip pattern tends to deviate from the parabolic profile with an offset towards one side of the fracture.

The KIGAM team presented their 3DEC model results on rough fracture slip. Simulations were conducted across nine different cases with varying resolutions (2, 5, and 10 mm) and fracture profiles (1, 2, and 3) (Figure 3.24). The boundary stress conditions involved  $\sigma_{xx} = 5$  MPa and  $\sigma_{yy} = 10$  MPa, with an inclination angle of  $60^\circ$ . The cohesion, friction angle and tensile strength were all zero.

The KIGAM team investigated the effect of roughness on fracture behavior and observed that the shear displacement of rough fractures was smaller compared to that of planar fractures, somewhat different from the results of other teams. The effect of profile resolution on fracture slip was tested. The results showed that the

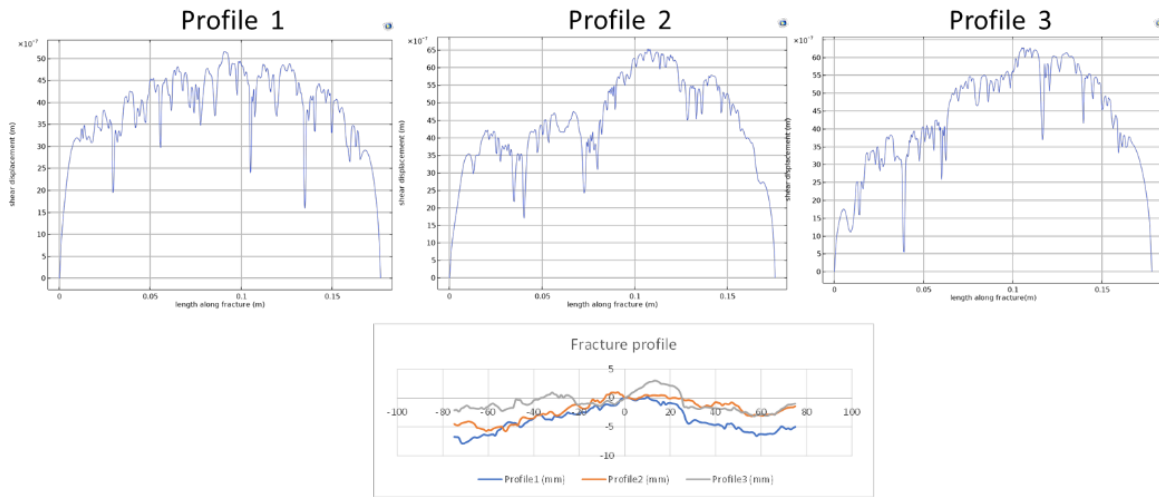


Figure 3.22: Slip profiles of rough fracture with different profiles (CNSC).

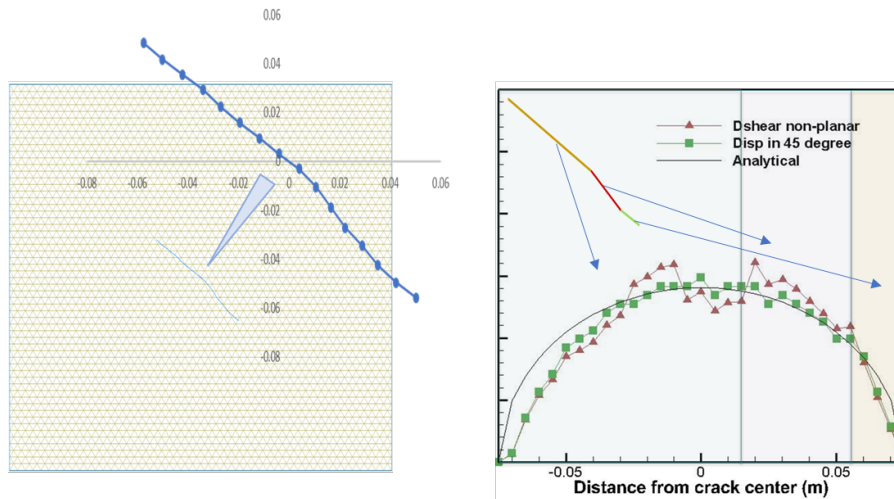


Figure 3.23: Slip profile of a rough fracture simulated by NMM (LBNL).

smaller the sampling interval, the less shear displacement modelled. A comparison between rough fractures with different resolutions (e.g., 10 mm) and planar fractures revealed that the level of detail within a sampling interval played a crucial role.

The Quintessa/UoE/RWM team presented their results using COMSOL (Figure 3.25), employing a novel approach to represent fractures either as an internal contact boundary or a thin elastic layer (TEL) within the Structural Mechanics module. The significant distinction lies in how the contact model represents opening, while the thin elastic layer maintains continuous connection. They observed differences in peak slip and gap along the fracture profile between "fine" and "fine with coarse stiffness" variants, emphasizing the impact of mesh-dependent parameterization on the contact model. A "soft" stiffness allowed for more fracture surface intrusion and a greater peak slip. These variations showed the importance of specifying suitable fracture stiffness. The team also demonstrated alternative ways to represent roughness due to the computational expense associated with fine discretization in a 3D model.

The SSM/DynaFrax team showed updated results, confirming that rough fracture slips consistently exhibit maximum slip at an off-centre position, particularly where surface roughness undergoes changes in the slope (Fig-

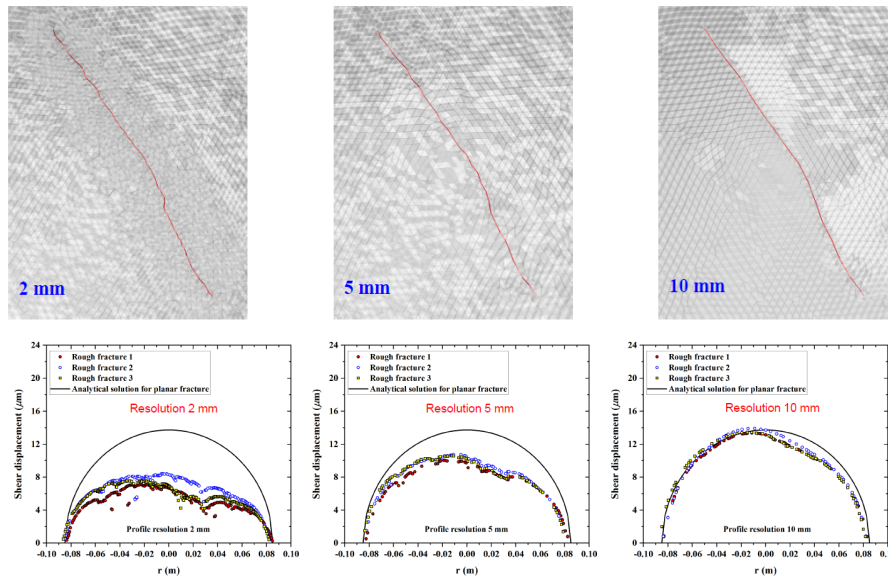


Figure 3.24: Rough fracture representation in three different mesh resolution and slip profiles (3DEC).

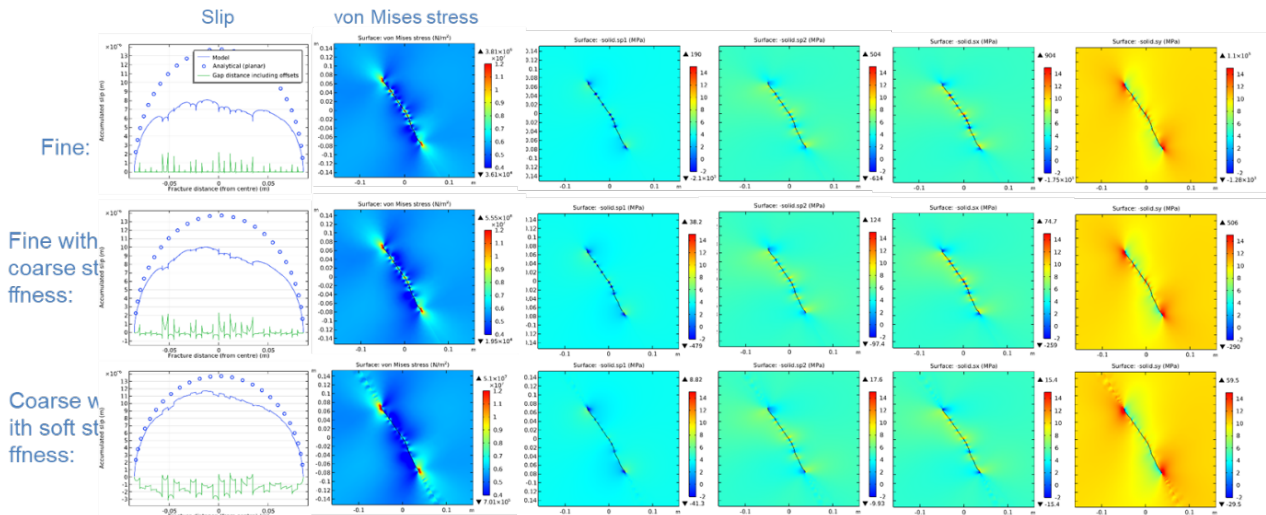


Figure 3.25: Slip profiles of rough fractures with different mesh resolutions and corresponding stress distributions (Quintessa/UoE/RWM).

ure 3.26). To validate this, they tested with differently oriented fractures, rotating the fracture by 180 degrees, and found that the location of maximum slip was influenced by the surface roughness (Figure 3.27). Furthermore, the impact of roughness levels was investigated by increasing it with factors of 1, 1.5, and 2. The outcomes indicated that larger changes in roughness led to more substantial differences in slip between the maximum and minimum sections. Non-planar fractures displayed asymmetric slip distributions, and the roughness effect resulted in locally high slip, especially as asperity increased, accentuating the local slip contrast (Figure 3.28).

### 3.3 Fracture slip under mechanical and thermal loading (TM processes)

The benchmark exercise modeling was extended to explore thermally induced slip of both planar and rough fractures initially under mechanical biaxial stress conditions. Following the mechanical benchmark, a constant temperature of 50°C was applied to the boundaries.

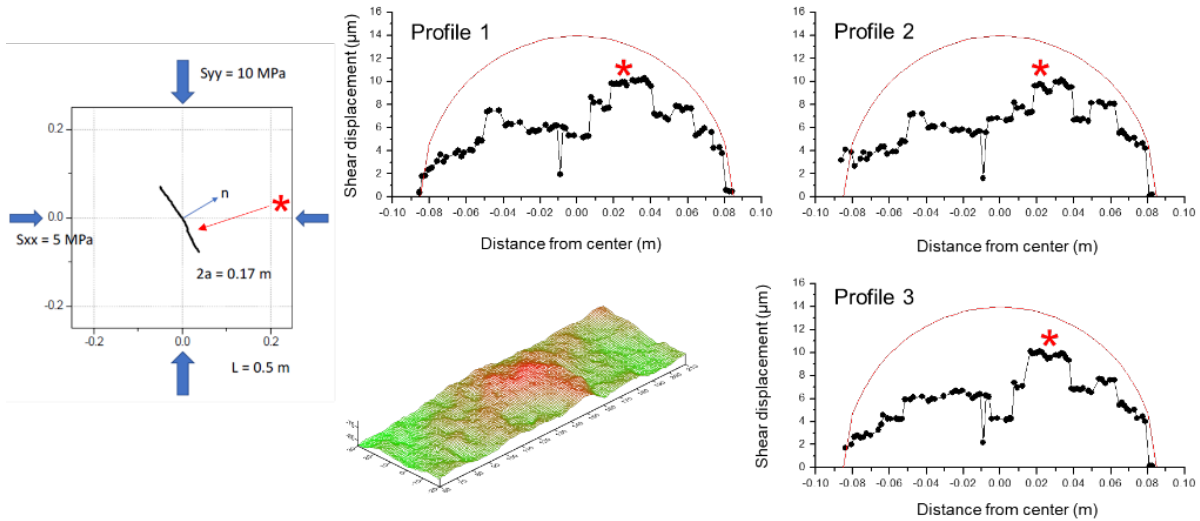


Figure 3.26: Slip profile of an inclined fracture with different roughness profiles (SSM/DynaFrax).

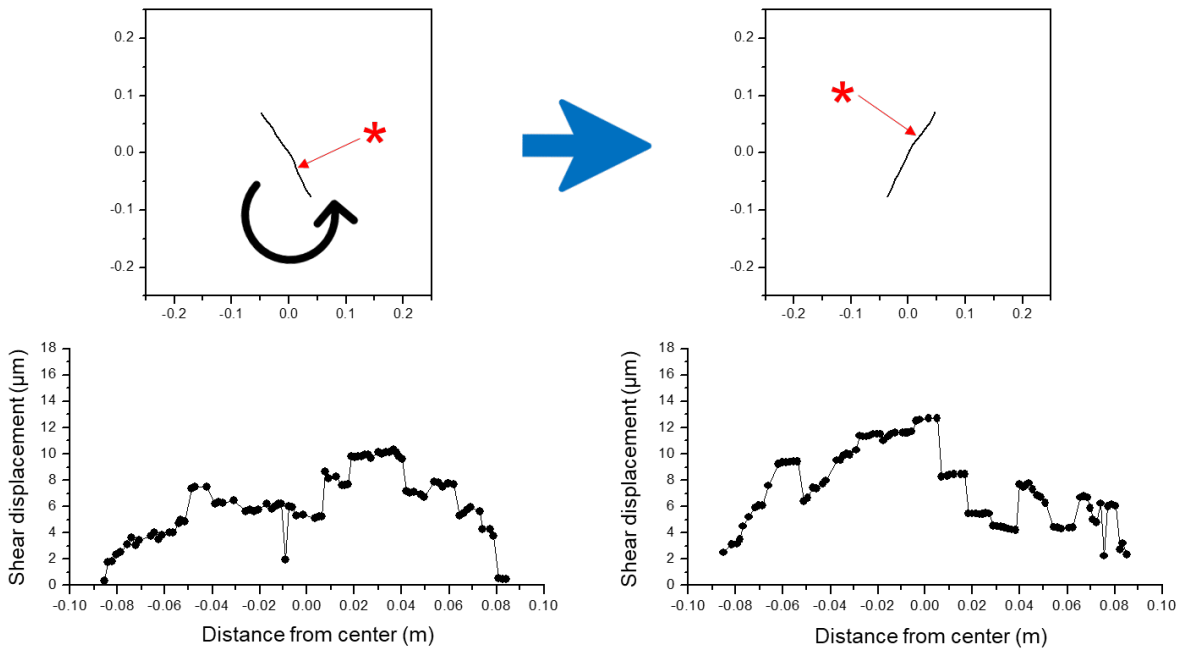


Figure 3.27: Slip profiles of rough fracture under different orientations (SSM/DynaFrax).

The SSM/DynaFrax team introduced a 3D fracture model, considering both mechanical and thermal-mechanical loading conditions. In the simulation of heat-induced fracture slip, a planar and a non-planar fractures cutting across the entire model were considered. The fracture plane was initially mechanically loaded under triaxial stress condition ( $S_{xx} = S_{yy} = 5$  MPa,  $S_{zz} = 10$  MPa), and then constant temperature of 50 degrees was applied to the top and bottom boundaries. The results demonstrated that heat conduction occurred, causing an increase in rock temperature. The elevated temperature in the rock resulted in the thermal expansion of the rock blocks. Due to the confinement, the thermally expanded rock blocks resulted in slip of the fracture plane. A comparison between planar and rough fracture cases revealed distinct differences. For the planar fracture, slip developed across the entire fracture surface. In case of the rough fracture, slip was arrested at the loca-

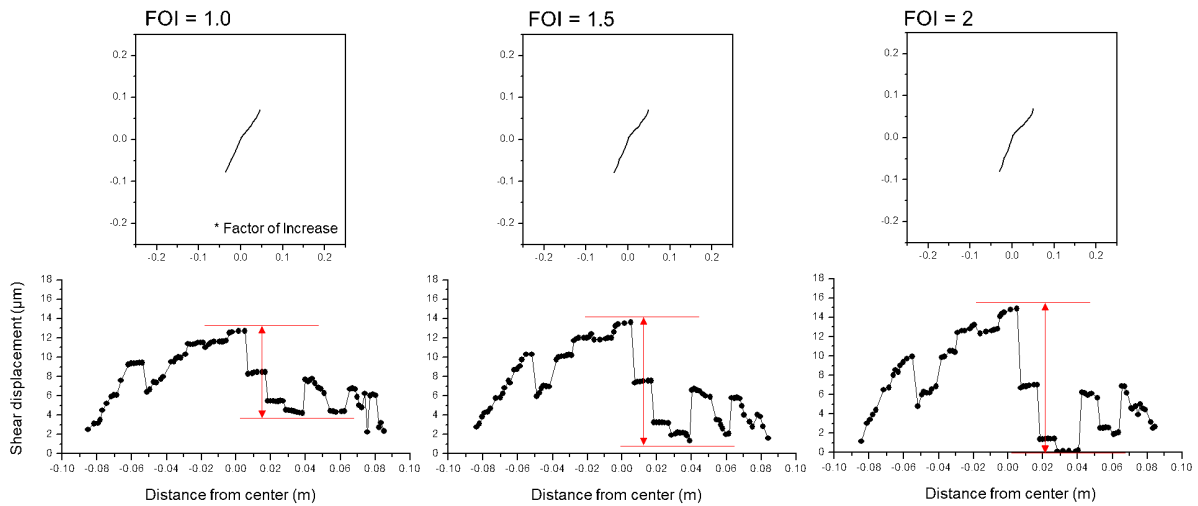


Figure 3.28: Slip profiles of rough fractures under different level of roughness (SSM/DynaFrax).

tions where the fracture slope changes. Stress concentrations were observed locally where slip was arrested, suggesting the potential for local damage if inelastic rock behaviour is present (Figure 3.29).

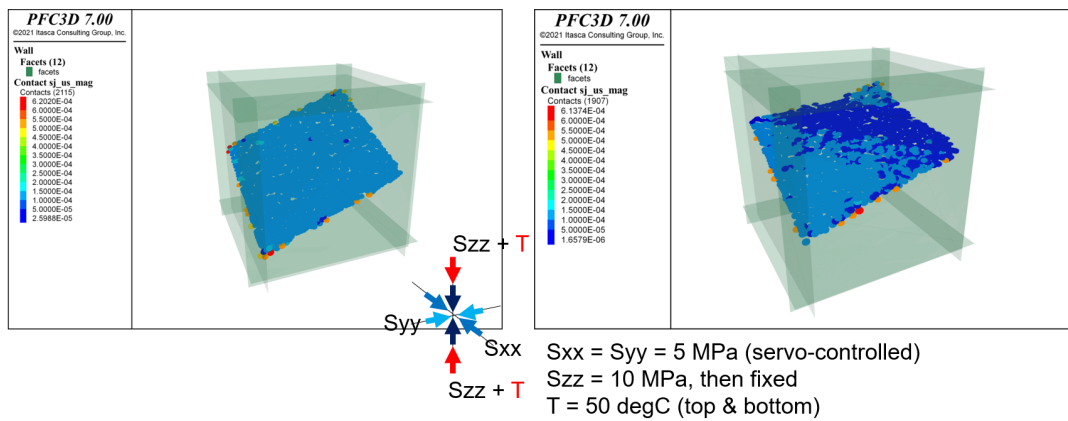


Figure 3.29: Comparison of fracture slip distribution between the planar and rough fractures under mechanical and thermal loading (SSM/DynaFrax).

The SNL team, utilizing COMSOL, presented 2D benchmark model examining heat-induced slip of a planar fracture under specific conditions. The objective was to investigate the impact of heat loading applied from the model boundary on the shear displacement of an inclined, isolated planar fracture embedded in an elastic rock model initially subjected to differential stress condition. The modeling began with a simplified problem based on the 2D planar fracture benchmark. The SNL team applied a constant temperature of  $T = 50 \text{ }^\circ\text{C}$  to the model boundaries. The results showed that the maximum slip occurred at the fracture centre. However, the results showed that the difference in the magnitude of maximum slip was negligible (Figure 3.30).

The LBNL team presented FLAC2D modeling of a rough fracture slip under mechanical and mechanical+thermal conditions. The results showed that the thermally induced slip profile of the rough fracture becomes highly heterogeneous, and slip at specific locations was larger than the parabolic slip profile approximated by the analytical solution (Figure 3.31). Such spiky pattern in the slip profile of the rough fracture is attributed to stress being concentrated locally along the fracture trace due to the roughness effect.

The CNSC and KIGAM teams carried out modelling of slip of a saw-cut fracture under mechanical and thermal



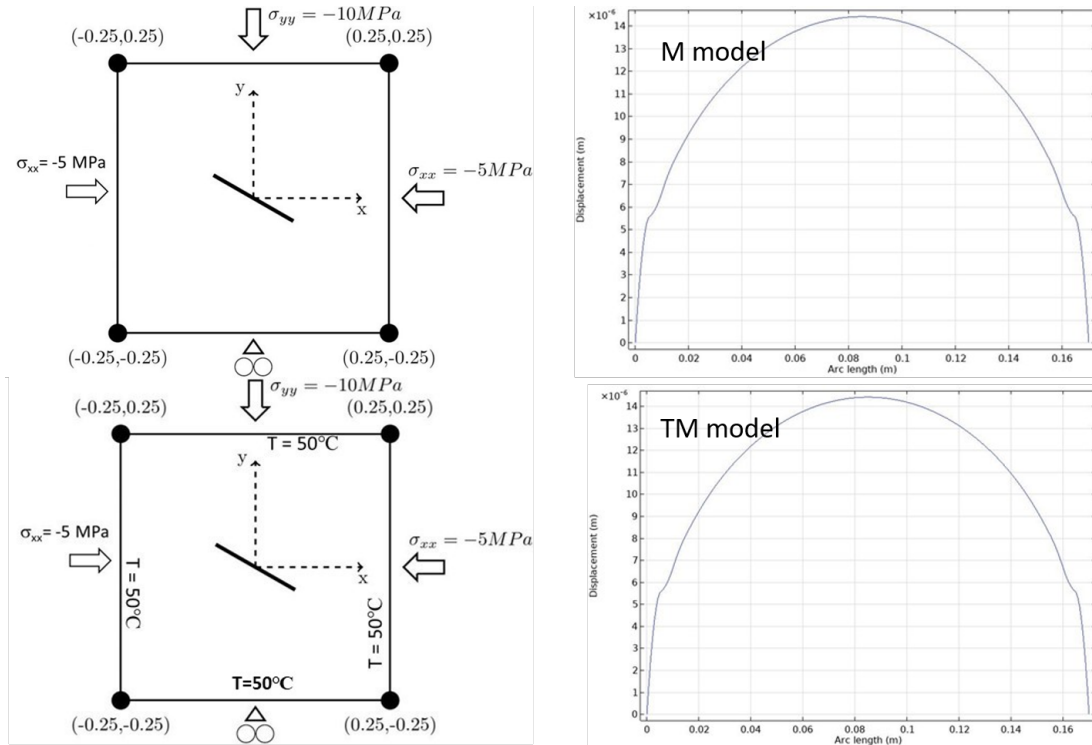


Figure 3.30: Comparison of planar fracture slip under mechanical and mechanical+thermal boundary conditions (SNL).

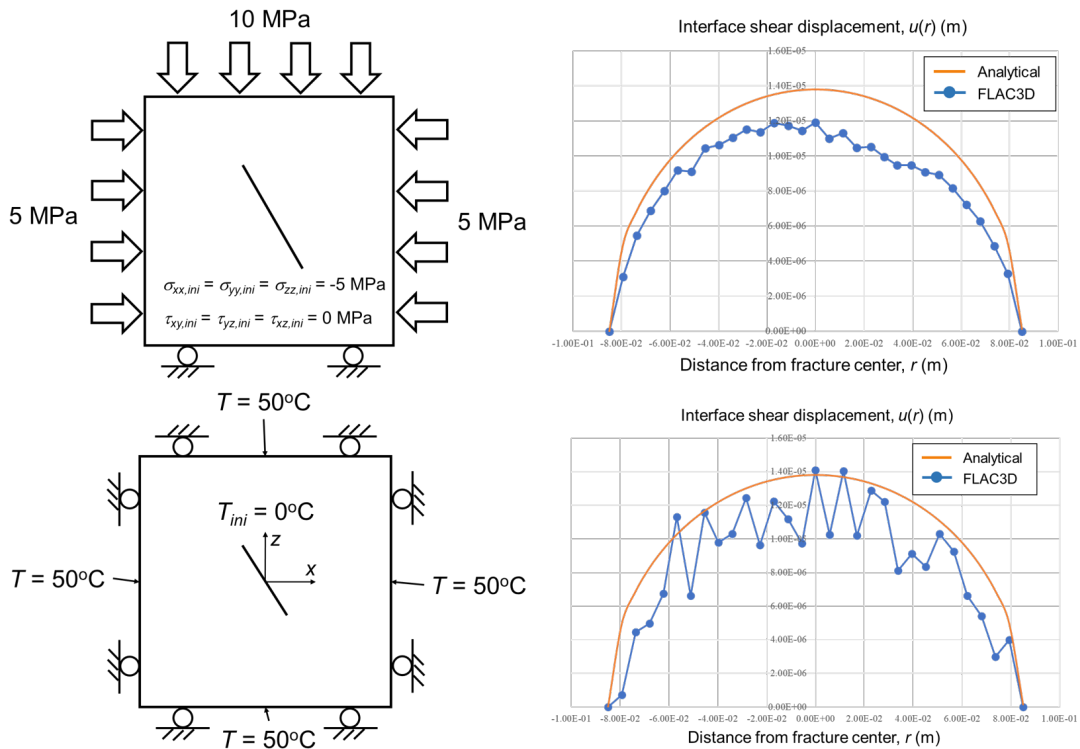


Figure 3.31: Comparison of rough fracture slip under mechanical and mechanical+thermal boundary conditions (LBNL).

loading conditions. The saw-cut fracture slip experiment was carried out by KICT and the results are presented in Section 6.4.

The CNSC team, using COMSOL, presented their developed model for a rock joint, considering factors such as

roughness and asperity degradation. The team employed this joint model to simulate thermoshearing experiments on a joint in Pocheon granite. Preliminary results indicated that the model successfully reproduced the basic physics of the joint, but there were challenges in fully capturing the joint’s rigid-plastic behavior. The model tended to underpredict joint displacement, and an unrecorded horizontal stress relaxation at the start of the heating phase was observed, deviating from KICT saw-cut thermal slip experimental data (Figure 3.32).

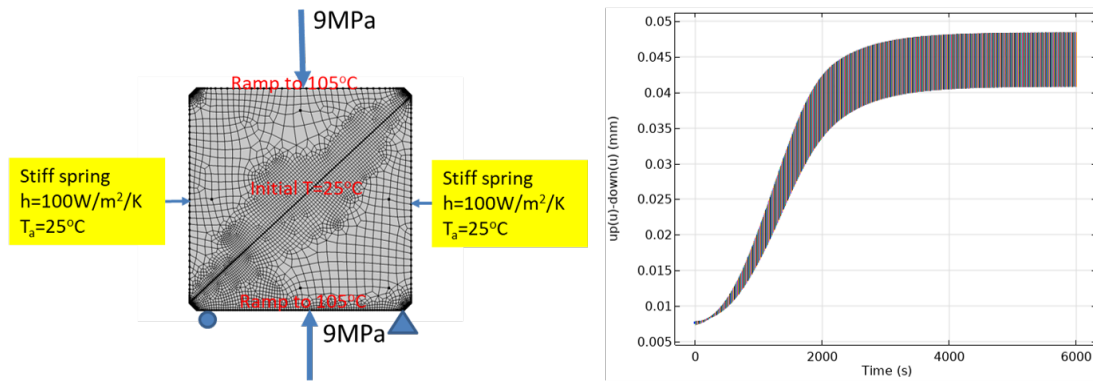


Figure 3.32: Saw-cut fracture thermal slip modelling by COMSOL (CNSC).

The KIGAM team presented their 3DEC modelling of the saw-cut fracture slip experiment. The results showed changes in rock temperature and fracture slip distribution data (Figure 3.33). While the simulation was preliminary, the overall behavior of the planar 3D fracture reasonably matched the laboratory experiment of saw-cut fracture slip (see Section 6.4).

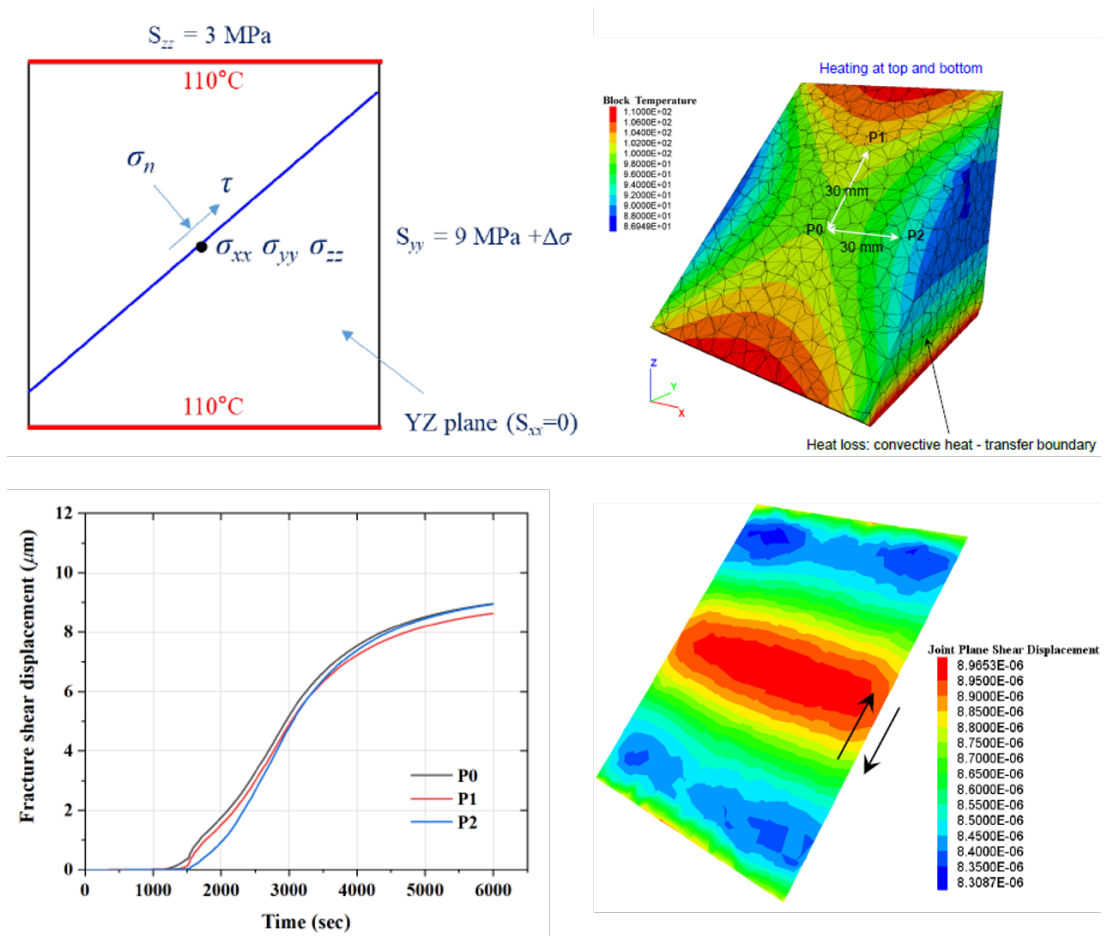


Figure 3.33: Saw-cut fracture thermal slip modelling by 3DEC (KIGAM).

### 3.4 Fracture networks

#### 3.4.1 Benchmarking study

A benchmark study to simplify DFN models for shearing of intersecting fractures and faults has been developed within Task G (Hu et al., 2024). Understanding of shear in fractures and faults is crucial for safe deposition of radioactive waste in deep geological repositories as well as efficient energy recovery and storage in subsurface reservoirs. This is because it can result in permeability changes or even induced seismicity. However, predicting the shearing of intersecting fractures and faults can be challenging due to dynamic frictional contacts and nonlinear rock deformation. This study presents a new conceptual model, the simplified DFN model, for analyzing the shearing of intersecting fractures and faults. The model uses major paths (MPs) to represent complicated DFNs for calculating shearing (see Figure 3.34).

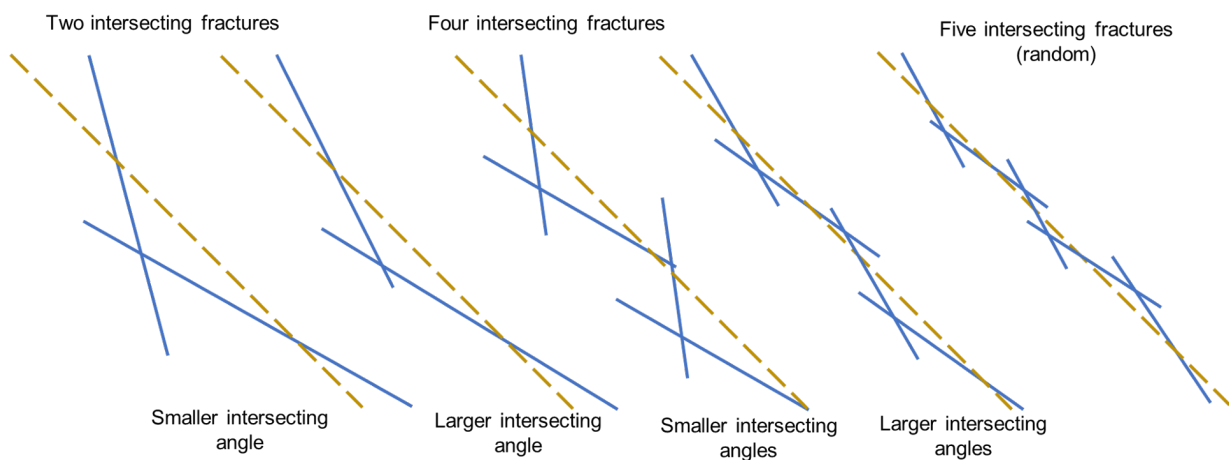


Figure 3.34: Intersecting fractures (blue lines) and hypothetical single major paths (yellow lines).

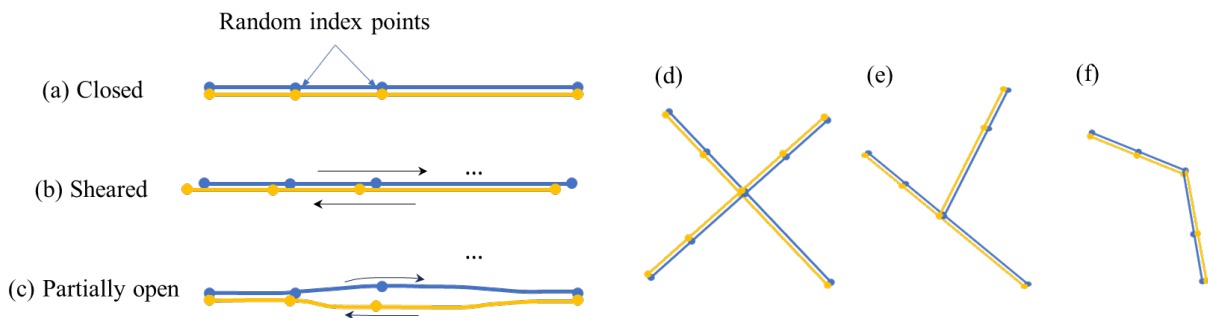


Figure 3.35: A single fracture in (a) closed, (b) sheared (off-set) and (c) partially open states; (d)-(f) three possible cases of two intersecting fractures.

To validate the model, simulations were conducted to compare multiple intersecting fractures with different levels of complexity with single or multiple major paths (MPs). Validation of the model involves comparison of results of MPs to those of DFNs and see if they are consistent. If consistent, that means the hypothetical MPs can represent the DFNs and the model is valid for the given case. At the discrete network scale, the physics of shearing a fracture or fault involves two discontinuous surfaces sliding against each other, satisfying certain friction laws. Additionally, there is a dynamic change of contact states and/or contact locations (see Figure 3.35a-c). A fracture can consist of multiple segments, and each segment has three possible contact

states: open, closed, or sliding. When sliding or shearing occurs, the contact pairs (i.e. the locations where contacts occur) may change. Additionally, the rock matrix may deform or fracture due to the stress generated by shearing. When two fractures or faults intersect, there are three basic scenarios as shown in Figure 1d-f: the two fractures intersecting (Figure 1d), one fracture terminating at another (Figure 3.35e), and the two fractures intersecting at the ends of each (Figure 3.35f). The intersection may introduce additional complexity in terms of the contact locations and states, depending on the intersecting angles, stress, confinement, fracture interfacial properties, and rock properties. Figure 3.35 shows different scenarios that may occur. Quantitative analysis of shearing of intersecting fractures and faults is challenging, particularly when considering the different contact states and dynamic contact pairs of the 4 (Figure 3.35d), 3 (Figure 3.35e) or 2 (Figure 3.35f) segments near one intersection, which can all be affected by and in turn influence the deformation of the intersection.

The initial demonstration of the new model is provided by the consistent results of DFN and MP cases calculated using NMM. Subsequently, we conducted a benchmark study using three examples with different codes and software based on continuum, discontinuum, and hybrid numerical methods. The software used in the study included NMM (LBNL), FLAC3D (LBNL), GBDEM (KIGAM), FRACOD (DynaFrax), and CASRock (CAS) (see Table 3.2).

Table 3.2: Overview of code/software and capabilities for the benchmark

Team	Method (Code/Software)	Continuum/ Discontinuum/ Hybrid	Representation of fractures/faults	Contact states	Rough fractures	DFNs
LBNL	NMM	Hybrid	Discontinuous interfaces across elements	Open, bonded, sliding	✓	✓
LBNL	FLAC3D	Continuum	Interfaces elements	Open, bonded, slip while bonded, sliding	✓	✓
KIGAM	GBDEM	Discontinuum	Discontinuous interfaces along grain boundaries	Open, bonded, sliding	✓	✓
CAS	hCA-FEM/xFEM (CASRock)	Hybrid	Discontinuous interfaces along or across elements	Open, bonded, sliding	✓	✓
DynaFrax	BEM (FRACOD)	Continuum	Boundaries	Open, elastic contact, or sliding	✓	✓

NMM: Numerical manifold method

GBDEM: Grain-based distinct element model

hCA-FEM/xFEM: Hybrid Cellular Automata-Finite Element Method/Extended Finite Element Method

CASRock: Cellular Automata Software for Engineering Rockmass Fracturing Process

BEM: Boundary element method

Three benchmark examples have been studied in detail (Hu et al., 2024):

- Two intersecting fractures

- Five intersecting fractures vs one major path
- A DFN vs four major paths

As major outcomes it has been shown in the study (Hu et al., 2024):

- Shearing of one or multiple major fractures can be reduced if there are multiple smaller intersecting fractures in that area. This may be particularly important for understanding and controlling induced seismicity in areas with multiple interacting faults in future studies.
- A new simplified Discrete Fracture Network (DFN) model, which simplifies the shearing of fracture networks by using major path(s), was verified and benchmarked for several examples involving different numbers of major path(s). The simplified DFN model can complement existing models, such as the equivalent continuum and discrete fracture models, by providing a new conceptual model for analyzing the shearing of intersecting fractures and faults. Additionally, it can be used in various software, even those with limitations in handling a large number of intersecting fractures.

The numerical investigations assumed the major path(s) for each DFN scenario. To obtain the optimized major path(s), we need to compare different choices of major paths and evaluate their consistency in terms of displacement and stress with the DFNs. With enough data and evaluation metrics, it may be possible to use machine learning to derive the optimized major paths.

The consistency between DFN and MP cases, as predicted by all the codes and software, demonstrates that these major paths can be used to represent DFNs in a wide range of software. The study demonstrates that the shearing of one or multiple major fractures can be reduced by the presence of multiple smaller intersecting fractures in the same area. This finding provides a useful basis for understanding and controlling induced seismicity in future studies. Additionally, the simplified Discrete Fracture Network (DFN) model shows promise as a new conceptual model that complements existing models, such as the equivalent continuum and discrete fracture models, for analyzing the shearing of intersecting fractures and faults.

### 3.4.2 Fracture networks - Damage processes

To investigate the impacts of discrete natural fractures on hydraulic fracturing, a two-dimensional model with a length and width of 100 m is generated, and two sets of natural fractures oriented at 60° and 120° are embedded in the model (Figure 3.36a). The model is divided into intensive fractured zones and sparse fractured zones, which exhibit strong anisotropy in terms of the natural fracture distribution (Cacas et al., 1990; Kolditz, 1995; Wang et al., 2022; Ji et al., 2023). The constant-volume injection mode is used, and the injection point located at the center of the model is set as the velocity boundary condition, while the outer boundary is set as the impermeable boundary. The minimum stress ( $\sigma_{\min}$ ) and maximum stress ( $\sigma_{\max}$ ) are set at the upper and right boundary of the model, respectively. The lower and left boundaries are roller boundaries. The parameters of the rock matrix, fractures, and fluid are listed in Table 3.3. They are generally similar to those of the Fenton Hill test site (Norbeck, McClure, and Horne, 2018; Lei, Gholizadeh Doonechaly, and Tsang, 2021). For the rock matrix, the porosity is approximately 0.05%, and the permeability is approximately  $0.5 \times 10^{-19}$  -  $2.0 \times 10^{-19}$  m<sup>2</sup> based on previous studies (Liu et al., 2020; Liu et al., 2021), and seepage in the matrix is negligible (Chen et al., 2022),

A maximum horizontal stress of 80 MPa and a minimum horizontal stress of 40 MPa are assigned. It is assumed that the initial pore pressure equals 31 MPa. Water is injected into the matrix at a constant flow rate of 2.5 kg/s for up to 1 hour. In the region with an area of 10000 m<sup>2</sup>, 8325 triangular finite elements are generated, as shown in Figure 3.36b.

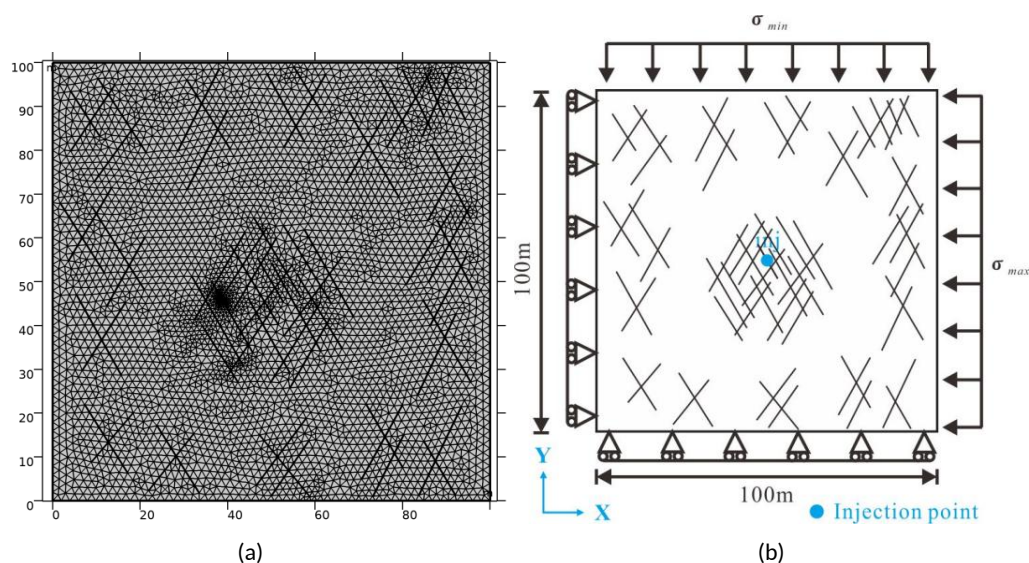


Figure 3.36: Schematic diagram of the model geometry, boundary conditions and mesh discretization.

Table 3.3: Material properties of the fractured rock mass, including the matrix, fractures and pore fluid (Norbeck, McClure, and Horne, 2018; Lei, Gholizadeh Doonechaly, and Tsang, 2021)

Material properties	Value	Units
<b>Matrix:</b>		
Density $\rho_m$	2650	kg/m <sup>3</sup>
Young's modulus E	60	GPa
Poisson's ratio $\nu$	0.25	-
Tensile strength $f_t$	10	MPa
Compressive strength $f_c$	350	MPa
Residual strength ratio $\eta$	0.1	-
Initial porosity $\varphi_0$	$1 \times 10^{-2}$	-
Residual porosity $\varphi_r$	$1 \times 10^{-3}$	-
Initial permeability $k_0$	$5 \times 10^{-19}$	m <sup>2</sup>
Biot's coefficient $\alpha$	0.4	-
Minimum stress $\sigma_{min}$	40	MPa
Specific heat of solids $C_p$	732	J/(kg·k)
Thermal conductivity of solids $\lambda_{eq}$	0.2	W/(m·k)
Temperature T	200	degC
The matrix thermal expansion coefficient	$6.2 \times 10^{-6}$	1/K
<b>Fractures:</b>		
Initial normal stiffness $K_{n0}$	50	GPa/m
Shear stiffness $K_s$	50	GPa/m
Friction angle $\phi_f$	30	deg
Dilation angle $\phi_d$	3	deg
Residual shear displacement $u_r$	5	mm
Residual aperture $b_r$	0.01	mm

Table 3.3: Material properties of the fractured rock mass, including the matrix, fractures and pore fluid (Norbeck, McClure, and Horne, 2018; Lei, Gholizadeh Doonechaly, and Tsang, 2021)

Fracture thermal capacity $C_f$	1200	J/(kg·K)
Fracture thermal conductivity $\lambda_f$	0.9	W/(m·K)
<b>Water:</b>		
Density $\rho_w$	1000	kg/m <sup>3</sup>
Viscosity $\mu_w$	$1.5 \times 10^{-4}$	Pa·s
Compressibility $c_w$	$4.4 \times 10^{-10}$	Pa <sup>-1</sup>

Figure 3.37 shows the evolution of the damage variable with the continuous injection of fluid under the relatively high initial stress state of  $\sigma_{\max}/\sigma_{\min} = 2$ . This demonstrates that the damage zone is mainly controlled by the maximum principal stress state, and the existence of natural fractures increases the complexity of the damage zone.

With the increase in the stress ratio ( $\sigma_{\max}/\sigma_{\min}$ ), the damage evolution in the minimum principal stress direction is restricted, while the fracture propagation in the maximum principal stress direction is greatly strengthened (Figure 3.38).

Three scenarios (with angles of 30, 45 and 60 degrees between the connecting line of the double wells and the maximum principal stress) are considered. The injection rate for both wells was 2.5 kg/s, and the injection time was 0.5 hours. The other parameters are shown in Table 3.3. The initial maximum principal stress is 80 MPa. Figure 3.39 illustrates that the largest fractured zone or damaged zone occurs in the double-well configuration 45° from the horizontal maximum principal stress, demonstrating that the configuration of the double wells should consider the distribution of the natural fracture system.



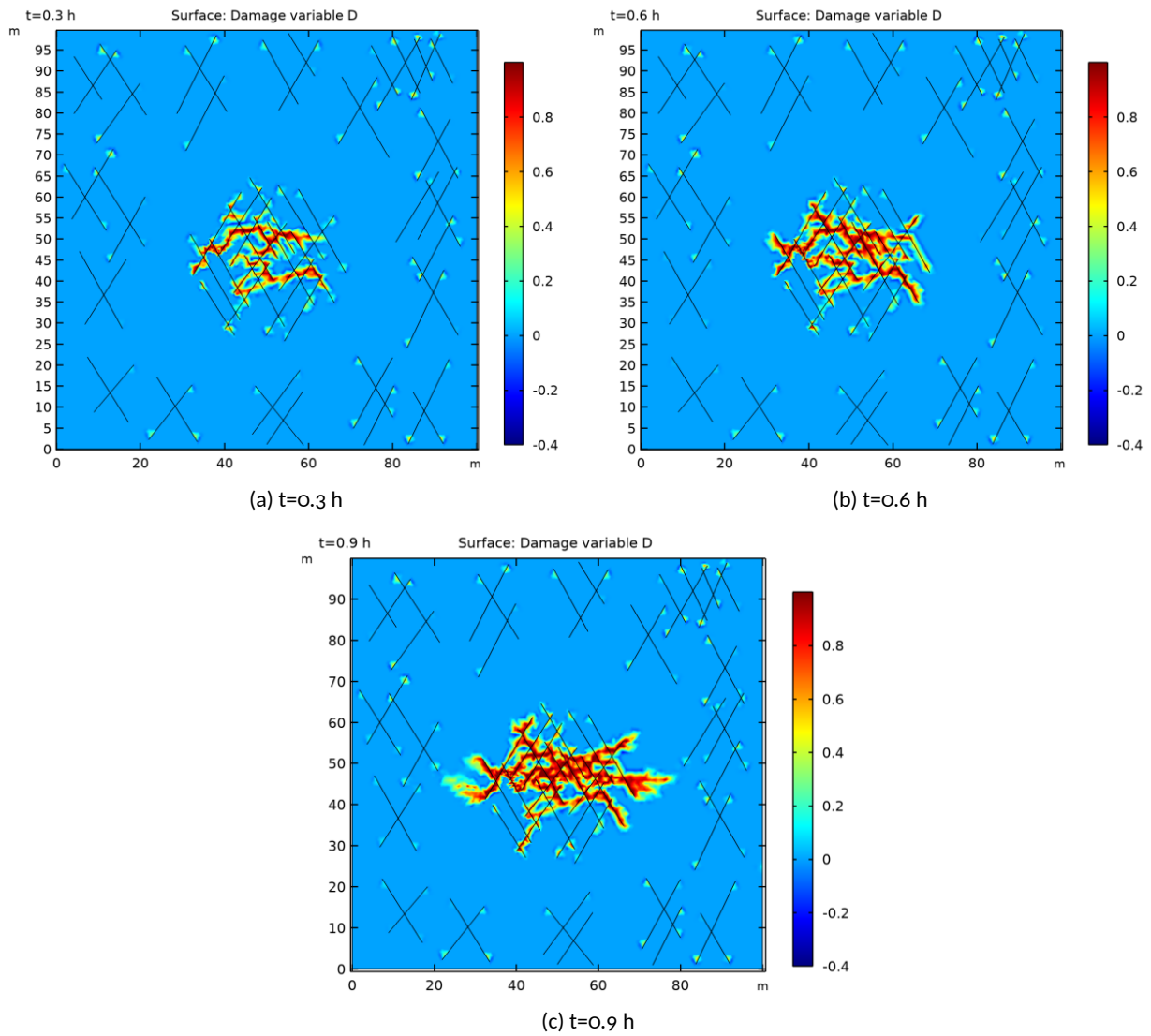


Figure 3.37: The evolution of fracture reservoir damage during fluid injection (the injection rate is constant at 2.5 kg/s).

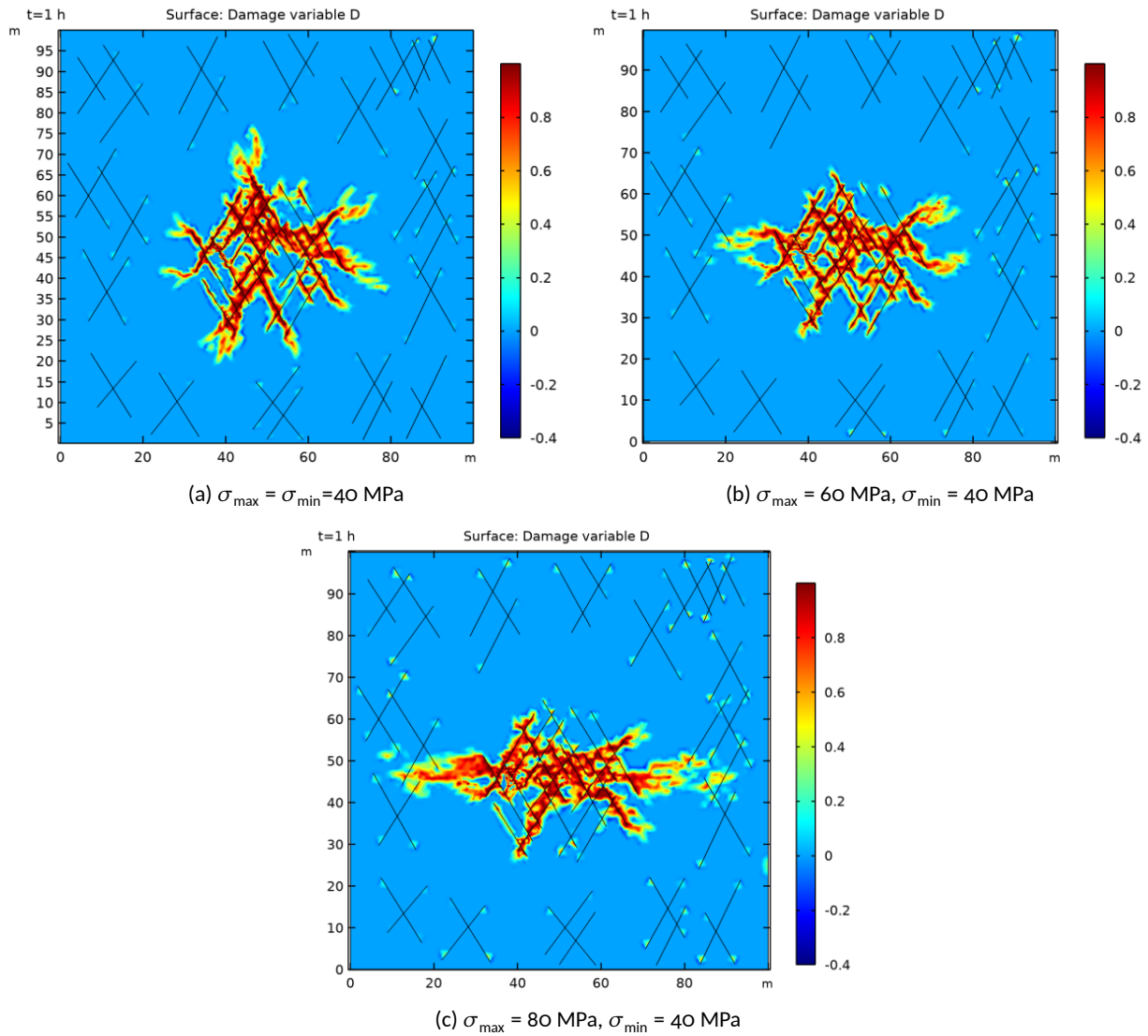


Figure 3.38: Damage evolution in the rocks after 1 hour of fluid injection under different stress states.

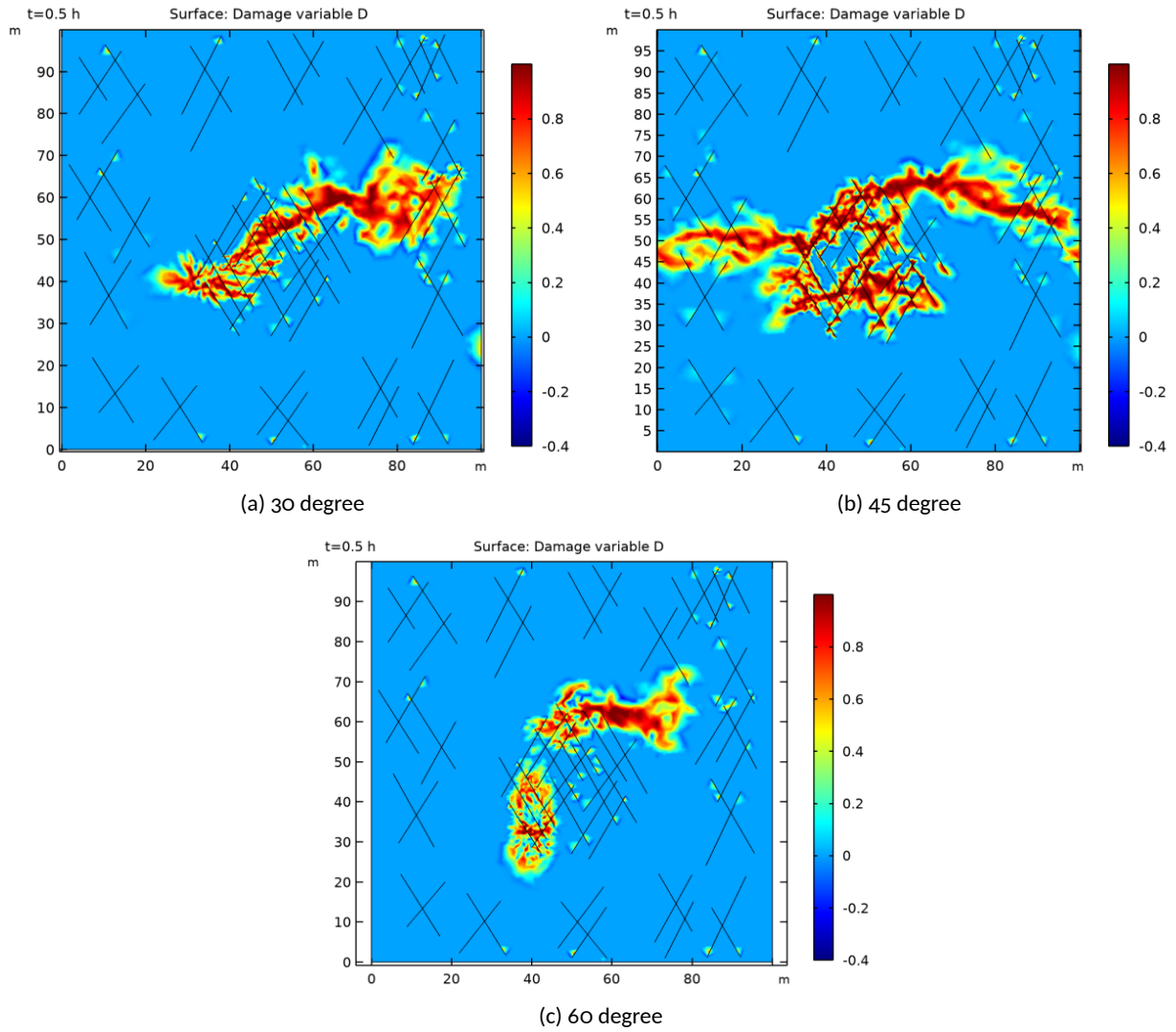


Figure 3.39: Damage evolution in the fractured rocks after 0.5 hours of simultaneous fluid injection in two wells

### 3.5 GREAT cell benchmarks

We briefly recall the benchmarking concept and guiding figure (Fig. 1.5) for GREAT cell experiments from section 1.1.2.

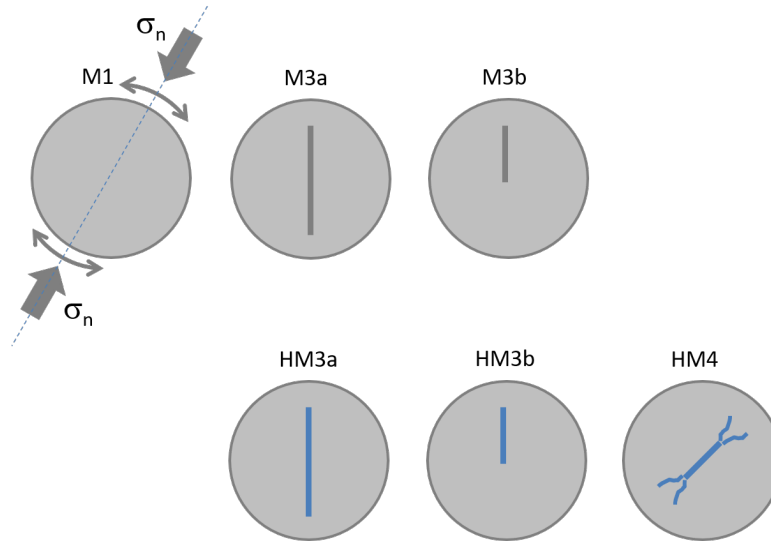


Figure 3.40: Benchmarking idea for 2D plane-strain conditions; upper figures represent M processes, lower figures represent HM processes

The results for the GREAT cell benchmarks are organized as follows:

- Intact samples (sec. 3.5.1)
- Fractured samples (sec. 3.5.2)
- Pressurised samples (sec. 3.5.3)
- Fracture propagation (sec. 3.5.4)

#### 3.5.1 Intact samples (M1)

The primary objective of the first benchmark exercise is to assess the mechanical deformation of the GREAT cell under different boundary conditions in a 2D plane strain (Figure 3.41). Two loading scenarios are considered: true-triaxial and axisymmetric loading.

The specimen consists of an opaque, non-crystalline thermoplastic polymer. Our computational model incorporates two distinct elastic materials within its domain: a central circle PMMA surrounded by a rubber sheath (in 2D). The material properties of the samples are provided in Table 3.5. To conduct the simulation, a 2D mesh is generated using GMSH, consisting of triangle elements. The mesh includes 2416 nodes and 4735 elements.

Figure 3.41b illustrates the 2D representation of the benchmark exercise, highlighting the locations of the Pressure-Exerting Elements (PEEs) and Dynamic-Sealing-Strips (DSS). The loading specifications for the PEEs are available in Table 3.4. Meanwhile, the load acting on the DSSs is determined as the average of the loads applied to adjacent PEEs. In the true triaxial scenario, the stress field follows  $\sigma_1 > \sigma_2 > \sigma_3$ , whereas, in the axisymmetric scenario:  $\sigma_1 > \sigma_2 = \sigma_3$ . To enforce boundary conditions, the zero circumferential displacement boundary condition is defined at the intersection of the sample with the x and y axes:

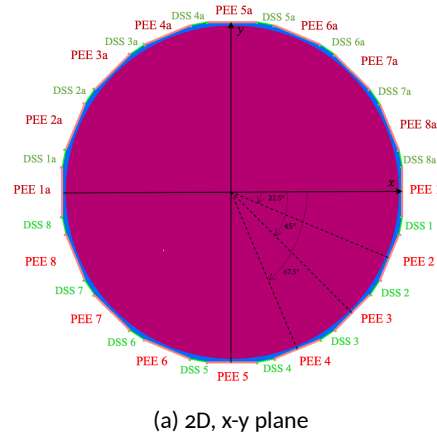


Figure 3.41: Geometry and location of Pressure-Exerting Elements (PEEs) and Dynamic-Sealing-Strips (DSSs).

$$\begin{aligned}
 u_x(x, y) &= 0, & \text{for } x = 0.0 \text{ and } (y = 0.9894 \text{ or } y = -0.09894), \\
 u_y(x, y) &= 0, & \text{for } y = 0.0 \text{ and } (x = 0.9894 \text{ or } x = -0.09894),
 \end{aligned} \tag{3.7}$$

these constraints ensure that the displacement components  $u_x$  and  $u_y$  are zero at the specified boundaries of the 2D domain.

Table 3.4: Loading scenarios for mechanical deformation benchmarks

True Triaxial	Axisymmetric
PEEs 1 & 1a: 7.73 MPa	PEEs 1 & 1a: 7.71 MPa
PEEs 2 & 2a: 5.70 MPa	PEEs 2 & 2a: 7.70 MPa
PEEs 3 & 3a: 4.39 MPa	PEEs 3 & 3a: 8.30 MPa
PEEs 4 & 4a: 2.40 MPa	PEEs 4 & 4a: 7.80 MPa
PEEs 5 & 5a: 2.30 MPa	PEEs 5 & 5a: 7.74 MPa
PEEs 6 & 6a: 4.00 MPa	PEEs 6 & 6a: 7.70 MPa
PEEs 7 & 7a: 6.40 MPa	PEEs 7 & 7a: 8.30 MPa
PEEs 8 & 8a: 7.70 MPa	PEEs 8 & 8a: 7.72 MPa
DSSs: average of loads of adjacent PEEs	DSSs: average of loads of adjacent PEEs

Table 3.5: Material properties

Material Property	Symbol	Value	Unit
Sample Young's modulus	E	3.85	GPa
Sample Poisson's ratio	$\nu$	0.4	-
Rubber sheath Young's modulus	E	0.1	GPa
Rubber sheath Poisson's ratio	$\nu$	0.4	-

In the post-processing step, we plot either the volumetric strain

$$\varepsilon_{\text{vol}} = \varepsilon_{xx} + \varepsilon_{yy} \tag{3.8}$$

or surface strain (a ratio of the change in length of the material to its initial length) as a function of the angle. The angle is measured clockwise from the positive x-axis and is evaluated at  $(x, y) \in \mathbb{R}^2 \mid |x^2 + y^2 - 0.065^2| < 10^{-6}$ . The length unit is the meter.

The result of the strain profile in *M1* benchmark for both loading scenarios in 2D is shown in Figure 3.42. Furthermore, the volumetric strain at various angles is graphically represented for both loading scenarios on the probe curve in Figure 3.43.

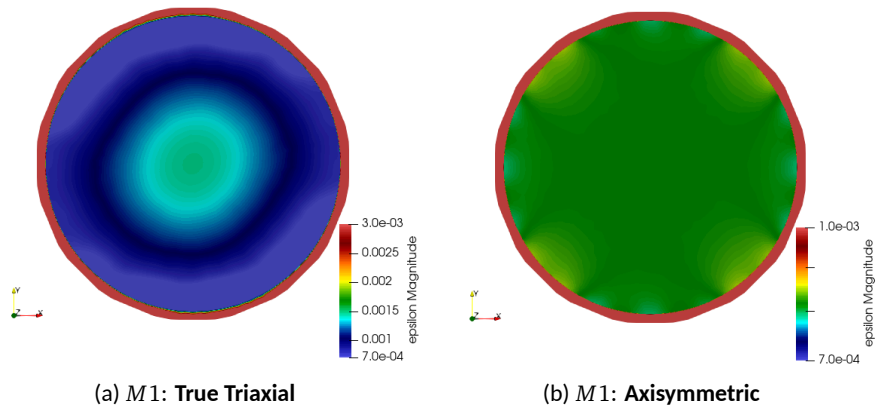
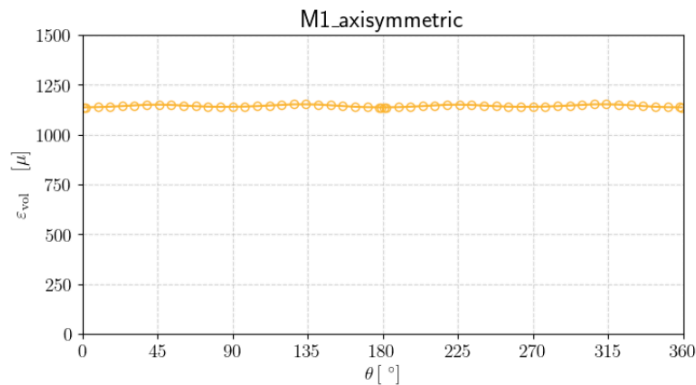
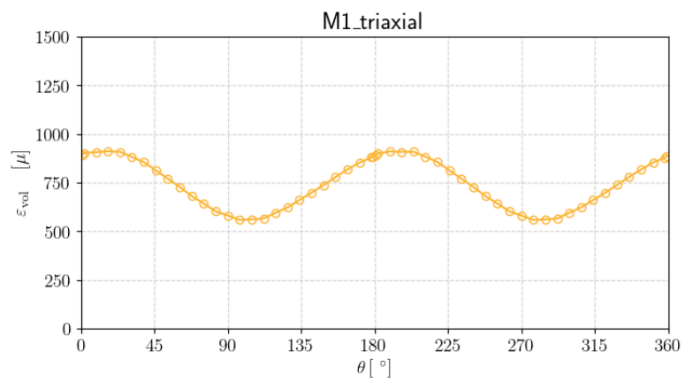


Figure 3.42: The results of the strain field for the 2D benchmark exercise *M1* are shown, with loading scenarios defined in Table 3.4. It's important to note the distinct strain ranges; the strain value at the sheath is much higher than the visualization range (UFZ–VPF/FEM–OGS6).



(a) *M1*: Axisymmetric



(b) *M1*: True Triaxial

Figure 3.43: Volumetric strain versus angle for an intact sample (*M1*) (UFZ–VPF/FEM–OGS6).

### 3.5.2 Fractured samples (M3a & M3b)

The objective of the second set of benchmarks is to explore the mechanical deformation in fractured samples. In the initial set of benchmarks, our focus was on a symmetric central line fracture denoted as  $\Gamma = [-0.065, 0.065] \times \{0\}$ . However, in the second set, we have only considered half of the fracture, specifically  $\Gamma = [0, 0.065] \times \{0\}$ , see figure 3.44. For the numerical simulations, we assume the fracture to be static by defining a high critical energy release rate ( $G_c$ ) for the fracture. The material properties utilized in the simulations are presented in Table 3.5. Essentially, we maintain a constant fracture angle and vary the loading by rotating the load orientation. This can be considered as rotating the fracture within the sample while keeping the load constant. The specific loading conditions for the benchmarks are outlined in Table 3.6. Additionally, we impose Dirichlet boundary conditions as given in equation 3.7. The result of the strain profile in *M3a* (two-wing fractures) and *M3b* (one-wing fracture) benchmarks for different loading scenarios in 2D are shown in Figures 3.45 and 3.46, respectively. Furthermore, the volumetric strain at various angles is graphically represented for both loading scenarios on the probe curve in Figure 3.47.

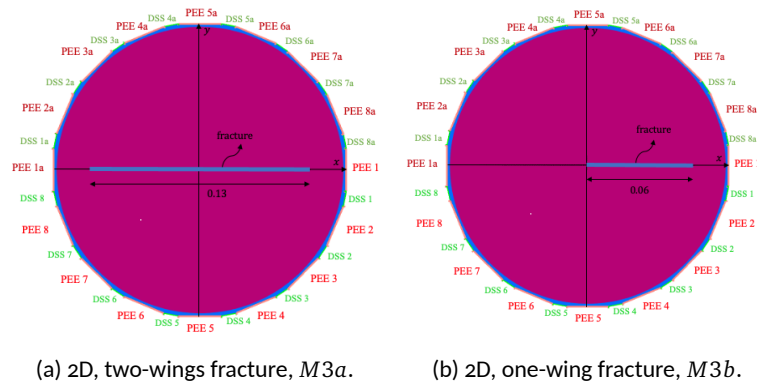


Figure 3.44: Geometry and location of PEEs and DSSs.

Table 3.6: Loading Conditions for Different Angles

Angle (°)	Loading Conditions
0	PEEs 1 & 1a: 8 MPa PEEs 5 & 5a: 8 MPa
22.5	PEEs 8 & 8a: 8 MPa PEEs 4 & 4a: 8 MPa
45	PEEs 7 & 7a: 8 MPa PEEs 3 & 3a: 8 MPa
67.5	PEEs 6 & 6a: 8 MPa PEEs 2 & 2a: 8 MPa
DSSs: zero	

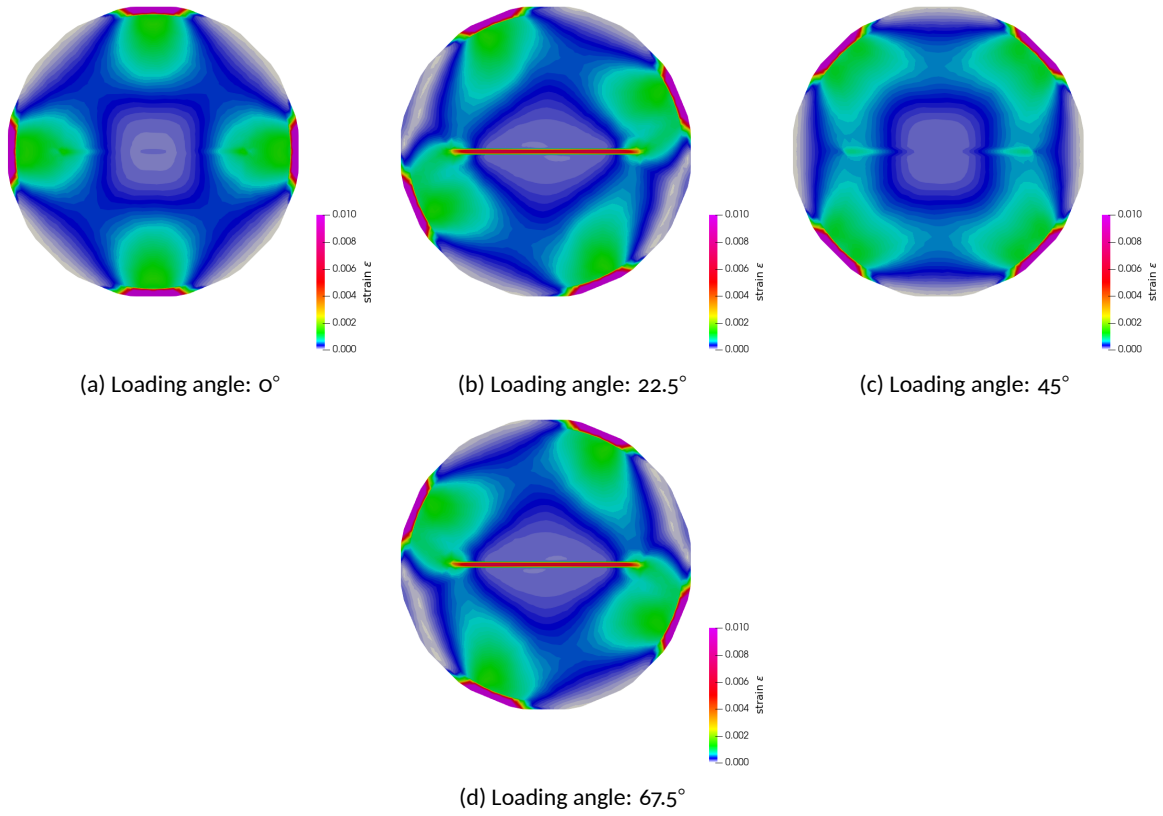


Figure 3.45: Strain profile for 2D specimens include two-wings fracture, *M3a* (UFZ-VPF/FEM-OGS6).

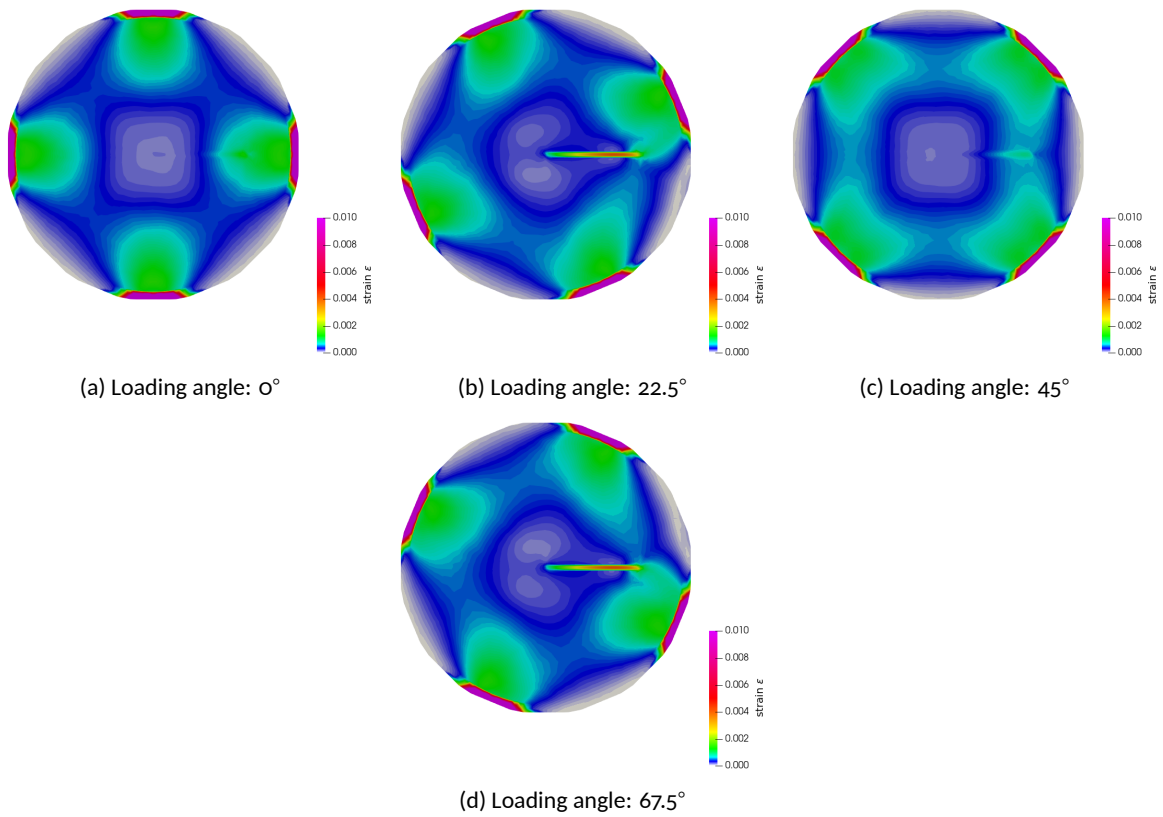
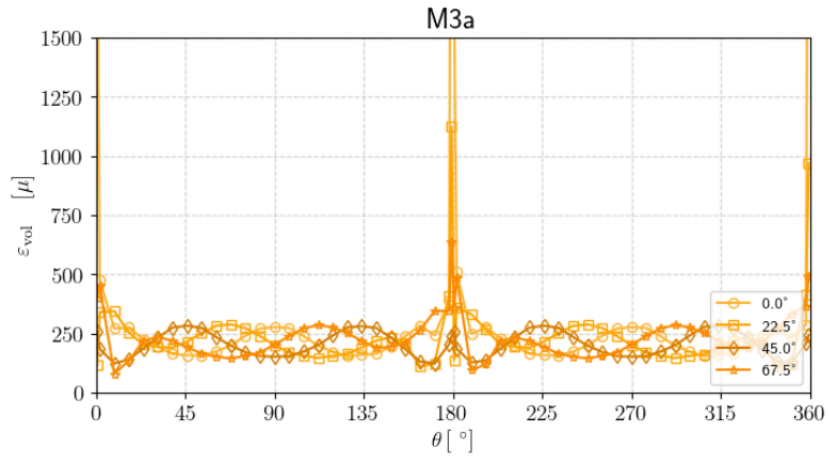
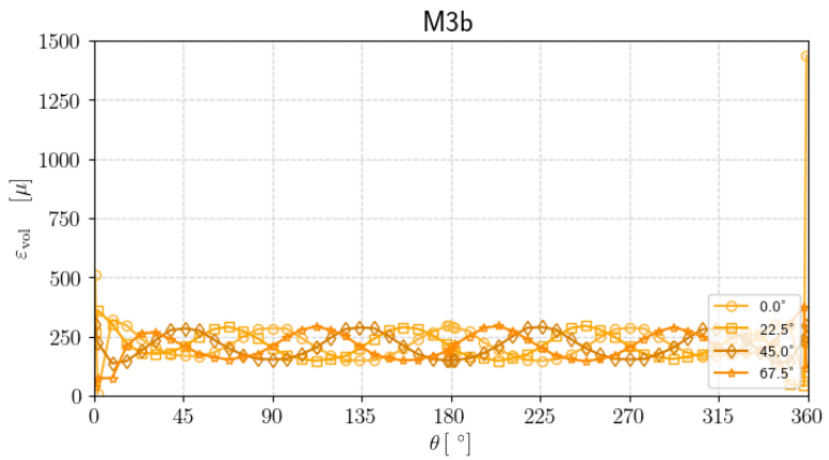


Figure 3.46: Strain profile for 2D specimens include one-wing fracture, *M3b* (UFZ-VPF/FEM-OGS6).





(a) *M3a*: one-wing fracture



(b) *M3b*: two-wings fracture

Figure 3.47: Volumetric strain versus angle for fractured samples, *M3a* and *M3b* (UFZ-VPF/FEM-OGS6).

### 3.5.3 Pressurized samples (HM3a & HM3b)

The main aim of the fourth benchmark is to examine the hydro-mechanical behavior exhibited by a fractured sample. To achieve this, we employ the identical samples and boundary conditions detailed in Section 3.5.2. In this particular benchmark, a pressure of 5 MPa is uniformly applied to the surfaces of the fracture (Figure 3.48). Moreover, we assume the fracture to be impermeable. These numerical experiment conditions provide insights into the coupled response of the fractured sample under the influence of both hydraulic and mechanical factors.

The result of the strain profile of *HM3a* and *HM3a* benchmarks for different loading scenarios in 2D are shown in Figures 3.49 and 3.50, respectively. Furthermore, the volumetric strain at various angles is graphically represented for both loading scenarios on the probe curve in Figure 3.51.

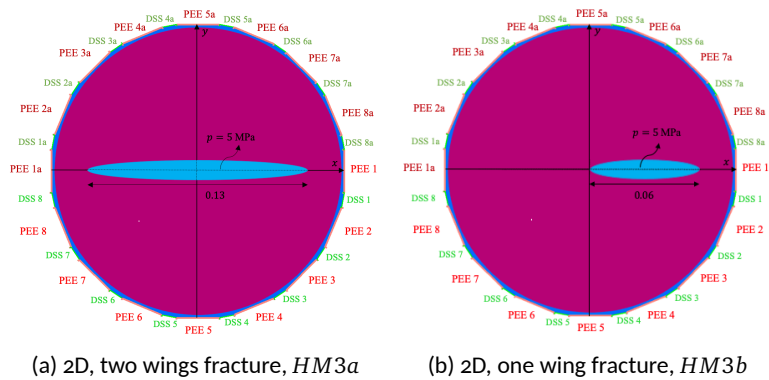


Figure 3.48: Geometry and location of PEEs and DSSs.

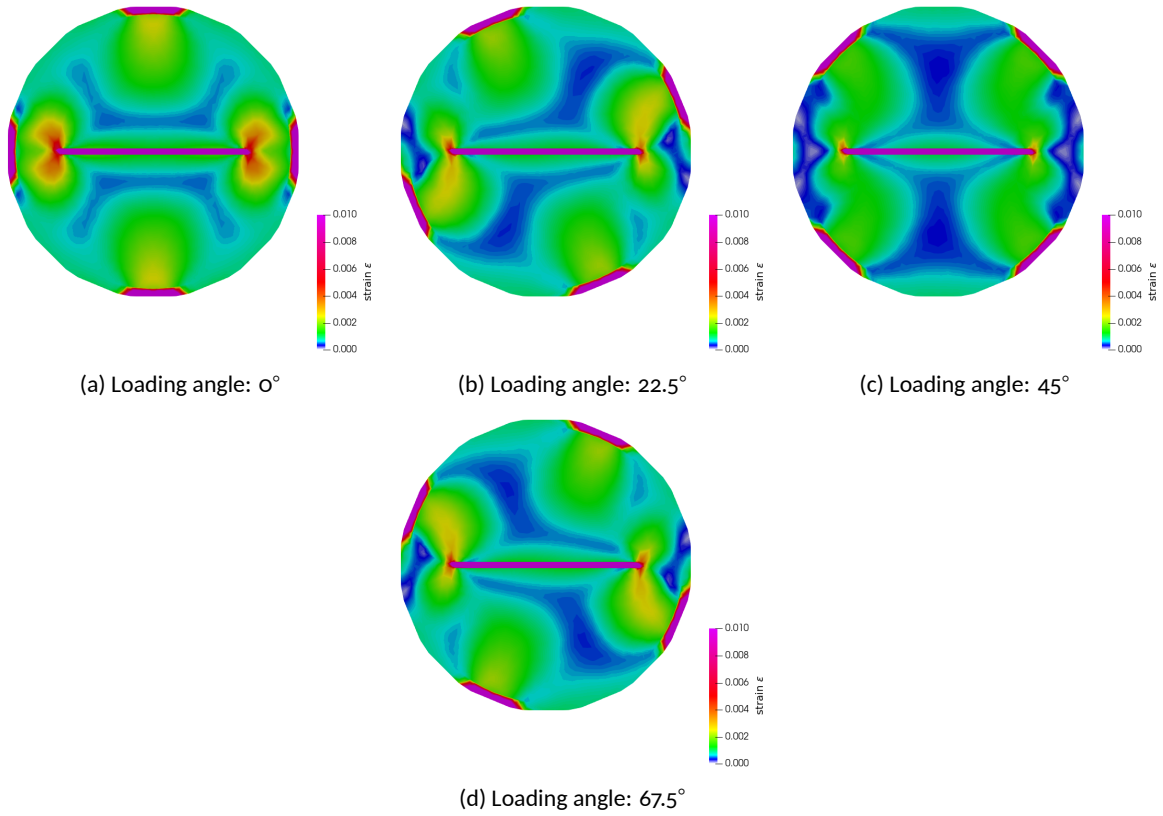


Figure 3.49: Strain profile for 2D specimens include a pressurised two-wings fracture, *HM3a* (UFZ-VPF/FEM-OGS6).

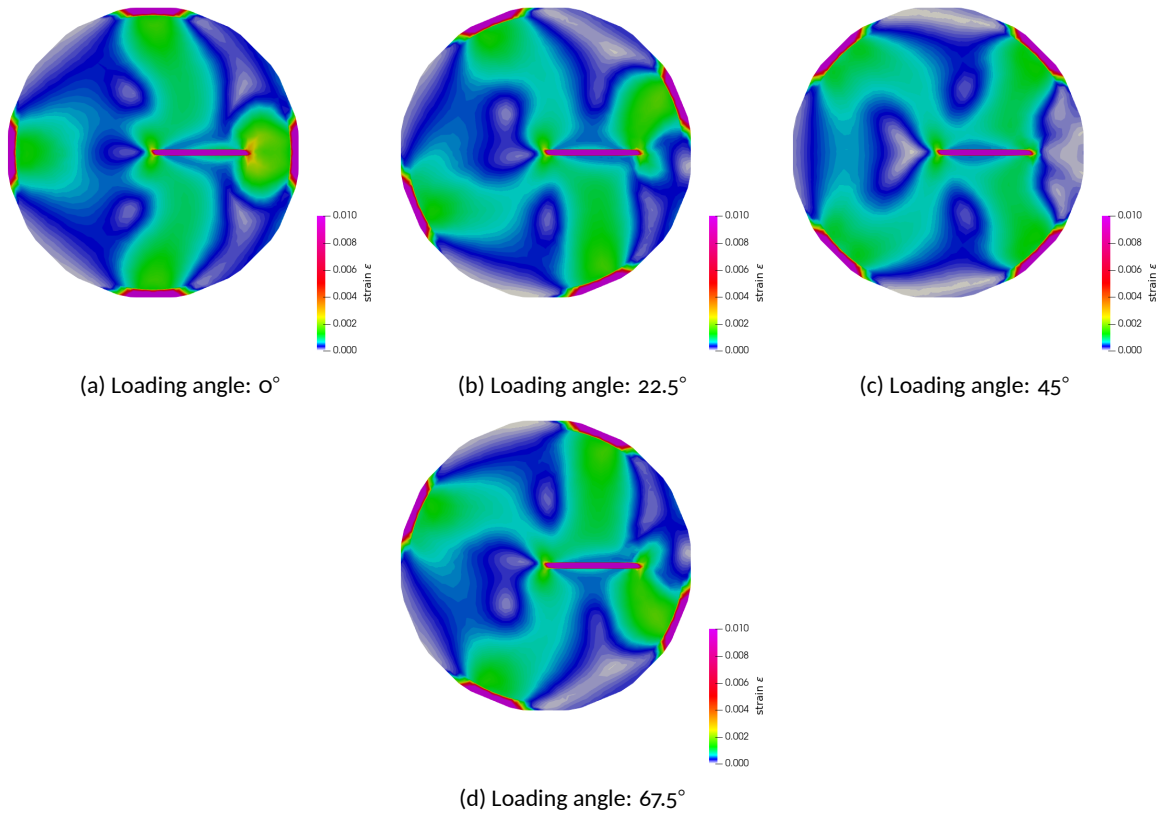
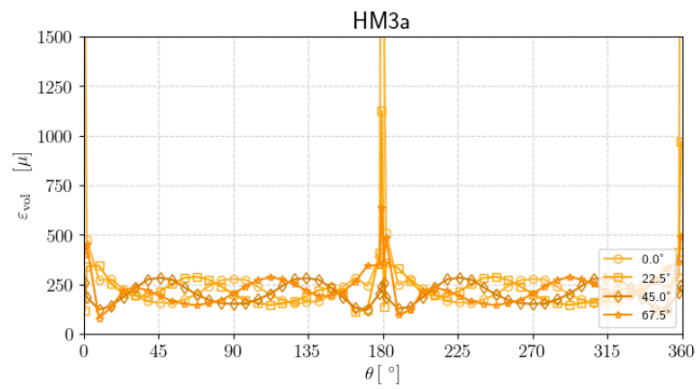
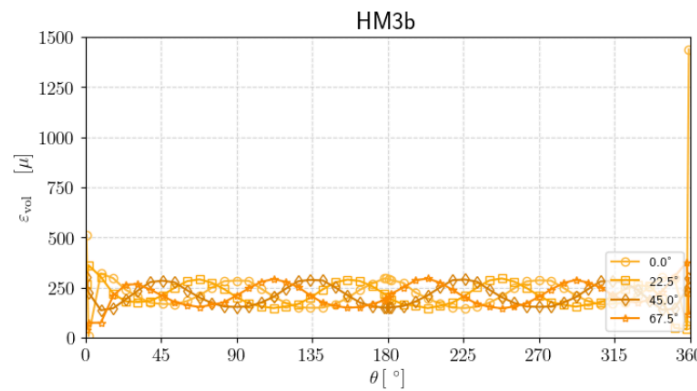


Figure 3.50: Strain profile for 2D specimens include a pressurised one-wing fracture, *HM3b* (UFZ-VPF/FEM-OGS6).



(a) *HM3a*: one-wing fracture



(b) *HM3b*: two-wings fracture

Figure 3.51: Volumetric strain versus angle for fractured samples, *HM3a* and *HM3b* (UFZ-VPF/FEM-OGS6).

### 3.5.4 Hydraulic Fracturing (HM4): Variational phase-field method (OGS and CAS Teams)

In the final set of 2D benchmarks, we aim to simulate hydraulic fracturing under various boundary conditions. The fluid is injected at the center of an inclined fracture to capture the hydraulic fracturing process. To examine the influence of polyaxial stress boundary conditions on fracture propagation, we define three different scenarios, as summarized in Table 3.8. The material properties and fluid properties used in the simulations are presented in Table 3.7. These parameters play a crucial role in determining the behavior of the fractured sample and the fluid flow within the fracture. By exploring these benchmarks, we can gain valuable insights into the mechanics of hydraulic fracturing and its response to different polyaxial stress boundary conditions.

Figures 3.53-3.55 depict snapshots of the phase field, pressure, and strain for various loading scenarios. In Figure 3.53 (Scenario I), the minimum stress applied in the x-direction leads to fracture propagation deviating towards the horizontal direction. Conversely, in Scenario II, where the minimum stress is applied in the Y-direction, Figure 3.54 illustrates hydraulic fracturing deviating towards the vertical direction. Furthermore, in Scenario III, where the far-field stresses perpendicular and parallel to the fracture are identical, fractures persist in propagating diagonally (Figure 3.55).

Table 3.7: Material and Fluid Properties

Properties	Values	Unit
$E$	$3.85 \times 10^9$	Pa
$\nu$	0.4	-
$K$	$5 \times 10^{-18}$	$\text{m}^2$
$\phi$	0.0	-
$\mu$	$10^{-8}$	Pa·s
$G_c$	6.8	N/m
$c_f$	0	-
$Q_0$	$2 \times 10^{-3}$	$\text{m}^2/\text{s}$

Table 3.8: Loading Conditions for Different Angles

Scenario	Loading Conditions
I	PEEs 1 & 1a: 0.5 MPa
	PEEs 5 & 5a: 2 MPa
II	PEEs 1 & 1a: 2 MPa
	PEEs 5 & 5a: 0.5 MPa
III	PEEs 7 & 7a: 1 MPa
	PEEs 3 & 3a: 1 MPa
DSSs: zero	

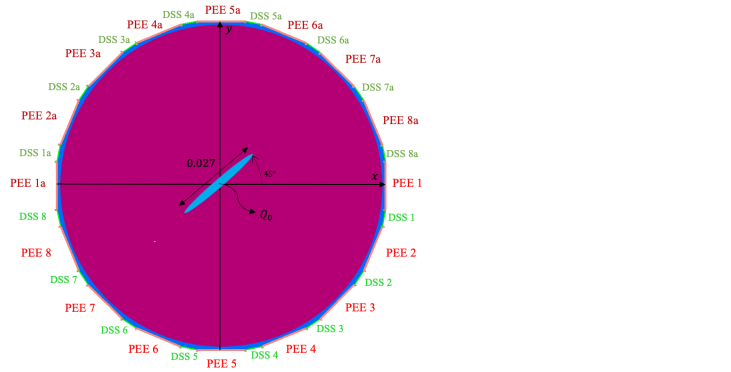


Figure 3.52: Geometry and location of PEEs and DSSs.

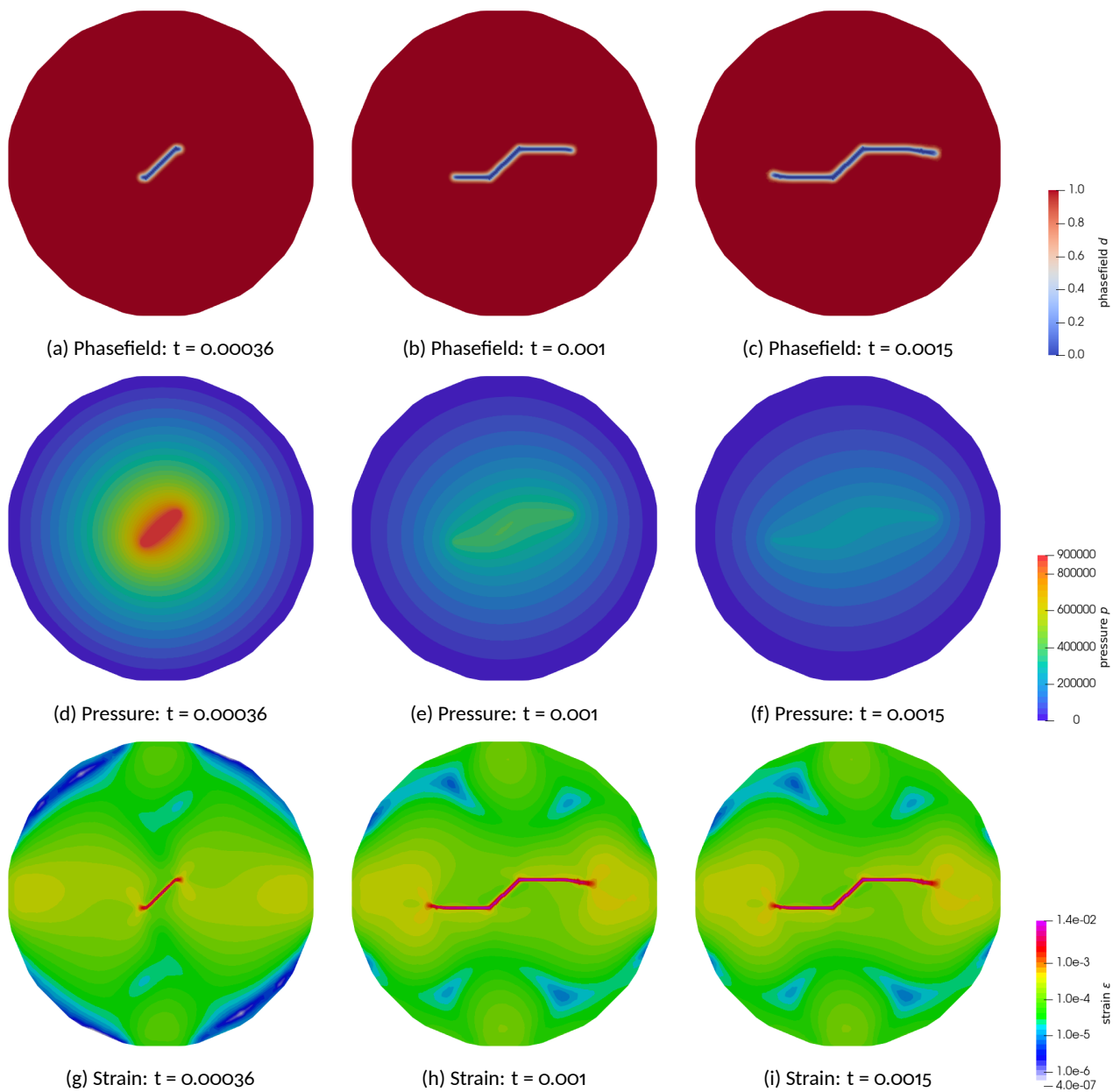


Figure 3.53: Resulting fields for benchmark HM4 Scenario I, for different time steps (UFZ-VPF/FEM-OGS6).

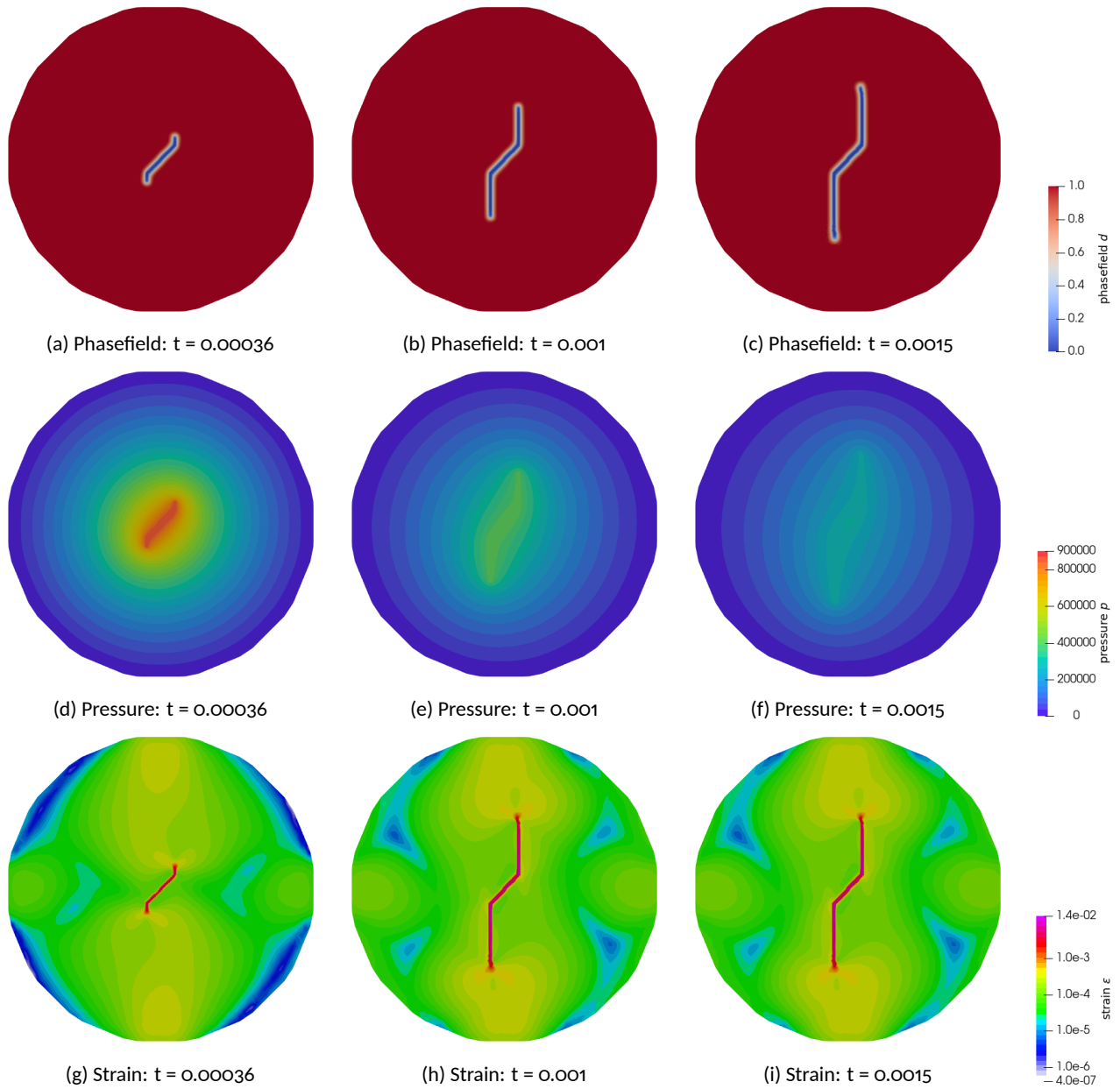


Figure 3.54: Resulting fields for benchmark HM4 Scenario II, for different time steps (UFZ-VPF/FEM-OGS6).

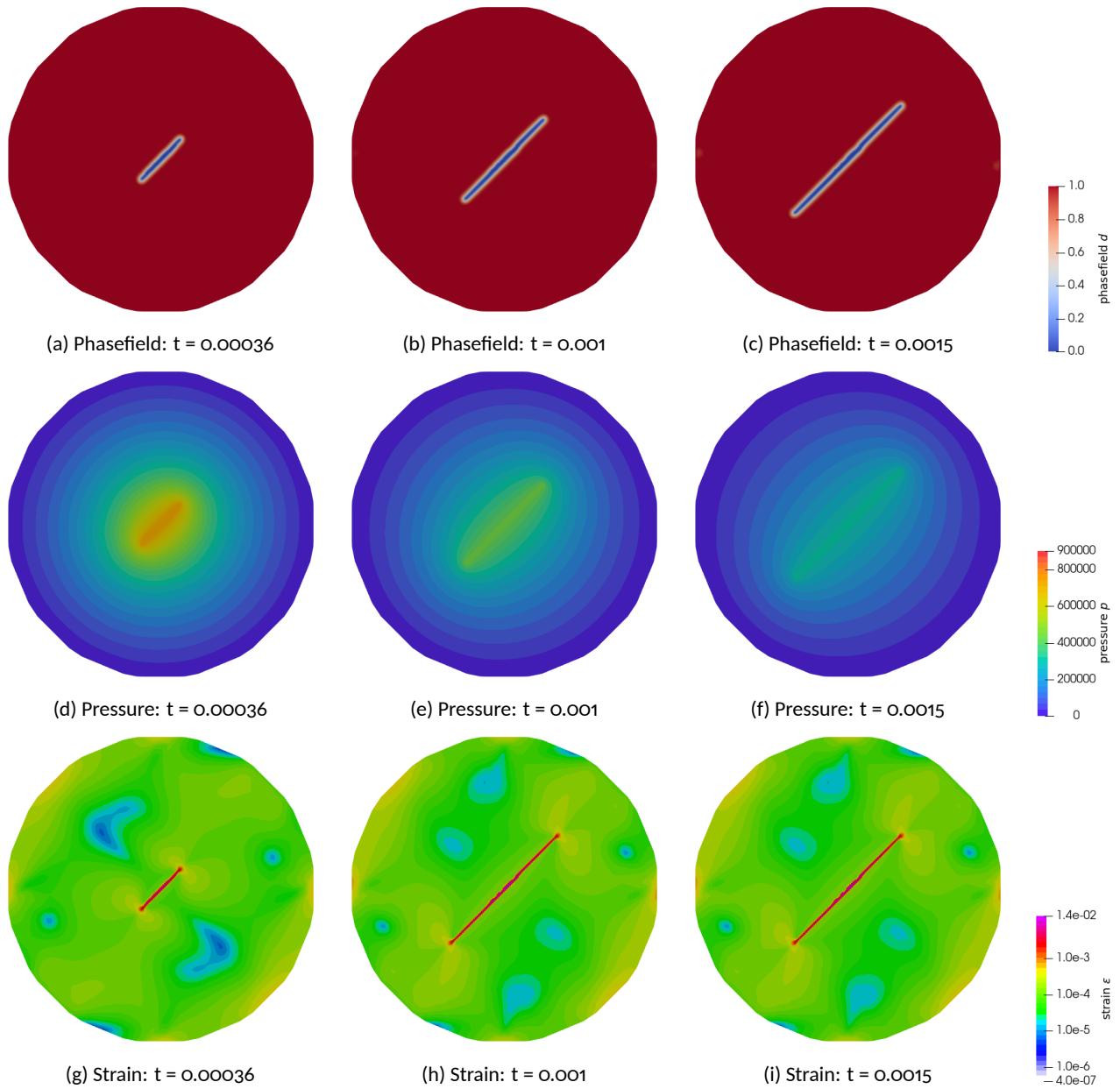


Figure 3.55: Resulting fields for benchmark HM4 Scenario III, for different time steps (UFZ-VPF/FEM-OGS6).



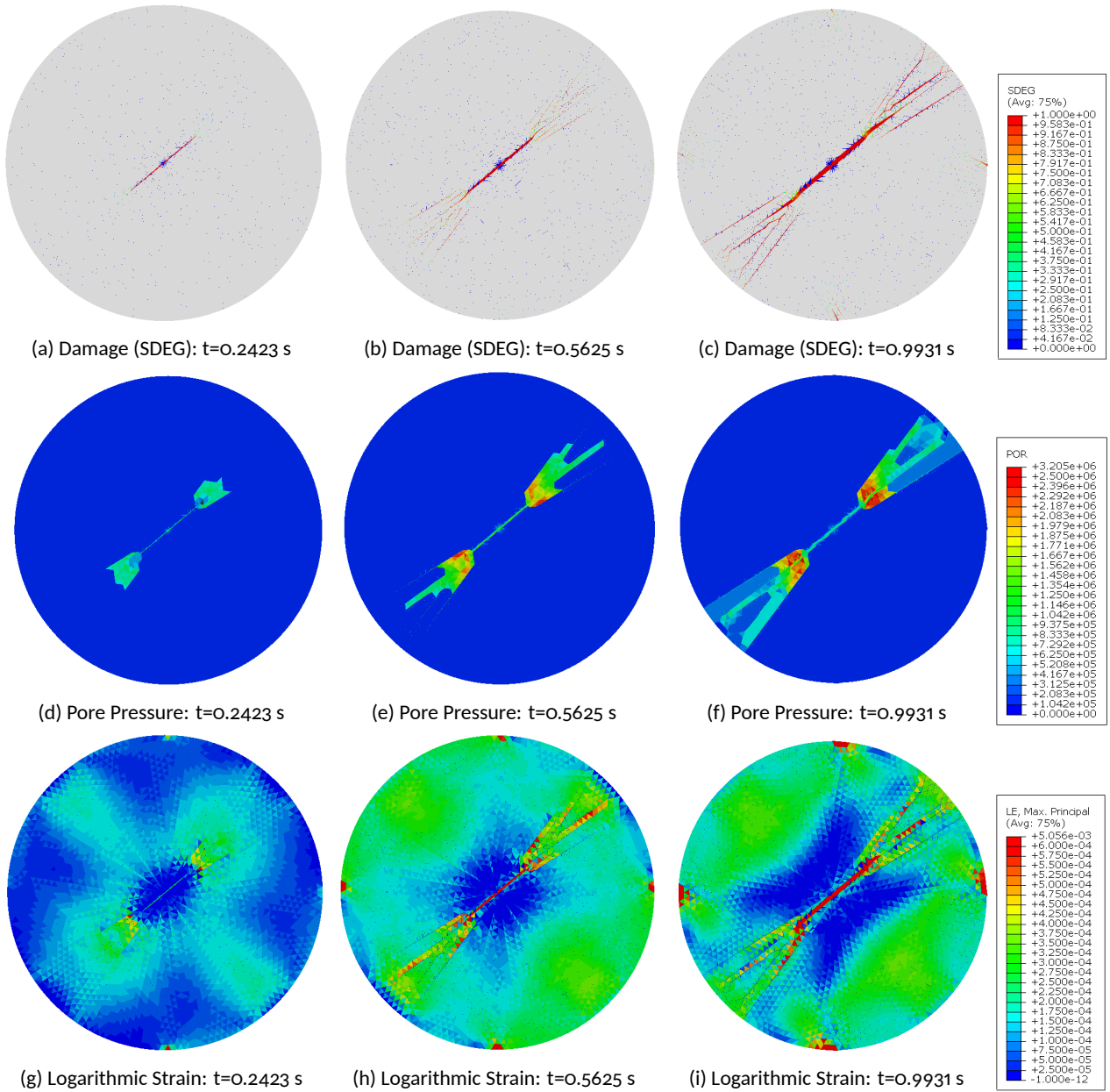


Figure 3.56: Resulting fields for benchmark HM4 Scenario III, for different time steps (CAS)

## References

- Bourdin, B., C. Chukwudozie, and K. Yoshioka (2012). “A variational approach to the numerical simulation of hydraulic fracturing”. In: *SPE ATCE 2012*.
- Cacas, M.C. et al. (1990). “Modeling fracture flow with a stochastic discrete fracture network: calibration and validation: 1. The flow model”. In: *Water Resources Research* 26.3. Cited by: 615, pp. 479 – 489. DOI: 10.1029/WR026i003p00479. URL: <https://www.scopus.com/inward/record.uri?eid=2-s2.0-0025591480&doi=10.1029%2fWR026i003p00479&partnerID=40&md5=78013936bef0d7ae241bb76bb232ee7f>.
- Chen, Bin et al. (2022). “A Review of Hydraulic Fracturing Simulation”. In: *Archives of Computational Methods in Engineering* 29.4. Cited by: 114; All Open Access, Green Open Access, Hybrid Gold Open Access, pp. 1 – 58. DOI: 10.1007/s11831-021-09653-z. URL: <https://www.scopus.com/inward/record.uri?eid=2-s2.0-85116857718&doi=10.1007%2fs11831-021-09653-z&partnerID=40&md5=66d9e866442f243da5086ef6f70d3e7b>.
- Dean, R H and Joseph H Schmidt (2009). “Hydraulic-fracture predictions with a fully coupled geomechanical reservoir simulator”. In: *SPE Journal* 14.04, pp. 707–714. ISSN: 1086055X.
- Detournay, E. (2016). “Mechanics of hydraulic fractures”. In: *Annual Review of Fluid Mechanics* 48, pp. 311–339.
- Frühwirt, Thomas, Daniel Pötschke, and Heinz Konietzky (2021). “Simulation of direct shear tests using a forces on fracture surfaces (FFS) approach”. In: *Environmental Earth Sciences* 80.8, pp. 1–10.
- Griffith, A. A. (1920). “The Phenomenon of Rupture and Flow in Solids”. In: *Phil. Trans. Roy. Soc. London* 7A 221, p. 163.
- Hu, Mengsu et al. (2024). “Benchmark Study of A New Simplified DFN Model for Shearing of Intersecting Fractures and Faults”. In: *Geomechanics for Energy and the Environment (GETE)*. submitted, pp. 1–27.
- Ji, Jiayan et al. (2023). “Study on fracture evolution model of the enhanced geothermal system under thermal-hydraulic-chemical-deformation coupling”. In: *Energy* 269. Cited by: 10. DOI: 10.1016/j.energy.2022.126604. URL: <https://www.scopus.com/inward/record.uri?eid=2-s2.0-85146641713&doi=10.1016%2fj.energy.2022.126604&partnerID=40&md5=42b8834c98df34f0000707c9f92cecb1>.
- Ji, Lujun, A. Settari, and R. B. Sullivan (2009). “A novel hydraulic fracturing model fully coupled with geomechanics and reservoir simulation”. In: *SPE Journal* 14.3, pp. 423–430. ISSN: 1086055X.
- Kolditz, O. (1995). “Modelling flow and heat transfer in fractured rocks: Conceptual model of a 3-D deterministic fracture network”. In: *Geothermics* 24.3. Cited by: 89, pp. 451 – 470. DOI: 10.1016/0375-6505(95)00020-Q. URL: <https://www.scopus.com/inward/record.uri?eid=2-s2.0-0029416487&doi=10.1016%2f0375-6505%2895%2900020-Q&partnerID=40&md5=766f97d0d32ca8a10f923441c3cd90d4>.
- Lei, Qinghua, Nima Gholizadeh Doonechaly, and Chin-Fu Tsang (2021). “Modelling fluid injection-induced fracture activation, damage growth, seismicity occurrence and connectivity change in naturally fractured rocks”. In: *International Journal of Rock Mechanics and Mining Sciences* 138. Cited by: 71; All Open Access, Hybrid Gold Open Access. DOI: 10.1016/j.ijrmms.2020.104598. URL: <https://www.scopus.com/inward/record.uri?eid=2-s2.0-85098557463&doi=10.1016%2fj.ijrmms.2020.104598&partnerID=40&md5=278954e4a6f1c3130943d0a08d929dd4>.
- Liu, Hejuan et al. (2020). “Numerical modeling of thermal breakthrough induced by geothermal production in fractured granite”. In: *Journal of Rock Mechanics and Geotechnical Engineering* 12.4. Cited by: 31; All Open Access, Gold Open Access, pp. 900 – 916. DOI: 10.1016/j.jrmge.2020.01.002. URL: <https://www.scopus.com/inward/record.uri?eid=2-s2.0-85087125825&doi=10.1016%2fj.jrmge.2020.01.002&partnerID=40&md5=f25318b41497b58bd8d0fc9e7d3eb0ab>.
- Liu, Hejuan et al. (2021). “Seepage characteristics of thermally and chemically treated Mesozoic granite from geothermal region of Liaodong Peninsula”. In: *Environmental Earth Sciences* 80.17. Cited by: 9. DOI: 10.1007/s12665-021-09838-6. URL: <https://www.scopus.com/inward/record.uri?eid=2-s2.0-85113715428&doi=10.1007%2fs12665-021-09838-6&partnerID=40&md5=749bcc7d9c45b82f7a98f3bc7b73666>.
- Norbeck, Jack H., Mark W. McClure, and Roland N. Horne (2018). “Field observations at the Fenton Hill enhanced geothermal system test site support mixed-mechanism stimulation”. In: *Geothermics* 74. Cited by: 71; All Open Access, Hybrid Gold Open Access, pp. 135 – 149. DOI: 10.1016/j.geothermics.2018.03.003. URL: <https://www.scopus.com/inward/record.uri?eid=2-s2.0-85043464822&doi=10.1016%2fj.geothermics.2018.03.003&partnerID=40&md5=117d5f6b9bfa46e786b777d7640f2ce1>.
- Sneddon, I.N. and M. Lowengrub (1969a). *Crack problems in the classical theory of elasticity*. The SIAM series in Applied Mathematics. John Wiley & Sons.
- (1969b). *Crack problems in the classical theory of elasticity*. John Wiley & Sons.
- Wang, Hongwei et al. (2022). “Thermal response of the fractured hot dry rocks with thermal-hydro-mechanical coupling effects”. In: *Geothermics* 104. Cited by: 8. DOI: 10.1016/j.geothermics.2022.102464. URL: <https://www.scopus.com/inward/>

[record.uri?eid=2-s2.0-85133940094&doi=10.1016%2fj.geothermics.2022.102464&partnerID=40&md5=5969e5a3ec0a99c4e54a318612be42b5](https://doi.org/10.1016/j.geothermics.2022.102464).

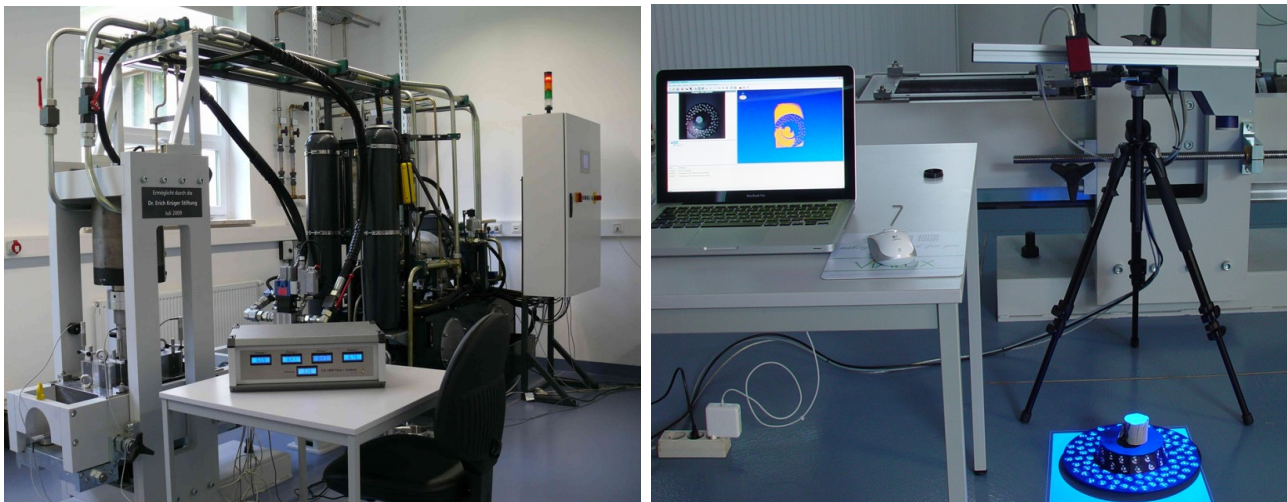
Yoshioka, Keita, Dmitri Naumov, and Olaf Kolditz (2020). "On crack opening computation in variational phase-field models for fracture". In: *Computer Methods in Applied Mechanics and Engineering* 369, p. 113210. ISSN: 0045-7825.

## 4 Freiberg experiments (M processes)

### Mechanical behaviour rough fractures before and after mechanical shear: Freiberg experiment

#### 4.1 Experimental facility

The experimental basis for Task G Step 1 is kindly provided by the University of Mining Technology Freiberg (TUBAF), Chair for Geomechanics, Rock Mechanics and Rock Engineering (Prof. Konietzky). In the frame of the GeomInt project<sup>3</sup> different kinds of direct shear tests have been conducted to investigate shear characteristics of fractures in crystalline rocks, namely Constant Normal Load (CNL) and Constant Normal Stiffness (CNS) tests. For conducting the CNL and CNS tests a shear box device developed at the Freiberg Rock Laboratory has been used<sup>4</sup>. In order to obtain high-resolution measurements of the rock fracture surfaces, a white light scanning device was used<sup>5</sup>. The experimental devices are shown in Figure 4.1, respectively.



(a) Shear box device GS-1000

(b) 3D surface and body scanner

Figure 4.1: TUBAF experimental facilities for direct shear tests forming the basis for Task G Step 1

#### 4.2 Experimental procedure and results

Figures 4.2a and 4.2b show the basic experimental concepts of Constant Normal Load (CNL) and Constant Normal Stiffness (CNS) tests, respectively. The presented results are from the GeomInt project ([www.ufz.de/geomint](http://www.ufz.de/geomint)) have been recently published in Frühwirt, Pötschke, and Konietzky, 2021.

The CNL test have been performed with Freiberg granite samples, the mechanical properties are summarised in Table 4.1 below. Four subsequent increasing normal loads have been applied to the samples, i.e. 1, 2.5, 5, 7.5 MPa, respectively. The first test at 1 MPa load exhibits a peak (threshold) before further shearing occurs. The subsequent test at 2.5, 5, 7.5 MPa show a similar shear behaviour with a linear increase between shear stress and displacement in the beginning and then a plateau (with a slight increase) when further shearing

<sup>3</sup><https://www.ufz.de/geomint>

<sup>4</sup><https://tu-freiberg.de/en/fakultaet3/gt/felsmechanik/rock-mechanics/large-shear-gs-1000>

<sup>5</sup><https://tu-freiberg.de/en/fakultaet3/gt/felsmechanik/rock-mechanics/3d-surface-and-body-scanners>

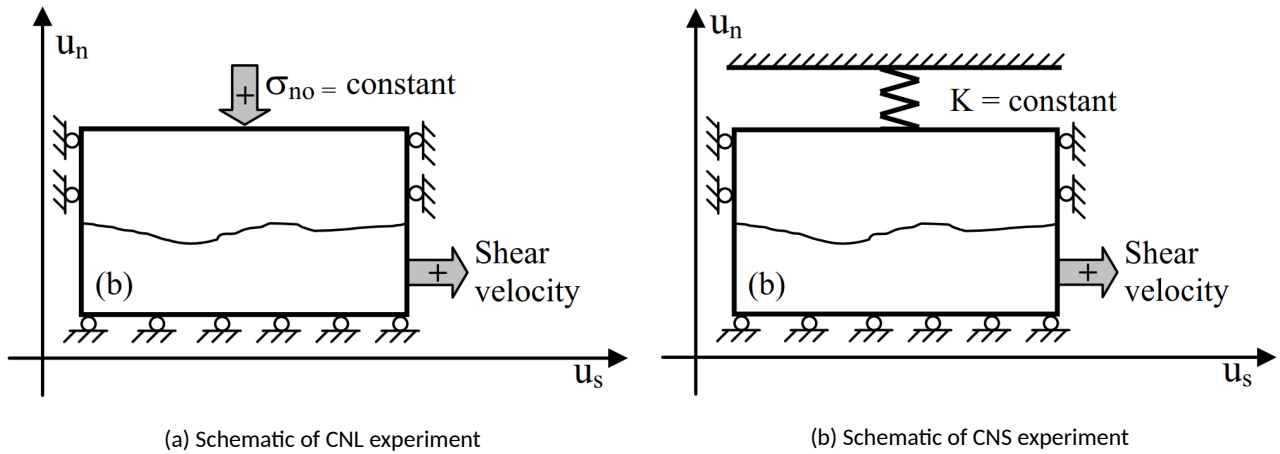


Figure 4.2: Experimental work concepts for the Constant Normal Load (CNL) and Constant Normal Stiffness (CNS) tests, respectively Nguyen, 2013

the sample (Figure 4.3a). An alternate illustration is shown in Figure (Figure 4.3b) where vertical and shear displacements are plotted.

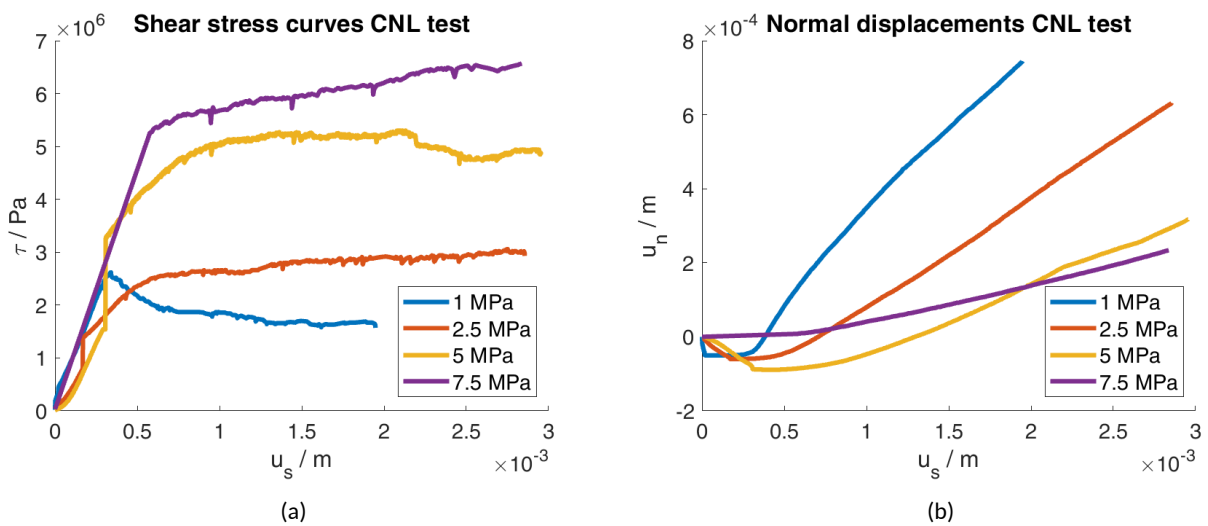


Figure 4.3: CNL test results Frühwirt, Pötschke, and Konietzky, 2021

For further information concerning the research concept, all experimental results and modelling please refer to Frühwirt, Pötschke, and Konietzky, 2021 and Kolditz et al., 2021.

### 4.3 Experimental data

The CNL data set contains four ASCII files:

- Rock properties of the used granite (Table 4.1)
- Scan data from the rock surface before shearing (Figure 4.4)
- Scan data from the rock surface after shearing
- CNL experimental data corresponding to four different shear stress levels (Figure 4.3)

#### 4.4 Fracture geometry

Surface scans have been conducted before and after shear experiments. The surface scans are represented as point clouds, a typical representation is shown in Figure 4.4.

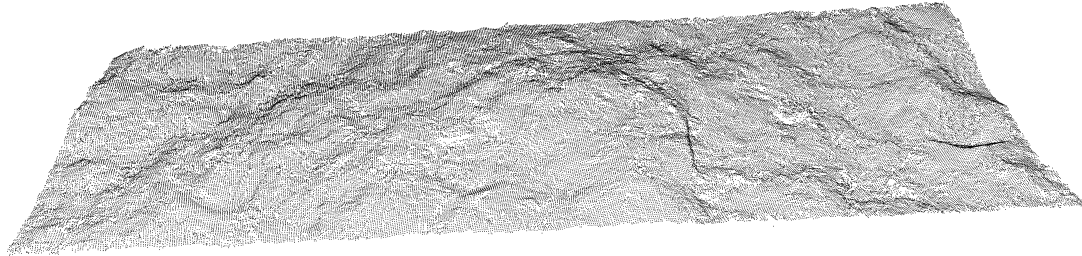


Figure 4.4: Point cloud representing the surface of a granite sample from Saxony. The size is 65 mm by 170 mm and the cloud contains approx. 98000 points.

#### Mechanical properties

The mechanical properties obtained by the shear tests are summarised in Table 4.1 below.

Table 4.1: Rock parameters of granite and basalt used in the direct shear tests.

Parameter	Symbol	Granite	Basalt	Unit
Density	$\rho$	2.59	3.06	$\text{g/cm}^3$
Compressive strength	$\sigma_c$	120.54	272.92	MPa
Tensile strength	$\sigma_t$	7.02	16.61	MPa
Elastic modulus	$E$	49.75	105.46	GPa
Poisson's ratio	$\nu$	0.26	0.26	-
Fracture toughness	$K_I$	0.95	2.61	$\text{MPa} \cdot \text{m}^{0.5}$
Friction angle (Mohr)	$\phi$	52.5	44	$^\circ$
Cohesion	$c$	22.5	25.00	MPa
Basic friction angle	$\phi_b$	30	31.2	$^\circ$

#### 4.5 Data access

Complete fracture data from the CNL and CNS experiments are persistently hosted at the UFZ data portal. A data overview is listed in Table 4.2.

Table 4.2: Data overview

Type	Spec.	Owner	Access	Comment
EXP	LAB	TUBAF	Open for D-2023	Available, UFZ-DMP
MOD	FFS	TUBAF	Open source Free	Available via GitHub I/O available

Link to the data set at UFZ data portal (DMP): [www.ufz.de/record/dmp/archive/7925/](http://www.ufz.de/record/dmp/archive/7925/)

The CNL data set contains four text files. One text file with the rock properties of the granite used (see Table 4.1). Two files with the scan data of the two surfaces. One point cloud is shown in Figure 4.4. The last file

contains the laboratory data. In Figure 4.3 the results for the four shear stress levels can be seen.

### Meta Data Overview (according to Dublin Core)

Table 4.3: CNL experiments (TUBAF)

Data label	GeomInt   TUBAF   Data Set CNL
URL	<a href="http://www.ufz.de/record/dmp/archive/7925">http://www.ufz.de/record/dmp/archive/7925</a>
Subject	Crystalline rock, direct shear test
Type of data	collection of various data
Data quality	quality assured data
Status of data	processed data
Data format	txt, jpg, png
Creators	TU Freiberg, Institut für Geotechnik, Gustav-Zeuner-Str. 1, 09599 Freiberg
Source/Origin	Rock mechanical laboratory
Publisher	TU Freiberg, Institut für Geotechnik, Gustav-Zeuner-Str. 1, 09599 Freiberg
Rights holders	TU Freiberg, Institut für Geotechnik, Gustav-Zeuner-Str. 1, 09599 Freiberg
Contributors	TU Freiberg, Institut für Geotechnik, Thomas Frühwirt and Daniel Pötschke
Time/period of creation	2018 - 2019
Language of the content	English
Update policy	Stored data will not be extended
Access permissions	Limited access

## 4.6 Simulation results

The Freiberg experimental data have been analysed by several teams, originally by TUBAF Frühwirt, Pötschke, and Konietzky, 2021 and as part of Task G by the CAS and CNL teams (see below).

### 4.6.1 CAS team

The two-dimensional model and numerical Freiberg shear tests are carried out in CASRock considering four loading stresses (1, 2.5, 5, 7.5 MPa). The fracture length is 0.17 m, and the height of the upper and lower parts of the Freiberg rock mass is 0.0325 m. The upper part of the rock mass is fixed and the lower part of the rock mass can move in the X direction. Accordingly, from the shear stress-shear displacement curves, the variation trends of the simulation results are consistent with those of the experimental results (Fig. 4.5). The deviation between them is thought to be caused by the morphology of the shear surface because, in the 2D simulation, the selected morphology of the shear surface is significantly different from that of the true 3D surface.

When the three-dimensional model is applied, there are still some deviations between the experimental results and simulation results for the shear stress-shear displacement curves (Fig. 4.6). This difference is possibly caused by the highly simplified morphology of the shear surfaces in the numerical simulations.

In Fig. 4.7, the shear stress-shear displacement curves under 1 MPa normal stress loading calculated by the Bar-Ban code, Frühwirt method (Frühwirt, Pötschke, and Konietzky, 2021) and CASRock simulation are compared with the experimental results. This demonstrates that the CASRock simulation results are reasonable to reflect

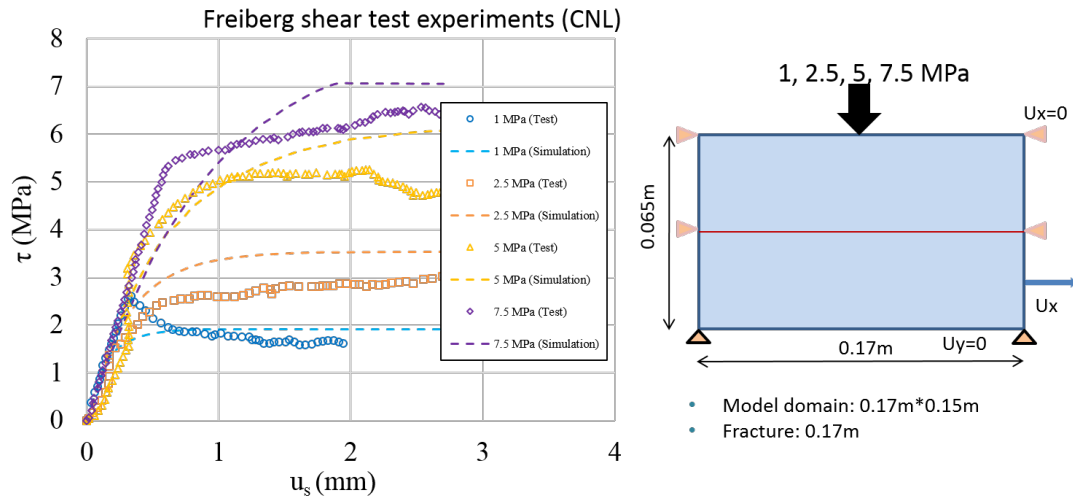


Figure 4.5: Comparison of shear stress–shear displacement curves under four normal loading stresses (1, 2.5, 5.0, and 7.5 MPa) between Freiberg shear tests and two-dimensional numerical simulation by CASRock

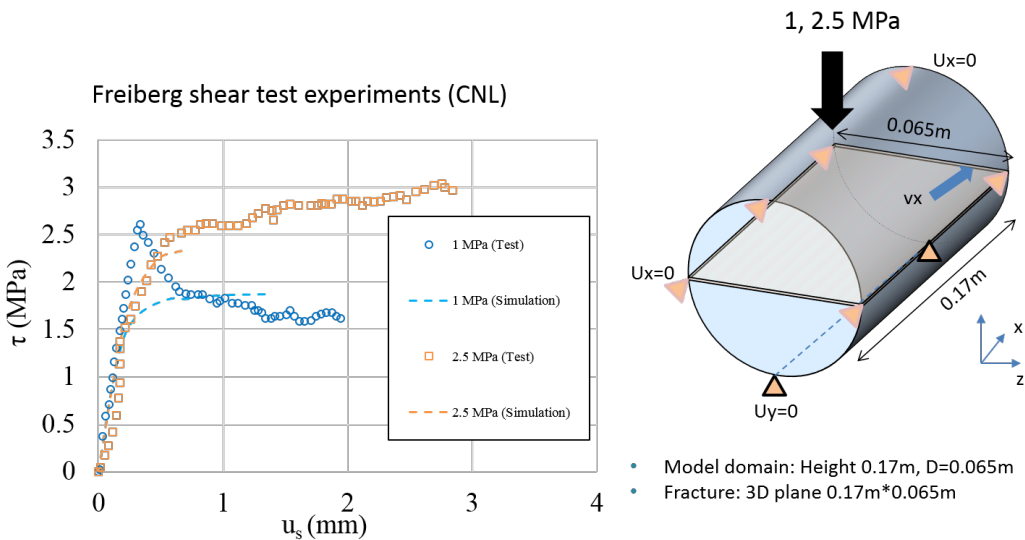


Figure 4.6: Comparison of shear stress–shear displacement curves under two normal loading stresses (1 and 2.5 MPa) between Freiberg shear tests and three-dimensional numerical simulation via CASRock simulator

the deformation behaviour in early stage. As a perfect plastic constitutive model is used for the fracture in the simulation, the stress drop after peak stress is not seen.

#### 4.6.2 CNSC team

Dependent on the waste disposal design concept, excessive shear movement of the confining host rock may cause nuclear waste containers to fail, leading to an earlier release of radionuclides. Additionally, shear may be accompanied by dilation, resulting in the joint aperture increasing and creating additional connectivity for radionuclide transport. Mathematical models are an important tool that can be developed and implemented to help evaluate joint shear and dilation under different loading conditions, including the heat generated from the emplaced waste. The CNSC team has created a mathematical model based on a macroscopic approach, using elasto-plasticity principles.



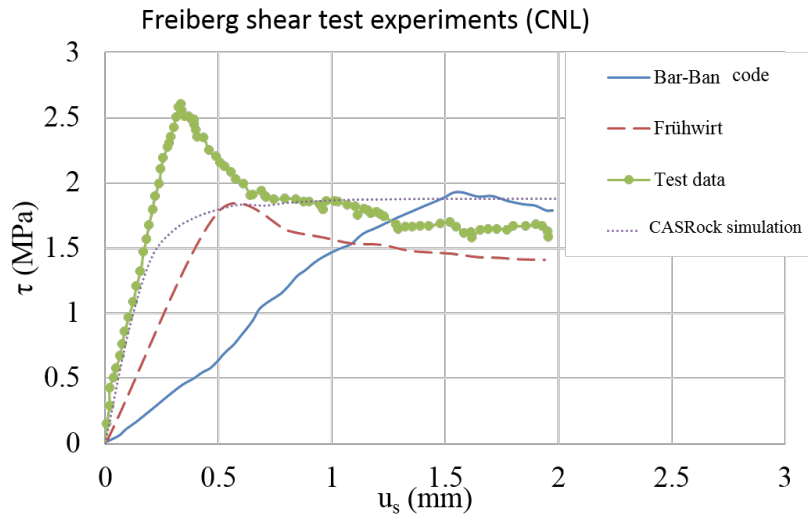
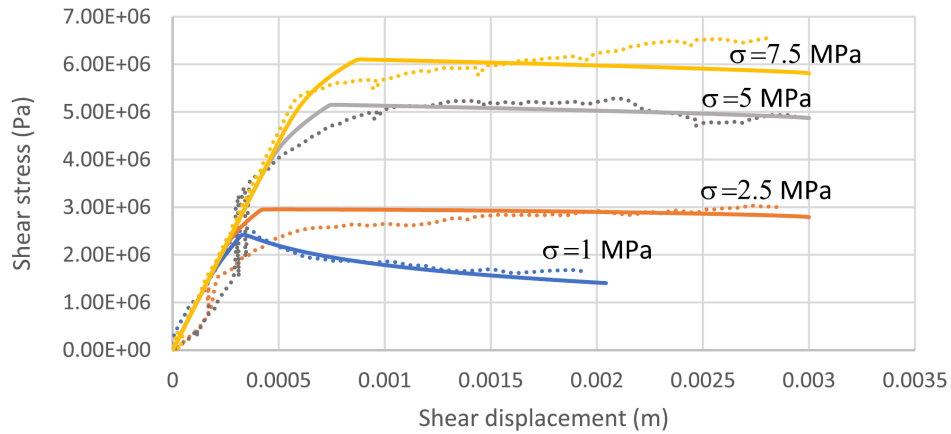


Figure 4.7: Comparison of shear stress–shear displacement curves under 1 MPa normal stress loading conditions among different calculation codes and experimental tests

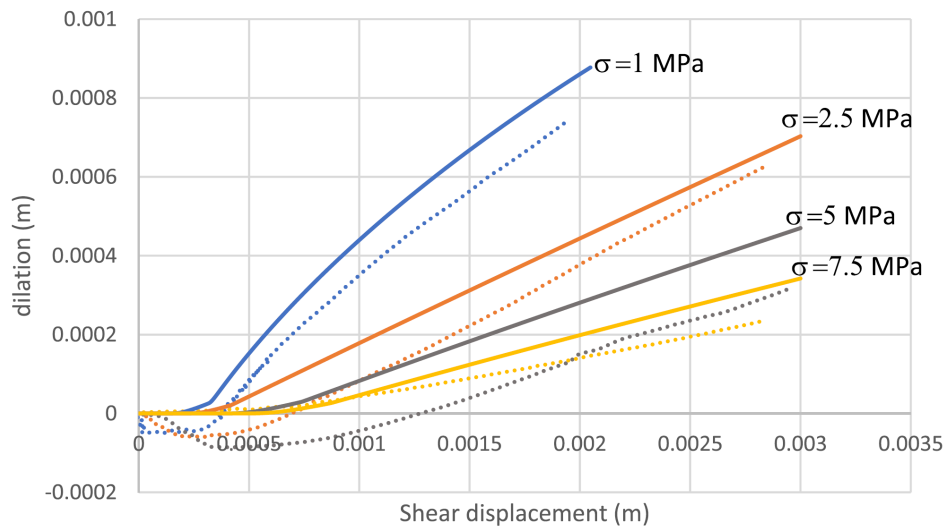
Two distinct approaches have been employed in Task G of DECOVALEX 2023. The first methodology employed was the microscopic approach, whereby the scanned surfaces' asperities (e.g. Fig. 4.4) of the joint are meticulously represented, and assumptions are made about the interaction between these asperities. Joint slip starts when the friction resistance along the asperity is exceeded. In contrast, the second approach is utilised, which was the macroscopic one. The model that was developed required input data on average joint characteristics that can be obtained from basic and inexpensive characterisation techniques. For estimation of the required parameters two widely used index parameters in rock engineering were utilised: the joint roughness coefficient (JRC) and the joint compressive strength (JCS). JRC and JCS are crucial parameters in the Barton-Bandis shear strength criterion for rock joints (Barton and Choubey, 1977; Nguyen and Selvadurai, 1998). This model underwent verification against analytical solutions and validation via shear testing under constant normal loads (Freiberg experiments) as well as thermal shearing tests of joints in granite (KICT experiments). Here, only the key findings are presented, as further details and parameterization of the model are outlined in the DECOVALEX Special Issue publication (Nguyen et al., 2024).

Here, the proposed joint model was verified via direct shear tests under constant normal stress conducted at the rock mechanics laboratory of TU Bergakademie Freiberg, Germany (Frühwirt, Pötschke, and Konietzky, 2021). The modelling results were compared to the experimental data in Figure 4.8, demonstrating a satisfying degree of agreement:

- The shear strength, as demonstrated by the stress-displacement curve, increases with normal stress (see Fig. 4.8a).
- Joint dilation is a result of asperity overriding during the shear process (see Fig. 4.8b). Dilatancy decreases with higher normal stress due to asperity degradation that was present during previous shearing phases at lower normal stress. The asperity angle relies on the accumulated plastic work. The initial value in the subsequent analysis at the higher normal stress level is the final value obtained at a normal stress level.
- Dilation is smaller for tests at higher normal stress levels due to joint asperity degradation, as shown



a) Shear stress vs shear displacement



b) Dilatation vs shear displacement

Figure 4.8: Validation of the joint model with shear under constant normal stress tests for Freiberg granite. Solid lines are modelling results; dotted lines are experimental values (Nguyen et al., 2024)

in Figure 4.8b. The modelled dilatation is consistent with the experimental data for this result. However, there is a noticeable numerical difference as the model does not incorporate the initial joint compression, caused by microcracks closing at the start of the shearing process.

- The majority of asperity degradation happened during the primary test at 1 MPa normal stress. This is characterised by a significant weakening behaviour (stress reduction), demonstrated in Fig. 4.8a. For higher normal stresses, the joint displayed hardening and almost perfect plastic behaviour. The modelling findings support the experimental data for this softening-hardening behaviour, with the exception of the peak normal stress of 7.5 MPa, where there was continuous hardening.

## References

- Barton, N. and V. Choubey (1977). "The shear strength of rock joints in theory and practice". In: *Rock Mechanics Felsmechanik Mécanique des Roches* 10.1-2. Cited by: 2553, pp. 1 – 54. DOI: [10.1007/BF01261801](https://doi.org/10.1007/BF01261801). URL: <https://www.scopus.com/inward/record.uri?eid=2-s2.0-0017582564&doi=10.1007%2fBF01261801&partnerID=40&md5=23cdb214cee5b9b21e5f43ddde1ccc93>.
- Frühwirth, Thomas, Daniel Pötschke, and Heinz Konietzky (2021). "Simulation of direct shear tests using a forces on fracture surfaces (FFS) approach". In: *Environmental Earth Sciences* 80.8. Cited by: 5; All Open Access, Hybrid Gold Open Access. DOI: [10.1007/s12665-021-09606-6](https://doi.org/10.1007/s12665-021-09606-6). URL: <https://www.scopus.com/inward/record.uri?eid=2-s2.0-85104006276&doi=10.1007%2fs12665-021-09606-6&partnerID=40&md5=38352a2edca39a24d14e93ed56c3fad>.
- Kolditz, Olaf et al. (2021). "GeomInt: geomechanical integrity of host and barrier rocks–experiments, models and analysis of discontinuities". In: *Environmental Earth Sciences* 80.16. Cited by: 6; All Open Access, Green Open Access, Hybrid Gold Open Access. DOI: [10.1007/s12665-021-09787-0](https://doi.org/10.1007/s12665-021-09787-0). URL: <https://www.scopus.com/inward/record.uri?eid=2-s2.0-85112398941&doi=10.1007%2fs12665-021-09787-0&partnerID=40&md5=0f2a2d665d8bdacf68f68fc7d3308803>.
- Nguyen, Thanh Son et al. (2024). "Modelling the thermo-mechanical behaviour of a rock joint". In: *Geomechanics for Energy and the Environment* 37. Cited by: 0. DOI: [10.1016/j.gete.2023.100520](https://doi.org/10.1016/j.gete.2023.100520). URL: <https://www.scopus.com/inward/record.uri?eid=2-s2.0-85178640689&doi=10.1016%2fj.gete.2023.100520&partnerID=40&md5=7e0c9fd5c407caa13438240e8cf484a0>.
- Nguyen, T.S. and A.P.S. Selvadurai (1998). "A model for coupled mechanical and hydraulic behaviour of a rock joint". In: *International Journal for Numerical and Analytical Methods in Geomechanics* 22.1. Cited by: 79, pp. 29 – 48. DOI: [10.1002/\(SICI\)1096-9853\(199801\)22:1<29::AID-NAG907>3.0.CO;2-N](https://doi.org/10.1002/(SICI)1096-9853(199801)22:1<29::AID-NAG907>3.0.CO;2-N). URL: <https://www.scopus.com/inward/record.uri?eid=2-s2.0-0031937642&doi=10.1002%2f%28SICI%291096-9853%28199801%2922%3a1%3c29%3a%3aAID-NAG907%3e3.0.CO%3b2-N&partnerID=40&md5=b7b91a68993f0ad5d370839f77bb7a97>.
- Nguyen, V.M. (2013). "Static and dynamic behaviour of joints in schistose rock, lab testing and numerical simulation". PhD thesis. Freiberg: Technische Universität Bergakademie Freiberg.

## 5 GREAT (Geo-Reservoir Experimental Analogue Technology) cell experiments (M and HM processes)

### Literature

The following papers contain a detailed description of the GREAT cell experiments which were modelled as part of this sub-task.

- McDermott et al., 2018: Description of the GREAT cell experimental facility in "New Experimental Equipment Recreating Geo-Reservoir Conditions in Large, Fractured, Porous Samples to Investigate Coupled Thermal, Hydraulic and Polyaxial Stress Processes".
- Fraser-Harris et al., 2020 "Experimental Investigation of Hydraulic Fracturing and Stress Sensitivity of Fracture Permeability Under Changing Polyaxial Stress Conditions"
- Fraser-Harris et al., 2023 "The influence of intermediate principal stress magnitude and orientation on fracture fluid flow characteristics of a fractured crystalline rock"

### 5.1 Experimental facility and programme

The GREAT cell, Figure 5.1, provides the capability to load hydraulically connected fractures in rock samples under a controlled triaxial stress field, and to change that stress field during the experiment enabling the investigation of the impact of normal and shear stress on fracture permeability. The sample size is 200 mm diameter x 200 mm height, and strain is measured along the middle circumference of the cylinder. Additionally fluid sampling during the experiments and later analysis facilitates the investigation of changes in water chemistry as a consequence of different dynamic loading states.

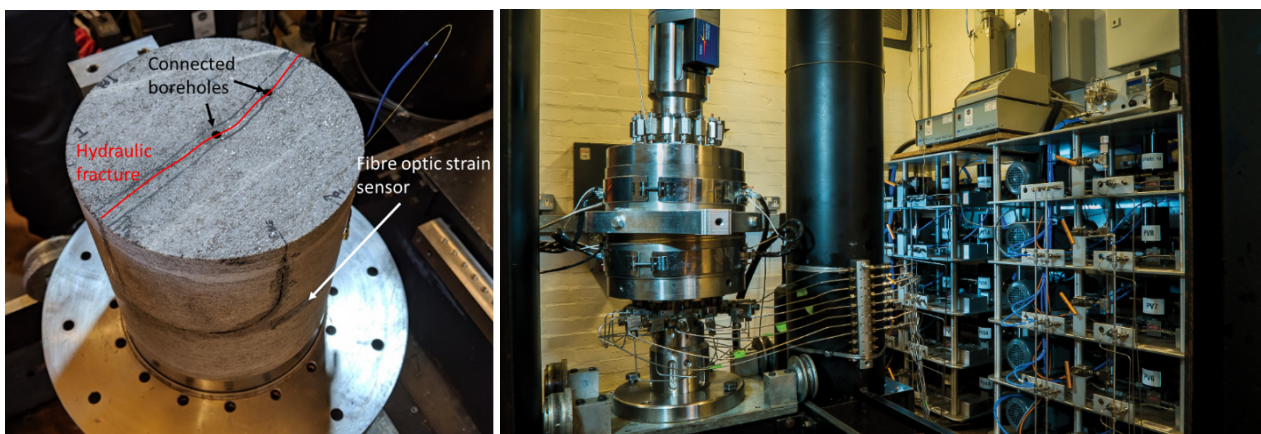


Figure 5.1: GREAT cell sample and apparatus

### Experimental geometry

A generic model/experimental overview is given below in Figure 5.2. Pressure Exerting Elements (PEE) comprising hydraulic cushions apply a controlled pressure around the surface of the sample, Dynamic Sealing Strips

(DSS) prevent the PEE's from influencing one another (Figure 5.2a & c). The vertical stress is controlled by a conventional uniaxial loading ram, the sample may or may not be hydraulically fractured (Figure 5.2b). An illustration of a typical loading condition is given in Figure 5.2d.

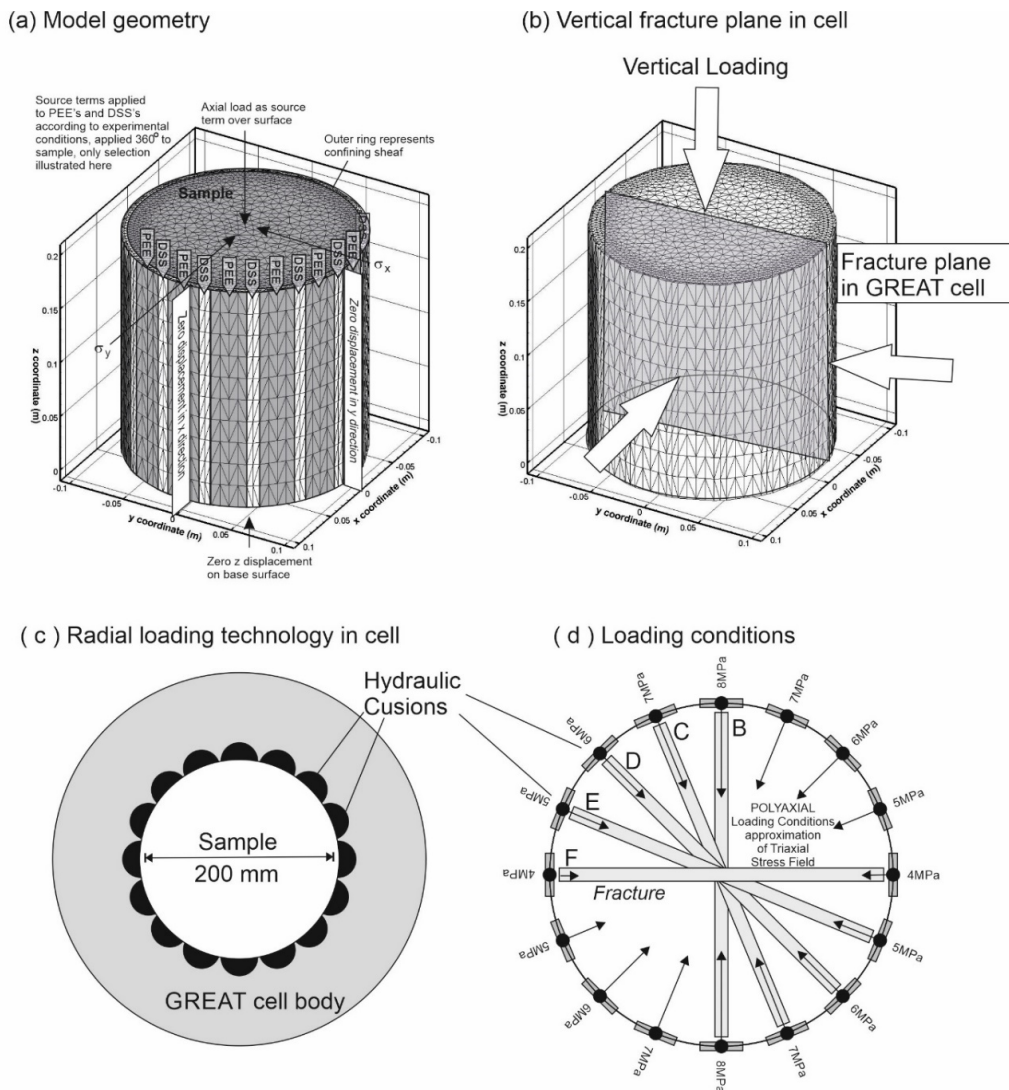


Figure 5.2: (a) Overview of model geometry used for McDermott et al., 2018; Fraser-Harris et al., 2020 (b) Vertical fracture plane in cell, generic geometry for prediction of normal and shear stress on fracture plane, (c) Radial hydraulic loading in cell, (d) Actual loading relative to fracture location for prediction of stress distribution in polyaxial stress field within cell.

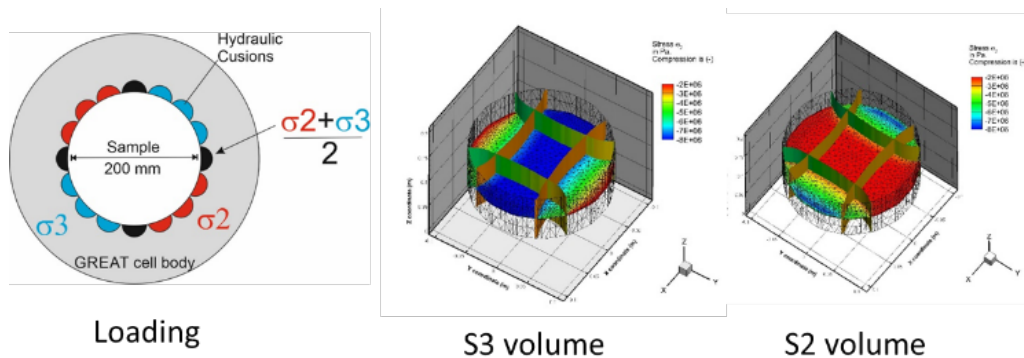


Figure 5.3: Modelling of internal stress tensor under different surface loading conditions

## HM Experimental Investigation for DECOVALEX 2023

The program of experiments and modelling challenges has been built up with increasing complexity both in terms of the processes involved, and in terms of moving from more simple homogeneous artificial samples through to real rock samples with clear fabric and texture. Initially the mechanical response of the samples are tested, the deformation measured using a circumferential fibre optic strain gauge. Then various principal stress magnitudes and orientations are set up, and the fracture permeability is measured. Teams selected different experiments from the list below depending on their own interest to simulate.

1. Mechanical deformation of a homogeneous artificial sample:  
Aim - simulate the near field mechanical deformation of a sample in response to changing values and orientations of a triaxial stress field. Validate the results with comparison against experimental data of sample surface deformation.  
Aim - predict the normal and shear stress in the plane of the fracture within the cylindrical coordinate system.
2. Mechanical deformation of a tensile fracture in an artificial sample in a triaxial stress field:  
Aim – building on the M benchmarking investigation (Mollaali et al., 2023; Papachristos et al., 2017) simulate the near field mechanical deformation of a sample in response to changing values and orientations of a triaxial stress field. Validate the results with comparison against experimental data of sample surface deformation.
3. Hydraulic-Mechanical coupling of a tensile fracture in an artificial sample in a triaxial stress field:  
Aim - investigation of normal stress, fluid flow, fracture pressure and permeability relationships of a tensile fracture in a triaxial stress field. Validate the results with comparison against experimental data.
4. Hydraulic-Mechanical coupling of a tensile fracture in a natural greywacke sample in a triaxial stress field:  
Aim - investigation of normal stress, fluid flow, fracture pressure and permeability relationships of a tensile fracture in a triaxial stress field. Validate the results with comparison against experimental data
5. Hydraulic-Mechanical coupling of a tensile fracture in a Freiberg Granite sample in a triaxial stress field:  
Aim - investigation of normal stress, fluid flow, fracture pressure and permeability relationships of a tensile fracture in a triaxial stress field. Validate the results with comparison against experimental data
6. Surface dynamic strain measurements during the hydraulic fracturing of a Freiberg Granite Sample.

## General data available to all teams

1. Overview of the experiments
2. Modelling geometry for GREAT cell samples and loading
3. Hydraulic stimulation data
4. Stress, Strain, Fluid Flow // Permeability data for Greywacke and artificial samples
5. Fracture surface scans for the Greywacke
6. Publications (McDermott et al., 2018; Fraser-Harris et al., 2020; Fraser-Harris et al., 2023)
7. Stress, Strain, Fluid Flow // Permeability data for Freiberg granite gneiss sample

**Augmented information**

During the modelling of the experimental results a number of questions have arisen extra to the information provided within the papers cited. The responses are summarised here.

McDermott et al., 2018 contains two graphics illustrating the modelling of strain observed experimentally for a solid sample and a fractures sample (Figure 6 and Figure 7 in McDermott et al., 2018). Calculation of surface displacement in accounting for “end effects” of the platen on the sample. i.e. the concept that the top and base platen can, through friction, restrain the sample from moving freely outwards during deformation. The model used to simulate the strain superimposes with equal weighting a friction free sample and the worst end effect possible.

For the solid sample with no fracture (Figure 6 in the paper), the sample is modelled under two different boundary conditions, representing friction free “unconstrained” conditions and “constrained” conditions. This is illustrated below in Figure 5.4.

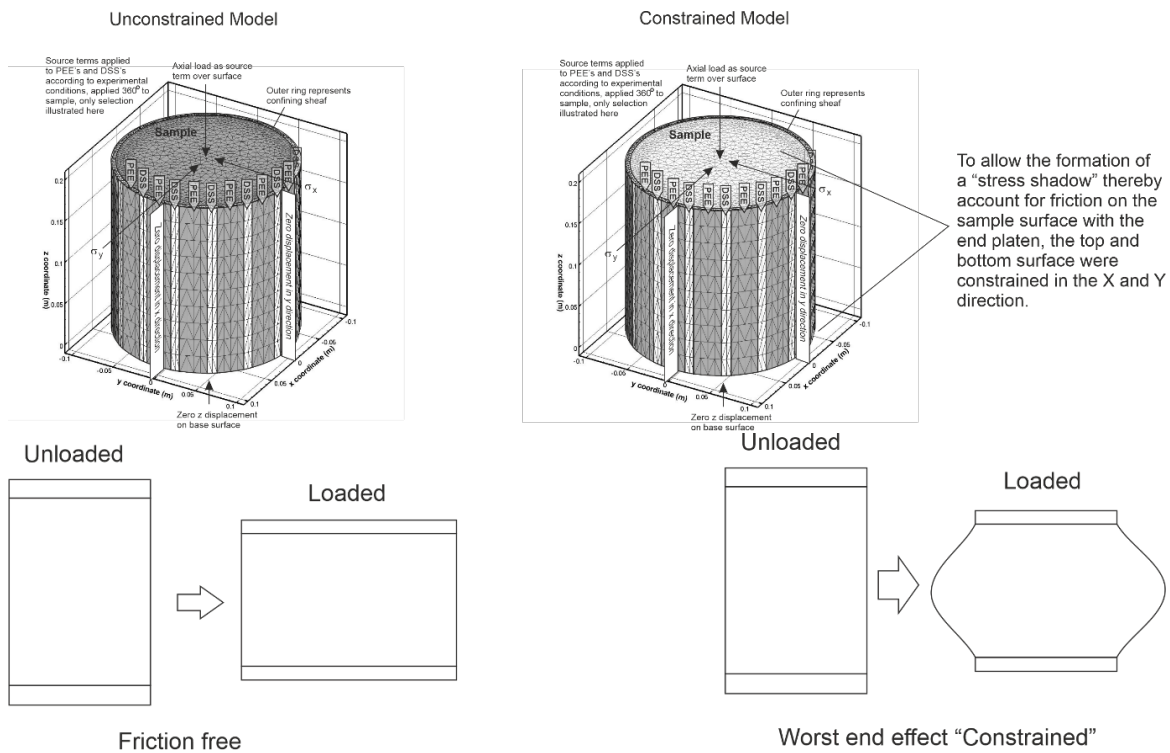
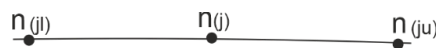


Figure 5.4: Additional information to calculation of displacement results and consideration of two different types of possible boundary condition at the platen sample interface, friction free, and totally restrained.

*Evaluation of surface circumferential strain measured by the fibre optic cable as opposed to volumetric strain*

The fibre optic cable is attached along the surface of the sample. It does not measure volumetric strain, it measured surface strain. To interpolate this from numerical models, the x,y,z coordinates of two nodes  $n_{(ju)}$  and  $n_{(jl)}$  located on the surface pre and post loading are compared, the change in length is calculated and the strain assigned to  $n_{(j)}$ . The code used to calculate this is listed following.



**Strain Interpolation**

Two methods of interpolation are provided, see <https://team2023.decovalex.org/#/1/10/Specification>.

1. The average value over a certain number of nodes (e.g. column H) line 270 LS.cpp ff
2. The interpolated value from two nodes to match the exact position (e.g. Column I) – line 294 LS.cpp

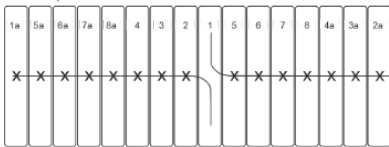
$$i_x = i_{x1} \frac{x - x_2}{x_1 - x_2} + i_{x2} \frac{x_1 - x}{x_1 - x_2} \quad (5.1)$$

### Loading Sequence and Strain Results

Once the vertical loading ONLY has been applied the strain results are “tarred” setting a new baseline against which to compare deformation. Then axial circumferential loading is added (sx=sy), leading to a compression of the sample, see column AQ-AS, experimental results, rows 48-62. Column AQ is the angle from sh clockwise. The sv>sx>sy results where all three stresses are different and rotated in a number of tests around the sample are found in column AR. These results are presented with an angle to sx, and so contain multiple orientations of measurements, with a final average value and standard deviation found in column AS.

#### At the experimental level we use

PEEs experimental nomenclature



Trace of fibre optic  
Location of strain measurement X

#### Experimental to Modelling

PEE 1	BAG_1_SURFACE
PEE 2	BAG_2_SURFACE
PEE 3	BAG_3_SURFACE
PEE 4	BAG_4_SURFACE
PEE 8A	BAG_5_SURFACE
PEE 7A	BAG_6_SURFACE
PEE 6A	BAG_7_SURFACE
PEE 5A	BAG_8_SURFACE
PEE 1A	BAG_9_SURFACE
PEE 2A	BAG_10_SURFACE
PEE 3A	BAG_11_SURFACE
PEE 4A	BAG_12_SURFACE
PEE 8	BAG_13_SURFACE
PEE 7	BAG_14_SURFACE
PEE 6	BAG_15_SURFACE
PEE 5	BAG_16_SURFACE

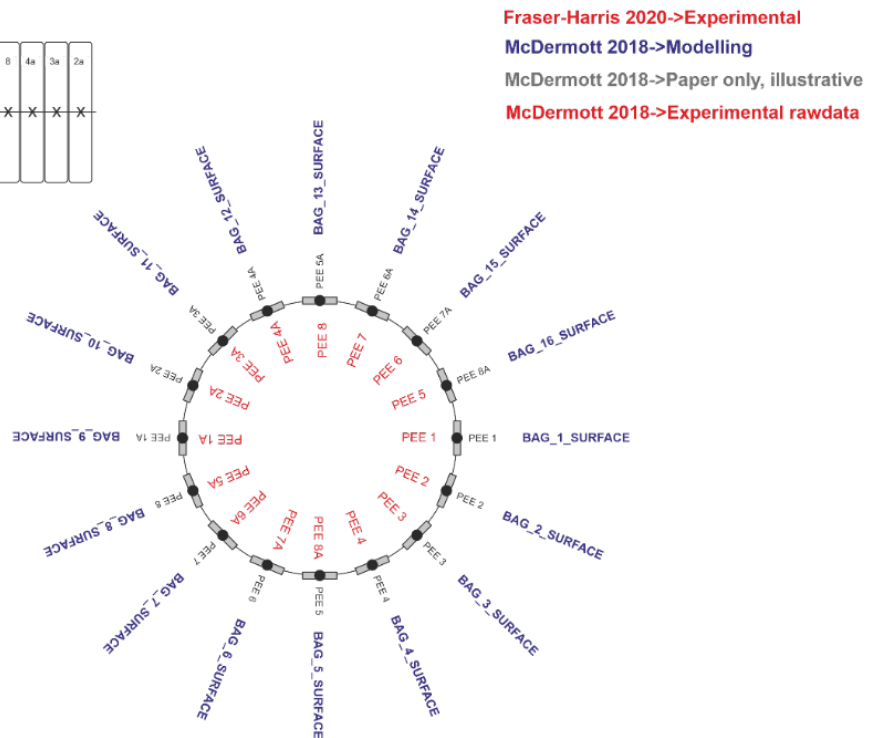


Figure 5.5: Different labelling of PEE’s in raw experimental data.

### Orientation of the PEEs

The experimental naming and order of the PEE’s is different from the modelling order and this has caused confusion. Unfortunately as the experimental procedure with the GREAT cell developed, so the labelling of some of the components as changed, totally logical at the time, but quite confusing later (Fig. 5.5).



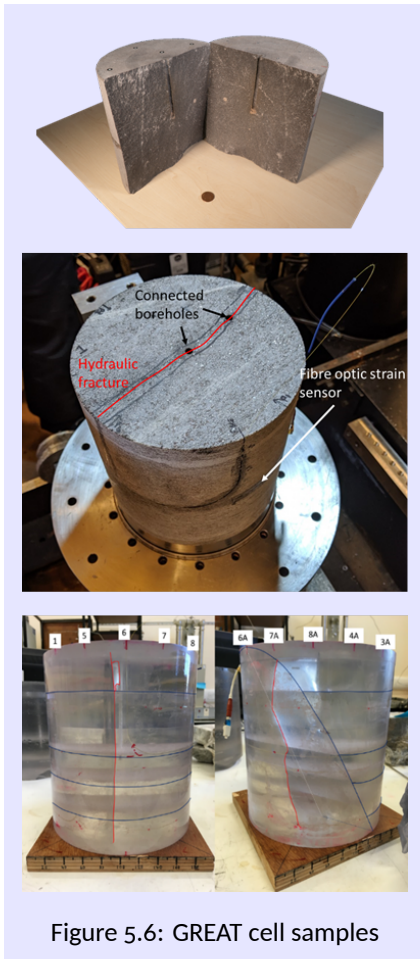


Figure 5.6: GREAT cell samples

## Samples and experiments

The GREAT cell experiments are dealing with various sample materials:

- Polymer (M1) (McDermott et al., 2018)
- Polyester resin with partial fracture, axisymmetric and triaxial conditions (HM1) (McDermott et al., 2018)
- Polyester resin with full fracture, axisymmetric and triaxial conditions (HM2) (McDermott et al., 2018)
- Polyester resin (Fraser-Harris et al., 2020)
- Greywacke (Fraser-Harris et al., 2020)
- Freiburger Gneiss (Frühwirt, Pötschke, and Konietzky, 2021; Fraser-Harris et al., 2023)

Table 5.1: Overview of material properties for the GREAT cell samples

Parameter	Unit	Containing Sheaf	Resin	Greywacke	Gneiss (Freiberg)*
Young's modulus, $E$ ,	(GPa)	0.1	3.85	26.85	83.9//57.1
Poisson's ratio, $\nu$	(-)	0.4	0.4	0.27	0.21//0.19
Tensile strength	(MPa)	-	17.96-25.08	17.01-16.67	16.8//6.2
Permeability, $k$	( $m^2$ )	-	-	$2.58 \times 10^{-19}$	$10^{-18}$ //< $10^{-19}$

Sources: Fraser-Harris et al., 2020 (Resin sample and Greywacke), personal communication (2019) for Gneiss (Freiberg), Thomas Fruehwirt, Lehrstuhl für Gebirgs- und Felsmechanik/Felsbau am Institut für Geotechnik der TU Bergakademie Freiberg (Frühwirt, Pötschke, and Konietzky, 2021).

## 5.2 Experimental analysis of synthetic samples

### 5.2.1 Overview

The primary aim of this section is to explore how samples respond to changes in a triaxial stress field's values and orientations through near-field mechanical deformation. We examine three sample types: an intact sample, a sample containing an internal fracture (partially fractured sample), and a sample with a vertical fracture positioned in the middle (fully fractured sample). As our focus is on investigating mechanical deformation, we prohibit fracture propagation within the fractured sample. In the numerical models, we treat the fracture as static by assigning it a high fracture toughness.

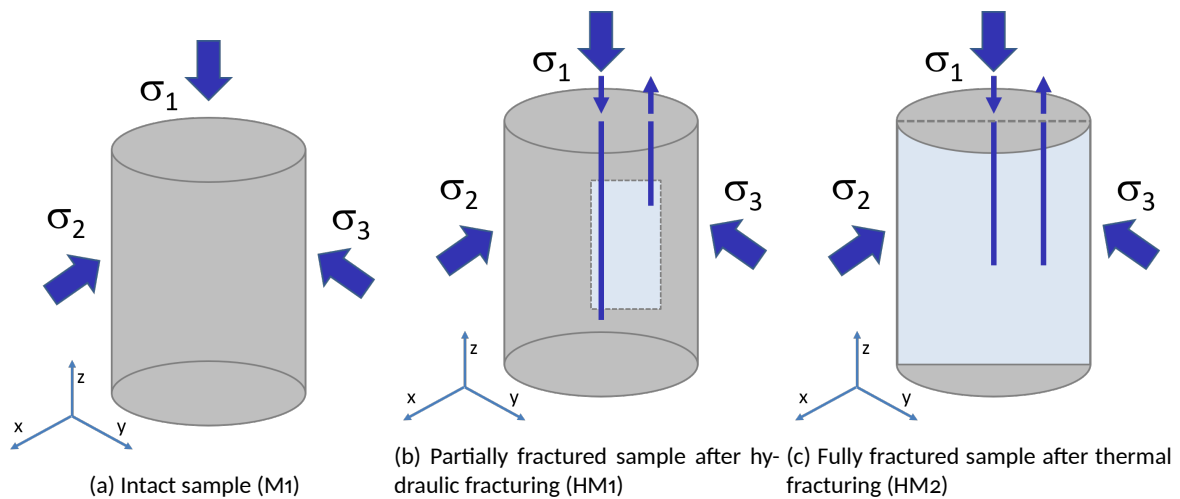
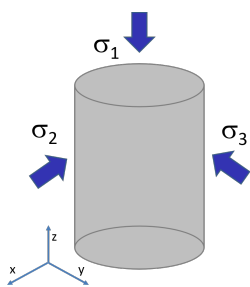


Figure 5.7: Experiment types conducted on synthetic samples (polymer and polyester resin) McDermott et al., 2018

### 5.2.2 Intact sample - Model set-up (M1)



The primary objective of the first benchmark exercise is to compare and validate the mechanical deformation of the GREAT cell under different boundary conditions in a 3D (Figure 5.7)a. Two loading scenarios are considered: true-triaxial and axisymmetric loading.

Our computational model incorporates two distinct elastic materials within its domain: a central circle PMMA surrounded by a rubber sheath (in 2D). The material properties of the samples are provided in Table 5.2. We generated a 3D mesh using GMSH, which consists of tetrahedral elements. The mesh contains 29,262 nodes and 180,386 elements.

We impose the following Dirichlet constraints:

$$\begin{aligned} u_x(x, y, z) &= 0, & \text{for } x = 0.0 \text{ and } y = 0.9894 \text{ or } y = -0.09894, \\ u_y(x, y, z) &= 0, & \text{for } y = 0.0 \text{ and } x = 0.9894 \text{ or } x = -0.09894, \\ u_z(x, y, z) &= 0, & \text{for } z = 0.0. \end{aligned}$$

These constraints ensure that the  $x$ ,  $y$ , and  $z$  components of the vector field  $u$  are zero at the specified boundaries of the 3D domain.

Table 5.2: Material properties

Material Property	Symbol	Value	Unit
Sample Young's modulus	E	3.85	GPa
Sample Poisson's ratio	$\nu$	0.4	-
Rubber sheath Young's modulus	E	0.1	GPa
Rubber sheath Poisson's ratio	$\nu$	0.4	-

The loading specifications for the PEEs are available in Table 5.3. Meanwhile, the load acting on the DSSs is determined as the average of the loads applied to adjacent PEEs. In the true triaxial scenario, the stress field follows  $\sigma_1 > \sigma_2 > \sigma_3$ , whereas, in the axisymmetric scenario:  $\sigma_1 > \sigma_2 = \sigma_3$ .

We conducted numerical simulations using a Quasi-static approach in five load steps. The load curves employed were  $[0, 1, 1, 1, 1]$  for axial loads and  $[0, 0, 0, 1, 1]$  for polyaxial circumstances loads. These load curves acted as coefficients for Table 5.3's components. For instance, at the initial condition (0), all loads were zero. During the first load step, only the axial load was applied, with other PEEs and DSSs loads (Table 5.3) set to zero. In the final time step, both axial and polyaxial circumferential loads (from Table 5.3) have a coefficient of one.

Specifically, we maintained a constant axial load throughout the simulations, introducing circumferential load only during the final two load steps.

To highlight the significance of 3D modeling, we perform a numerical benchmark in the 2D plane strain. Our computational domain represents the cross-section of a 3D sample within the x-y plane, located at  $z = 0.1$ .

Table 5.3: Loading scenarios for mechanical deformation benchmarks

True Triaxial	Axisymmetric
PEEs 1 & 1a: 7.73 MPa	PEEs 1 & 1a: 7.71 MPa
PEEs 2 & 2a: 5.70 MPa	PEEs 2 & 2a: 7.70 MPa
PEEs 3 & 3a: 4.39 MPa	PEEs 3 & 3a: 8.30 MPa
PEEs 4 & 4a: 2.40 MPa	PEEs 4 & 4a: 7.80 MPa
PEEs 5 & 5a: 2.30 MPa	PEEs 5 & 5a: 7.74 MPa
PEEs 6 & 6a: 4.00 MPa	PEEs 6 & 6a: 7.70 MPa
PEEs 7 & 7a: 6.40 MPa	PEEs 7 & 7a: 8.30 MPa
PEEs 8 & 8a: 7.70 MPa	PEEs 8 & 8a: 7.72 MPa
DSSs: average of loads of adjacent PEEs	DSSs: average of loads of adjacent PEEs

In the post-processing step, we plot either the volumetric strain

$$\varepsilon_{\text{vol}} = \varepsilon_{xx} + \varepsilon_{yy} + \varepsilon_{zz} \quad (5.2)$$

or circumferential strain (a ratio of the change in length of the material to its initial length) as a function of the angle. The angle is measured counterclockwise from the positive x-axis and is evaluated at  $(x, y, z) \in \mathbb{R}^3 \mid |x^2 + y^2 - 0.065^2| < 10^{-6} \wedge |z - 0.1| < 10^{-6}$ . The length unit is the meter.

The strain profile of both loading scenarios in 2D and 3D are shown in Figure 5.8. In Figure 5.9 and 5.10, the volumetric strain results from 2D simulations are compared to three-dimensional simulations under varying

axial loads. In addition to the case detailed in Section 5.2.3 with an axial load of 10 MPa along the z-axis, three-dimensional simulations are performed with axial loading (4, 6, and 10 MPa) as well as with no axial load. The findings suggest that in true tri-axial loading conditions, the three-dimensional simulation with a 4 MPa axial load accurately replicates the response seen in the 2D plane strain scenario. Conversely, in the axisymmetric loading test, the 6 MPa axial load aligns more closely with the 2D plane strain response. This highlights that while 2D plane strain simulations qualitatively capture the essence of the real 3D cases, they may not provide accurate quantitative representations.

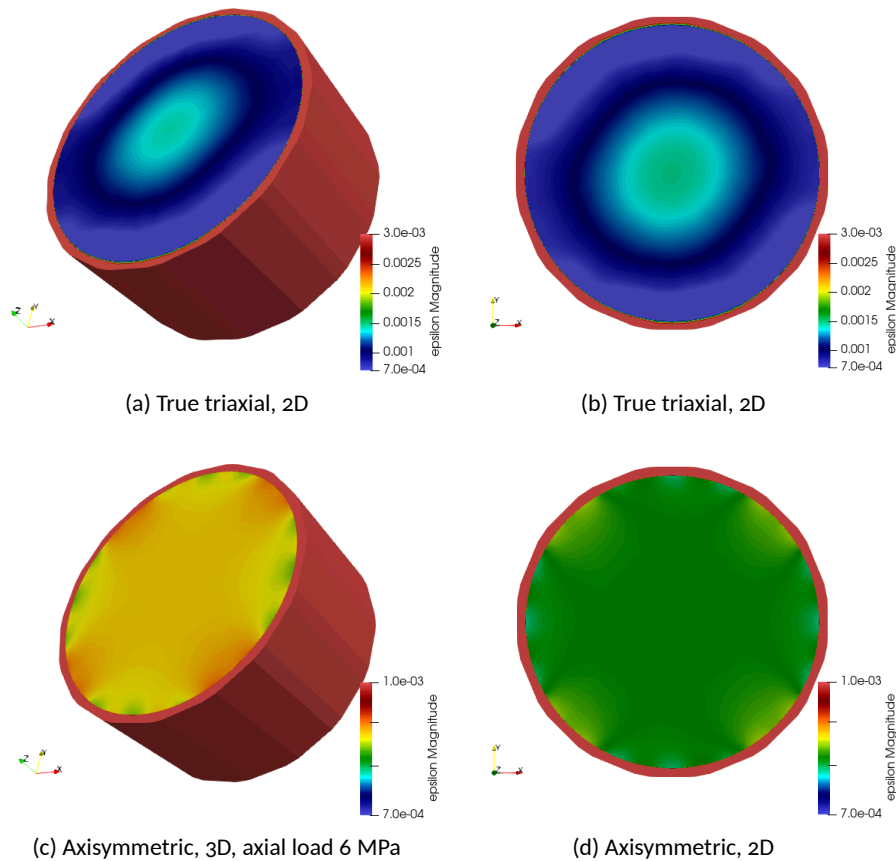


Figure 5.8: The results of the strain field for the 2D/3D benchmark exercise M1 are shown, with loading scenarios defined in Table 5.3. It's important to note the distinct strain ranges; the strain value at the sheath is much higher than the visualization range.

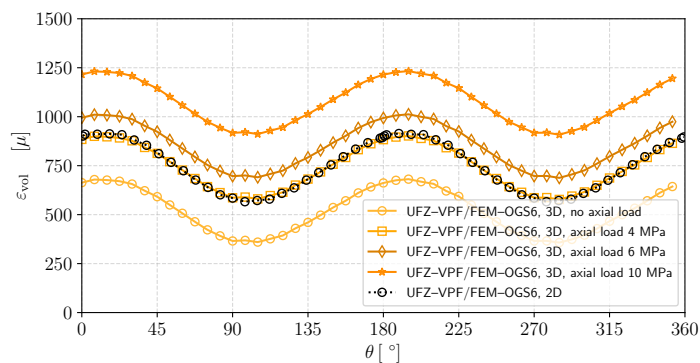


Figure 5.9: Comparing volumetric strain at different angles for 2D and 3D cases in the M1 benchmark under true triaxial loading

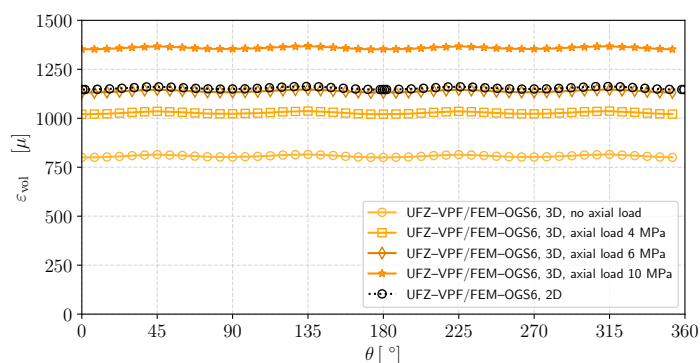


Figure 5.10: Comparing volumetric strain at different angles for 2D and 3D cases in the *M1* benchmark under axisymmetrical loading

### 5.2.3 Intact sample - Analysis (M1) (McDermott et al., 2018)

The main objective of this section is to compare and validate the mechanical deformation of GREAT cell for various boundary conditions in 3D. Following the modeling phase's completion and obtaining results from both 2D and 3D simulations using the OGS6 software, our next step involves comparing. We specifically examine the outcomes of the 3D simulations under a 10 MPa axial load. This comparison involves looking at various numerical methods used in different software packages. Our goal is to compare these outcomes against experimental circumferential strain. Additionally, we aim to compare the volumetric strain results obtained from different numerical methods.

The simulations are carried out in 3D for both axisymmetric and true triaxial loading scenarios, following the loading and boundary conditions specified in Section 5.2.2. It's important to note that various groups employed different mesh structures according to their unique numerical methods. Furthermore, some groups chose not to include the rubber sheath in their simulation models.

Figures 5.11 and 5.12 display a comparison between measured laboratory strain and numerical experiment results. They illustrate the comparison of circumferential and volumetric strains for both the axisymmetrical and true triaxial loading scenarios.

To obtain the circumferential strain from deformation results, we utilized the Python script in Listing 1. As outlined in Section 5.1, to calculate circumferential strain, we utilized the results from the second load step, where only axial load was applied, as a reference configuration. These results were then compared with those obtained in the last load step, where both axial and circumferential stresses were applied.

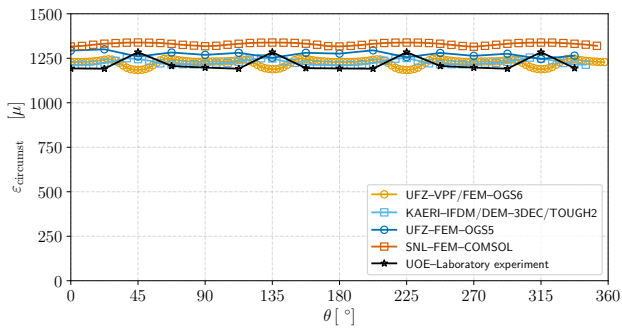
It is noteworthy that in the experimental setup, circumferential strain measurements were obtained at the interface between the sample and the rubber sheath. However, during the post-processing in OGS6, based on the Python code outlined in Listing 1, analyzing the interface between the two materials resulted in significant oscillations and inaccuracies. This phenomenon could potentially be attributed to boundary effects on the results. Consequently, we opted to consider results obtained at a radius of 0.09 m. In other simulations conducted by different collaborators, for the sake of simplicity, the rubber sheath was omitted from the model, and only a PMMA sample with a radius of 0.1 m was considered

```

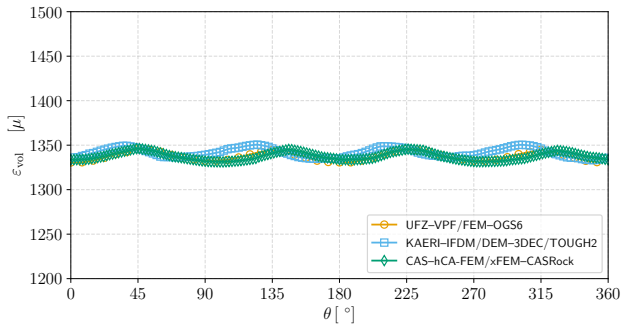
1 def get_surf_strain(out):
2
3     out_dir=out
4     if os.path.exists(f"{out_dir}/GreatCell_3D_ts_4_t_4.000000.vtu"):
5         mesh = pv.read(f"{out_dir}/GreatCell_3D_ts_4_t_4.000000.vtu")
6         mesh_o = pv.read(f"{out_dir}/GreatCell_3D_ts_2_t_2.000000.vtu")
7     else:
8         print('There is no result file with that naming...')
9     disp= mesh.point_data["displacement"]
10    disp_o= mesh_o.point_data["displacement"]
11
12    phi=[]
13    xyz = []
14    u = []
15    u_o = []
16    # getting points at radius of 0.097
17    for node_id, x in enumerate(mesh.points):
18        if (abs(x[2]-0.1)<1e-6 and abs(x[0]**2+x[1]**2-0.09**2)<1e-6): #0.097
19            theta =math.atan2(x[1], x[0])
20            if theta < 0:
21                theta += 2*math.pi
22            phi.append(theta)
23            u.append(disp[node_id])
24            u_o.append(disp_o[node_id])
25            xyz.append(x)
26
27    # sort by angle
28    sort_idx = np.argsort(phi)
29    phi_sorted = [phi[i] for i in sort_idx]
30    u_sorted = [u[i] for i in sort_idx]
31    u_o_sorted = [u_o[i] for i in sort_idx]
32    xyz_sorted = [xyz[i] for i in sort_idx]
33    eps_l_sorted = []
34
35    # calc circumferential strain
36    for ii in range(0,len(u_sorted)):
37        #assign neighbor nodes
38        if ii == 0:
39            a = len(u_sorted)-1
40            b = 1
41        elif ii == len(u_sorted)-1:
42            a = ii-1
43            b = 0
44        else:
45            a = ii-1
46            b = ii+1
47
48        #collect position and displacement
49        xl = xyz_sorted[a][0] + u_o_sorted[a][0]
50        yl = xyz_sorted[a][1] + u_o_sorted[a][1]
51        zl = xyz_sorted[a][2] + u_o_sorted[a][2]
52        ddxl = u_sorted[a][0] - u_o_sorted[a][0]
53        ddy1 = u_sorted[a][1] - u_o_sorted[a][1]
54        ddz1 = u_sorted[a][2] - u_o_sorted[a][2]
55        xu = xyz_sorted[b][0] + u_o_sorted[b][0]
56        yu = xyz_sorted[b][1] + u_o_sorted[b][1]
57        zu = xyz_sorted[b][2] + u_o_sorted[b][2]
58        ddxu = u_sorted[b][0] - u_o_sorted[b][0]
59        ddyu = u_sorted[b][1] - u_o_sorted[b][1]
60        ddzu = u_sorted[b][2] - u_o_sorted[b][2]
61
62        # distance before loading
63        dx1 = xu-xl
64        dy1 = yu-yl
65        dz1 = zu-zl
66        len1 = np.sqrt(dx1**2+dy1**2+dz1**2)
67        # distance after loading
68        dx2 = (xu+ddxu)-(xl+ddxl)
69        dy2 = (yu+ddyu)-(yl+ddy1)
70        dz2 = (zu+ddzu)-(zl+ddz1)
71        len2 = np.sqrt(dx2**2+dy2**2+dz2**2)
72
73        # strain
74        strain = (len1-len2)/len1
75        eps_l_sorted.append(strain)
76
77
78    return np.array(phi_sorted), np.array(eps_l_sorted)

```

Listing 1: Python code for circumferential strain calculation

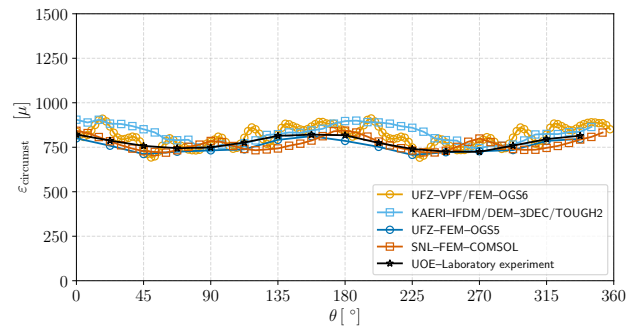


(a) Circumferential strain

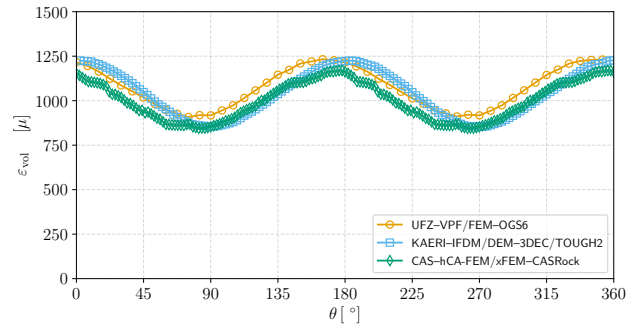


(b) Volumetric strain

Figure 5.11: A comparison of measured strain in the laboratory and numerical experiments (3D axisymmetric case): Circumferential and Volumetric strains compared.



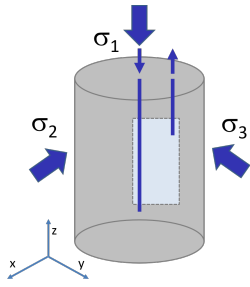
(a) Circumferential strain



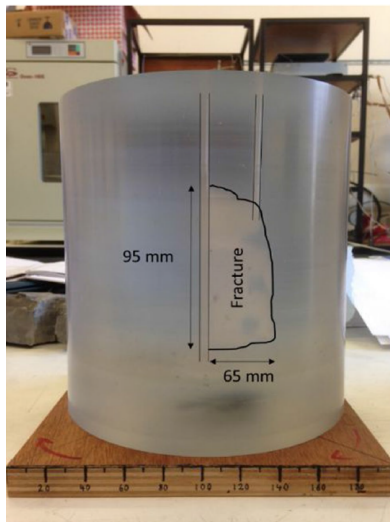
(b) Volumetric strain

Figure 5.12: A comparison of measured strain in the laboratory and numerical experiments (3D Triaxial Case): Circumferential and volumetric strains compared.

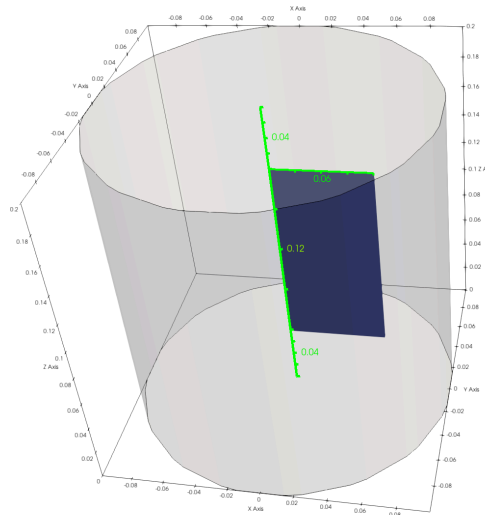
### 5.2.4 Partially fractured sample (M2)



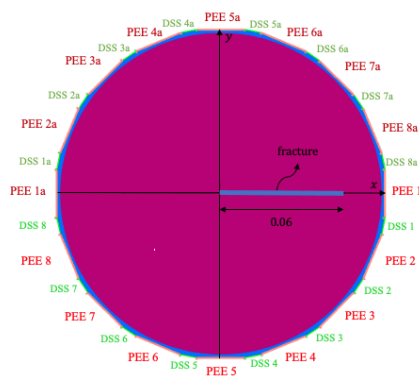
In this task, we conduct numerical simulations to compare circumferential and volumetric strain data in the presence of fracture with laboratory experimental data in McDermott et al., 2018. Our main goal is to establish a baseline model for understanding how fractures impact circumferential strain distribution under polyaxial loading. We consider a planar fracture within the specimen  $\Gamma = \{(r, \theta, z) \mid 0 \leq r \leq 0.06, \theta, 0.04 \leq z \leq 0.16\}$ . The laboratory experimental results that we are utilizing are from McDermott et al., 2018, and these results are associated with the PMMA samples (Figure 5.13). The material properties of the sample are provided in Table 5.2. The sample has a Young's modulus of 4.3 GPa, and we utilized the same material properties for the rubber sheath. Figure 5.13 illustrates the geometrical aspects and boundary conditions. We subjected the top cap of the sample to a 10 MPa axial compression in the z-direction in all cases in this Section. The PEE and DDS loads are provided in Table 5.4. To account for the influence of fracture orientation, we replicate this benchmark by rotating the fracture.



(a) Synthetic PMMA sample



(b) Model representation



(c) 2D, x-y plane

Figure 5.13: Analyses of fracture impact on circumferential strain under polyaxial loading (synthetic PMMA sample). To account for the influence of fracture orientation, we replicate this benchmark by rotating the fracture. In the clockwise direction, the fracture orientation is considered clockwise from the positive x-axis.



Table 5.4: Loading Conditions for partially fractured sample (reference: supplemental materials within McDermott et al., 2018).

Angle PEE1 to $\sigma_2$	PEEs							
	1 & 1a	2 & 2a	3 & 3a	4 & 4a	5 & 5a	6 & 6a	7 & 7a	8 & 8a
$\sigma_2 = \sigma_3$	8.8	8.8	9.2	9.0	8.9	8.7	9.3	8.7
$-56.25^\circ$	7.1	6.3	6.3	6.9	7.9	8.7	8.8	7.8
$33.75^\circ$	7.7	8.7	8.7	7.7	7.3	6.3	6.3	6.6
$56.25^\circ$	7.2	8.2	8.7	8.7	7.8	6.8	6.3	6.2
$-78.75^\circ$	6.2	7.2	8.3	8.7	8.7	7.7	6.9	6.3
$-11.25^\circ$	6.2	6.2	7.3	8.1	8.7	8.7	7.8	6.7
$67.5^\circ$	6.8	6.4	6.9	7.5	8.2	8.7	8.3	7.2

DSSs: average of loads of adjacent PEEs

Figures 5.14a and 5.14a depict the volumetric strain under various loading conditions outlined in Table 5.4, observed along the probe curve (at a radius of 0.065 m). The comparison is made between two distinct fracture orientations of  $78.75^\circ$  and  $112.5^\circ$ , and the experimental data detailed in McDermott et al., 2018. The notable spike in results arises from strain measurements near the fracture tip, where strain levels are significantly higher.

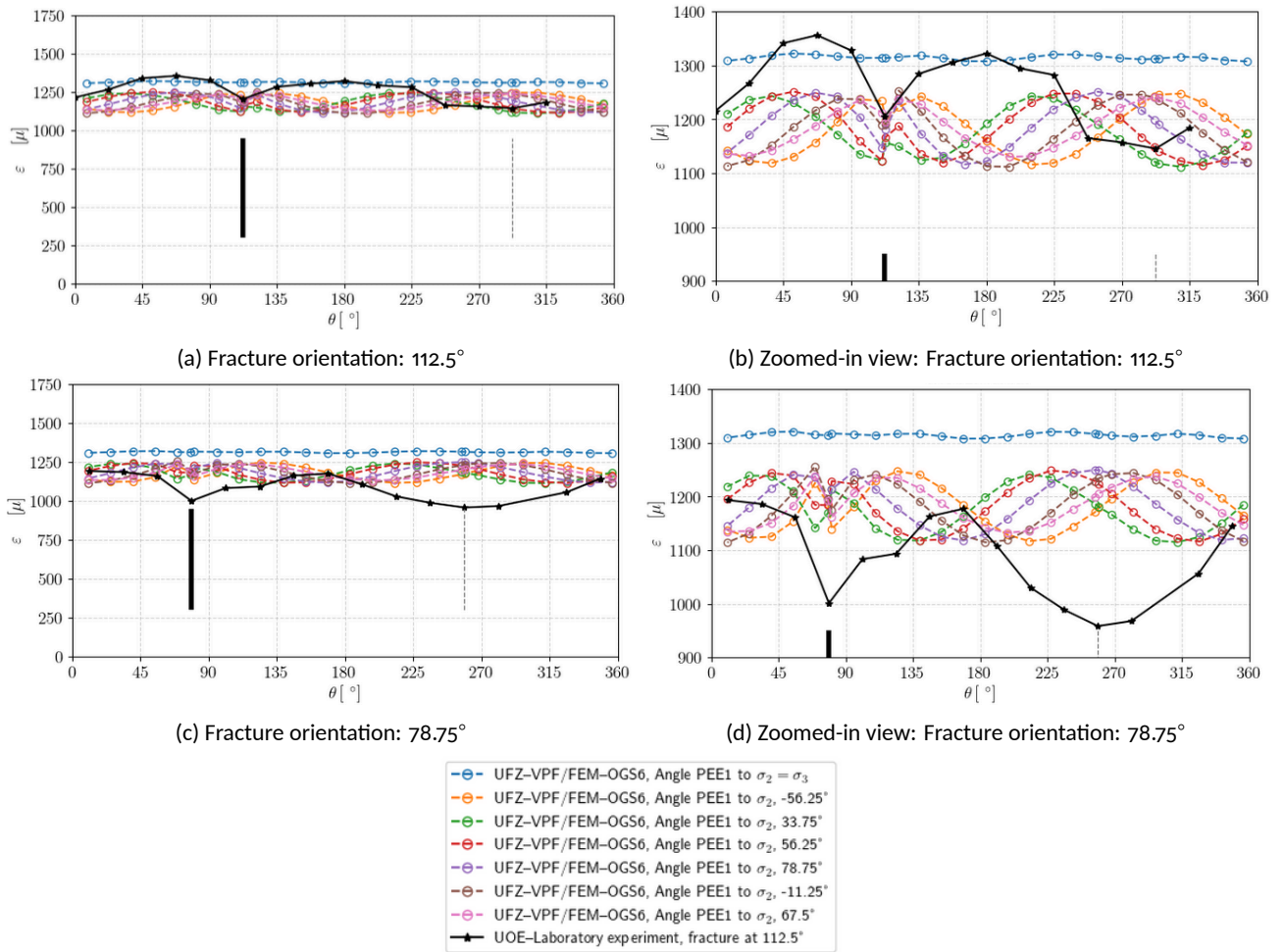


Figure 5.14: Volumetric strain at  $(x, y, z) \in \mathbb{R}^3 \mid |x^2 + y^2 - 0.065^2| < 10^{-6} \wedge |z - 0.1| < 10^{-6}$  for different loading scenarios compare with the experimental circumferential strain. The angle is measured clockwise from the positive x-axis (OGS-6.)

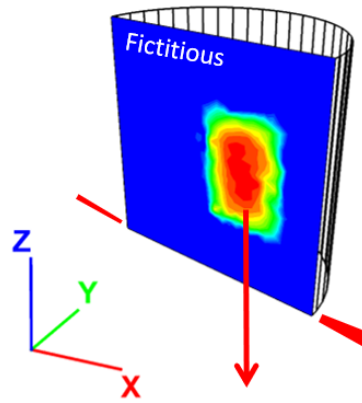


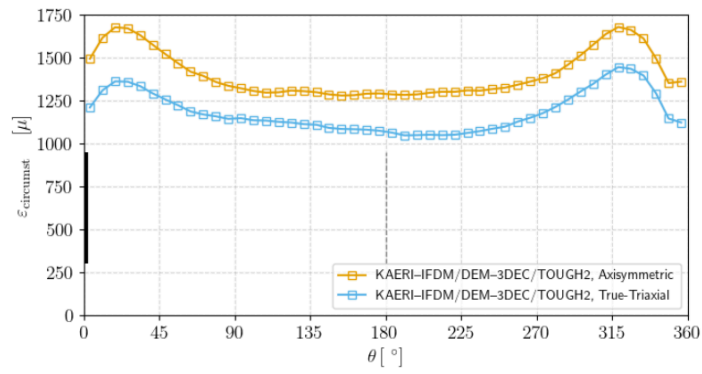
Figure 5.15: 3DEC model with an internal fracture

In the 3DEC model from KAERI, the internal fracture within the synthetic sample is reflected by applying the different fracture properties from the outer side of fracture (Fig. 5.15). The specific fracture properties assigned to the inner side of fracture is provided in Tab. 5.5. On the outer side of fracture, which is the fictitious area, high fracture stiffness and strength are assigned to prevent deformation and failure. Both axisymmetric stress conditions and true triaxial stress conditions are applied on the fractured model in 3DEC based on the PEE pressures in Table 5.3 to describe the experimental conditions in McDermott et al., 2018.

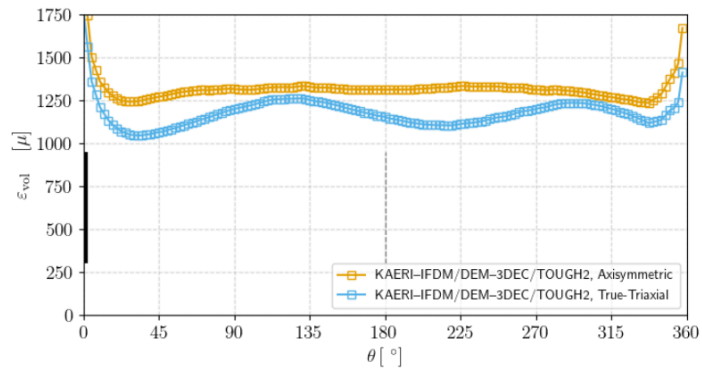
Table 5.5: Fracture properties for 3DEC model

Property	Value	Unit
Fracture normal stiffness	10.0	GPa/m
Fracture shear stiffness	4.0	GPa/m
Cohesive strength	0.0	MPa
Tensile strength	0.0	MPa

Figure 5.16 show the volumetric and circumferential strains extracted from the fractured model. The bold red line at  $0^\circ$  indicates the orientation of the internal partial fracture, and the thin red line at  $180^\circ$  indicates the opposite direction of partial fracture on the same surface. In both volumetric and circumferential strain results, a sharp spike appears at  $0^\circ$  due to the existence of fracture. In particularly, the drop of the circumferential strain at the fracture orientation is also observed in the experimental results from McDermott et al., 2018. The strain distributions on the other parts, including the opposite direction of partial fracture, follow the volumetric and circumferential strain trends of axisymmetric and true triaxial stress conditions, as depicted in Figure 5.11 and 5.12. The existence of fracture induces a drop of circumferential strain and drastic increases of volumetric strain. The internal fracture relaxes the compressive stress through normal and shear deformation according to the assigned fracture stiffness, so the element close to the internal fracture shows less compression than the neighbor elements and accompany the drop of circumferential strain. However, the volumetric strain is extracted from the monitoring line with 0.065 m of radius, which is adjacent to the internal fracture. The elements adjacent to the boundary of internal fracture can be affected by the normal and shear deformations of fracture and accompany the larger strains than neighbor elements.



(a) Fracture orientation: 0°, Circumferential Strain



(b) Fracture orientation: 0°, Volumetric Strain

Figure 5.16: Volumetric and circumferential strain results obtained from the partially fractured 3DEC model

### 5.2.5 Partially fractured sample (HM2)

In this task, we conduct numerical analysis to simulate the hydro-mechanical flow tests performed in the GREAT cell (Fraser-Harris et al., 2020). The flow tests in the GREAT cell are parts of the hydraulic injection tests introduced in Figure 5.17a. The fluid is injected through the propagated fracture at a constant flow rate (25 ml/min) and drained by the constant back pressure (3.45 MPa). During the flow tests, the rotatable polyaxial stress conditions are applied by changing PEE pressures. In this numerical analysis, the true triaxial stress conditions are applied with 12 MPa of axial stress, 7 MPa of horizontal maximum stress, and 3 MPa of horizontal minimum stress. The detailed PEE pressures applied to the numerical model is provided in Table 5.6. Fraser-Harris et al., 2020 estimated the fracture permeability during the flow tests by measuring the pressure difference between inlet and outlet. The numerical simulations performed in this task also extracts the pressure difference between the inlet element and outlet element at the steady-state of hydro-mechanical analysis, and calculates the fracture permeability to allow the plot of these results with the averaged normal stress on fracture surfaces (Figs. 5.20 and 5.22).

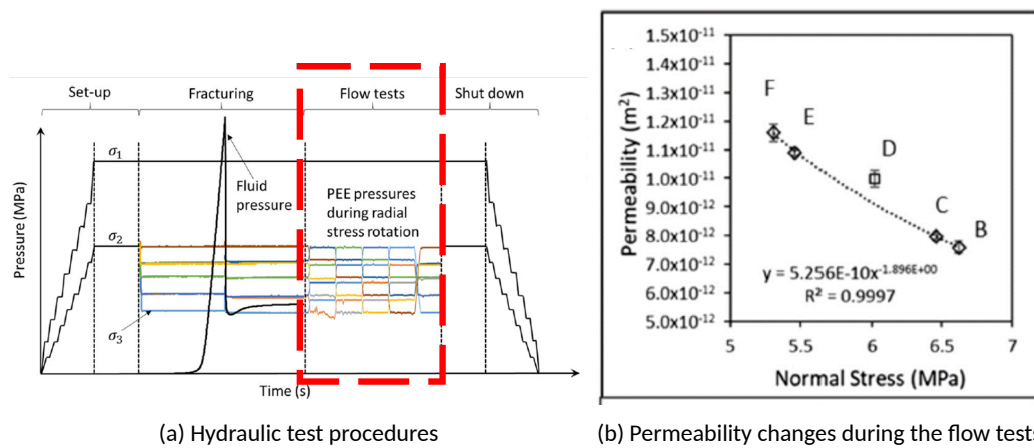


Figure 5.17: Information of the flow test performed within the GREAT cell (modified from Fraser-Harris et al., 2020)

Table 5.6: Loading scenarios for hydro-mechanical simulation in partially fractured sample

PEE number	PEE Pressures in each case (MPa)				
	B(0°)	C(22.5°)	D(45°)	E(67.5°)	F(90°)
PEEs 1 & 1a	3.0	4.3	5.6	7.0	7.0
PEEs 2 & 2a	4.3	5.6	7.0	7.0	5.6
PEEs 3 & 3a	5.6	7.0	7.0	5.6	4.3
PEEs 4 & 4a	7.0	7.0	5.6	4.3	3.0
PEEs 5 & 5a	7.0	5.6	4.3	3.0	3.0
PEEs 6 & 6a	5.6	4.3	3.0	3.0	4.3
PEEs 7 & 7a	4.3	3.0	3.0	4.3	5.6
PEEs 8 & 8a	3.0	3.0	4.3	5.6	7.0

To perform the coupled hydro-mechanical simulations of fractured media, KAERI team constructed the discontinuum model by TOUGH-3DEC simulator linking TOUGH2 and 3DEC. The fractured rock model is based on the 3DEC model which is already constructed in Figure 5.15 with additionally generated two groups of elements representing inlet and outlet boreholes (Figure 5.18). The deformation, failure and fluid flow are only allowed through the internal fracture surface between inlet and outlet elements. The initial aperture of fracture is assumed as 300  $\mu\text{m}$ . The mechanical properties are assigned as Table 5.5, and the shear dilation is ignored in this

fracture model. In the coupled hydro-mechanical analysis of fractured media, the fracture normal stiffness can be a key property deciding the permeability changes. Therefore, another model which has different fracture normal stiffness (100 GPa/m) was prepared.

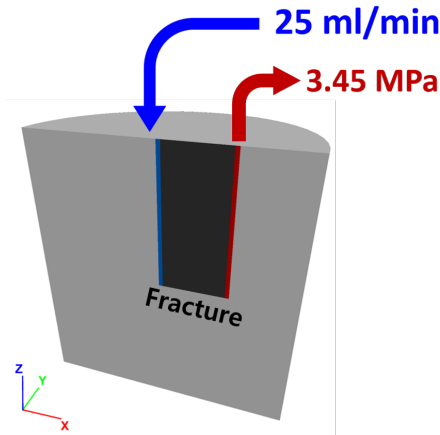


Figure 5.18: TOUGH-3DEC model for the hydro-mechanical flow tests

Before the simulations of flow tests, the polyaxial stress are applied based on the PEE pressures in Table 5.6. The initial pore pressure of entire model is assumed as 3.45 MPa same as the back pressure. After the mechanical equilibrium, the fluid injection through the inlet elements is proceeded until the TOUGH-3DEC model reaches the steady-state. At the steady-state, the normal stress and fluid pressure data is extracted from the entire fracture surfaces to plot the averaged normal stress - permeability graph. Figure 5.19 shows the distributions of the effective normal stress and fluid pressure on the fracture surface at the end of the simulation. Fluid pressure distribution indicates that the fluid flow is only allowed through the internal fracture.

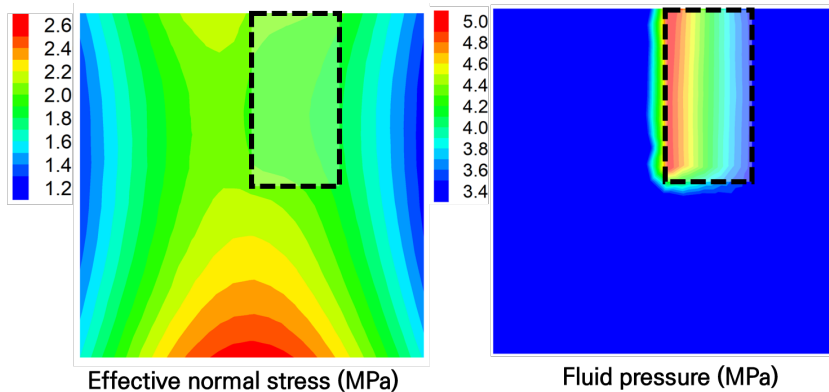


Figure 5.19: Effective normal stress and fluid pressure distribution of 3DEC model with 10 GPa/m of fracture normal stiffness under case C

The equivalent permeability of fracture is calculated by Darcy's law and the pressure differences between inlet and outlet fluid pressures. Figure 5.20 shows the relationship between the applied normal stress and calculated permeability of internal fracture. The fracture permeabilities are distributed from  $1\text{E-}10$  to  $5\text{E-}9$   $m^2$  depending on the applied normal stress. The increase of normal stress induces the decrease of permeability due to the normal closure based on the fracture normal stiffness, and the relationships are depicted as following the exponential curves which are similar to the experimental results depicted in Figure 5.17b. With the smaller fracture normal stiffness, the exponential curves of the stress-permeability relationship becomes clearer and

more drastic. The quantitative values of the fracture permeability have discrepancies with the experimental results of flow tests, but the simulated permeability can be highly dominated by the assumed fracture normal stiffness and initial aperture.

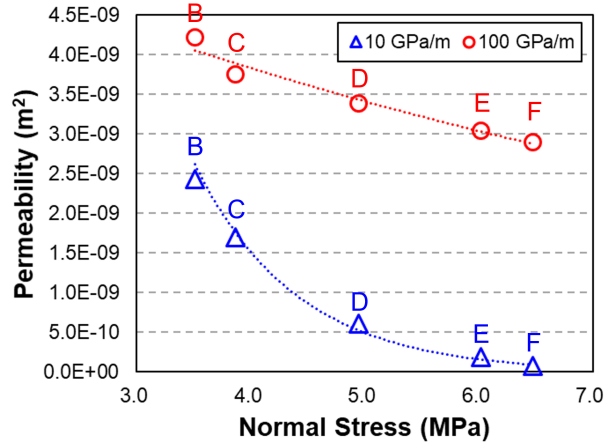


Figure 5.20: Permeability changes by applied normal stress under five different polyaxial stress conditions

**Simulation by UFZ team** UFZ team considers the lower-dimensional interface element (LIE) method (Watanabe et al., 2012) for the simulation the hydro-mechanical process in the fracture sample. In the LIE, the displacement difference between two sides of the surfaces is defined as a fracture relative displacement  $\mathbf{w}$ , which is defined in the local system as:

$$\mathbf{w} = \begin{bmatrix} w_t \\ w_n \end{bmatrix} = \begin{bmatrix} u_t^+ - u_t^- \\ u_n^+ - u_n^- \end{bmatrix}, \quad (5.3)$$

where  $u$  stands for displacement, subscripts  $t$  and  $n$  denote tangential and normal directions to the fracture plane, respectively. Superscripts  $+$  and  $-$  indicate one side and the other side of the surfaces, respectively. The normal fracture relative displacement represents the change of fracture aperture. Therefore the fracture aperture  $b$  is given by

$$b = b_0 + w_n,$$

with  $b_0$  the initial fracture aperture. On the fracture plane, the applied total total stresses are  $\sigma^f = [\sigma_t, \sigma_n]^T$ , which is defined as

$$\sigma^f = \sigma'^f - \alpha_B^f [p^f, p^f]^T, \quad (5.4)$$

where  $\sigma'^f$  is the effective stresses on the fracture,  $\alpha_B^f$  is the Biot's constant for fracture, and  $p^f$  is the liquid pressure in the fracture. The relationship between the fracture relative displacement and the effective fracture stress is given by

$$d\sigma'^f = \mathbf{K}dw, \quad (5.5)$$

where  $\mathbf{K}$  is the stiffness tensor defined as

$$\mathbf{K} = \begin{bmatrix} k_{tt} & k_{tn} \\ k_{nt} & k_{nn} \end{bmatrix}, \quad (5.6)$$

with  $k_{tt}$  and  $k_{nn}$  are the joint shear and normal stiffness, respectively.  $k_{tn}$  and  $k_{nt}$  govern the coupling effects between normal and shear displacements. Normally, the coupling effects are neglected.

The joint shear and normal stiffnesses can be estimated by the following formulas

$$k_{nn} = \frac{E_i E_m}{L(E_i - E_m)} \quad (5.7)$$

$$k_{tt} = \frac{G_i G_m}{L(G_i - G_m)}, \quad (5.8)$$

where  $E$  represents the Young's modulus,  $G$  represents the shear modulus, the subscripts  $i, m$  stand for intact rock and mass rock, respectively, and  $L$  the mean joint spacing (Barton, 1972).

The volume balance equation and volumetric flux equation for the discrete fracture can be derived from the mass balance law and the linear momentum balance law as

$$bS_s^f \frac{\partial p^f}{\partial t} + \alpha_B^f \frac{\partial b}{\partial t} + \nabla \cdot (b\mathbf{q}^f) + q^+ - q^- = 0, \quad (5.9)$$

$$\mathbf{q}^f = -\frac{k^f}{\mu} (\nabla p^f - \rho^l \mathbf{g}) \quad (5.10)$$

where  $S_s^f$  is the specific storage for the fracture,  $q^+$  and  $q^-$  are the leakage flux from each side of the fracture surfaces to the surrounding porous media,  $k_f = b^2/12$  is the fracture permeability,  $\mu$  is the liquid viscosity,  $\rho^l$  is the liquid density, and  $\mathbf{g}$  is the gravitational force vector.

The balance equations for the rock mass are the conventional ones, which are coupling to the balance equations of fracture via displacement, pressure, and liquid flux on the fracture interface.

Fig. 5.21 shows the numerical model for the simulation by the LIE method. As shown in Fig. 5.21, the injection

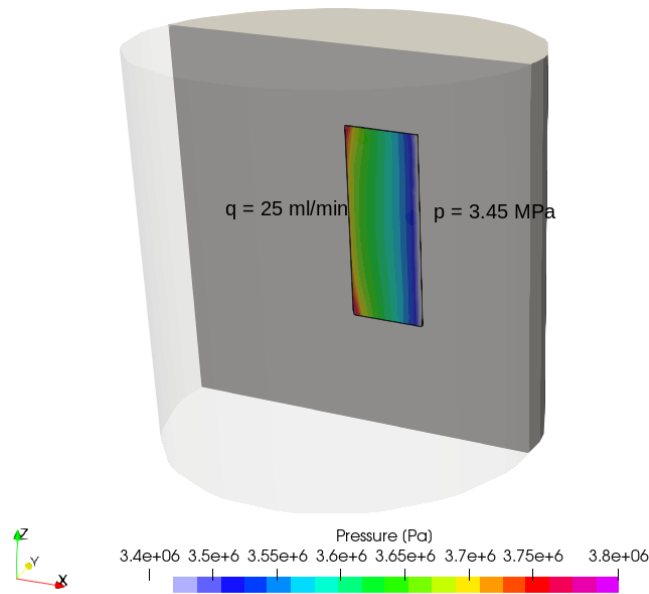


Figure 5.21: OGS#LIE model for the hydro-mechanical flow tests.

rate of 25 ml/min and the down stream pressure of 2.35 MPa are applied on the two vertical fracture interfaces, respectively. For the numerical simulation the injection rate is treated as the uniformly Neumann boundary

condition with a value

$$q = 25 \text{ ml /ml /H} = 0.41667 \cdot 10^{-6} \text{ m}^3 / 0.1 \text{ m}$$

with  $H = 0.1 \text{ m}$  the fracture height.

The domain is discretized into a conformable mesh with 328,785 tetrahedra for the matrix, and 402 triangles for the fracture. The initial fracture aperture is assumed to be  $10^{-5} \text{ m}$ . The load conditions are the same as that given in Table 5.6.

Simulations with high joint stiffness  $k_{nn} = 100 \text{ GPa/m}$ ,  $k_{tt} = 100 \text{ GPa/m}$ , and with low joint stiffness  $k_{nn} = 10 \text{ GPa/m}$ ,  $k_{tt} = 5 \text{ GPa/m}$  (the same as what are specified in Table 5.5), are carried out. Fig. 5.22 shows the simulated fracture permeability change with respect to the estimated normal stress from the load cases.

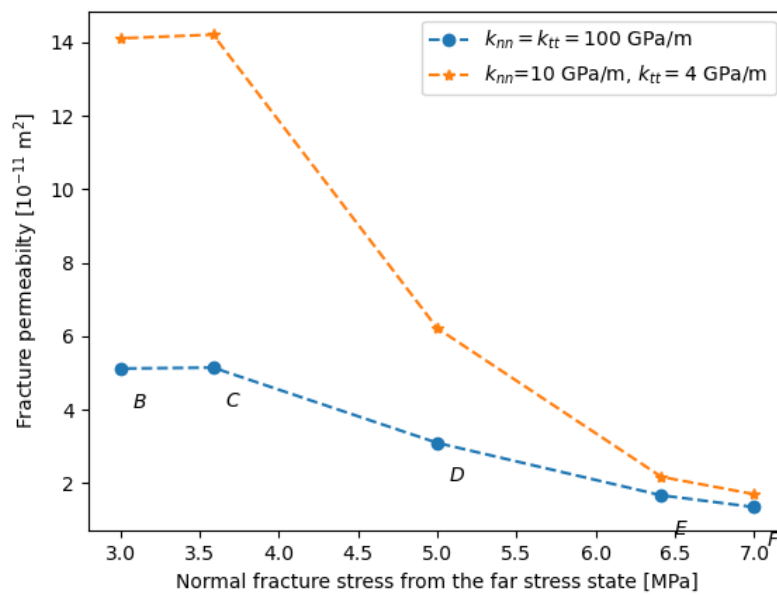


Figure 5.22: OGS#LIE simulation: permeability obtained with different high joint stiffnesses.

Fig. 5.23 shows the change of the calculated normal fracture stress with respect to the estimated normal fracture stress from the load cases, which displays that the change displays a monotonic increment as what expected.

Fig. 5.24 shows the distribution of permeability and normal stress in the fracture under one load case.

Fig. 5.24 shows the distribution of stress and strain in the matrix under one load case.



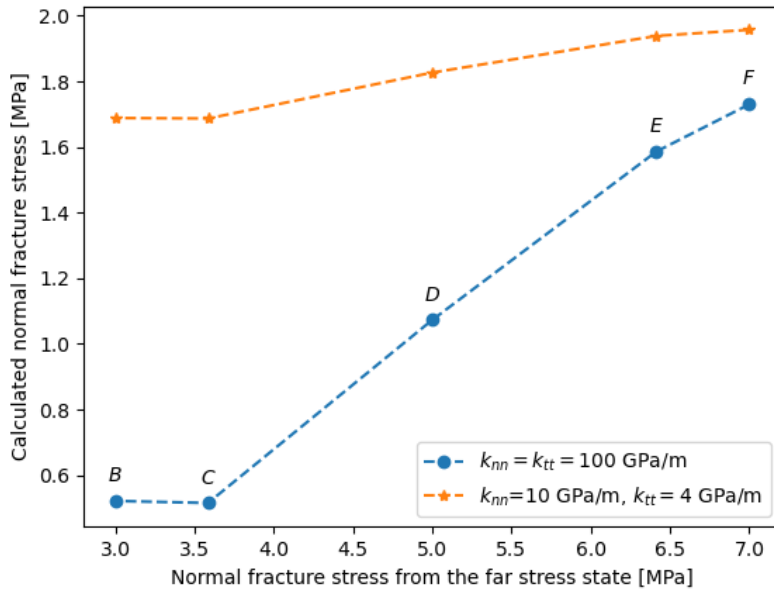


Figure 5.23: OGS#LIE simulation: Fracture normal stress obtained with two joint stiffnesses.

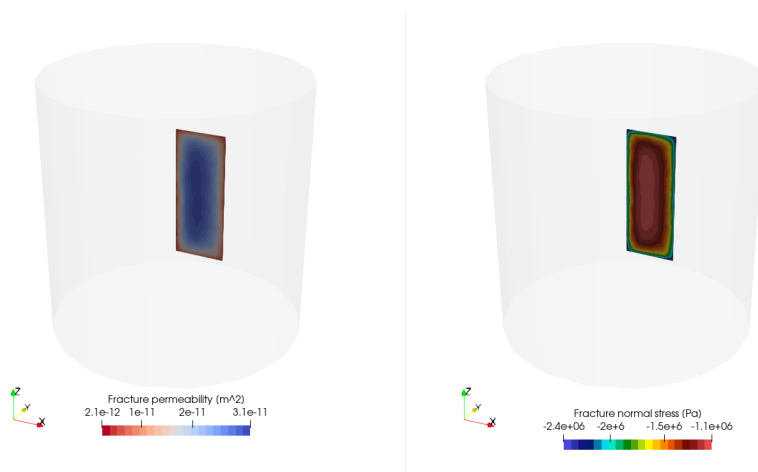


Figure 5.24: OGS#LIE simulation: permeability and normal stress distribution in the fracture.

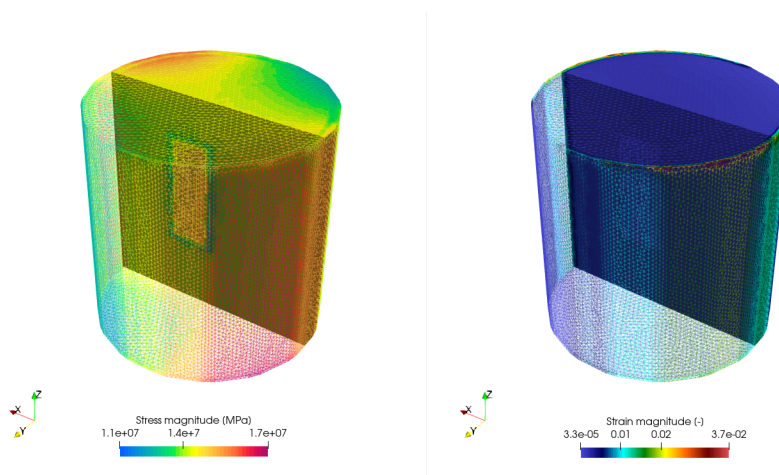
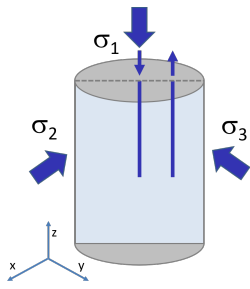


Figure 5.25: OGS#LIE simulation: stress and strain distribution in the matrix.

### 5.2.6 Fully fractured sample (M3)



In this task step, we consider a two-wing planar fracture in the specimen defined as  $\Gamma = \{(r, \theta, z) \mid -0.065 \leq r \leq 0.065, \theta, 0 \leq z \leq 0.2\}$ . The geometric aspects and boundary conditions are depicted in Figure 5.26. To account for the influence of fracture orientation, we replicate this benchmark by rotating the fracture. In all cases within this section, a 10 MPa axial compression is applied to the top cap of the sample in the z-direction. Detailed load values are provided in Table 5.4. We used the material properties of PMMA mentioned in Table 5.2.

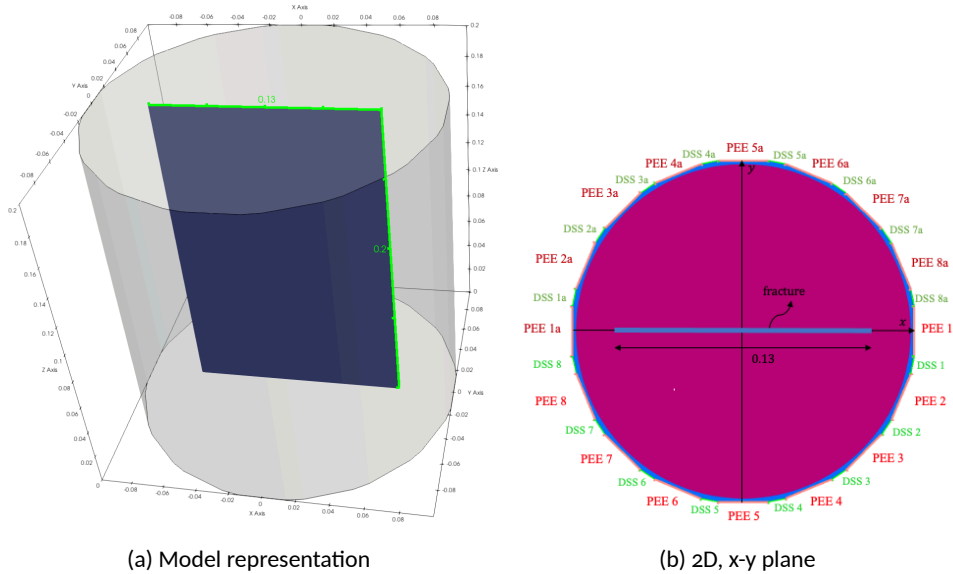


Figure 5.26: Analyses of fracture impact on circumferential strain under polyaxial loading (synthetic PMMA sample). To account for the influence of fracture orientation, we replicate this benchmark by rotating the fracture. In the clockwise direction, the fracture orientation is considered positive, with the zero value starting at 3 o'clock.

Figures 5.27a and 5.27b depict the volumetric strain under various loading conditions outlined in Table 5.4, observed along the probe curve (at a radius of 0.065 m). The comparison is made between two distinct fracture orientations of  $78.75^\circ$  and  $112.5^\circ$ , respectively. The notable variations in results arise from strain measurements near the fracture tip, where strain levels are significantly higher.

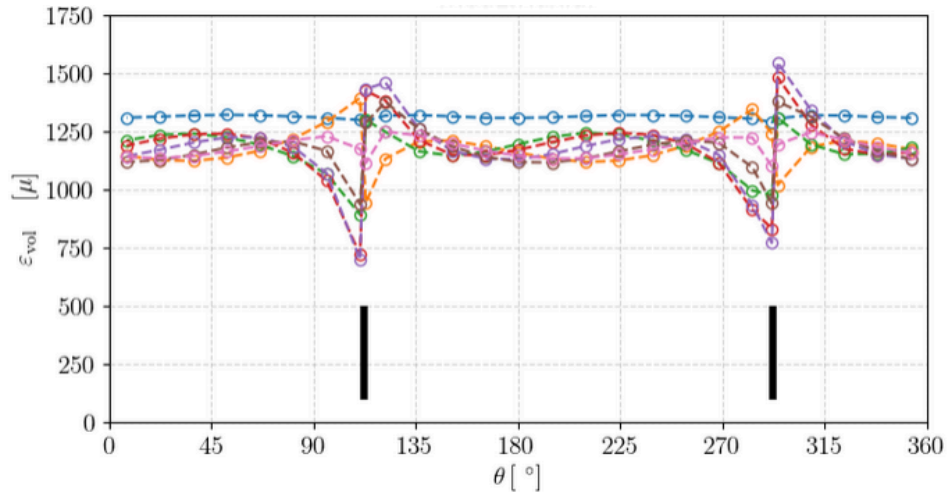
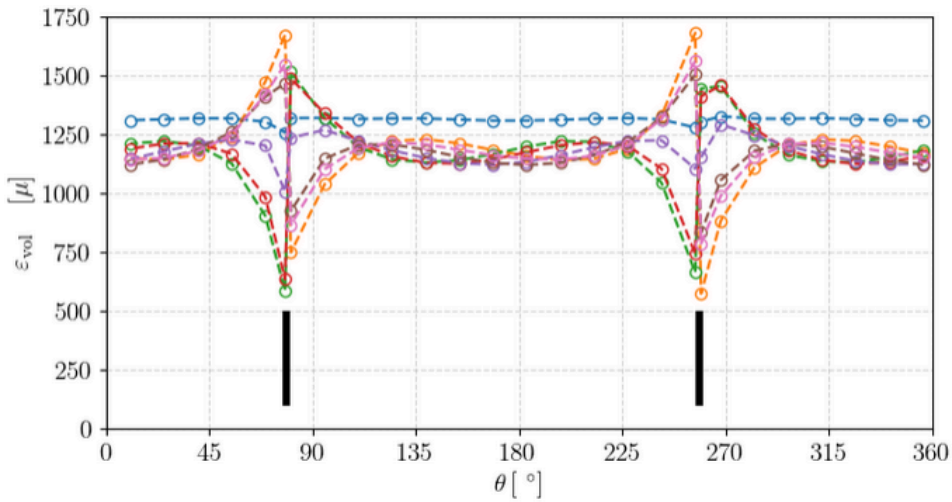

 (a) Fracture orientation:  $112.5^\circ$ 

 (b) Fracture orientation:  $78.75^\circ$ 


Figure 5.27: Volumetric strain at  $(x, y, z) \in \mathbb{R}^3 \mid |x^2 + y^2 - 0.065^2| < 10^{-6} \wedge |z - 0.1| < 10^{-6}$  for different loading scenarios. The angle is measured clockwise from the positive  $x$ -axis (OGS-6.)

### 5.3 Fully fractured sample (HM3)

Coupled hydro-mechanical modeling with explicit representation of a single fracture in a low permeability porous medium was also conducted by the SNL team. In this model the domain is subject to external loading, and fluid flow occurs in the fracture as described in Fraser-Harris et al., 2020. For this modeling study the uniform resin sample was selected. For the simulations COMSOL Multiphysics software (version 6.0) was used, with coupled solid mechanics and Darcy flow. The model geometry includes a cylinder with 200 mm diameter and 200 mm height, just as in the mechanical modeling case (Test M1). The geometry also includes a vertical fracture at the center of the cylinder, and a 3 mm diameter hole at the center, 125 mm long from top. Elastic material properties of the sample and the fracture are as in McDermott et al., 2018; Fraser-Harris et al., 2020 and given in Table 5.7.

Figure 5.28 shows a schematic diagram with a cross-section through the center of the domain (figure on the left) showing the fracture and the hole as described in Fraser-Harris et al., 2020. The figure on the right is a COMSOL representation of the model setup, with the cylinder surface subdivided to apply horizontal external stress.

For this exercise triaxial loading of the uniform resin sample was used. The external stress components applied were:  $\sigma_1 = 12$  MPa,  $\sigma_2 = 8$  MPa,  $\sigma_3 = 4$  MPa. To apply triaxial loading around the circumference of the sample, the cylinder surface was subdivided as shown in Figure 5.28. Stress was distributed around the circumference according to Equation:

$$\sigma = \frac{\sigma_2 + \sigma_3}{2} + \frac{\sigma_2 - \sigma_3}{2} \cos(2\theta) \quad (5.11)$$

where,  $\theta$  is the angle from positive x-axis. The same boundary condition as for the mechanical case (Test M1) was used: zero circumferential-displacement boundary conditions along the vertical lines that define the sample circumference intersection with the x- and y-axes. Zero displacement in the z-direction across the entirety of the sample base.

Fluid flow through the fracture was modeled using Darcy Flow. A flowrate of  $4.2e-7$  m<sup>3</sup>/s (25 ml/min) is applied at inlet, which is the bottom of the 3 m hole (125 mm from top). A pressure boundary condition is applied at outlet, which for this study was assumed as the entire bottom of the fracture. A pressure of 3.45 MPa was used. As was done in Fraser-Harris et al., 2020, the horizontal loads  $\sigma_2$  and  $\sigma_3$  were rotated by multiples of 22.5° to evaluate permeability at different stress conditions. The selected positions were: B ( $\sigma_2$  at 0° positive x-axis); C (23° from positive x-axis); D (45° from positive x-axis); E (267.5° from positive x-axis); F (90° from positive x-axis). Position B is shown in Figure 5.29a.

COMSOL coupled hydro-mechanical modeling was conducted for the different stress positions. Selected simulation results are shown in Figures 5.29b to 5.30 for stress Position D. The results represent the effects of external triaxial loading, the boundary conditions and fluid flow in the fracture. Figure 5.29b shows distribution of surface strain on the fracture surface, representing the loading condition and fluid flow. Distribution of the vertical-component of Darcy velocity together with direction arrows are shown in Figure 5.29c. The arrows indicate the magnitude and direction of flow from the inlet to outlet. Figure 5.29d shows the corresponding pressure distribution, with increased pressure at inlet.

Model results were used to estimate fracture hydraulic aperture and fracture permeability using below equa-

tions, respectively, as was done in McDermott et al., 2018; Fraser-Harris et al., 2020. As in Fraser-Harris et al., 2020, estimates were obtained using the pressure difference between the hole inlet and the outlet (bottom of fracture). For Position D, the pressure difference is 0.53 MPa (Figure 3.10). Using the pressure difference and other input data shown below, the estimated hydraulic aperture is  $1.53 \times 10^{-5}$  m, and the corresponding fracture permeability is  $1.95 \times 10^{-11}$  m<sup>2</sup>. Similar calculations were performed for the rest of the stress positions. Figure 5.30 shows a plot of estimated permeability against normal stress for all stress positions. The results show a linearly decreasing permeability with increased normal stress. The results are in line with previous work.

$$b = \sqrt[3]{\frac{12 \mu Q L}{\Delta P w}} \quad (5.12)$$

$$K_f = \frac{b^2}{12} \quad (5.13)$$

Where  $b$  is fracture aperture (m),  $Q$  is volume flowrate ( $4.2 \times 10^{-7}$  m<sup>3</sup>/s),  $L$  is the distance between the inlet of the hole and the outlet (75 mm),  $\Delta P$  is pressure difference between inlet and outlet (MPa),  $w$  is fracture width (200 mm) and  $K_f$  is hydraulic fracture permeability. Values of  $b$ ,  $\Delta P$  and  $K_f$  vary with leading position, and thus stress.

Table 5.7: Material properties

Parameter	Sample	Fracture
Elastic Modulus (GPa)	3.85	0.3
Poison's Ratio	0.4	0.4

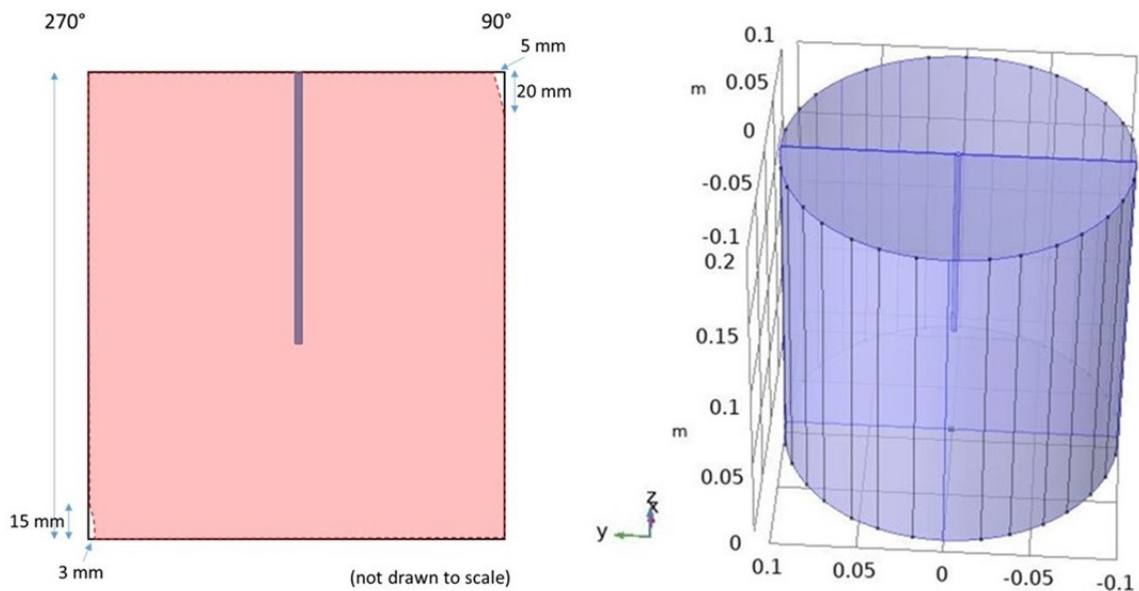


Figure 5.28: Left: Representation of vertical fracture (Fraser-Harris et al., 2020, Figure 11); Right: Model representation of domain with fracture.

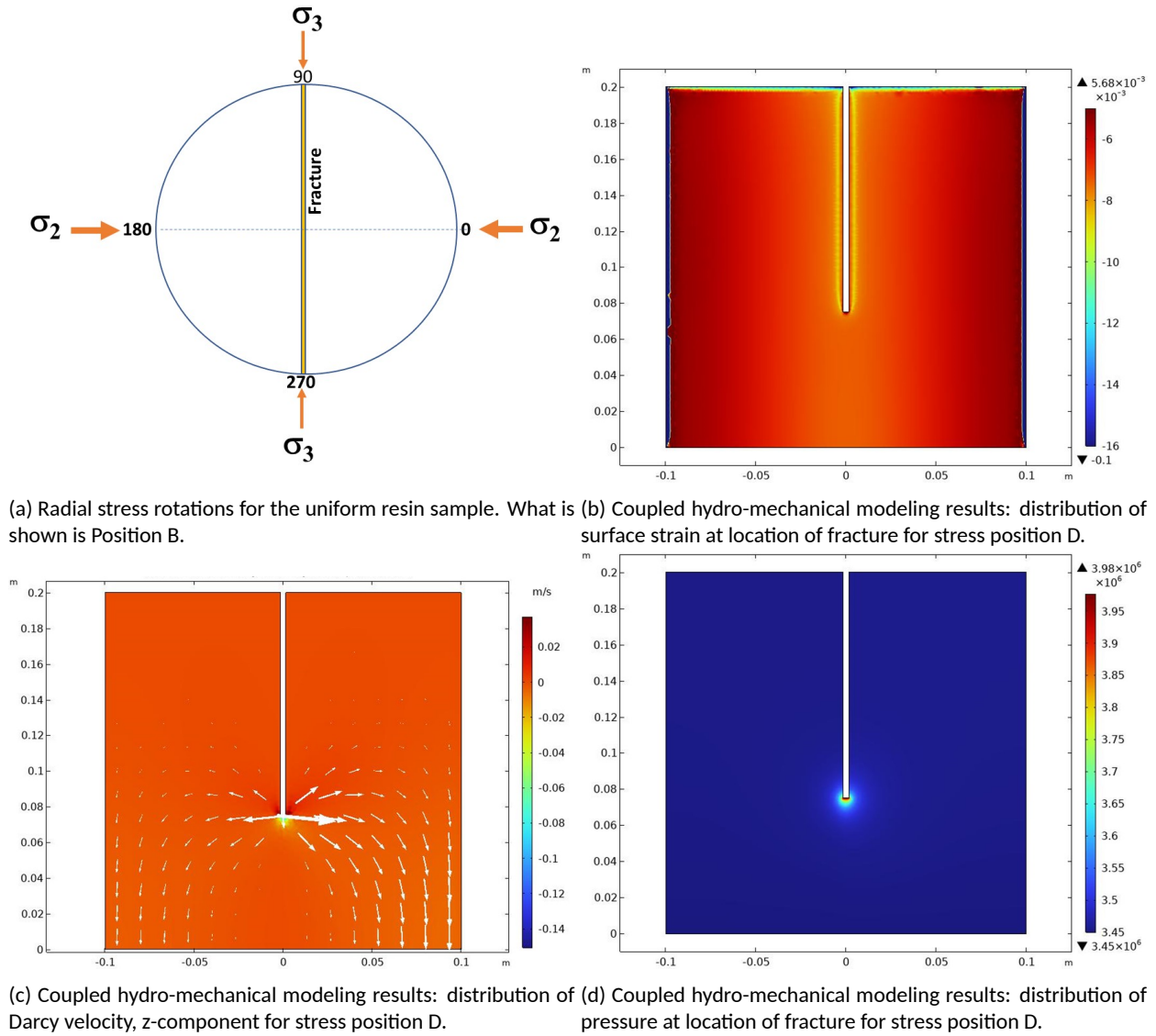


Figure 5.29: HM simulation results for the fully fractured sample

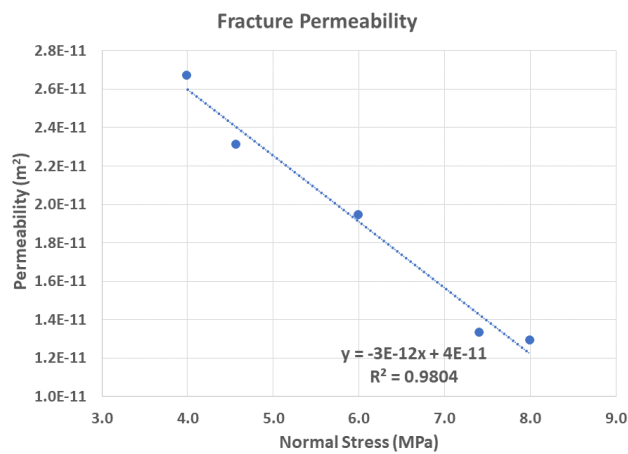


Figure 5.30: Coupled hydro-mechanical modeling results: calculated fracture permeability vs. normal stress.

## References

- Barton, NR (1972). "A model study of rock-joint deformation". In: *International Journal of Rock Mechanics and Mining Sciences & Geomechanics Abstracts*. Vol. 9. 5. Elsevier, pp. 579–582.
- Fraser-Harris, A.P. et al. (2020). "Experimental Investigation of Hydraulic Fracturing and Stress Sensitivity of Fracture Permeability Under Changing Polyaxial Stress Conditions". In: *Journal of Geophysical Research: Solid Earth* 125.12. Cited by: 10; All Open Access, Green Open Access. DOI: [10.1029/2020JB020044](https://doi.org/10.1029/2020JB020044). URL: <https://www.scopus.com/inward/record.uri?eid=2-s2.0-85098225724&doi=10.1029%2f2020JB020044&partnerID=40&md5=705e37470080c4eaa99398d33dfa22d>.
- Fraser-Harris, A.P. et al. (2023). "The influence of intermediate principal stress magnitude and orientation on fracture fluid flow characteristics of a fractured crystalline rock". In: in preparation.
- Frühwirt, Thomas, Daniel Pötschke, and Heinz Konietzky (2021). "Simulation of direct shear tests using a forces on fracture surfaces (FFS) approach". In: *Environmental Earth Sciences* 80.8. Cited by: 5; All Open Access, Hybrid Gold Open Access. DOI: [10.1007/s12665-021-09606-6](https://doi.org/10.1007/s12665-021-09606-6). URL: <https://www.scopus.com/inward/record.uri?eid=2-s2.0-85104006276&doi=10.1007%2fs12665-021-09606-6&partnerID=40&md5=38352a2edca39a24d14e93ed56c3fad>.
- McDermott, C.I. et al. (2018). "New Experimental Equipment Recreating Geo-Reservoir Conditions in Large, Fractured, Porous Samples to Investigate Coupled Thermal, Hydraulic and Polyaxial Stress Processes". In: *Scientific Reports* 8.1. Cited by: 6; All Open Access, Gold Open Access, Green Open Access. DOI: [10.1038/s41598-018-32753-z](https://doi.org/10.1038/s41598-018-32753-z). URL: <https://www.scopus.com/inward/record.uri?eid=2-s2.0-85054070649&doi=10.1038%2fs41598-018-32753-z&partnerID=40&md5=dbe9cf549a76065fee706766d0597676>.
- Mollaali, Mostafa et al. (2023). "Comparative verification of hydro-mechanical fracture behavior: Task G of international research project DECOVALEX-2023". In: *International Journal of Rock Mechanics and Mining Sciences* 170. DOI: [10.1016/j.ijrmms.2023.105530](https://doi.org/10.1016/j.ijrmms.2023.105530). URL: <https://www.scopus.com/inward/record.uri?eid=2-s2.0-85166325287&doi=10.1016%2fj.ijrmms.2023.105530&partnerID=40&md5=3a43688518353d27ce8a084a093cb90c>.
- Papachristos, E. et al. (2017). "Intensity and volumetric characterizations of hydraulically driven fractures by hydro-mechanical simulations". In: *International Journal of Rock Mechanics and Mining Sciences* 93, pp. 163–178.
- Watanabe, N. et al. (2012). "Lower-dimensional interface elements with local enrichment: Application to coupled hydro-mechanical problems in discretely fractured porous media". In: *International Journal for Numerical Methods in Engineering* 90.8, pp. 1010–1034.

## 6 KICT experiments (M and TM processes)

### 6.1 Experimental concept and procedure

Experimental design is based on the concept of Mohr-Coulomb failure as described in Fig. 6.1. The half-circle in blue indicates the initial critical stress state on a fracture with an inclination of  $\beta$  with the maximum principal stress. Supposing that the minimum principal stress was constant, and thermal stress ( $\sigma_T$ ) was added to the maximum principal stress, the Mohr circle becomes bigger and the stress state of the fracture will reach the failure envelope for a given stress increment (e.g., thermal stress).

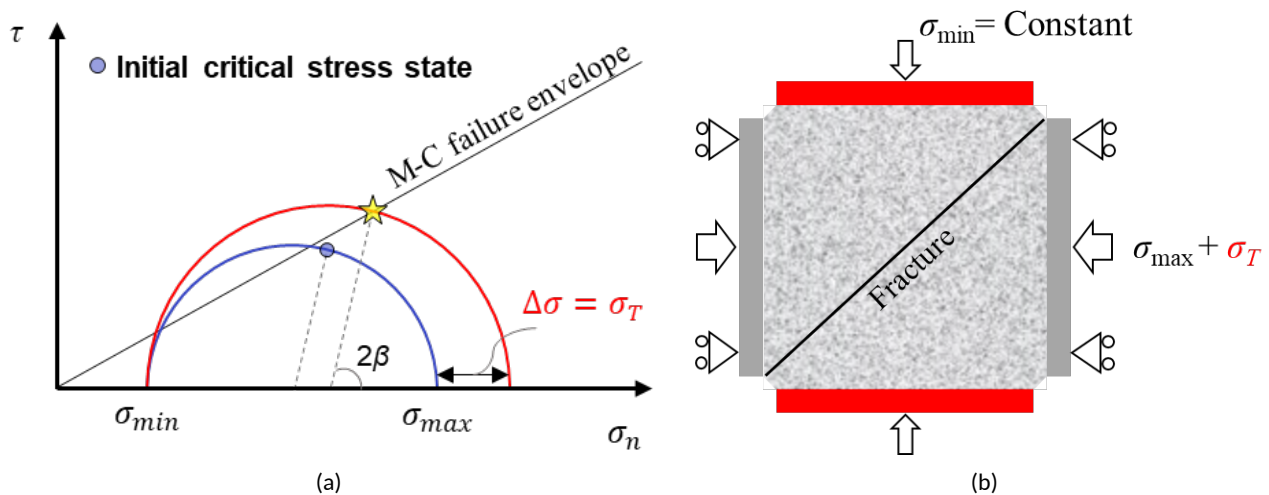


Figure 6.1: Experimental concept. (a) Initial critical stress state (blue half-circle) and expected failure stress state (red half-circle), and (b) Heating boundaries were set in the direction of  $\sigma_{min}$  and thermal stress will be induced in the direction of  $\sigma_{max}$  due to restraints of expansion

As the testing equipment is limited to a true triaxial testing machine available for only cubic rock samples with the side length of either 50 mm, 100 mm or 200 mm, in the following experiment, biaxial stress conditions were applied on an approximately 100 mm-length specimen containing a through-going fracture. The experiment was divided into two steps: named M loading and TM loading. First, two principal stresses were increased to the target values (estimated based on the measured frictional strength of fractures (Sun et al., 2021b) to reach an initial critical state, then the heating started. During this process, thermal stress is expected to generate in the maximum stress orientation, while  $\sigma_{min}$  is kept constant through a servo-control.

### 6.2 Experimental setup and monitoring data

A true-triaxial testing equipment with the capacity of 1100 kN load in each axis, and 150° C heating was used in all experiments (Sun et al., 2021a). The general purpose was to reproduce and evaluate thermally induced shear deformation of granite fractures in laboratory. In this study, the minimum and maximum principal stresses were applied along the vertical (z-axis) and horizontal (y-axis) directions, respectively, while the cell was open in the x-axis. As shown in Fig. 6.3(a), vertical and horizontal displacements were measured by the linear variable displacement transducers (LVDTs) installed at the back sides of loading rams. In each direction, loading ram was composed of a loading plate (contact platen) and an adapter. Four heating probes either with 100 W or 125 W are inserted in the respective ram to fulfill heating function. Heating conditions can be selected



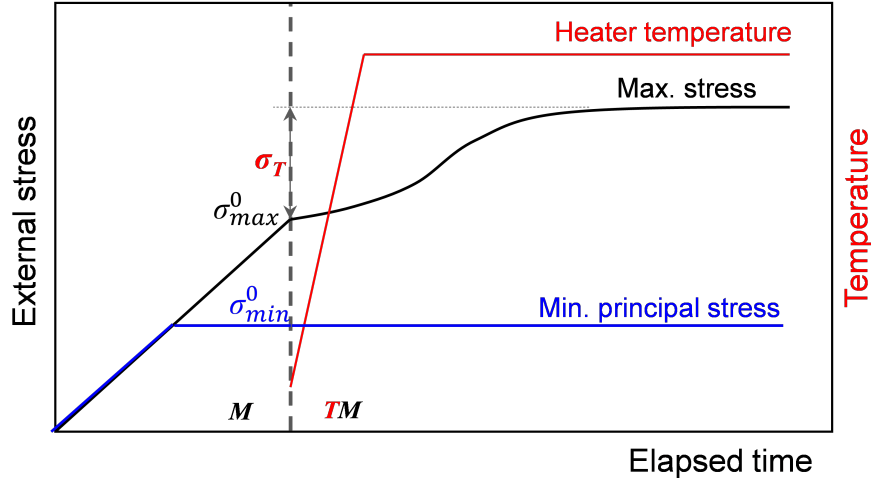


Figure 6.2: Experimental procedure

by turning on the switch in each single side of loading, and controlling the heating rate and target temperature. Heating alters between on and off based on the comparison of the magnitude of the temperature sensor installed near the heaters and the given target temperature (e.g., 150° C in this study).

Figure 6.6(b) illustrates the locations of AE sensors, heaters, clip-on gauges, and thermocouples from the full front view as well as on the six square faces of a cube. Heaters were installed in the top and bottom adapters. The powers of the top four heaters are 100 W, and that of the bottom four heaters are 125 W in this study. Five thermocouples (T1–T5) were attached to the front surface of each granite specimen during heating, and an additional one (T0) was installed near the heaters in the bottom adapter. Two clip-on displacement transducers were installed parallel and perpendicular to the fracture surface, respectively, to measure fracture slip and fracture open/closure. Eight R15S AE sensors were installed in loading plates with four each at the left and right sides. On the front side of specimen, two additional AE sensors were directly attached to the granite surface.

The DIC method directly computes the full-field surface deformations along the  $y$  ( $dy$ ) and  $z$  ( $dz$ ) axes by comparing the digital image subsets of a specimen surface acquired before and after deformation. We employed this method to measure the local fracture slip and shear dilation along the fracture. Photos of the back side of the specimens taken during thermoshearing tests were used for DIC analysis. Local deformation along the shear and normal directions were calculated using:

$$\delta_s = d_z \cos \beta + d_y \sin \beta \quad (6.1)$$

$$\delta_n = d_z \sin \beta - d_y \cos \beta \quad (6.2)$$

where  $\delta_s$  is the deformation field along the shear direction,  $\delta_n$  the deformation field along the normal direction. Five locations labelled 1–5 (see Fig. 6.3b) with the same distance interval of 22.4 mm along the fracture were picked on the back side, and the local fracture slip and shear dilation at these locations were calculated based on two reference lines at around 3.5 mm from the fracture. For example, the fracture slip and shear dilation at DIC5 can be calculated based on the relative shear and normal displacements at the points 5' and

5'' noted in Fig. 6.3(b).

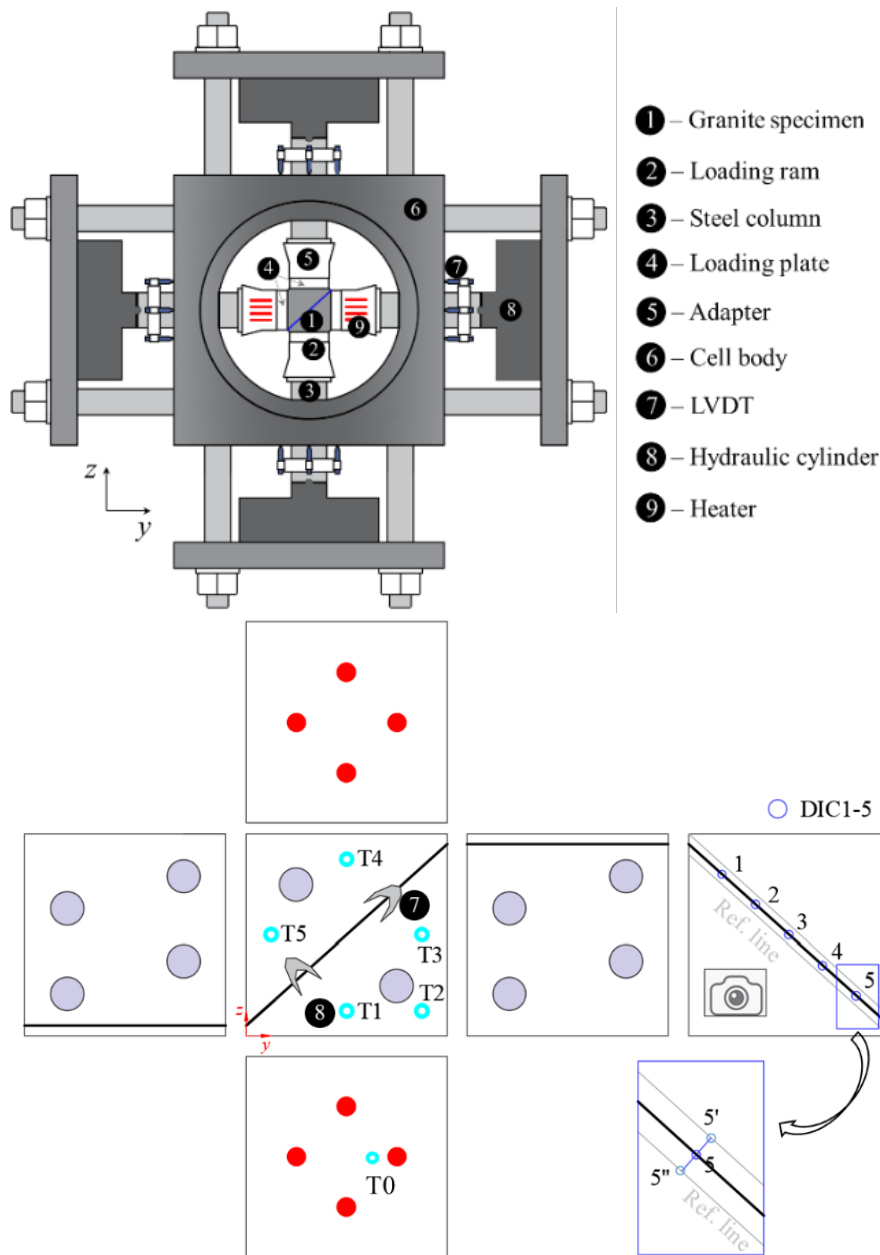


Figure 6.3: Schematic diagrams showing the locations of heaters, clip-on gages, thermocouples, and AE sensors (a) from the full front view and (b) on the six square faces of a cube. On the back side of the specimen, a camera was used to take photos of the back side for DIC analysis, and the fracture slip and shear dilation at the five locations (labeled 1–5) were indirectly measured.

### 6.3 Characterization of test specimen

Pocheon granite was used in all experiments. The main properties of this granite are listed in Table 6.1. A cubic specimen containing a smooth sawcut fracture labelled SF and a specimen containing a rough tensile-splitting fracture labelled RF were compared in this study. More details about the specimens were given in Sun et al., 2023, which was firstly presented on the EUROCK2022 conference. Fig. 6.4 shows the typical surface topography of the two fractures measured through an optical 3D scanner. The joint roughness coefficients of

the smooth fracture and rough fracture were calculated as 0.66 and 12.51 using the empirical equation based on the ultimate slope ( $\lambda$ ) of each profile (Li and Zhang, 2015):

$$JRC = 89.9971 \cdot \lambda^{0.6601} \quad (6.3)$$

$$\lambda = a/L_F \quad (6.4)$$

where  $L_F$  is the 2D fracture profile length and  $a$  is the maximum vertical distance of each profile.  $L_F$  is taken as 100 mm in the present study.

Table 6.1: Material properties

Property	Value
Density (kg/m <sup>3</sup> )	2650
Elastic modulus (GPa)	55.09
Poisson's ratio	0.275
Internal friction angle (°)	60.4
Cohesion (MPa)	27.58
Average linear thermal expansion coefficient (/K)	$6.49 \times 10^{-6}$
Thermal conductivity (W/m/K)*	2.19
Specific heat (J/kg/K)*	645

\* Laser flash method, 25~200 °C

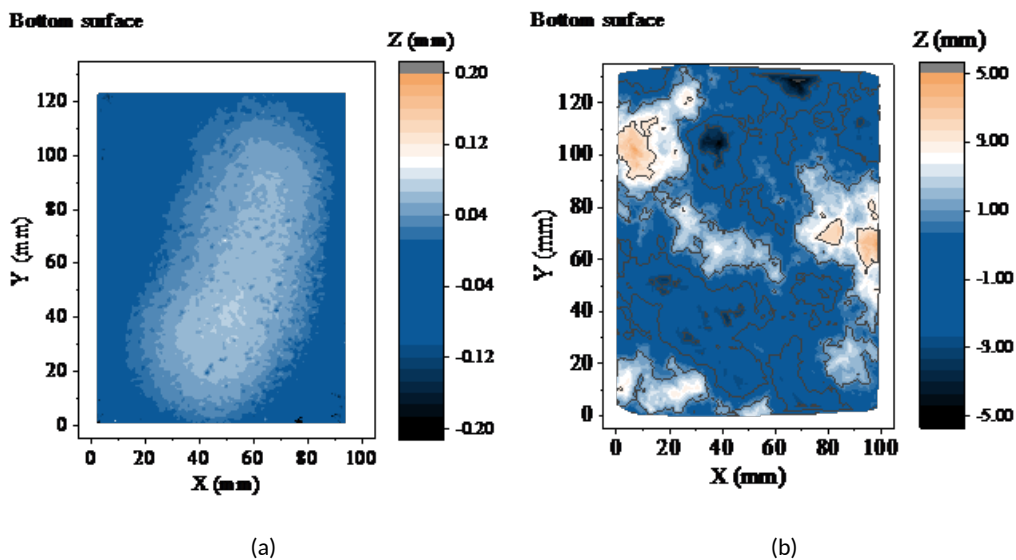


Figure 6.4: Asperity distribution (topography) for the bottom surface of (a) SF, and (b) RF

Table 6.2: Average JRC values before and after thermoshearing tests, static friction coefficients ( $\mu_s$ ), and the critical stress states for thermoshearing tests of SF and RF

Fracture surface	Average JRC		$\mu_s$	Initial stress ( $\sigma_3, \sigma_1$ ) (MPa)
	Pre-test	Post-test		
SF	Top	0.62	0.60	0.58 (3.00, 9.00)

Table 6.2: Average JRC values before and after thermoshearing tests, static friction coefficients ( $\mu_s$ ), and the critical stress states for thermoshearing tests of SF and RF

Fracture surface	Average JRC		$\mu_s$	Initial stress ( $\sigma_3, \sigma_1$ ) (MPa)
	Pre-test	Post-test		
RF	Bottom	0.69	0.65	(3.00, 24.61)
	Top	12.53	12.62	
	Bottom	12.48	12.69	

\*this was measured based on only one pair of normal and shear stress data

During the mechanical shear test on SF, the minimum principal stress ( $\sigma_3$ ) was set as 1 and 2 MPa, and the maximum principal stress ( $\sigma_1$ ) was increased to obtain the fracture resistance and then fit the linear M-C failure envelope with zero cohesion. The fracture resistances of RF were obtained by only setting the  $\sigma_3$  as 3 MPa and increasing the  $\sigma_1$  till fracture slip occurs to avoid the significant change of roughness caused by shear displacement. The static friction coefficients  $\mu_s$  ( $\mu_s = \tau/\sigma_n$  measured at the onset of fracture slip) were calculated assuring the inclination angle,  $\beta$ , has a unique value (i.e.,  $48^\circ$ ) along the fracture ignoring fracture tortuosity. The static frictional coefficients of SF and RF are 0.58 and 0.86, respectively (see Table 6.2).

The topography of the surfaces from cutting and extremely smooth to tensile-splitting and very rough is one of the major parameters affecting their frictional resistance showing an increasing tendency with fracture roughness. However, the measurement of the  $\mu_s$  of RF is only based on one data point, assuming zero cohesion. In addition, the  $\mu_s$  of the RF was measured with an initial offset of 3 mm along the shear direction between the top and bottom surfaces. This means that the two surfaces in rough fracture are not perfectly interlocked. After the Mechanical shearing test, the critical stress state at the beginning of the thermoshearing test was set as  $\sigma_3 = 3$  MPa for both the SF and RF, and  $\sigma_1$  was set as approximately 1 MPa lower than the predicted failure stress based on the estimated  $\mu_s$  through mechanical loading. The critical stress levels for SF and RF are also listed in Table 6.2. The maximum and minimum principal stresses can be resolved into shear and normal stresses acting along fractures during heating by assuming the homogeneous stress distribution.

## 6.4 Experimental results and analysis

### 6.4.1 Temperature evolution and distribution

The influence of fracture types on the temperature distribution in fractured rock masses was ignored. Figure 6.5(a) shows typical results of temperature evolution and the heating rates at several selected locations (T1–T5) during the thermoshearing test conducted on the SF.

The heating rates were averaged every five minutes. Temperatures measured at T1, T2, and T4 show an earlier increase than those measured at T3 and T5 because they are very close to the heaters. When the temperature on the specimen surface reaches a plateau, the total temperature increments at locations of T1, T2, T3, T4, and T5 are 62.8, 60.2, 50.1, 54.6, and 42.7 $^\circ\text{C}$ , respectively. The peak heating rates lower than 3 $^\circ\text{C}/\text{min}$  of T1, T2, and T4 are at around 900 s, and that of T3 and T5 are at around 1,200 s. For more details about how heat was transferred in granite specimens, we refer to Yoon, Zang, and Stephansson, 2014.

Figure 6.5(b) show that the temperature distribution in granite specimens is non-uniform, and the temperature at the location closer to the heating source is higher. The temperature of the T1 is larger than that of the T4

because the top four heaters are 100 W, and the bottom four heaters are 125 W. Therefore, it is reasonable to estimate that local deformation and stress along the fracture vary due to geometric properties and non-uniform temperature distribution. In this study, however, shear and normal stresses on the fracture are interpreted from the external principal stresses in Mohr’s circle treating the specimen as a representative element.

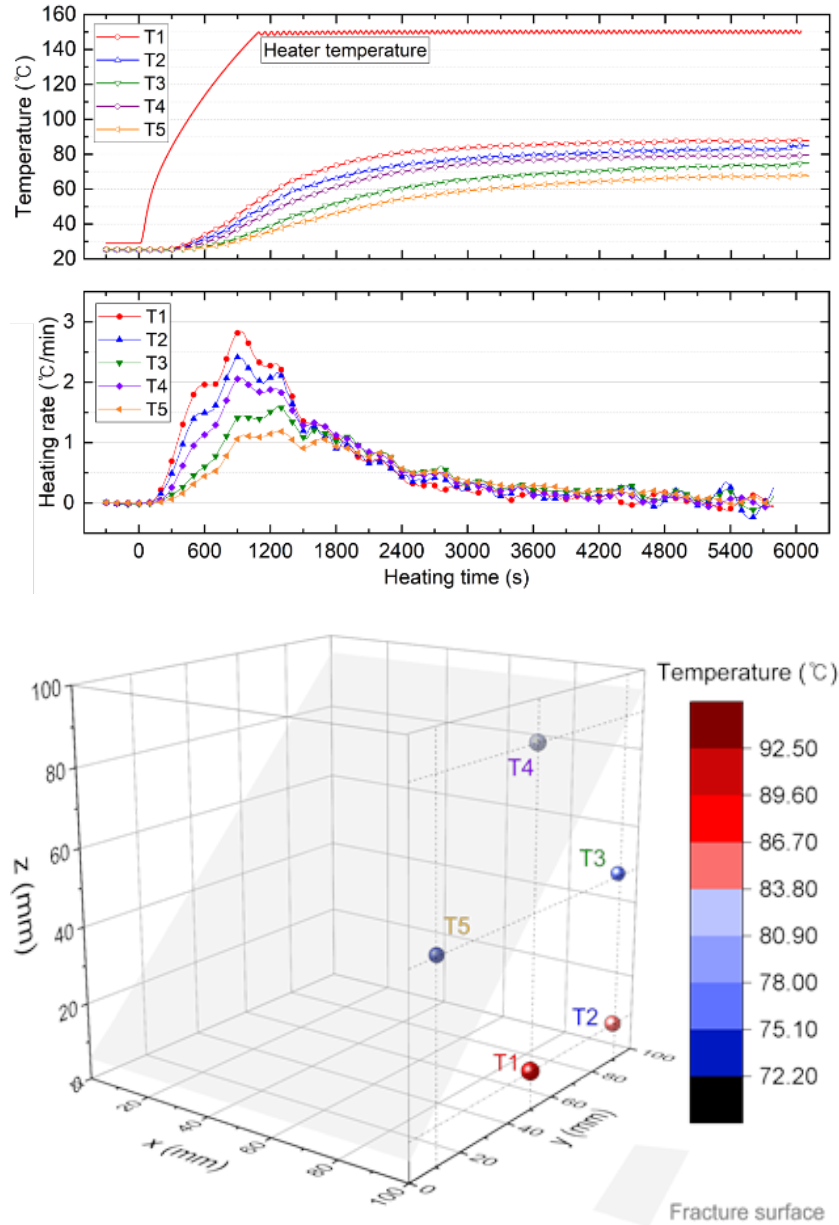


Figure 6.5: Results of temperatures. (a) Evolutions of temperatures at the five measure points of T1-T5 on the specimen surface and their heating rates; (b) Spatial distribution of T1-T5 after heating duration of 6,000 s. The plane in grey represents the location of the fracture surface

#### 6.4.2 Thermally induced fracture slip and shear dilation

Stress increments (increments in the maximum principal stress, i.e., thermal stress), as well as fracture shear and normal displacements in these two cases, are compared in Table 6.3. Evolution of the stresses and displacements during the total heating duration of 6,000 s for SF and RF are plotted in Figure 6.6(a) and (b),

respectively.

### (1) Effective thermal stress

Thermal stresses in the SF increased at the beginning of heating to reactivate the critically-stressed fracture. Unlike that in SF, thermal stress was minus (the maximum principal stress decreased) in RF at the very beginning of heating in RF. At the same time, shear displacement increased. We therefore speculated that the slip occurred immediately at the start of heating on RF. Fracture slip will cause a stress drop, and reduction in the stress (the maximum principal stress in this case) when the thermal stress induced by heating cannot balance the stress drop caused by slip. After 6,000 s heating, the total increment in the maximum principal stress (we call this the effective thermal stress) is measured to be 3.32 MPa and 0.5 MPa in SF and RF, respectively, corresponding to the normal stress increment of 1.49 MPa and 0.23 MPa for the fractures. In both cases, the fracture thermoshearing was finally stabilized with an increase in stresses on the fracture surface.

### (2) Shear displacement and slip rate

Shear displacement measured by the parallel clip-on displacement transducer in SF slightly decreases at the very beginning of heating, mainly due to the thermal expansion of fixing jigs and transducer legs. Net fracture slip can be approximately estimated as the increment in the relative shear displacement referring to the initial value at the lowest point of the shear displacement-time curve. The total shear displacements measured by the parallel transducer were 100.3  $\mu\text{m}$  and 97.4  $\mu\text{m}$  in SF and RF, respectively, at the heating duration of 6,000 s. There was no significant difference in the total shear displacement between the SF and the RF, for the given test conditions in this study. The approximate slope of the shear displacement-time curve for every duration of 10 minutes during the thermoshearing test was calculated and its maximum value is defined as the peak slip rate. As a result, the peak slip rate was estimated to be  $3.77 \times 10^{-2} \mu\text{m/s}$  and  $4.15 \times 10^{-2} \mu\text{m/s}$  for SF and RF, respectively, which are considered quite similar. In general, we think that the thermally induced slip grows slowly in the two specimens investigated in this study. For the given heating boundaries, no stick-slip was found.

Results of shear displacements in SF and RF measured by the non-contact DIC method are plotted in Fig. 6.6 for comparison. In Fig. 6.6(a), there is nearly no shear displacement in SF at the beginning of heating. The slip displacements at the five different locations along the length of SF are very close, indicating that the fracture thermoshearing is relatively uniform in the smooth fracture. The average slip displacement is 81.4  $\mu\text{m}$ , and the average peak slip rate is  $2.78 \times 10^{-2} \mu\text{m/s}$ , which are lower than those measured by the transducer, i.e., 100.3  $\mu\text{m}$  and  $3.77 \times 10^{-2} \mu\text{m/s}$ . The results measured by the DIC method are less affected by the increasing temperature and are considered to be more reliable than the measurements given by the transducer.

Before the start of heating, we observed an off-fracture crack at the back side of the RF specimen, which was initiated at the location between locations DIC3 and DIC4, and propagated in the matrix in a direction approximately perpendicular to the fracture surface. We did not observe any induced cracks at the front side, implying that this is not a throughgoing crack. Shear displacements at locations DIC4 and DIC5, which are below the crack initiation location, are larger than those at locations DIC1, DIC2, and DIC3. From the DIC analysis, the average slip displacement below the crack is 156.0  $\mu\text{m}$ , and the average slip displacement above the crack is 93.9  $\mu\text{m}$ . The shear displacements of the lower half of the fracture are larger than those measured at the upper half, mainly due to the opening of the off-fracture crack during the thermoshearing as observed from DIC analysis. In addition, the average peak fracture slip rate at locations DIC4 and DIC5 is  $5.94 \times 10^{-2} \mu\text{m/s}$ , which

is higher than the magnitude of  $3.19 \times 10^{-2} \mu\text{m/s}$  at locations DIC1, DIC2, and DIC3. The off-fracture crack influences the thereafter fracture thermoshearing behavior, which is first reported and going to be further investigated. The initiation and propagation of off-fracture cracks is closely related to the fracture surface morphologies which causes concentrated stress that exceed the strength of the granite matrix.

### (3) Fracture dilation

The decrease in the normal displacements observed from the perpendicular transducer are due to the thermal expansion of fixing jigs and transducer legs at the early stage of heating. Therefore, fracture shear dilation is taken as the net increment in the normal displacement, referring to the lowest point of the normal displacement-time curve. As shown in Table 6.3, the total fracture normal displacement measured by transducers at 6,000 s were  $4.5 \mu\text{m}$  and  $11.5 \mu\text{m}$  in SF and RF, corresponding to the dilation angle of  $2^\circ$  and  $10^\circ$  being estimated by the equation proposed by Barton and Choubey (1977). The shear dilation angle was higher for the rougher joint surface, as expected. From the DIC analysis, the total normal displacement in PF is insignificant ( $\sim 4 \mu\text{m}$ ). A similar result has been reported in a previous study of mechanical shear tests (Kim and Jeon, 2019). The dilation in the RF reaches  $20 \mu\text{m}$  at DIC1-DIC5, which is higher than the measurement given by the transducer. There was no obvious difference in the dilation at the five different locations.

Table 6.3: Comparison of measurements of displacements by DIC analysis and stresses in the two fractures

Sample	Shear disp. ( $\mu\text{m}$ )	Normal disp. ( $\mu\text{m}$ )	Peak velocity ( $\times 10^{-2} \mu\text{m/s}$ )	Dilation angle ( $^\circ$ )	Thermal stress (MPa)	Normal stress increment (MPa)
SF	81.4	4	2.78	$3^\circ$	3.32	1.49
RF	93.9(156.0*)	20	3.19(5.94**)	$12^\circ$	0.50	0.23

\* Local large shear displacement due to induced cracks; \*\* Local large peak shear velocity due to induced cracks.

#### 6.4.3 Discrepancy between the measurements by the transducers and the DIC analysis

The UB-5 clip-on type displacement transducer is used and it is equipped with a pair of RAF-11 fixing jigs. The groove of the fixing jig matches with the transducer tips (Figure 6.7(a)). For more specifications we refer to the manual provided by the manufacture (Tokyo Measuring Instruments Laboratory Co., Ltd.). The transducer is made in metal and the displacement measurements have inevitably been affected by the temperature changes. The temperature-induced displacement was determined by heating the intact rock using the same transducer arrangement under the same heating condition. Figure 6.7(b) gives an example of the true displacement derived by subtracting the temperature-induced displacement from the measured displacement.

#### 6.4.4 Fracture surface change

There are no visible slickensides and sheared-off particles after the thermoshearing for the SF specimen, except for very limited powders observed on the fracture surface. Several reasons are considered: (1) the maximum principal stress ( $\sim 12 \text{ MPa}$ ) and the resulted stresses in the SF specimen are not high compared to the strength of the rock matrix, and (2) the smooth fracture surface has no visible asperities being sheared for the very limited total shear displacement of  $\sim 0.1 \text{ mm}$ .

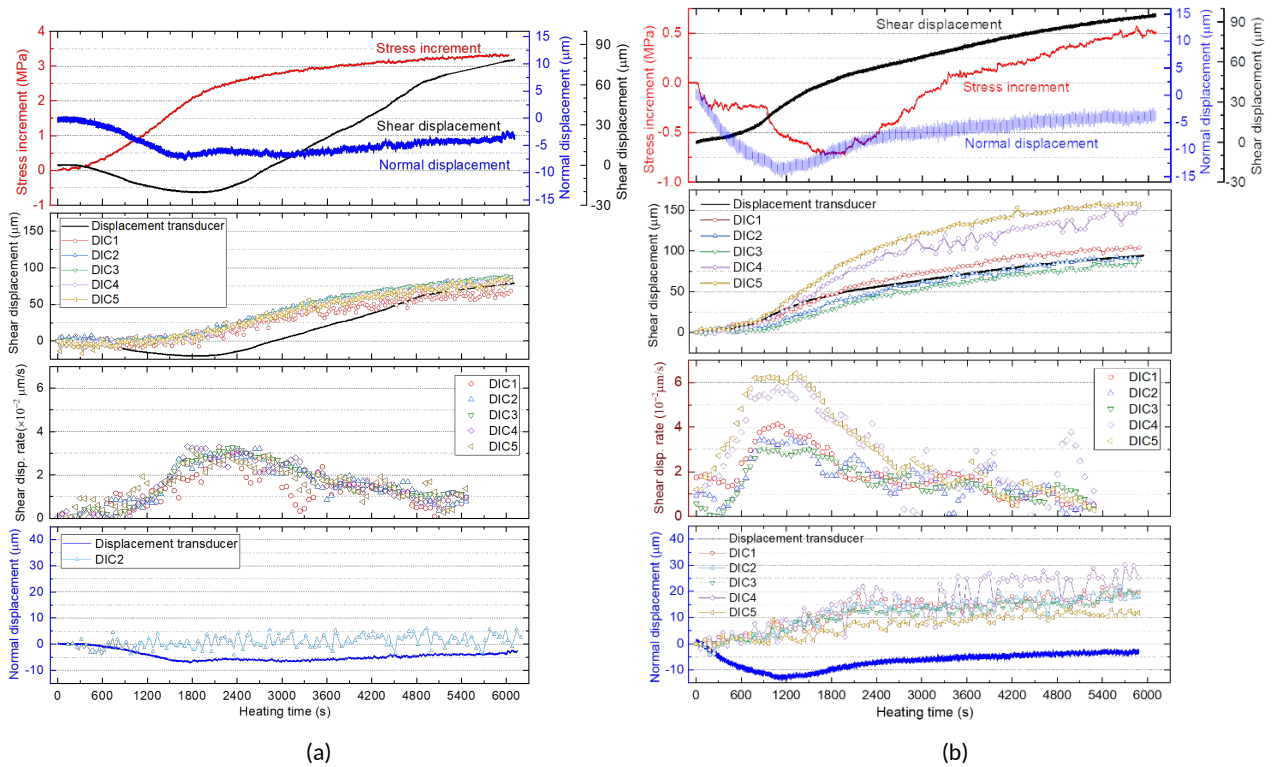


Figure 6.6: Evolutions of the maximum principal stress, as well as shear and normal displacements in (a) SF and (b) RF during the heating

Fracture surface asperity damages in RF after thermoshearing were observed, as shown in Fig. 6.8(a). There are more sheared-off particles from RF due to its larger fracture surface roughness and the higher stress level (~25 MPa of the maximum principal stress). We also observed a large number of rock chips (~20 mm in the long axis, Fig. 6.8a) occurred at the specimen edges. They are considered to correlate to the stress concentration induced off-fracture crack during the mechanical loading stage as the crack propagate to the specimen surfaces. The isolated zones in red shadows in Fig. 6.8(a) illustrate the slickensides at the surface contact where asperity damages occurred due to the shear. Surface contact ratio is around 10% in RF with a 3 mm offset. Asperities contact on the side facing the shear direction and a few irregularly shaped slickensides were formed. The damaged slickensides predominated where the local steep zones facing the shear direction, which are controlled by the fracture surface topographies and offset. The sheared-off asperities from the fracture surfaces are collected after the test was finished. Most of sheared-off particles are smaller than the measured mean grain size of 1 mm of Pocheon granite, which proves that the generated gouge materials were further cracked and crushed during thermoshearing.

The top and bottom surfaces in SF and RF were scanned again after thermoshearing tests, and the surface deformation in the RF is shown in Fig. 6.8(b) in terms of changes in asperity heights. The negative values correspond to asperity degradation (sheared-off), while the positive values refer to asperities having been ploughed but still adhered to the surface. An interesting result is that both increase and decrease in the asperity heights due to ploughing and degradation were observed. This behavior is closely correlated to fracture surface topography as well as the compressive strength of fracture walls, which need further investigation. In Table 6.2, the average JRC values on the top and bottom surfaces in SF and RF after thermoshearing tests were measured to be 0.63 and 12.66, respectively, showing insignificant changes. Thermoshearing process did not



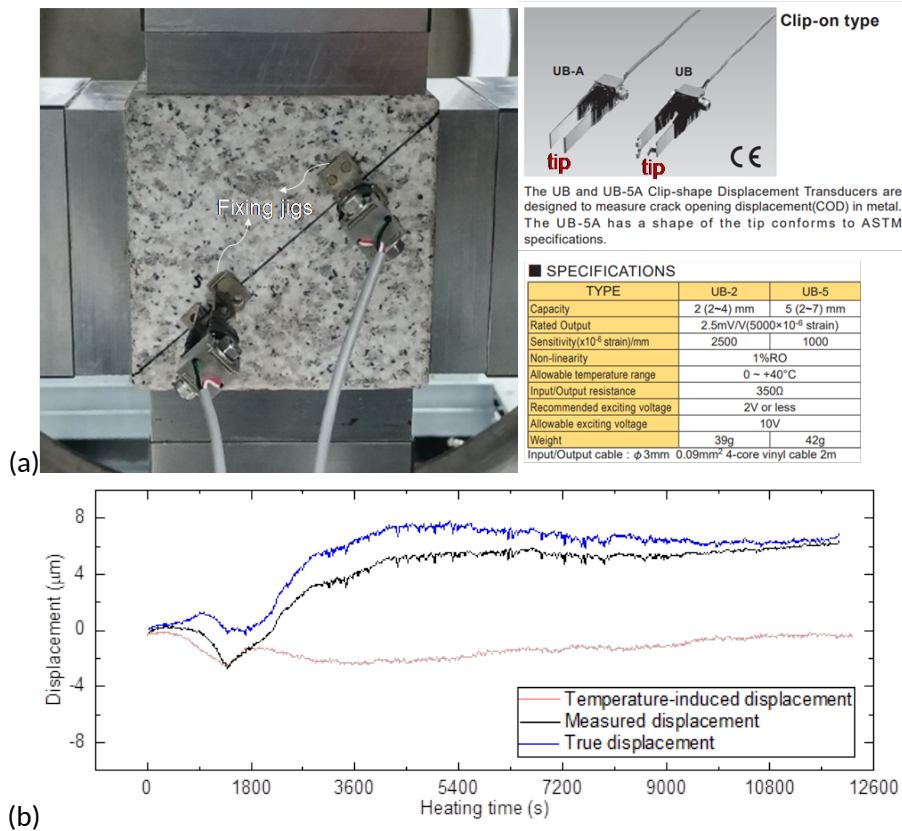


Figure 6.7: (a) Working principal of the clip-on displacement transducers used in this study ([Clip-on Displacement Transducer | Tokyo Measuring Instruments Laboratory Co., Ltd. \(tml.jp\)](#)), and (b) the influence of temperature on the displacement measurement by the transducer.

cause any significant influence on the surface roughness of fractures, which is probably due to very limited shear displacement  $\sim 0.1$  mm in both cases investigated in this study.

#### 6.4.5 Acoustic emission (AE) characteristics

The concurrent AE signals were monitored during the experiments, while the AE data needs further in-depth analysis to understand what do these signals mean, a few directly measured data including hit amplitude, cumulative absolute energy, and cumulative hit number are plotted in Fig. 6.9 to assist understanding the failure process.

At the very beginning of heating (before fracture slip occurs) on SF specimen, AE hits and increase in the cumulative absolute energy were observed, as shown in in Fig. 6.8(a). It is probably due to the thermal stress increment that can cause further closure of both preexisting microcracks and the sawcut fracture in the fractured granite specimen. AE hit number gradually increased, but some abrupt AE energy releases was observed intermittently, such as at 1,800 s. AE hits are much denser in the RF case than that in the SF case. This is reasonably attributed to one main reason: the SF fracture slipped at the very beginning, and the slip occurred at the limited (it was estimated to be under 10%) contact area of the unmated rough fracture RF. Asperity damage has occurred during the slip, and this is analyzed in more details in the next section. Increased rates of AE hit number and the energy release gradually decreased with heating duration in the RF case.

In general, AE characteristics behaved differently in the two cases. A few measurable AE parameters were

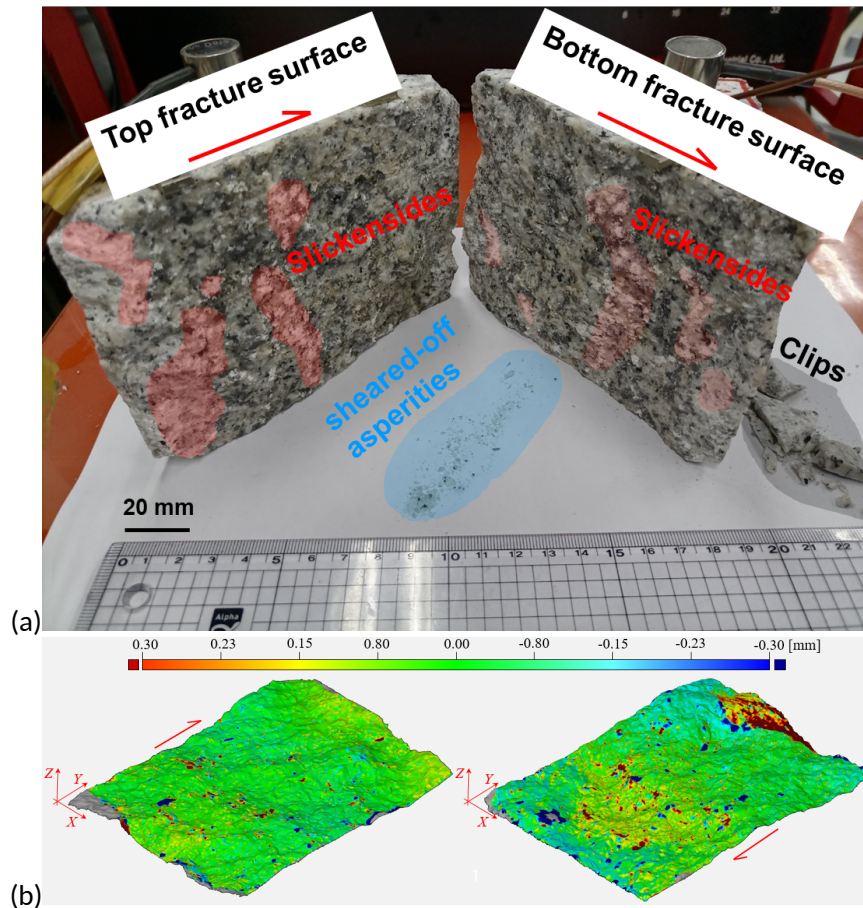


Figure 6.8: (a) Photographs of the sheared-off particles and slickensides on the fracture surfaces in SF; (b) the top and bottom surface deformation in RF after thermoshearing test. The red arrows show the shear direction of fractures.

compared in Table 6.4. The peak hit amplitude was 85 dB (3 counts) in the SF case, which is much lower than that the observation of 99 dB (73 counts) in the RF case. The cumulative absolute energies in SF and RF are 47 pJ and 9,907 pJ, and the cumulative hit numbers are 2,207 and 90,909, indicating that AE singles are much more intense in the RF case.

Table 6.4: Acoustic emission (AE) signals during thermoshearing, including cumulative energy, hit number, peak hit amplitude, and counts of peak hit amplitude

Sample	Cumulative Energy (pJ)	Hit number (count)	peak hit amplitude (dB)	Counts
SF	47	2216	85	3
RF	9907	90909	99	73

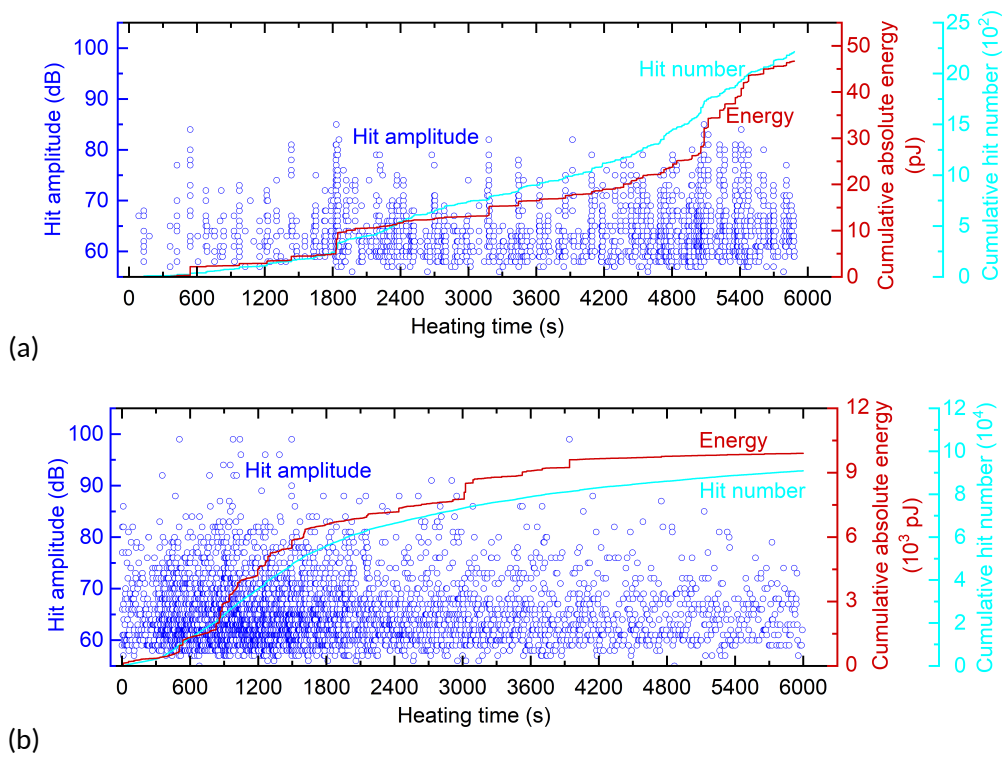


Figure 6.9: AE hit amplitude, cumulative absolute energy, and cumulative hit number (a) SF and (b) RF

## 6.5 Test case modelling of KICT thermoslip experiment

In this section, we compiled the results of the test case modelling of KICT thermoslip experiment. Table 6.5 lists the participating teams in the test case modelling, their adopted numerical codes, methods.

Team	Numerical code/method	Test case modelling
SSM/DynaFrax	PFC / DEM	Rough fracture (mated) case
LBNL	FLAC3D / FDM	Flat and rough fracture (mated+unmated) case
CNSC	COMSOL / FEM	Flat fracture (mated) case
KIGAM	3DEC / DEM	Flat and rough fracture (mated+unmated) case
KAERI	3DEC / DEM	Flat and rough fracture (mated) case

Table 6.5: Numerical codes and methods of the research teams adopted for the test case modelling of the KICT thermoslip experiment.

### 6.5.1 PFC modelling by the SSM/DynaFrax team

The SSM/DynaFrax team used PFC3D (Particle Flow Code 3D) for the test case modelling of the KICT experiment, focusing on the heat-induced slip of a mated rough fracture. Fracture surface data (in .stl file format) obtained from laser scanning was used to construct the rough fracture model. Upon the randomly packed particle assembly cube block (0.1 m x 0.1 m x 0.1 m), the fracture surface geometry was overlain. Then the particle contacts at the locations of fracture surface were converted to smooth joint contact model (Figure 6.10). The model parameters, including zero friction, zero strength, and normal and shear stiffness of 300 GPa/m and 50 GPa/m, were chosen based on reasonable estimates due to the absence of stiffness measurements for the tested rock fracture.

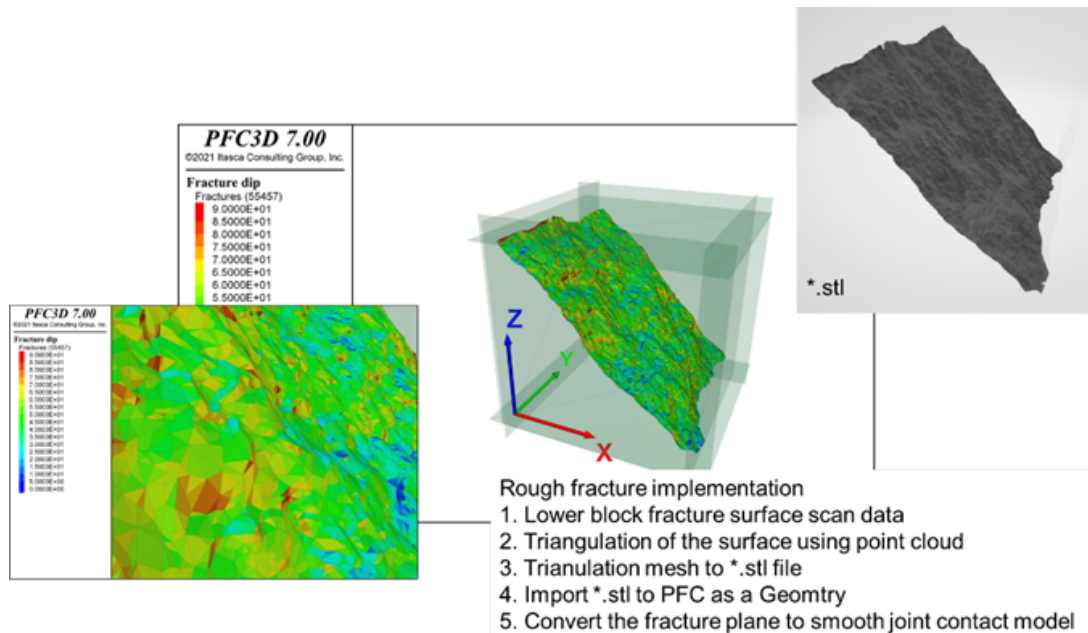


Figure 6.10: Generation of KICT test case model with a mated rough fracture surface (SSM/DynaFrax).

The thermal properties of the PFC3D model, especially thermal pipe resistance at particle contacts are important for the TM coupled modelling. The thermal pipe resistance should be therefore calibrated using an analytical solution of heat conduction. A back calculation method was developed in order to properly set the

thermal pipe resistance ( $\eta$ ) using the rock sample based thermal conductivity ( $K = 1.96 \text{ W/mK}$ ). Then, the calibrated model was tested to see if the actual thermal conductivity of the model ( $K = 1.98 \text{ W/mK}$ ) is close to the target thermal conductivity of the KICT Pocheon granite specimen ( $K = 1.96 \text{ W/mK}$ ), and a close match was confirmed. The experiment involved heating the top and bottom walls, and the temperature increase distribution displayed a biconical shape due to heat loss at the surrounding surfaces (Figure 6.11). The temperature evolutions at selected locations in the model were compared to the experiment measurements. Despite the rapid temperature increase in the early phase of the heating, the modelled temperatures were in fair agreement with the experiment recordings.

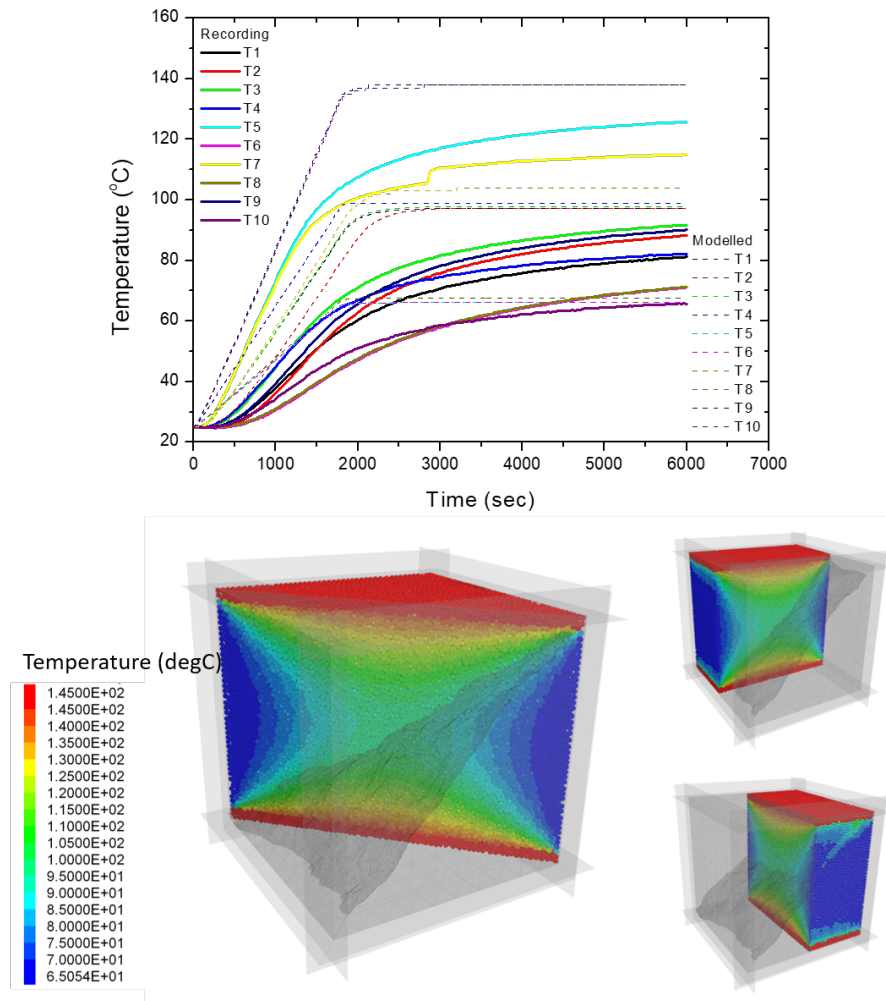


Figure 6.11: Comparison of temperature evolutions (model vs. experiment) and temperature distribution inside the PFC3D model showing biconical pattern (SSM/DynaFrax).

Normal and shear displacements of five groups of smooth joint contacts along the fracture edge were monitored and compared with the experimental measurements (DIC and Transducer). In case of normal displacement (Figure 6.12), the modelled normal displacement curves were in good agreement with the DIC measurements. Due to well mateness of the fracture surface, the initial decrease of the normal displacement (initial compaction of the fracture face) was not simulated in the PFC model. Similar to the DIC measurement, the modelled normal displacement curves showed gradual increase throughout the heating time. In case of shear displacement (Figure 6.12), the modelled shear displacement curves showed gradual increase, and the magni-

tudes of the shear displacement were in the range of the experimental data.

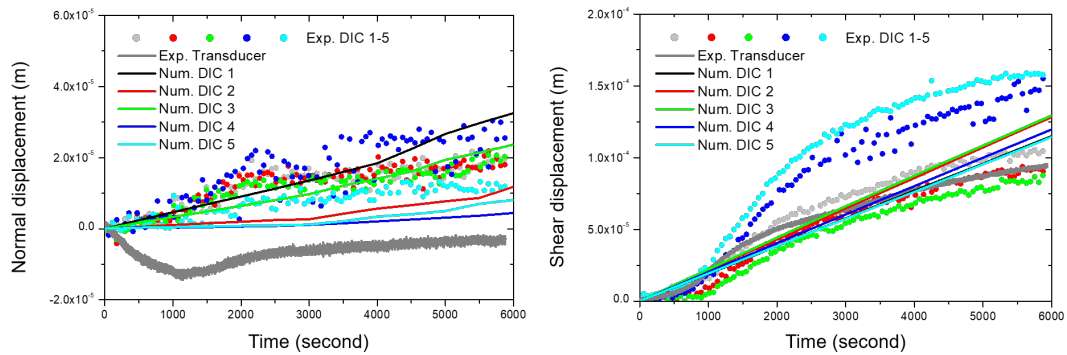


Figure 6.12: Comparison of fracture normal and shear displacement evolution between the rough fracture KICT experiment and PFC3D modelling (SSM/DynaFrax).

Displacement of the smooth joints that define the fracture surface were monitored as shown in Figure 6.13. The figure demonstrated that the locations where the normal displacement increases (compression, red colour) is highly correlated with the locations on the fracture surface with low dip angle. The figure also demonstrated that relatively larger shear displacement were concentrated at the location on the fracture surface with high dip angle. This suggests that as the rough surface fracture slips, distributions of normal and shear displacement are highly inhomogeneous.

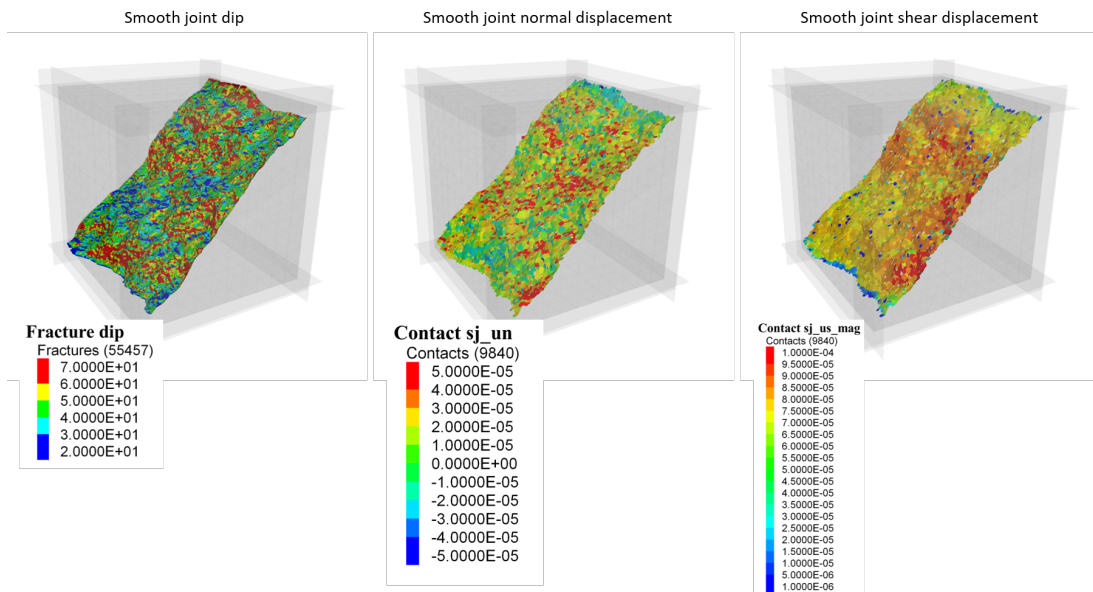


Figure 6.13: Distribution of smooth joint contact dip angle, normal displacement and shear displacement after applying heat (SSM/DynaFrax).

### 6.5.2 FLAC3D modelling by the LBNL team

The LBNL team presented the KICT test case modeling using FLAC3D for both flat planar and rough fracture cases. Convection boundary was applied to four sides (front, back, left and right) of the model to mimic heat exchange between the rock surface and the air. For top and bottom of the model, time-varying temperature

boundary condition was applied. The temperature distribution after 6000 seconds exhibited a biconical shape similar to the PFC3D results (Figure 6.14). Temperature evolution at selected locations in the model were compared with the experiment measurements as shown in Figure 6.15). The modelled temperature curves showed good matching with the experiment measurements.

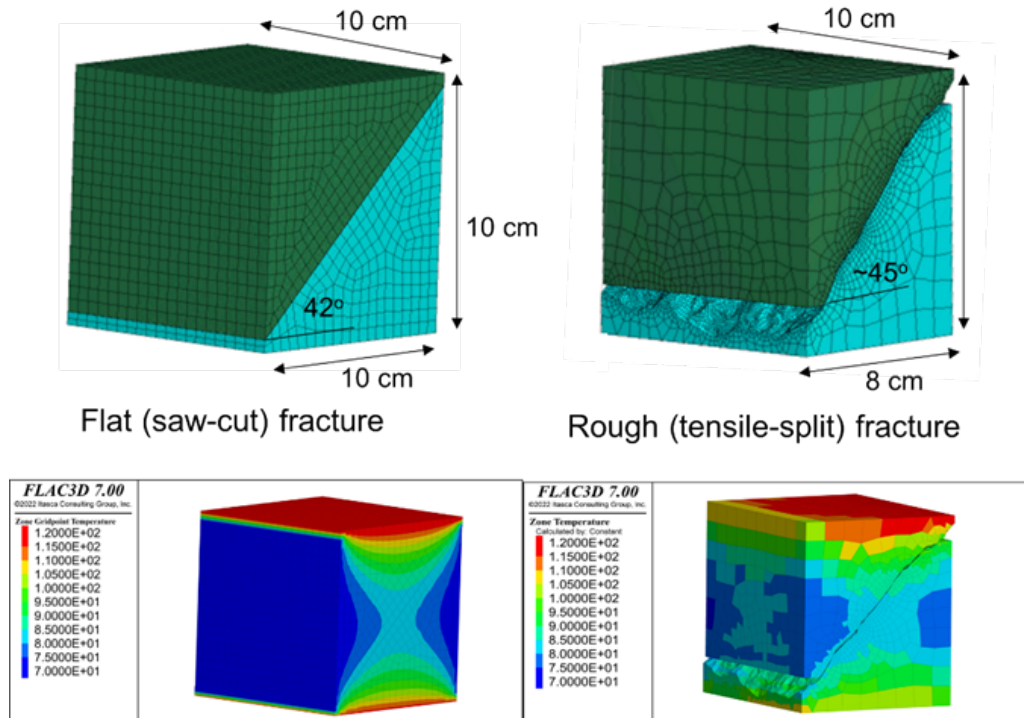


Figure 6.14: Generation of FLAC3D model for planar fracture and rough unmated fracture, and temperature distribution (LBNL).

The modelled normal displacement showed a fair agreement with the experimental data. However, the modelled shear displacement showed a deviation from the experimental monitoring (Figure 6.16). The displacement distribution on the fracture surface appeared homogeneous over the entire fracture surface in the case of the planar fracture. In contrast, for the rough surface fracture, the slip was more localized (Figure 6.17), aligning with the results obtained from PFC3D. Experimental results also indicated that shear was more localized in the case of a rough fracture, as evidenced by the rock debris observed after the experiment. This localization of shear was consistent with the asperity changes monitored by precise laser scanning on the fracture surface.

LBNL team conducted a sensitivity study on fracture properties and rock thermal expansion coefficients. Fracture friction coefficient was varied between 25, 30, and 40 degrees, and the thermal expansion coefficient was varied from  $6.5 \times 10^{-6}$  to  $13 \times 10^{-6}$  1/K. The results revealed that changing the interface friction and/or thermal expansion of the rock alone could not effectively match the experimental data. The study indicated that asperity damage might be a crucial factor in modelling thermal shearing. For effective modelling of asperity damage in a rough fracture, it was recommended to use DEM (Discrete Element Method) modelling, which enables local failure, specifically asperity damage, through fracture shearing.

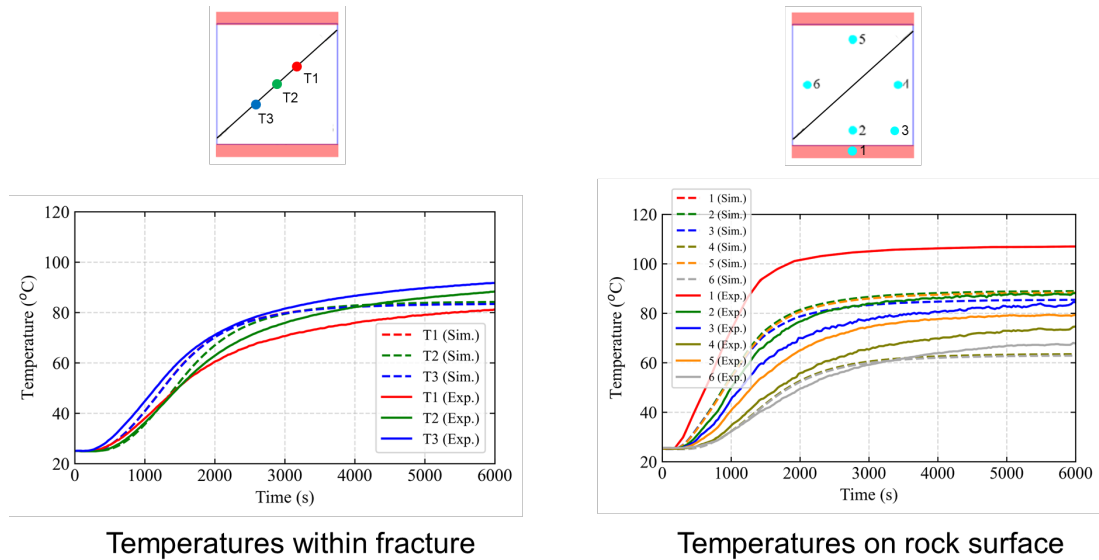


Figure 6.15: Temperature evolution comparison: (left) temperature within fracture, (right) temperature on rock/model surface (LBNL)

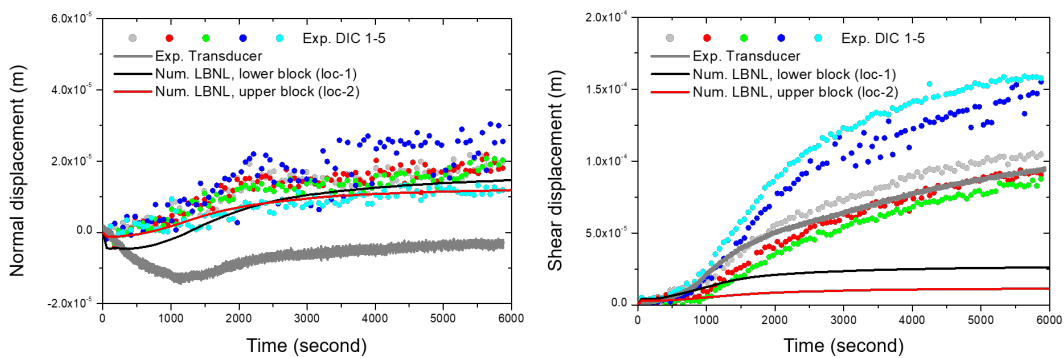


Figure 6.16: Comparison of fracture normal and shear displacement evolution between the rough fracture KICT experiment and FLAC3D modelling (LBNL).

### 6.5.3 COMSOL modelling by the CNSC team

CNSC team presented the KICT experiment modelling using COMSOL for both saw-cut fracture (SF) having a smooth surface and tensile-split fracture (TF) having a rough surface. Figure 6.18) shows the model setup.

The calculated temperature evolution was compared to the measured evolution at different thermometers positions on the front face of the specimen. The comparison showed reasonably good matching for all positions. The modelling results also compared well with the experimental values for shear displacements as measured by the transducer and camera recordings (DIC). For dilation, the modelled results also compared well with the DIC results. The measurement of dilation from the transducer was how unreliable, since it was reported that the sensor experienced thermal expansion during the heating process. Compared to SF specimen, shear displacement of TF is larger, mainly due to the larger asperity degradation. The fracture dilation was also larger due to the more pronounced roughness of the fracture surface (Figure 6.19).



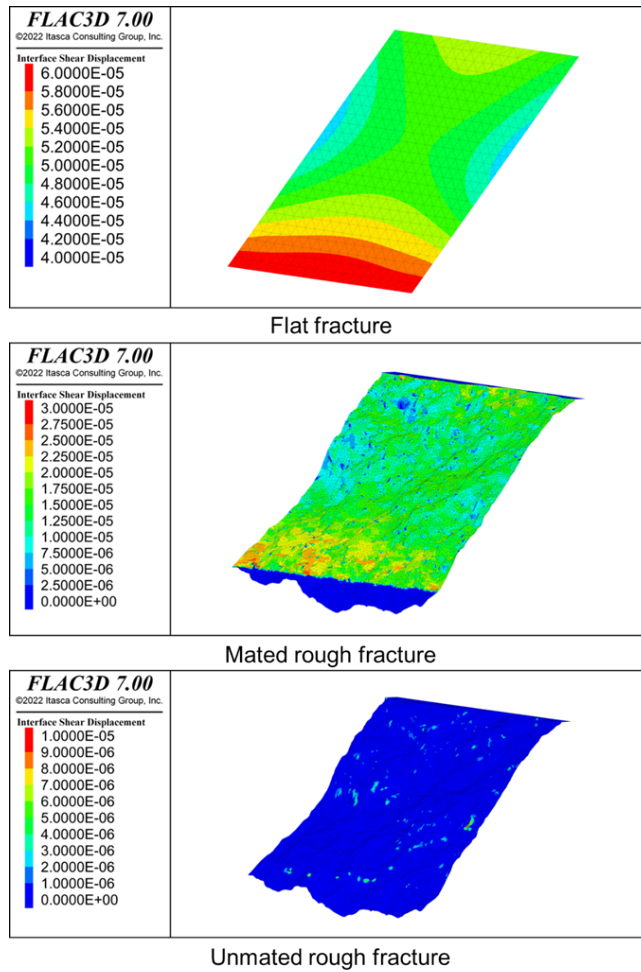


Figure 6.17: Distribution of shear displacement on fracture surface: flat fracture, mated rough fracture, and unmated rough fracture (LBNL).

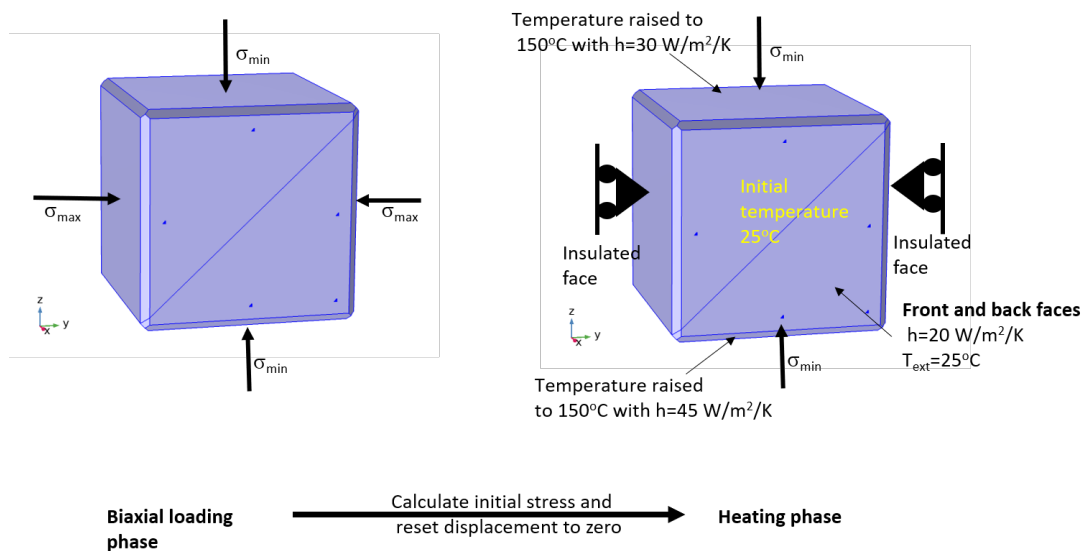


Figure 6.18: Model setup, initial and boundary conditions (CNSC).

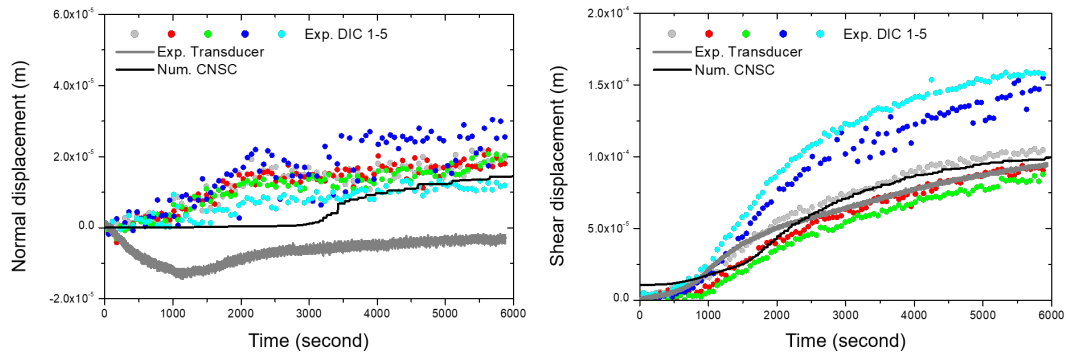


Figure 6.19: Comparison of fracture normal and shear displacement evolution between the rough fracture KICT experiment and COMSOL modelling (CNSC).

#### 6.5.4 3DEC modelling by the KIGAM team

KIGAM team presented KICT test case modelling using 3DEC for both planar surface saw-cut fracture and rough surface fractures. In the case of the saw-cut, planar fracture, a comparison between experimental and numerical results revealed a notable discrepancy (Figure 6.20). Specifically, shear dilation exhibited a delayed pattern compared to the numerical model. Regarding normal displacement, the experiment indicated more substantial fracture closure, suggesting potential differences in the normal stiffness of the fracture between the model and actual rock fractures.

KIGAM team developed a numerical model of implementing fracture roughness in 3DEC. Their simulations considered both mated and unmated cases (Figure 6.21). In the mated fracture scenario, the fracture contact area, following the application of boundary stress, covered nearly the entire fracture surface. In contrast, the unmated fracture case showed highly localized contacts (Figure 6.22).

The temperature evolution in the model closely matched the experimental measurements for both mated and unmated fracture cases (Figure 6.23). Analyzing the displacement monitoring data of the model, it was evident that mated fractures exhibited abrupt shear displacement and dilation. On the other hand, unmated fractures displayed small shear displacement and smooth dilation (Figure 6.24).

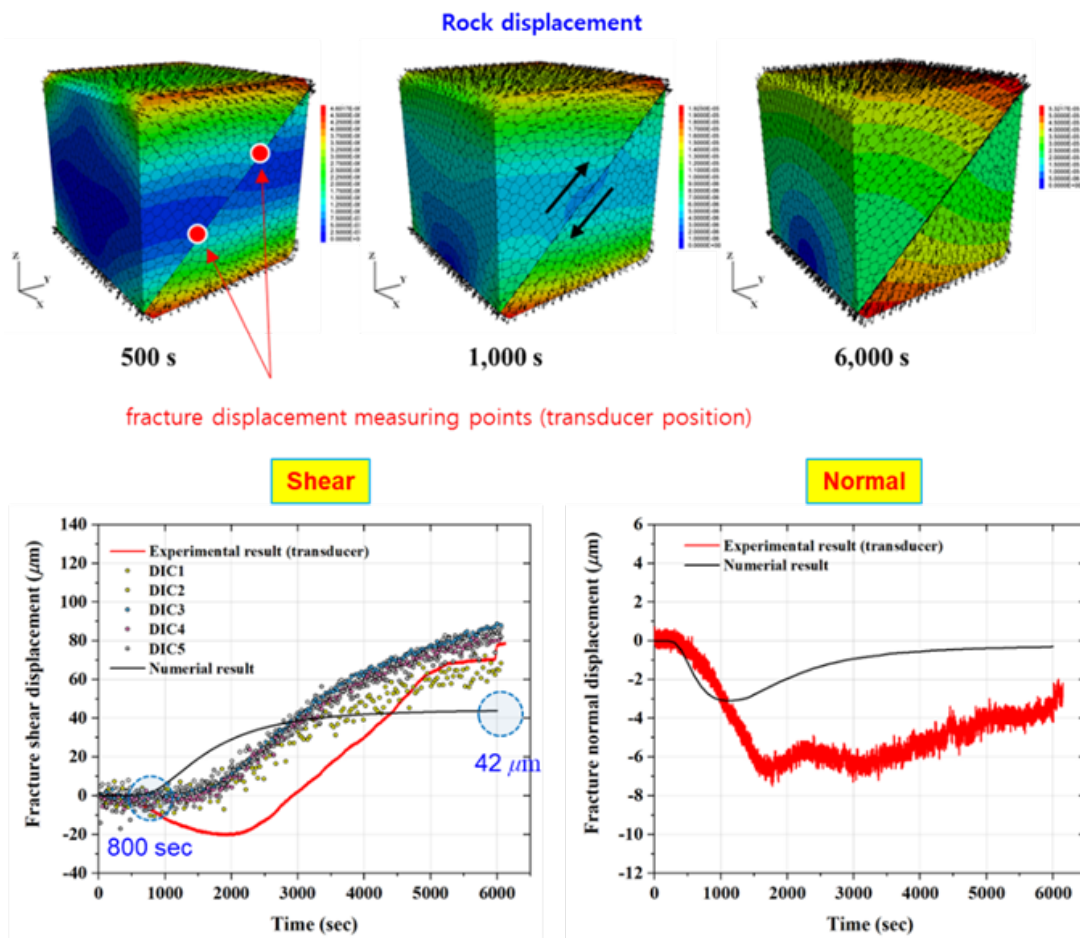


Figure 6.20: Distribution of rock displacement at different selected times, and evolution of shear and normal displacement and comparison with experiment monitoring.

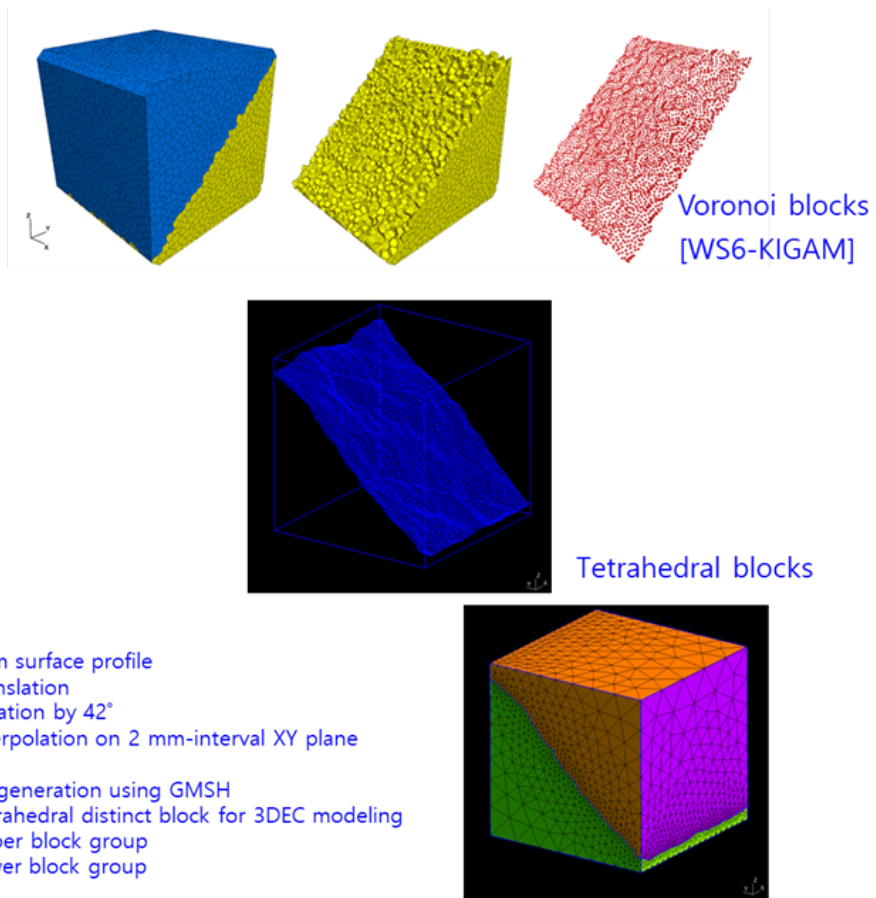


Figure 6.21: Generation of rough fracture surface model in 3DEC (KIGAM).

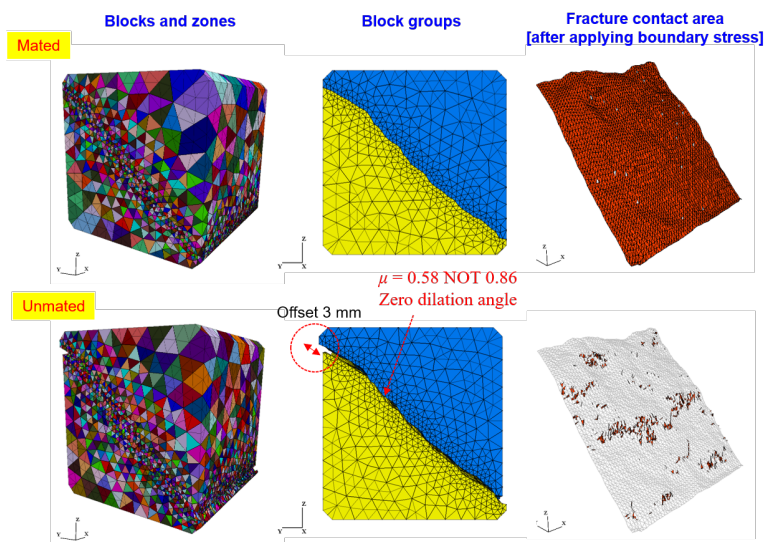


Figure 6.22: Generation of a mated and an unmated rough fracture model (KIGAM).

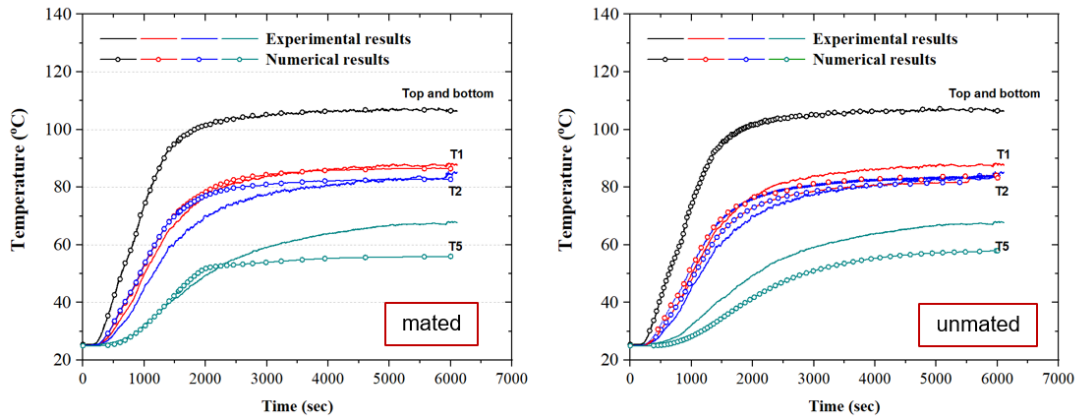


Figure 6.23: Comparison of experimental and numerical results of surface temperature evolution (KIGAM).

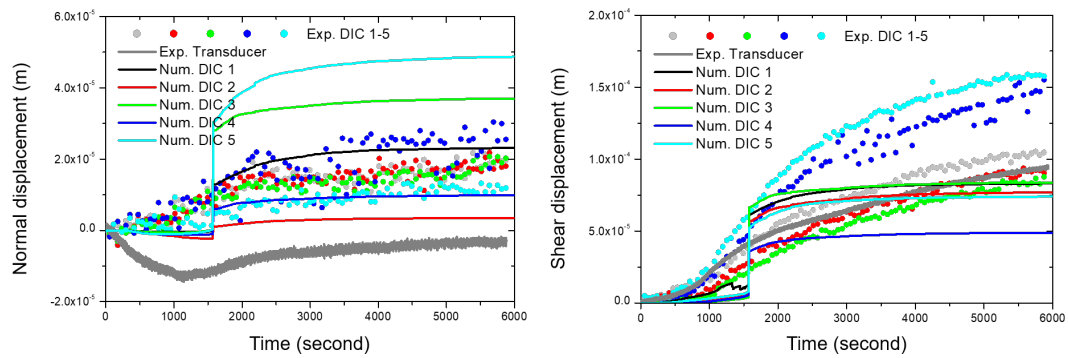


Figure 6.24: Comparison of mated fracture normal and shear displacement evolution between the rough fracture KICT experiment and 3DEC modelling (KIGAM).

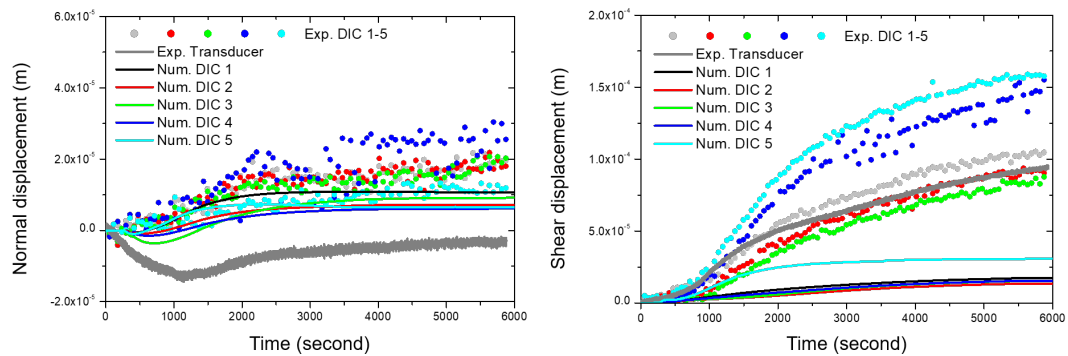


Figure 6.25: Comparison of unmated fracture normal and shear displacement evolution between the rough fracture KICT experiment and 3DEC modelling (KIGAM).

### 6.5.5 TOUGH-3DEC modelling by the KAERI team

The KAERI team utilised TOUGH-3DEC coupled model to perform the test case modeling, focusing on the rough fracture slip (Figure 6.26). A comparison of temperature evolution at selected locations in the model with experimental monitoring revealed noteworthy similarities (Figure 6.27). The temperature distribution within the model exhibited a biconical shape, aligning with the experimental observations. Examining the shear displacement distribution on the fracture plane, a heterogeneous pattern emerged, with concentrations predominantly at the bottom and upper parts of the plane.

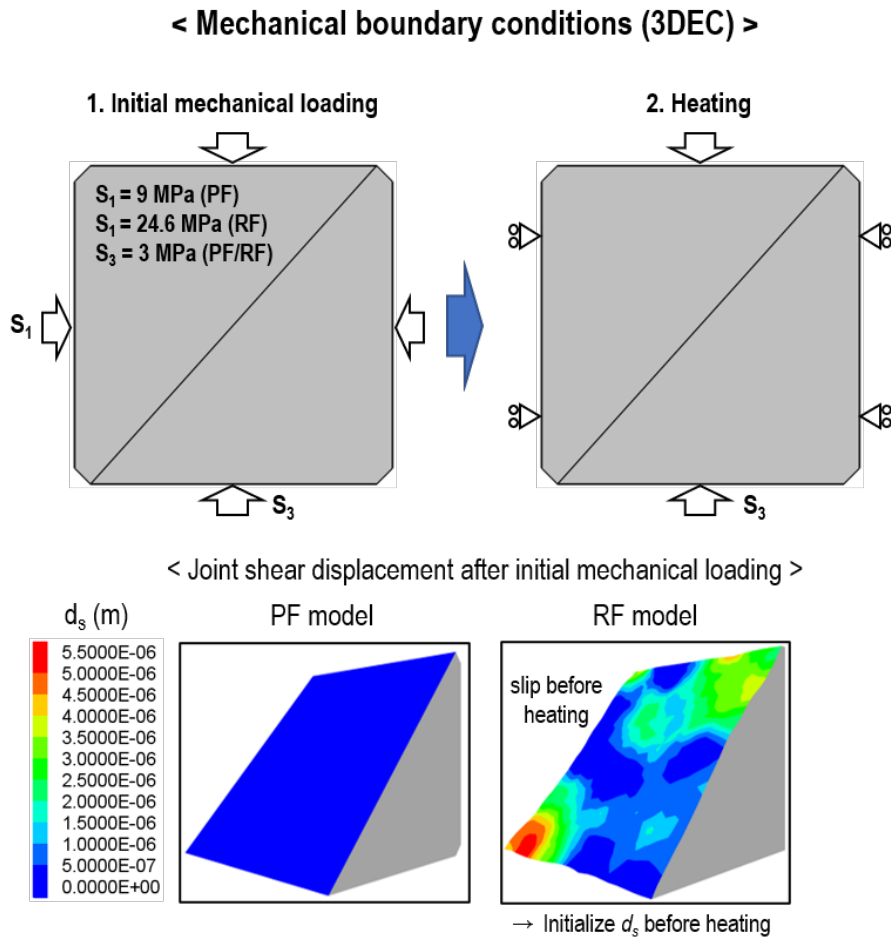


Figure 6.26: Planar and rough fracture models and slip distribution on the fracture surface before applying heat (KAERI).

Displacement monitoring at selected points demonstrated a moderate agreement with the experimental displacement monitoring results (Figure 6.28). For the planar fracture case, the modelled shear displacement curves showed early increase compared to the experiment measurements by the DIC and the displacement transducer. For the rough fracture case, the modelled shear displacement curves showed fair matching in the early time of the heating. However, at the end of the heating (6000 sec) the modelled displacements were lowered than the experiments by a factor of maximum 2.

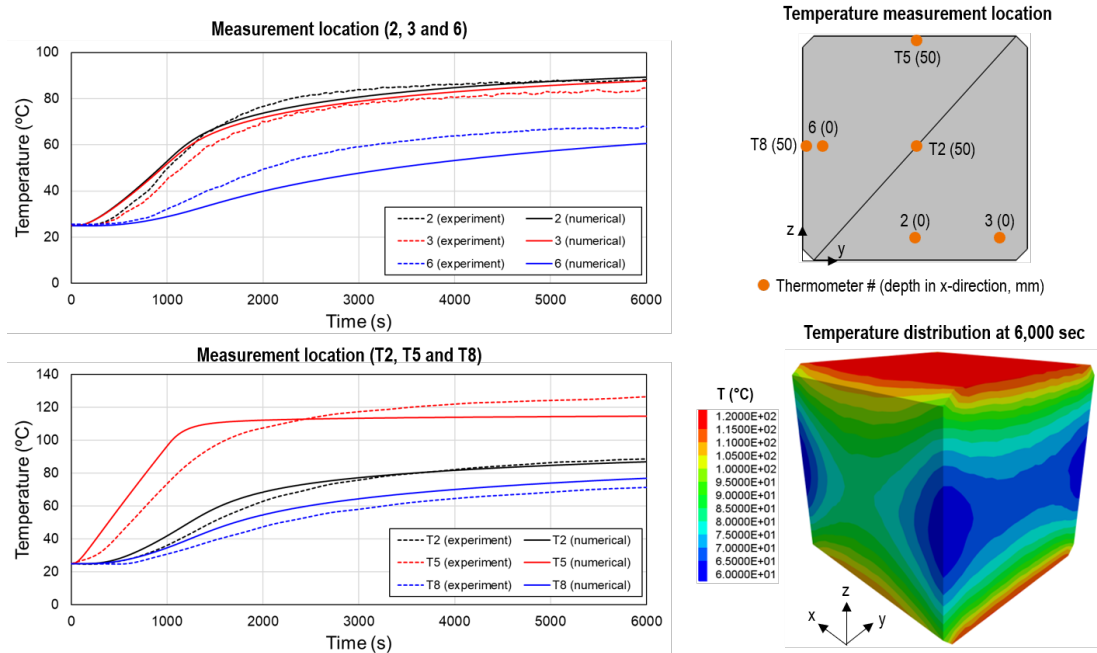


Figure 6.27: Evolution of temperature at selected locations in the model and its biconical distribution in the model.

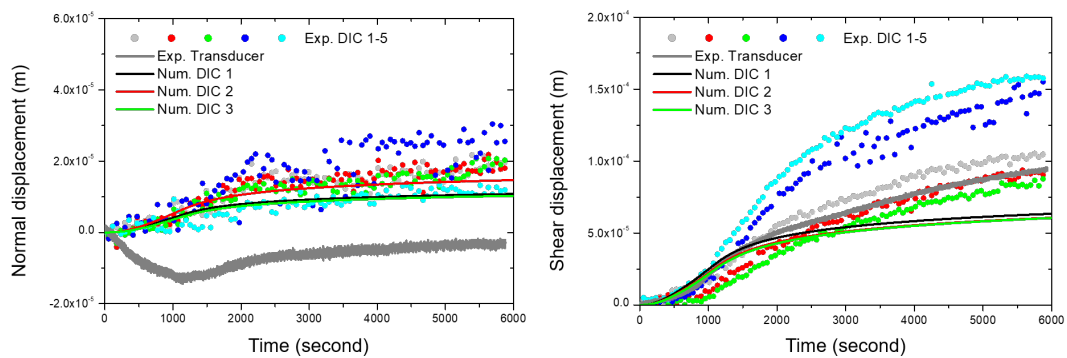


Figure 6.28: Comparison of fracture normal and shear displacement evolution between the rough fracture KICT experiment and TOUGH-3DEC modelling (KAERI).

### 6.5.6 Summary

The test case modeling of the KICT thermal slip experiment conducted by different teams using different numerical codes demonstrated the following key outcomes:

- 1) The temporal evolution of the temperature in all models showed good matching with the experimental measurements. This demonstrated that all different modelling codes well simulated the heat conduction process.
- 2) Despite the fair matching of the temperature evolution, the simulated fracture shear displacements (normal and shear) showed discrepancy to the experimental data and between the teams (Figure 6.29). The discrepancies might be attributed to several reasons, such as inconsistency in the fracture frictional properties between the rock fracture and/between the fracture models adopted in different numerical codes, high dependency on the fracture surface meshing resolution, enabled and disabled numerical representation of initially mated and initially unmated settings of the rock fracture faces, and the ability to simulate local asperity failure on the fracture surface. Among these possible reasons, the most important factor that should be considered

when modelling such system is the local asperity failure on the rough fracture surface. From the comparison of the teams' results, the DEM based model results are considered more appropriate for simulation of such processes.

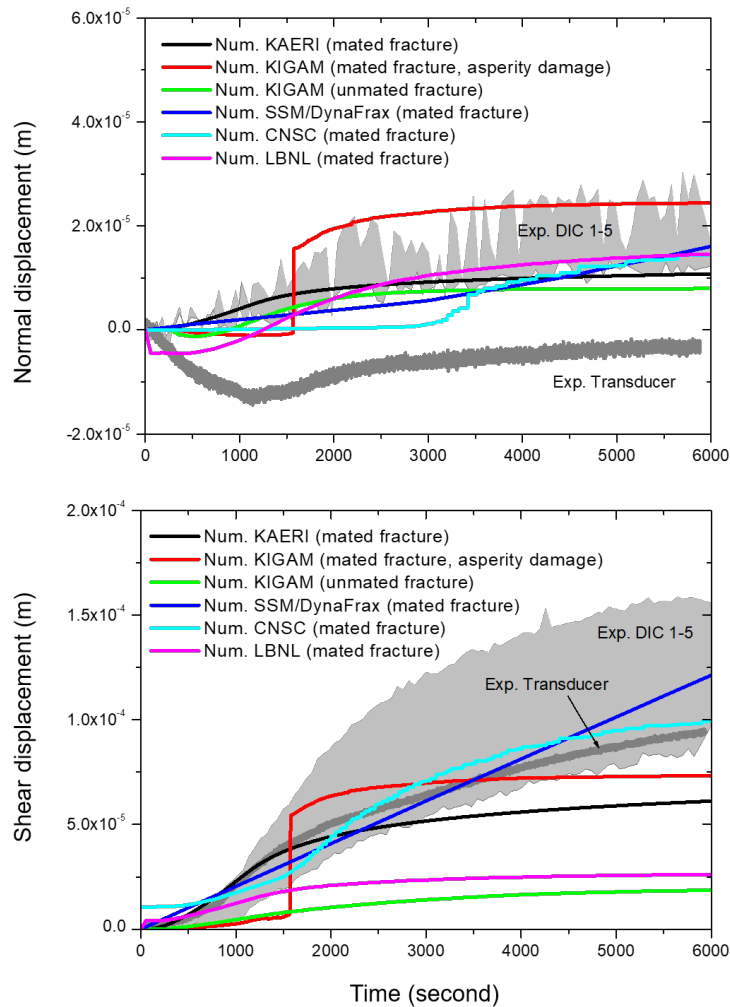


Figure 6.29: Comparison of fracture normal and shear displacement evolution between the rough fracture KICT thermal slip experiment and the modelling results from all teams.

## References

- Barton, N. and V. Choubey (1977). "The shear strength of rock joints in theory and practice". In: *Rock Mechanics Felsmechanik Mécanique des Roches* 10.1-2. Cited by: 2553, pp. 1 – 54. DOI: [10.1007/BF01261801](https://doi.org/10.1007/BF01261801). URL: <https://www.scopus.com/inward/record.uri?eid=2-s2.0-0017582564&doi=10.1007%2fBF01261801&partnerID=40&md5=23cdb214cee5b9b21e5f43dde1ccc93>.
- Kim, T. and S. Jeon (2019). "Experimental Study on Shear Behavior of a Rock Discontinuity Under Various Thermal, Hydraulic and Mechanical Conditions". In: *Rock Mechanics and Rock Engineering* 52.7. Cited by: 41, pp. 2207 – 2226. DOI: [10.1007/s00603-018-1723-7](https://doi.org/10.1007/s00603-018-1723-7). URL: <https://www.scopus.com/inward/record.uri?eid=2-s2.0-85059544121&doi=10.1007%2fs00603-018-1723-7&partnerID=40&md5=a72037a5aefae70a8d310ee5c19c444f>.
- Li, Y. and Y. Zhang (2015). "Quantitative estimation of joint roughness coefficient using statistical parameters". In: *International Journal of Rock Mechanics and Mining Sciences* 77. Cited by: 140; All Open Access, Hybrid Gold Open Access, pp. 27 – 35. DOI: [10.1016/j.ijrmms.2015.03.016](https://doi.org/10.1016/j.ijrmms.2015.03.016). URL: <https://www.scopus.com/inward/record.uri?eid=2-s2.0-84927618812&doi=10.1016%2fj.ijrmms.2015.03.016&partnerID=40&md5=e1157af29e361b36361eebe2aee3306f>.



- Sun, C. et al. (2021a). "Loading rate-dependent frictional resistance of a sawcut fracture in granite for prediction of thermoshearing". In: *IOP Conference Series: Earth and Environmental Science* 861.4. DOI: [10.1088/1755-1315/861/4/042125](https://doi.org/10.1088/1755-1315/861/4/042125). URL: <https://www.scopus.com/inward/record.uri?eid=2-s2.0-85118843999&doi=10.1088%2f1755-1315%2f861%2f4%2f042125&partnerID=40&md5=04f224da0c681d6d7dc9fd78be65bfe9>.
- Sun, C. et al. (2021b). "Thermally induced slip of a single sawcut granite fracture under biaxial loading". In: *Geomechanics and Geophysics for Geo-Energy and Geo-Resources* 7.4. Cited by: 4. DOI: [10.1007/s40948-021-00293-y](https://doi.org/10.1007/s40948-021-00293-y). URL: <https://www.scopus.com/inward/record.uri?eid=2-s2.0-85117579821&doi=10.1007%2fs40948-021-00293-y&partnerID=40&md5=8db43fd9e65668ab9345c29bcf06011f>.
- Sun, C. et al. (2023). "Thermally induced shear reactivation of critically-stressed smooth and rough granite fractures". In: *IOP Conference Series: Earth and Environmental Science* 1124.1. DOI: [10.1088/1755-1315/1124/1/012119](https://doi.org/10.1088/1755-1315/1124/1/012119). URL: <https://www.scopus.com/inward/record.uri?eid=2-s2.0-85146558465&doi=10.1088%2f1755-1315%2f1124%2f1%2f012119&partnerID=40&md5=b0a8c674baeb8d07dfe817c5c220b3f0>.
- Yoon, J.S., A. Zang, and O. Stephansson (2014). "Numerical investigation on optimized stimulation of intact and naturally fractured deep geothermal reservoirs using hydro-mechanical coupled discrete particles joints model". In: *Geothermics* 52, pp. 165–184.

## 7 Outlook to SAFENET-2: THM Fracture Mechanics - From Lab to Field Scale

### Outline Description

Proponents: Helmholtz Centre for Environmental Research, University of Edinburgh, DynaFrax

Objectives of the task: To better understand fracture nucleation and evolution processes in crystalline rocks, with applications in nuclear waste management, but also in geothermal reservoir engineering. To improve models of these geosystems, with implications for performance and safety assessment, but also for reservoir optimisation. As a continuation of SAFENET with a previous focus on benchmarking fracture models and experimental laboratory analyses (see D2023 Task G references below), SAFENET-2 is dedicated to model extension and validation from laboratory to field scale.

Rock types and engineered materials to be considered: The focus is on crystalline rock systems at the Teaching and Research Mine URL Reiche Zeche (Freiberg granite, Germany). At a later stage, the activities will be extended to the newly planned geothermal URL (GeoLaB) in hydrothermally altered crystalline rocks (Odenwald or Black Forest in the Upper Rhine Valley). Construction of GeoLaB will start in 2025. Therefore, core samples for laboratory experiments will be available in the later phase of D2027.

Principal experimental data: The experimental basis comes from both laboratory and field scale: Laboratory experiments (GREAT cell, polyaxial THM cell), field experiments (hydraulic stimulation and seismic monitoring) at the Teaching and Research Mine "Reiche Zeche" (STIMTEC experiments, Boese et al., 2021; Boese et al., 2022; Martínez, Alegría, and Renner, 2021).

Data scale and duration: Extensive data sets from the GREAT cell experiments are available for various rock samples (Fraser-Harris et al., 2023). New experimental data from the STIMTEC experiments at the Reiche Zeche research mine (Boese et al., 2021; Boese et al., 2022; Martínez, Alegría, and Renner, 2021) have recently been published. A database for model upscaling from laboratory to field scale for crystalline rock systems is available (we are in direct contact with STIMTEC team).

Relevance to radioactive waste disposal safety cases (Performance and Safety Assessment): The laboratory and field experiments have a direct impact on PA/SA and are essential for the assessment of the barrier integrity of crystalline host rocks and therefore support the design, implementation and evaluation of repository systems in crystalline rocks. Fracture evolution can provide pathways from the repository into the geosystem and can influence radionuclide transport in the far field. Understanding and modelling fracture initiation and evolution processes is of paramount importance for PA/SA.

Applicability to other disposal concepts/rock types/engineered materials: The knowledge gained from understanding fracture processes and mechanisms is relevant to all repository concepts (brittle and ductile rocks). In addition, SAFENET-2 will have added value for other geo-energy applications in crystalline geosystems (see below).

Special and/or novel features: SAFENET-2 is dedicated to the upscaling of fracture models from laboratory to field scale. The concept is based on unique data sets for both laboratory and field scale. A key research question is: Can we characterise and predict THM processes for barrier AND reservoir systems using a single fracture mechanics model approach?

Relevance to non-radioactive waste management applications: Engineered Geothermal Systems Funded Task

Leader: Partially. Task Leaders would require partial DECOVALEX funding.

### Summary of Proposed Work

Description and Justification of the Technical Focus Based on prior works in D2023 the fracture task aims at characterization and prediction of fracture processes from lab to field scales in D2027. The potential field sites both are located in crystalline rocks, the URL Reiche Zeche (Freiberg, Germany) representing barrier type geosystems. Whereas new GeoLaB site will be established in hydrothermally altered rock with higher permeabilities and therefore seen as a reservoir type rock (e.g. for enhanced geothermal applications).

Laboratory experiments (GREAT THM cells) with crystalline rocks will be continued in order to complement the data basis for characterizing THM fracture evolution processes at the lab scale. With the GREAT cell facilities of Edinburgh and now also Göttingen unique facilities for experimental work mimicking polyaxial HM conditions and related fracture processes will be available to DECOVALEX 2027 teams. Various data sets are available, e.g. fracture evolution in Bench Scale Analogue Shale (PMMA) samples with detailed strain measurements (Mouli-Castillo et al. 2022, submitted) and strain data for multiple fracture propagation in various crystalline granite samples (including Freiberg gneis). The University of Göttingen is developing a larger diameter GREAT cell and will undertake as commissioning fracture experiments in Freiberg gneis. KICT plans an advanced experiment of thermally induced slip of natural rock joints representing a small mock-up of KBS-3V disposal system. The thermally induced fracture slip and propagation under true triaxial stress state will be characterized by acoustic emission monitoring, X-ray CT scanning and high-resolution laser scanning. The objective of the experiment is to understand how a brittle rock fracture would develop, especially at disposal hole near field when the fracture is subjected both to a shear loading and a concentrated heat loading.

The experimental basis at field scale is provided by the STIMTEC experiment in the URL Reiche Zeche where stimulation tests with periodic pumping tests and high-resolution seismic monitoring have been conducted (Boese et al., 2021; Boese et al., 2022; Martínez, Alegría, and Renner, 2021; Schmidt, Steeb, and Renner, 2021). Together with the laboratory experimental data, the STIMTEC experiment will provide a basis for upscaling fracture models from lab to field scale concerning hydro-mechanically induced fracture processes.

SAFENET-2 includes a methodological step. Here, THM fracture mechanics numerical approaches (e.g. phase field methods, discrete element methods, ...) will be further developed. We will investigate the potential of AI (machine learning) methods for building surrogates of complex THM fracture mechanics models. These surrogates can be trained from full complexity THM models. Furthermore, we will introduce new benchmarking techniques that promote interactivity in collaboration by using web-based Jupyter notebooks for online benchmarking.

### Proposed Work Programme

Figure 7.1 is providing a sketch of the structured work program. An incremental approach to the development of this task is proposed based on increasing levels of complexity from lab to field scale.

- Step 1: Simulation of lab scale HM fracture propagation experiments (3D bench scale hydraulic fracture under polyaxial stress experiments with fibre optic strain measurements)

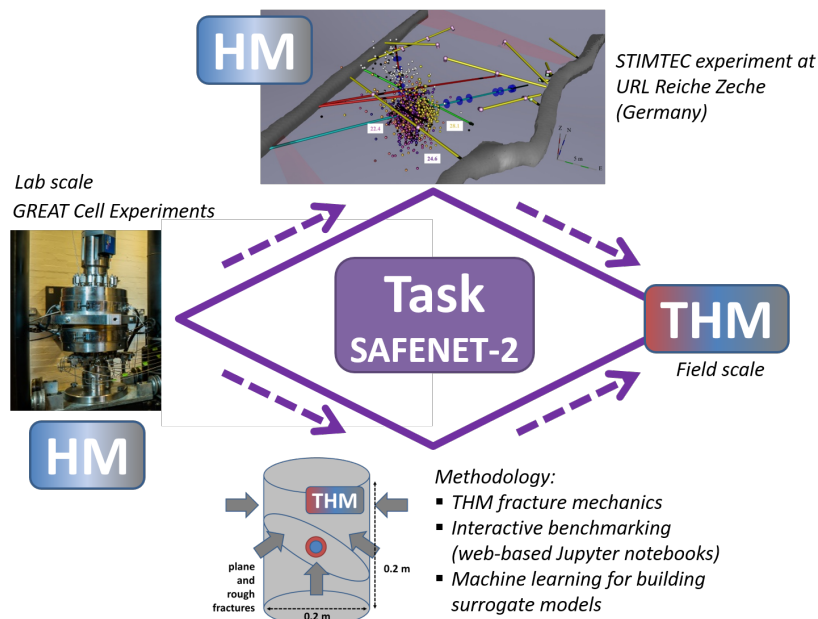


Figure 7.1: Concept and routes of SAFENET-2

- Step 2: Simulation of field scale HM and coupled seismicity (fluid injection into rock mass and measurement of seismicity, URL Reiche Zeche)
- Step 3: Methodology, computer and data science: THM fracture mechanics (including the analysis of KICT lab experiments), interactive and collaborative benchmarking, machine learning
- Step 4: Synthesising the knowledge concerning upscaling of fracture models from lab to field scale for PA/SA of waste disposal concepts in crystalline host rocks. Knowledge transfer to related geenergy applications (i.e. enhanced geothermal systems in crystalline reservoir rocks).

## References

- Boese, Carolin M. et al. (2022). "Seismic monitoring of the STIMTEC hydraulic stimulation experiment in anisotropic metamorphic gneiss". In: *Solid Earth* 13.2. Cited by: 7; All Open Access, Gold Open Access, Green Open Access, pp. 323 – 346. DOI: [10.5194/se-13-323-2022](https://doi.org/10.5194/se-13-323-2022). URL: <https://www.scopus.com/inward/record.uri?eid=2-s2.0-85125101012&doi=10.5194%2fse-13-323-2022&partnerID=40&md5=28d4b373a2b0e0b33d8302c080023655>.
- Boese, C.M. et al. (2021). "AE-type hydrophone performance during the STIMTEC and STIMTEC-X hydraulic stimulation campaigns at Reiche Zeche Mine, Germany". In: *55th U.S. Rock Mechanics / Geomechanics Symposium 2021* 4. Cited by: 0. URL: <https://www.scopus.com/inward/record.uri?eid=2-s2.0-85123058188&partnerID=40&md5=5b69c9badb6dbcb7bc06ff8f6bec68cc>.
- Fraser-Harris, A.P. et al. (2023). "The influence of intermediate principal stress magnitude and orientation on fracture fluid flow characteristics of a fractured crystalline rock". In: in preparation.
- Martínez, Jiménez, Victoria Alegría, and Jörg Renner (2021). "Injectivity Enhancement of Freiberg Gneiss by Hydraulic Stimulation". In: *55th U.S. Rock Mechanics / Geomechanics Symposium 2021* 5. Cited by: 3. URL: <https://www.scopus.com/inward/record.uri?eid=2-s2.0-85123363421&partnerID=40&md5=3cd293a2aad50f8c1d89b79d7559ef7>.
- Schmidt, Patrick, Holger Steeb, and Jörg Renner (2021). "Investigations into the opening of fractures during hydraulic testing using a hybrid-dimensional flow formulation". In: *Environmental Earth Sciences* 80.15. Cited by: 5; All Open Access, Green Open Access, Hybrid Gold Open Access. DOI: [10.1007/s12665-021-09767-4](https://doi.org/10.1007/s12665-021-09767-4). URL: <https://www.scopus.com/inward/record.uri?eid=2-s2.0-85111490331&doi=10.1007%2fs12665-021-09767-4&partnerID=40&md5=10eb6bc1b001e0d201a73c9ae3845d51>.

## 8 Planned and Completed Publications

This section gives the planned and completed publications under this task, correct at the time of writing.

### Published

C.I. McDermott et al. (2018). “New Experimental Equipment Recreating Geo-Reservoir Conditions in Large, Fractured, Porous Samples to Investigate Coupled Thermal, Hydraulic and Polyaxial Stress Processes”. In: *Scientific Reports* 8.1. Cited by: 6; All Open Access, Gold Open Access, Green Open Access. DOI: [10.1038/s41598-018-32753-z](https://doi.org/10.1038/s41598-018-32753-z). URL: <https://www.scopus.com/inward/record.uri?eid=2-s2.0-85054070649&doi=10.1038%2fs41598-018-32753-z&partnerID=40&md5=dbe9cf549a76065fee706766d0597676>

A.P. Fraser-Harris et al. (2020). “Experimental Investigation of Hydraulic Fracturing and Stress Sensitivity of Fracture Permeability Under Changing Polyaxial Stress Conditions”. In: *Journal of Geophysical Research: Solid Earth* 125.12. Cited by: 10; All Open Access, Green Open Access. DOI: [10.1029/2020JB020044](https://doi.org/10.1029/2020JB020044). URL: <https://www.scopus.com/inward/record.uri?eid=2-s2.0-85098225724&doi=10.1029%2f2020JB020044&partnerID=40&md5=705e37470080c4eaa99398d33dfa22d>

Thomas Frühwirt, Daniel Pötschke, and Heinz Konietzky (2021). “Simulation of direct shear tests using a forces on fracture surfaces (FFS) approach”. In: *Environmental Earth Sciences* 80.8. Cited by: 5; All Open Access, Hybrid Gold Open Access. DOI: [10.1007/s12665-021-09606-6](https://doi.org/10.1007/s12665-021-09606-6). URL: <https://www.scopus.com/inward/record.uri?eid=2-s2.0-85104006276&doi=10.1007%2fs12665-021-09606-6&partnerID=40&md5=38352a2edca39a24d14e93ed56c3fad>

Teklu Hadgu and Yifeng Wang (2022). “Modeling of Fractured Rock Under Stress for Nuclear Waste Disposal Applications”. In: 2022 International High Level Radioactive Waste Management Conference. SAND2022-8357 C. Phoenix, Arizona

Mostafa Mollaali et al. (2023). “Comparative verification of hydro-mechanical fracture behavior: Task G of international research project DECOVALEX-2023”. In: *International Journal of Rock Mechanics and Mining Sciences* 170. DOI: [10.1016/j.ijrmms.2023.105530](https://doi.org/10.1016/j.ijrmms.2023.105530). URL: <https://www.scopus.com/inward/record.uri?eid=2-s2.0-85166325287&doi=10.1016%2fj.ijrmms.2023.105530&partnerID=40&md5=3a43688518353d27ce8a084a093cb90c>

Olaf Kolditz et al. (2023). “Digitalisation for nuclear waste management: predisposal and disposal”. In: *Environmental Earth Sciences* 82.1. Cited by: 2; All Open Access, Green Open Access, Hybrid Gold Open Access. DOI: [10.1007/s12665-022-10675-4](https://doi.org/10.1007/s12665-022-10675-4). URL: <https://www.scopus.com/inward/record.uri?eid=2-s2.0-85145415563&doi=10.1007%2fs12665-022-10675-4&partnerID=40&md5=b25a80bca286c383d6353e25cfa85002>

Thanh Son Nguyen et al. (2024). “Modelling the thermo-mechanical behaviour of a rock joint”. In: *Geomechanics for Energy and the Environment* 37. Cited by: 0. DOI: [10.1016/j.gete.2023.100520](https://doi.org/10.1016/j.gete.2023.100520). URL: <https://www.scopus.com/inward/record.uri?eid=2-s2.0-85178640689&doi=10.1016%2fj.gete.2023.100520&partnerID=40&md5=7e0c9fd5c407caa13438240e8cf484a0>

## Submitted

J. Mouli-Castillo., Jackie Kendrick, Alexander Lightbody, Andrew Fraser-Harris, Katriona Edlmann, Christopher Ian McDermott, Zoe Kai Shipton (2022): Reducing Breakdown Pressure and Recording Dynamic Fracture Growth Applying Cyclical Hydraulic Pressure Pulses in Bench Scale Analogue Shale (PMMA) Samples. Geomechanics and Geophysics for Geo-Energy and Geo-Resources (submitted)

J.W. Park, C.H. Park, L. Zhuang, J.S. Yoon, O. Kolditz, C.I. McDermott, E.S. Park, C. Lee (2024): Grain-based distinct element modelling of thermally induced slip of critically stressed rock fracture (submitted to Geomechanics for Energy and the Environment - GETE)

O Kolditz, CI McDermott, JS Yoon, Mostafa Mollaali, Wenqing Wang, Mengsu Hu, Tsubasa Sasaki, Jonny Rutqvist, Jens Birkholzer, Jung-Wook Park, Chan-Hee Park, Hejuan Liu, Peng-Zhi Pan, Thomas Nagel, Son Nguyen, Saeha Kwon, Changsoo Lee, Kwang-Il Kim, Alex Bond, Teklu Hadgu, Yifeng Wang, Li Zhuang, Keita Yoshioka, Gonçalo Benitez Cunha, Andrew Fraser-Harris (2024): DECOVALEX Task G Synthesis Paper: A systematic model- and experimental approach to hydro-mechanical and thermo-mechanical fracture processes in crystalline rocks (submitted to Geomechanics for Energy and the Environment - GETE)

## In preparation

A. Fraser-Harris, C. McDermott, A. Lightbody, K. Edlmann, M. Sauter (2023): The influence of intermediate principal stress magnitude and orientation on fracture fluid flow characteristics of a fractured crystalline rock (in preparation for Geomechanics for Energy and the Environment - GETE)

J.S. Yoon, M. Hu, J. Rutqvist, O. Kolditz, C. McDermott, N. Chittenden, A. Bond, J.W. Park, C.H. Park, H. Liu, Z. Wang, J. Zhou (2024): Numerical analyses and benchmark comparison of rock fracture deformation subjected to mechanical shear loading (in preparation for Geomechanics for Energy and the Environment - GETE)

M. Hu, J.S. Yoon, T. Sasaki, H. Liu, Z. Wang, J.W. Park, C.H. Park, J. Rutqvist, O. Kolditz, J. Birkholzer (2024): Benchmark Study of A New Simplified DFN Model for Shearing of Intersecting Fractures and Faults (in preparation for Geomechanics for Energy and the Environment - GETE)

A. Strader, J. Zhou, L. Zhuang, J.S. Yoon, C.H. Pettersson (2024): Thermo-mechanical coupled bonded particle modelling of slip evolution of an inclined rough rock fracture under thermal loading (in preparation for Geomechanics for Energy and the Environment - GETE)

## 9 Acknowledgements

DECOVALEX is an international research project comprising participants from industry, government and academia, focusing on development of understanding, models and codes in complex coupled problems in sub-surface geological and engineering applications; DECOVALEX-2023 is the current phase of the project. The authors appreciate and thank the DECOVALEX-2023 Funding Organisations Andra, BASE, BGE, BGR, CAS, CNSC, COVRA, US DOE, ENRESA, ENSI, JAEA, KAERI, NWMO, NWS, SÚRAO, SSM and Taipower for their financial and technical support of the work described in this paper. The statements made in the paper are, however, solely those of the authors and do not necessarily reflect those of the Funding Organisations.

CAS team's work was financially supported by National Natural Science Foundation of China (Grant No. 52125903).

## **A List of symbols**



Table A.1: Nomenclature

Symbol	Meaning	Dimension, Unit
$T$	temperature	temperature, K
$p$	pore pressure	pressure, Pa
$\mathbf{u}$	displacement vector	length, m
$\boldsymbol{\varepsilon}$	strain tensor	-
$\boldsymbol{\varepsilon}_p$	plastic strain part	-
$\boldsymbol{\sigma}_S^E$	effective stress tensor	pressure, Pa
$\tilde{\mathbf{w}}_{FS}$	Darcy filter velocity	velocity
$Q_T$	heat source term	power/volume, W/m <sup>3</sup>
$Q_H$	fluid mass source term	mass/volume/time, kg/(m <sup>3</sup> s)
$\alpha_B$	Biot-Willis coefficient ( $\alpha_B \leq 1$ )	-
$\phi$	porosity, $\phi \in (0, \alpha_B]$ ,	-
$\rho_{SR}$	intrinsic (real) density of the solid phase	mass/volume, kg/m <sup>3</sup>
$\lambda_{SR}$	thermal conductivity of the solid phase	power/length/temperature, W/(m K)
$\alpha_T^S$	linear thermal expansion coefficient	1/temperature, 1/K
$\beta_T^*$	volumetric thermal expansion coefficient ( $\beta_T^* = 3\alpha_T^*$ )	1/temperature, 1/K
$K_*$	bulk modulus of phase *	pressure, Pa
$\beta_p^*$	compressibility ( $\beta_p^* = 1/K_*$ )	1/stress
$\mu_{FR}$	fluid viscosity	pressure·time, Pa s
$\rho_{FR}$	intrinsic mass density pore fluid	mass/volume
$c_{pF}$	effective volumetric heat capacity	energy/volume/temperature
$(\rho c_p)^{eff}$	effective volumetric heat capacity	energy/volume/temperature
$\boldsymbol{\lambda}^{eff}$	effective heat conductivity tensor	power/length/temperature
$\mathbf{g}$	gravity acceleration vector	force/mass, N/kg
$\mathbf{k}$	intrinsic permeability tensor	length·length, m <sup>2</sup>
$\mathbf{I}$	second order identity tensor	-
$\mathbb{C}$	fourth order elasticity tensor	stress, Pa
$\Omega \subset \mathbb{R}^d$	$d$ -dimensional physical domain ( $d = 2, 3$ )	in which the THM problem is formulated
$\sigma_c$	Compressive strength	pressure, Pa
$\sigma_t$	Tensile strength	pressure, Pa
$E$	Elastic modulus	pressure, Pa
$\nu$	Poisson's ratio	-
$K_I$	Fracture toughness	pressure · square root of length, Pa·m <sup>0.5</sup>
$\phi$	Friction angle	angle, degrees
$c$	Cohesion	pressure, Pa
$\Delta\tau$	Shear stress on the fracture	pressure, Pa
$G$	Shear modulus of the rock	pressure, Pa
$a$	Fracture half-length	length, m
$r$	Distance from fracture center to occurrence point of shear displacement	length, m
$\varepsilon_{vol}$	Volumetric strain	-
$\varepsilon_{cir}$	Circumferential strain	-
$Q$	Volumetric flow rate	volume/time, m <sup>3</sup> /s
$L$	Fracture length in the flow direction	length, m
$w$	Fracture width along the sample axis	length, m
$\Delta p$	Pressure difference at the fracture edges	pressure, Pa
$k_{nn}$	Normal fracture stiffness	pressure/length, Pa/m
$k_{tt}$	Tangential fracture stiffness	pressure/length, Pa/m
$d$	Phase field	-

## B Details of numerical methods

### B.1 Lower-dimensional interface element (LIE) method

We consider the lower-dimensional interface element (LIE) method Watanabe et al., 2012 for the simulation the hydro-mechanical process in the fracture sample. In the LIE, the displacement difference between two sides of the surfaces is defined as a fracture relative displacement  $\mathbf{w}$ , which is defined in the local system as:

$$\mathbf{w} = \begin{bmatrix} w_t \\ w_n \end{bmatrix} = \begin{bmatrix} u_t^+ - u_t^- \\ u_n^+ - u_n^- \end{bmatrix}, \quad (\text{B.1})$$

where  $u$  stands for displacement, subscripts  $t$  and  $n$  denote tangential and normal directions to the fracture plane, respectively. Superscripts  $+$  and  $-$  indicate one side and the other side of the surfaces, respectively. The normal fracture relative displacement represents the change of fracture aperture. Therefore the fracture aperture  $b$  is given by

$$b = b_0 + w_n,$$

with  $b_0$  the initial fracture aperture. On the fracture plane, the applied total stresses are  $\sigma^f = [\sigma_t, \sigma_n]^T$ , which is defined as

$$\sigma^f = \sigma'^f - \alpha_B^f [p^f, p^f]^T, \quad (\text{B.2})$$

where  $\sigma'^f$  is the effective stresses on the fracture,  $\alpha_B^f$  is the Biot's constant for fracture, and  $p^f$  is the liquid pressure in the fracture. The relationship between the fracture relative displacement and the effective fracture stress is given by

$$d\sigma'^f = \mathbf{K}d\mathbf{w}, \quad (\text{B.3})$$

where  $\mathbf{K}$  is the stiffness tensor defined as

$$\mathbf{K} = \begin{bmatrix} k_{tt} & k_{tn} \\ k_{nt} & k_{nn} \end{bmatrix}, \quad (\text{B.4})$$

with  $k_{tt}$  and  $k_{nn}$  are the joint shear and normal stiffness, respectively.  $k_{tn}$  and  $k_{nt}$  govern the coupling effects between normal and shear displacements. Normally, the coupling effects are neglected.

The joint shear and normal stiffnesses can be estimated by the following formulas

$$k_{nn} = \frac{E_i E_m}{L(E_i - E_m)} k_{tt} = \frac{G_i G_m}{L(G_i - G_m)}, \quad (\text{B.5})$$

where  $E$  represents the Young's modulus,  $G$  represents the shear modulus, the subscripts  $i, m$  stand for intact rock and mass rock, respectively, and  $L$  the mean joint spacing Barton, 1972.

The volume balance equation and volumetric flux equation for the discrete fracture can be derived from the mass balance law and the linear momentum balance law as

$$bS_s^f \frac{\partial p^f}{\partial t} + \alpha_B^f \frac{\partial b}{\partial t} + \nabla \cdot (b\mathbf{q}^f) + q^+ - q^- = 0, \quad \mathbf{q}^f = -\frac{k^f}{\mu} (\nabla p^f - \rho^l \mathbf{g}) \quad (\text{B.6})$$

where  $S_s^f$  is the specific storage for the fracture,  $q^+$  and  $q^-$  are the leakage flux from each side of the fracture

surfaces to the surrounding porous media,  $k_f = b^2/12$  is the fracture permeability,  $\mu$  is the liquid viscosity,  $\rho^l$  is the liquid density, and  $\mathbf{g}$  is the gravitational force vector.

The balance equations for the rock mass are the conventional ones, which are coupling to the balance equations of fracture via displacement, pressure, and liquid flux on the fracture interface.

## B.2 Fundamentals of NMM (LBNL)

The numeral manifold method (NMM) (Shi, 1992) is based on the concept of “manifold” in topology. In NMM, independent meshes for interpolation and integration are defined separately. Based on this approach, an initially one-time generated, non-conforming mesh (not necessarily conforming with the physical boundaries) can be used and flexible local approximations can be constructed and averaged to establish global approximations for both continuous and discontinuous analysis.

In NMM, independent mathematical and physical covers are defined. A mathematical cover is a set of connected patches that cover the entire material domain. For example, we can use a quadrilateral patch, a circular patch, or a rectangular patch as a mathematical cover (such as the A, B, C in Figure B.1). Features such as density and shape of these mathematical patches define the precision of the interpolation. The physical patches are mathematical patches divided by boundaries and discontinuities, determining the integration fields. The union of all the physical patches forms a physical cover. For example, physical patch C is the entire model domain, while physical patch B is divided from mathematical patch B by boundaries. Physical patch A (divided from mathematical patch A by boundaries) is further divided into physical patches  $A_1$  and  $A_2$  by the inner discontinuity. The overlapping areas by multiple physical patches are defined as elements. As a result, the model domain  $\Omega$  is discretized into five elements:  $A_1BC$  (the overlap of physical patches  $A_1$ , B and C),  $A_1C$ ,  $A_2C$ , BC, and C. From Figure B.1, we can see that the shape of the mathematical patches can be arbitrary; the relative location of the mathematical patches to the model domain can also be arbitrary (only if satisfying  $\Omega \subset A \cup B \cup C$ ), and the number of physical patches on each element can be arbitrary.

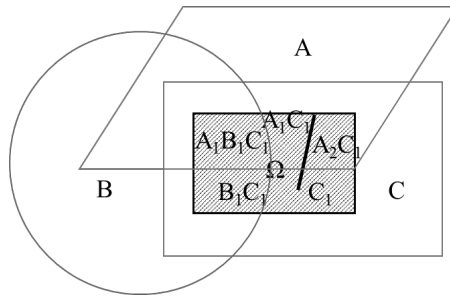


Figure B.1: NMM mathematical and physical meshes

On each physical patch, a local function is assigned, such as one that is constant, one that is linear, or any function that is able to capture the behavior of the solution on the patch. The weighted average of the local patch functions forms the global approximation. For example, if using linear local functions, we can construct a global second-order approximation (Figure B.2a, Wang et al., 2016). If using a local function with a jump of the first derivative, we can simulate a material interface crossing patches and elements (Figure B.2b, Hu, Wang, and Rutqvist, 2015). Or most commonly, if using discontinuous local functions, we can simulate fractures (Figure B.2c, Hu, Rutqvist, and Wang, 2016a; Hu, Rutqvist, and Wang, 2017). With this dual-mesh concept, the NMM is capable of simulating both continuum and discontinuum with accurate geometric representation and flexible

numerical approximation. With the advantages of dual-mesh concept, NMM also has been successfully applied to analyzing moving interface problems such as free surface flow (Wang et al., 2014; Wang et al., 2016).

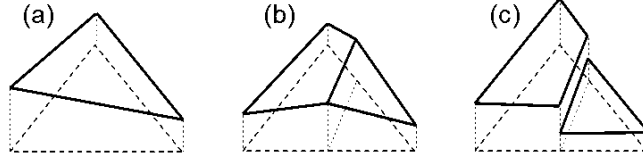


Figure B.2: Flexible choice of local approximation functions: (a) linear function (Wang et al., 2016), (b) a jump junction for a weak discontinuity (Hu, Wang, and Rutqvist, 2015), (c) a discontinuous function for a fracture (Hu, Rutqvist, and Wang, 2016a; Hu, Rutqvist, and Wang, 2017)

## Discontinuous Fracture Model in Numerical Manifold Method

**Contacts of Discontinuous Fractures** The mechanical state of a fracture is complicated. A fracture may have several segments and every segment from the two sides of this fracture (a contact pair) have three possible contact states: open, bonded, or sliding. When sliding or shearing occurs, contact pairs (i.e., the locations of where contacts occur) may be altered.

Corresponding to these three contact states for each contact pair, different boundary constraints are applied. When a fracture segment (a contact pair) is open, a linear constitutive behavior is assumed:

$$\delta \sigma'_f = \mathbf{k}_f \|\mathbf{u}_f\| \quad (\text{B.7})$$

where  $\sigma'_f$  denotes a tensor of effective stress in both normal and tangential directions of a segment of a fracture,  $\mathbf{k}_f$  is the stiffness tensor of the segment, and  $\mathbf{u}_f$  is the jump of displacements in both normal and tangential directions of the fracture segment. When  $\mathbf{k}_f$  is set as zero, a mechanically open fracture can be described.

When a segment of a fracture is bonded, the distance and relative shear displacement between the two sides of the segment should be zero, satisfying:

$$\mathbf{d} = 0 \quad \cap \quad \|\mathbf{u}_s\| = 0 \quad (\text{B.8})$$

where  $\mathbf{d}$  is the time-dependent normal distance between the two surfaces of the fracture segment, and  $\mathbf{u}_s$  is the relative displacement between the two surfaces in the direction along the contacting face.

When a segment of a fracture is sliding, Coulomb's law of friction is satisfied in the tangential direction, while the normal distance between the two surfaces of the fracture segment should be zero:

$$\mathbf{d} = 0 \quad \cap \quad \mathbf{F}_s = \mathbf{F}'_n \tan \varphi \text{sgn}(\|\mathbf{u}_s\|) \quad (\text{B.9})$$

where  $\mathbf{F}_s$  is the contact force in the direction of the sliding face,  $\mathbf{F}'_n$  is the effective normal contact force by considering fluid pressure,  $\varphi$  is the friction angle, and  $\text{sgn}(\|\mathbf{u}_s\|)$  denotes the direction of  $\mathbf{F}_s$  that depends on the direction of relative shear displacement. When sliding occurs along the two surfaces of a fracture, the locations of contacts change with time, possibly leading to changes of contact pairs as well as contact states

among several segments of this fracture (Hu and Rutqvist, 2020b; Hu, Steefel, and Rutqvist, 2021).

So far, we have described a fracture segment (a contact pair) in open, bonded and sliding contact states. In dynamic conditions, these contact states may be changed as follows:

If a fracture segment was open, but become bonded later, constraints in Equation (2) should be added. If the fracture segment was open, but then they are in sliding state, constraints in Equation (3) should be added.

If a fracture segment was bonded but become open later, the constraints in Equation (2) should be removed.

If a fracture segment was bonded but transfer to a sliding state, we need to consider one condition: in order to initiate sliding of A and B against each other, the force in the direction of contacting face  $F_s$  needs to be larger than the shear strength  $S$ . The shear strength may consist of frictional force (satisfying Coulomb's law of friction) and cohesive force  $F_{cohe}$ . This criterion for shearing a bonded fracture segment in the direction along its contact face can be expressed as:

$$F_s > S = F'_n \tan \varphi' + F_{cohe} \quad (B.10)$$

where  $\varphi'$  is the internal friction angle. If Equation (4) is satisfied, the fracture segment is transferred from bonded to sliding state. Comparing Equation (2) and (3) we find that the constraint in the direction normal to contacting face should be retained, while in the sliding direction, the constraint needs to be changed.

If a fracture segment was in a sliding state but becomes open, constraints in Equation (3) should be removed. If they become bonded, the constraints should be modified in the direction along the fracture segment so that no relative shear displacement will occur.

With Equations (1)-(4), we are able to describe the three different contact states of a fracture segment, dynamic changes of these contact states, and criteria that need to be satisfied for changes of the contact states.

**Geometric Representation** An important issue for calculation of discrete fractures is how to simulate intersections of fractures. Figure B.3 demonstrates a geometric representation of two fractures that intersect with each other as well as with one triangular mathematical mesh. As we can see, the two intersecting fractures divide the triangle to four different parts (A, B, C, D). Then contact states (satisfying constraints described by Equations (1)-(3)) will be applied on the four pairs of parallel interfaces (interfaces between A and B, C and D, B and C, and A and D) to account for the opening, bonded and sliding states of the surfaces of each fracture.

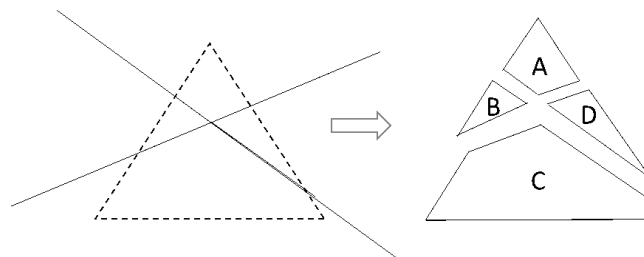


Figure B.3: Geometric representation of an element with one intersection by two fracture

Fractures in open and bonded states or alteration between these two states are easier to simulate because this does not require changes of contact pairs. It is assumed that a fracture is approximated by two surfaces are parallel at the beginning, but these two surfaces can be non-parallel after deformation and motion, or opened.

This capability is included in the algorithm.

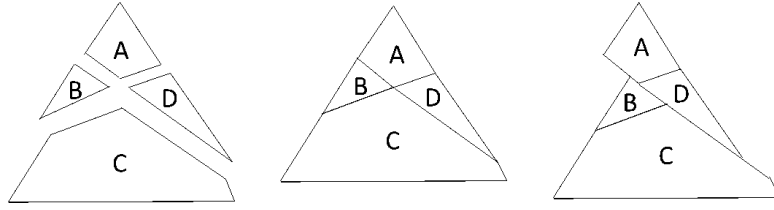


Figure B.4: Geometric representation of open, bonded and sliding contact states for elements divided by intersecting fractures

It is challenging to simulate shearing along fractures because shearing leads to dynamic changes of contacts between different elements. As shown in Figure B.4, when the four blocks A, B, C, D in contact (when the fractures are completely bonded), the contact pairs are A and B, B and C, C and D, and A and D. But when sliding (slip) occurs at one of the fractures, the contact pairs become A and B, B and C, B and D, C and D, D and A. By using a rigorous contact algorithm that updates contact pairs each time step, sliding along fractures can be rigorously and explicitly represented.

### NMM Calculation of Shearing of Discontinuous Fractures

#### *Updating Contact Pairs*

As demonstrated before, a fracture is approximated by two surfaces that are parallel at the beginning. After shearing, the contact pairs (i.e., where exactly contacts occur) will be updated. This may involve changes of contact locations on the same contact elements, or contact between different elements. The latter results in changes between zero and non-zero values at the off-diagonal elements of the calculating matrix.

#### *Enforcement of Contact Constraints*

The distance and displacement constraints for bonded and sliding states are imposed by using penalty methods (Shi, 1992). The penalty method is based on the concept of constructing a penalty function  $g$  to penalize the deviation from the displacement constraint  $c(u)$ . The key to effectively using a penalty method is to choose a reasonable value of the penalty parameter. We assume a significantly stiff spring applied to the deviation of a constraint associated with displacements. Therefore, the stiffness of the spring becomes the penalty parameter  $p$ . Minimization of deviation of the displacement constraint can be achieved by minimizing the potential energy associated with the work done by the penalty spring. The potential energy  $\Pi_c$  by the penalty spring to enforce the constraint can be generally expressed as:

$$\Pi_c = gc(u) = \frac{1}{2}pc^2(u) \quad (\text{B.11})$$

The second constraint, i.e., Coulomb's law of friction is imposed directly by constructing the potential energy:

$$\Pi_{\text{friction}} = gc(u) = -\mathbf{F}_s \cdot \mathbf{u}_s \quad (\text{B.12})$$

Note that (1) because Equation (6) includes a dot product, it requires calculation of projecting shearing force on the sliding face, and (2) on the two sides of the sliding face, the absolute shear displacements are different due to sliding (as a relative displacement).

### Iteration for Contact State Convergence

Within each time step, iterations may be carried out several times and pre-estimated contact states may be adjusted until the enforced contacts reach convergence. In a dynamic process, contact pairs may change continuously (Hu and Rutqvist, 2020a; Hu and Rutqvist, 2020b). For the same contact pair (a segment of fracture discretized by a numerical mesh in NMM), the three possible states may change dynamically. Thus, for every iteration within a time step, the global equilibrium equations are solved with enforcement of contact constraints from the pre-estimated contact states. At this point, the contact states are re-evaluated to check for consistency with the pre-estimated contact states. If they are consistent for each contact pair, the calculation proceeds to the next time step. If they are not consistent, the contact states will be adjusted, and the calculation is looped back to re-solve the equilibrium equations until such consistency (i.e., convergence) is achieved.

## B.3 Fundamentals of FLAC3D (LBNL)

**Computing package.** FLAC3D is a finite volume code, in which unstructured meshes such as tetrahedral elements can be used to discretize the model domain. As such, the smallest component of a FLAC3D zone is a tetrahedral element (Figure B.5a) and five of them comprises one hexahedral zone (Figure B.5b). In addition, one hexahedral zone has two “overlays” of the tetrahedral elements as shown in Figure B.5b (i.e., one zone effectively consists of ten tetrahedral elements), which is implemented to make the distribution of model outputs, such as stresses and strains, symmetric within a zone.

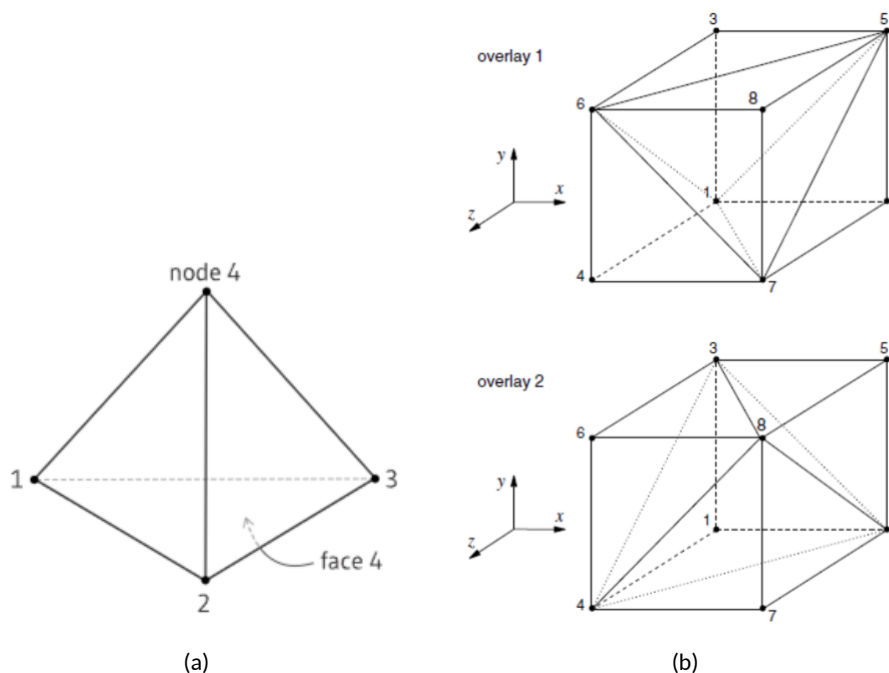


Figure B.5: The components of a FLAC3D zone.

FLAC3D calculates the mechanical outputs such as velocities, displacements, stresses, and strains, in the following order:

1. Calculate new strain rates from nodal velocities

2. Calculate new stresses from the strain rates and previous stresses (via constitutive equations)
3. Calculate new nodal forces from the stresses, applied loads, and body forces (via the theorem of virtual work)
4. Calculate new nodal velocities and displacements from the velocities and forces (via the equations of motion)

The above calculation steps 1 to 4 are repeated while marching in terms of time to obtain the final solution, which means that FLAC3D employs the explicit time difference scheme to discretize the time derivatives. The detailed calculation processes are provided below.

### Interface node and elements

The interface elements of FLAC3D are triangular elements attached on zone faces (i.e., surfaces of the model) (Figure B.6). At each vertex of an interface element is an interface node, which is used to detect contact and calculate interface forces. Along an interface, in which two zone surfaces face against each other, interface elements are generally attached only on one side, as this is usually sufficient to simulate interface contact behaviors. The side where interface elements are attached is called the host face, while the other side without interface elements is called the target face. The orientation of the target face determines the normal direction for contact force calculation, which is then performed on the host face using the interface nodes.

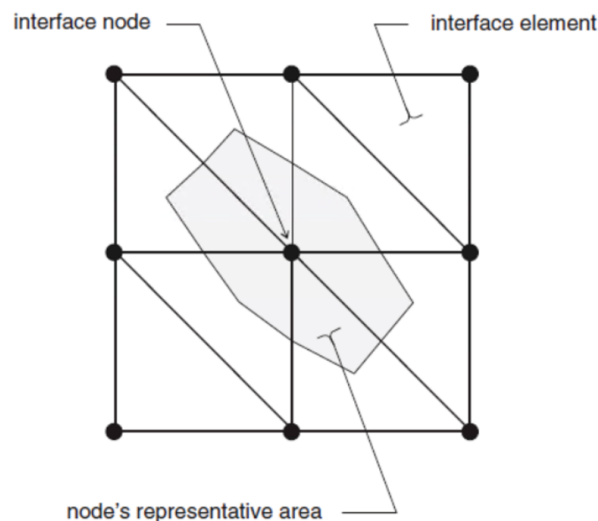


Figure B.6: Interface elements, nodes, and the representative interface area (Itasca Consulting Group, 2020).

### Solution procedure

The normal and shear forces calculated at an interface node on the host face are equal in magnitude and opposite in direction to those projected on the target face. The interface forces are then distributed in a weighted fashion to the gridpoints of each face (a gridpoint is a vertex point of a zone, i.e., an element in FLAC3D). The distributed interface forces are then incorporated into the solution of the equation of motion to calculate the displacements of the gridpoints, which update the interface forces and contact states. If a change in the contact state is detected, the interface forces and stresses are adjusted so as to comply with the interface constitutive model. The resultant interface forces are then used to calculate the displacements for the next time step.



### Interface contact states

There are three possible interface states: bonded, sliding, and open interfaces. A bonded interface in FLAC3D means an intact interface due to the contact forces remaining below the interface strengths. Thus, bonded interfaces result in the model behaving as if it does not have the interfaces. When the bond is broken, an interface can no longer take tension. If a broken interface separates (i.e., open interface), all interface forces becomes zero, and so they remain until new contact is detected. A broken interface can also slide while the interface is closed (in contact).

The interface forces of a bonded interface are calculated using linear normal and shear springs, while those of a sliding interface not only with the springs also with the Coulomb friction constitutive model, the details of which are provided next.

### Interface constitutive model

Figure B.7 shows FLAC3D's interface constitutive model, which consists of the normal (i.e.,  $k_n$ ,  $D$ ,  $T_s$  and tangential  $k_s$ ,  $S$ ,  $S_s$  components.

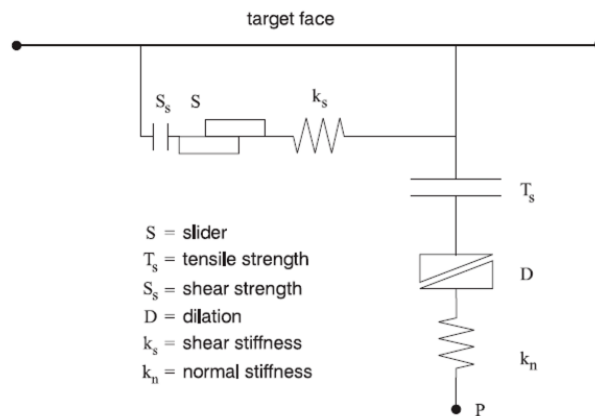


Figure B.7: The constitutive model of an interface node (Itasca Consulting Group, 2020).

The tangential contact is modeled using a linear shear spring; the interface shear force is generated when an interface node slides along the contacting surface, as shown in the following equation:

$$F_s = k_s \Delta u_s A \leq F_{smax}$$

where  $F_s$  is the interface shear force (N),  $k_s$  is the interface shear stiffness (i.e., stiffness of the shear spring) (Pa/m),  $\Delta u_s$  is the interface relative displacement in the contact tangent direction (m), and  $A$  is the representative contact area of an interface node ( $m^2$ ). Also shown in this equation is the maximum interface shear force,  $F_{smax}$ , which is determined via the Coulomb friction law as shown in the equation below:

$$F_{smax} = S + S_s A = (F_n - p_{pore} A) \tan \phi_I + S_s A$$

where  $S$  is the frictional (slider) strength (N),  $S_s$  is the shear strength (i.e., tangential cohesion) (Pa),  $F_n$  is the normal force applied on the contact surface (N),  $p_{pore}$  is pore pressure (Pa), and  $\phi_I$  is the friction angle between the node and contact surface ( $^\circ$ ).

Similar to the tangential contact behavior, the normal contact behavior is also modeled with a linear spring. The interface normal force develops when an interface node penetrates the contacting surface, and the magnitude of the normal force is linearly proportional to the penetration distance as shown in the following equation:

$$F_n = k_n u_n A + DA \geq F_{nmin} = T_s A$$

where  $F_n$  is the interface normal force (N),  $k_n$  is the normal stiffness (i.e., stiffness of the normal spring) (Pa/m),  $u_n$  is the penetration distance (m),  $A$  is the representative contact area (m<sup>2</sup>). Note that compression is positive for the interface normal force. The minimum normal force ( $F_{nmin}$ ) is specified as the tensile strength ( $T_s$ ) multiplied by the representative contact area ( $A$ ). The normal contact model also contains the dilation-induced normal stress ( $D$ ), which is defined as follows:

$$D = k_n \left( \frac{(F_{s>max} - F_{smax})}{(k_s A)} \right) \tan \psi_I$$

where  $F_{s>max}$  is the interface shear force before correction (i.e., predicted shear force above  $F_{smax}$ ),  $F_{smax}$  is the maximum shear force determined via the Coulomb friction law, and  $\psi_I$  is the interface dilation angle. The term  $\left( \frac{(F_{s>max} - F_{smax})}{(k_s A)} \right)$  indicates an irrecoverable shear displacement; it is converted into the interface dilation in the contact normal direction by multiplying it with the dilation angle,  $\tan \psi_I$ . Finally, the interface dilation is converted into the dilation-induced normal stress by multiplying it with the normal stiffness,  $k_n$ .

The shear and normal interface stiffnesses can be calculated as follows:

$$k_s = k_n = 10 \frac{(K + 4\frac{G}{3})}{\Delta z_{min}}$$

where  $K$  and  $G$  are respectively the bulk and shear moduli of the material to which an interface is attached. If the material is different across the interface, the stiffness values of the stiffer material are used. Also, if the interface mesh size is different, the smallest mesh width of the interface,  $\Delta z_{min}$ , is used. Finally, to avoid excessive penetration, the interface stiffnesses are set to ten times the term,  $\frac{(K + 4\frac{G}{3})}{\Delta z_{min}}$ . Note that this is only a general guideline; the stiffness values can also be determined by trial-and-error as the minimum values that can prevent the excessive penetration of the interface.

Software reference: Itasca Consulting Group. (2020). *Griddle — Advanced Meshing Tools for Numerical Modeling*, Ver. 2.

<https://www.itascacg.com/software/griddle>

## References

- Barton, NR (1972). "A model study of rock-joint deformation". In: *International Journal of Rock Mechanics and Mining Sciences & Geomechanics Abstracts*. Vol. 9. 5. Elsevier, pp. 579–582.
- Hu, M. and J. Rutqvist (2020a). "Fully coupled process modeling of fractured media across scales". In: Cited by: 0. URL: <https://www.scopus.com/inward/record.uri?eid=2-s2.0-85097959358&partnerID=40&md5=a0bdc7c88a3443273e87c090613706de>.
- Hu, Mengsu and Jonny Rutqvist (2020b). "Numerical manifold method modeling of coupled processes in fractured geological media at multiple scales". In: *Journal of Rock Mechanics and Geotechnical Engineering* 12.4. Cited by: 29; All Open Access, Gold Open Access, Green Open Access, pp. 667 – 681. DOI: 10.1016/j.jrmge.2020.03.002. URL: <https://www.scopus.com/inward/record.uri?eid=2-s2.0-85084946435&doi=10.1016%2fj.jrmge.2020.03.002&partnerID=40&md5=2fe077a17a8cd632314a67fcbbb61cb8>.
- (2022). "Multi-scale Coupled Processes Modeling of Fractures as Porous, Interfacial and Granular Systems from Rock Images with the Numerical Manifold Method". In: *Rock Mechanics and Rock Engineering* 55.5. Cited by: 23; All Open Access, Green Open Access, Hybrid Gold Open Access, pp. 3041 – 3059. DOI: 10.1007/s00603-021-02455-6. URL: <https://www.scopus.com/inward/record.uri?eid=2-s2.0-85104128087&doi=10.1007%2fs00603-021-02455-6&partnerID=40&md5=400b87306a2d6b6e5a0a6e2f43db5cc9>.
- Hu, Mengsu, Jonny Rutqvist, and Yuan Wang (2016a). "A fully coupled hydro-mechanical model for discrete fractured porous rock masses based on numerical manifold method". In: vol. 1. Cited by: 0, pp. 318 – 328. URL: <https://www.scopus.com/inward/record.uri?eid=2-s2.0-85010280535&partnerID=40&md5=b5cca195e9cb092d7b48ce4c834f4fda>.
- (2016b). "A practical model for fluid flow in discrete-fracture porous media by using the numerical manifold method". In: *Advances in Water Resources* 97. Cited by: 44; All Open Access, Bronze Open Access, Green Open Access, pp. 38 – 51. DOI: 10.1016/j.advwatres.2016.09.001. URL: <https://www.scopus.com/inward/record.uri?eid=2-s2.0-84986887884&doi=10.1016%2fj.advwatres.2016.09.001&partnerID=40&md5=977ae3a0a4d58300ab25a1b3a7ae2df1>.
- (2017). "A numerical manifold method model for analyzing fully coupled hydro-mechanical processes in porous rock masses with discrete fractures". In: *Advances in Water Resources* 102. Cited by: 70; All Open Access, Bronze Open Access, Green Open Access, pp. 111 – 126. DOI: 10.1016/j.advwatres.2017.02.007. URL: <https://www.scopus.com/inward/record.uri?eid=2-s2.0-85013197165&doi=10.1016%2fj.advwatres.2017.02.007&partnerID=40&md5=c8332562aa8bda810d0c837a9522f9c6>.
- Hu, Mengsu, Carl I. Steefel, and Jonny Rutqvist (2021). "Microscale Mechanical-Chemical Modeling of Granular Salt: Insights for Creep". In: *Journal of Geophysical Research: Solid Earth* 126.12. Cited by: 5; All Open Access, Green Open Access. DOI: 10.1029/2021JB023112. URL: <https://www.scopus.com/inward/record.uri?eid=2-s2.0-85121718795&doi=10.1029%2f2021JB023112&partnerID=40&md5=a32d56084d4d36fd1439ede78faa5abc>.
- Hu, Mengsu, Yuan Wang, and Jonny Rutqvist (2015). "An effective approach for modeling fluid flow in heterogeneous media using numerical manifold method". In: *International Journal for Numerical Methods in Fluids* 77.8. Cited by: 18, pp. 459 – 476. DOI: 10.1002/flid.3986. URL: <https://www.scopus.com/inward/record.uri?eid=2-s2.0-84946166824&doi=10.1002%2fflid.3986&partnerID=40&md5=b5f472dcbed0b68c2d0c04ab1b9cfcff>.
- Shi, Gen-Hua (1992). "Modeling rock joints and blocks by manifold method". In: *33rd U.S. Symposium on Rock Mechanics, USRMS 1992*, pp. 639 – 648. URL: <https://www.scopus.com/inward/record.uri?eid=2-s2.0-85055653811&partnerID=40&md5=bb6c38775ffd128c61cb0e3d3f752f05>.
- Wang, Yuan et al. (2014). "Energy-work-based numerical manifold seepage analysis with an efficient scheme to locate the phreatic surface". In: *International Journal for Numerical and Analytical Methods in Geomechanics* 38.15. Cited by: 40, pp. 1633 – 1650. DOI: 10.1002/nag.2280. URL: <https://www.scopus.com/inward/record.uri?eid=2-s2.0-84908232497&doi=10.1002%2fnag.2280&partnerID=40&md5=6cd81dd0f4a06b94f18984fe14285774>.
- (2016). "A new second-order numerical manifold method model with an efficient scheme for analyzing free surface flow with inner drains". In: *Applied Mathematical Modelling* 40.2. Cited by: 44; All Open Access, Green Open Access, pp. 1427 – 1445. DOI: 10.1016/j.apm.2015.08.002. URL: <https://www.scopus.com/inward/record.uri?eid=2-s2.0-84927557390&doi=10.1016%2fj.apm.2015.08.002&partnerID=40&md5=50697f3bee63ec2a66e22ff48526dc4d>.
- Watanabe, N. et al. (2012). "Lower-dimensional interface elements with local enrichment: Application to coupled hydro-mechanical problems in discretely fractured porous media". In: *International Journal for Numerical Methods in Engineering* 90.8, pp. 1010–1034.

## List of Figures

0.1	Graphical abstract fo Task G . . . . .	6
1.1	DECOVALEX 2023 Task G structure . . . . .	13
1.2	Geometric cases (cubes) for KICT experiments by processes: $M > HM > TM > THM$ . . . . .	14
1.3	Geometric cases (cylinders) for GREAT cell experiments by processes: $M > HM > TM > THM$ . . . . .	14
1.4	Benchmarking concept of 2D horizontal cross-sections (plane-strain) . . . . .	15
1.5	Benchmarking idea for 2D plane-strain conditions; upper figures represent M processes, lower figures represent HM processes . . . . .	15
2.1	h-Scatterplot data acquisition examples. Example a) shows the data acquisition for an h-Scatterplot in the South-North direction for lag = 1. Similarly, b) shows the data acquisition for an h-Scatterplot in the Southwest-Northeast direction for a lag of $\sqrt{2}$ , (Isaaks and Srivastava, 1989). . . . .	28
2.2	Illustration of the cone of investigation for scattered data: $h=\text{lag}$ , $h\text{-tol}/h+\text{tol} = \text{lag tolerance}$ , angle tolerance and bandwidth, (Pyrcz and Deutsch, 2014 - 2014). . . . .	28
2.3	Dataset: Matched greywacke top and bottom surfaces. The red square depicts a sub-dataset used for the study. . . . .	30
2.4	Fracture map of the greywacke top surface original data for the red square area only (Quadrant 4). X, Y and Z values are in mm. . . . .	31
2.5	Variogram map of Figure 2.4 using normalised data and lag = 5 mm. X and Y values are in mm. . . . .	31
2.6	Semi-variograms for $0^\circ$ orientation (top) and $90^\circ$ (bottom), note the change in y-axis scale between the two graphs. . . . .	32
2.7	Fracture map of residuals after trend has been subtracted (inset top-left). X and Y values are in mm. . . . .	33
2.8	Variogram map of Figure 2.7 using raw data and lag = 1 mm. X and Y values are in mm. Red arrows are the interpreted minor and major directions of spatial continuity whilst the green ones refer to the trended data from Figure 2.5. . . . .	33
2.9	Upscaling technique illustration using a plane fitting in each bounding box and taking the bounding box central point's z-value. . . . .	34
2.10	Comparison of a kriged dataset (top) based on the upscaled surface data compared with the original high-resolution dataset (bottom). . . . .	35
2.11	a) Normalised original data's residuals and b) Kriging results (using Figure 2.9 base points). . . . .	35
2.12	Frequency distribution of the normalised GW1Q4 residual fracture points (related to Figure 2.11a) ) and the frequency distribution of the kriged surface using GW1Q4 scale 2 upscaled residual points (related to Figure 2.11b) ). . . . .	36
2.13	Difference (error) between original normalised fracture aperture and kriged fracture aperture using upscaled scale 2 points. . . . .	36

2.14	Normalised Greywacke Quadrant 4 (GWQ4): a) Aperture map; b) Log10 Aperture Variogram Map. . . . .	37
2.15	Normalised Greywacke Quadrant 4 (GWQ4): a) Aperture semi-variogram for 67.5° direction; b) Aperture semi-variogram for 157.5° direction. . . . .	37
2.16	Normalised Greywacke Quadrant 4 (GWQ4) Upscale 9: a) Aperture map; b) Aperture Variogram Map . . . . .	37
2.17	Normalised Greywacke Quadrant 4 (GWQ4) Upscale 9: a) Aperture semi-variogram for 67.5° direction; b) Aperture semi-variogram for 157.5° direction. . . . .	38
2.18	Normalised Greywacke Quadrant 4 (GWQ4) Upscale 19: a) Aperture map; b) Aperture Variogram Map . . . . .	38
2.19	Normalised Greywacke Quadrant 4 (GWQ4) Upscale 19: a) Aperture semi-variogram for 67.5° direction; b) Aperture semi-variogram for 157.5° direction. . . . .	38
2.20	Within red square: Greywacke Quadrant 4 (GWQ4) Upscale 1 Aperture field. Between red square and blue polygon: extrapolation using spatial continuity analysis. . . . .	40
2.21	Predict the value at the centre of the model's element using kriging and the spatial continuity of the data, which uses only the points that are statistically correlated to each other. . . . .	40
2.22	Model comparison: The top row shows the coarse model (32x32 elements) and the bottom row the fine model (64x64 elements) – The 2 and 4 fringes' elements in either side (coarse and fine models respectively) are not accounted for. Left and right columns display the averaging method (arithmetic averaging and kriging, respectively). The colour map represents the hydraulic aperture, the white vectors the fluid velocity and the pink arrows the fluid flow lines. The models are blanked where the fracture is deemed in contact across the two faces. . . . .	41
2.23	Greywacke Quadrant 4 Hydro-Mechanical model . The colour map represents the hydraulic aperture, the white vectors the fluid velocity and the pink arrows the fluid flow lines. The models are blanked where the fracture is deemed in contact across the two faces. . . . .	42
3.1	Benchmarks overview. (a) <i>benchmark 1</i> : static horizontal fracture under a constant pressure, (b) <i>benchmark 2</i> : propagating horizontal fracture in the toughness dominated regime, (c) <i>benchmark 3</i> : static horizontal fracture under a constant pressure with differential in-situ stress and (d) <i>benchmark 4</i> : static inclined fracture under a constant pressure with differential in-situ stress. The unit of domain size is meter [m]. . . . .	45
3.2	(a) Fracture half-aperture profiles and (b) error from different numerical methods compared against the closed-form solution. . . . .	46
3.3	(a) Pressure and (b) fracture length evolution against injected volume . . . . .	47
3.4	Aperture profile for the Granite specimen with a plane horizontal fracture. . . . .	48
3.5	Aperture profiles for the Granite specimen with a plane inclined 30° fracture. . . . .	49

3.6	Mesh discretization for the mesh study using VPF-FEM: the middle square has structured quadrilateral elements with a mesh size $h = 0.01$ , and outside of that, there is an unstructured mesh with mesh size $h = 0.1$ . . . . .	50
3.7	Fracture aperture profiles of (a) VPF-FEM, (b) hCA-FEM/xFEM, (c) BPM-DEM and (d) CMEFM-FEM with different mesh sizes compared against the analytical solution. . . . .	50
3.8	Convergence curve for the error of maximum aperture with different mesh sizes for benchmark 1. . . . .	51
3.9	Initial phase field profile (a) not aligned mesh with inclined fracture and (b) aligned mesh with inclined fracture in VPF-FEM approach. . . . .	51
3.10	Aperture profiles for the Granite specimen with a plane inclined $30^\circ$ fracture using VPF-FEM approach. . . . .	52
3.11	Domain size study for benchmark 3: $\Omega = [-0.125, 0.125] \times [-0.125, 0.125]$ , $\Omega = [-0.25, 0.25] \times [-0.25, 0.25]$ , $\Omega = [-0.5, 0.5] \times [-0.5, 0.5]$ , and $\Omega = [-0.75, 0.75] \times [-0.75, 0.75]$ . The unit of domain sizes is meter [m]. . . . .	53
3.12	Aperture profiles of (a) VPF-FEM, (b) hCA-FEM/xFEM, (c) BPM-DEM, (d) CMEFM-FEM, and (e) IFDM-DEM for the Granite specimen with a plane horizontal fracture with different domain sizes. . . . .	54
3.13	Freiberg granite fracture surface scan data in four different mesh resolution. . . . .	55
3.14	Three traces (roughness profiles) taken from the fracture surface scan data. . . . .	56
3.15	2D rough fracture slip analysis (CAS). . . . .	56
3.16	Distribution of max and min principal stresses around the 45 deg inclined rough fracture under shear slip (CAS). . . . .	57
3.17	Slip profiles of planar and rough fractures modelled by smooth joint contact model (SSM/DynaFrax). . . . .	57
3.18	Slip profiles of rough fracture simulated by FRACOD2D and PFC2D (SSM/DynaFrax). . . . .	58
3.19	Distribution of stresses around a 45 deg inclined fracture under shear in different model size and fracture length ratios (SSM/DynaFrax). . . . .	58
3.20	Comparison of rough fracture slip profiles with different orientations (CAS). . . . .	58
3.21	Effect of presence of small cracks and their spacings on slip profiles of the main fracture (CAS). . . . .	59
3.22	Slip profiles of rough fracture with different profiles (CNCS). . . . .	60
3.23	Slip profile of a rough fracture simulated by NMM (LBNL). . . . .	60
3.24	Rough fracture representation in three different mesh resolution and slip profiles (3DEC). . . . .	61
3.25	Slip profiles of rough fractures with different mesh resolutions and corresponding stress distributions (Quintessa/UoE/RWM). . . . .	61
3.26	Slip profile of an inclined fracture with different roughness profiles (SSM/DynaFrax). . . . .	62

3.27 Slip profiles of rough fracture under different orientations (SSM/DynaFrax). . . . .	62
3.28 Slip profiles of rough fractures under different level of roughness (SSM/DynaFrax). . . . .	63
3.29 Comparison of fracture slip distribution between the planar and rough fractures under mechanical and thermal loading (SSM/DynaFrax). . . . .	63
3.30 Comparison of planar fracture slip under mechanical and mechanical+thermal boundary conditions (SNL). . . . .	64
3.31 Comparison of rough fracture slip under mechanical and mechanical+thermal boundary conditions (LBNL). . . . .	64
3.32 Saw-cut fracture thermal slip modelling by COMSOL (CNCS). . . . .	65
3.33 Saw-cut fracture thermal slip modelling by 3DEC (KIGAM). . . . .	66
3.34 Intersecting fractures (blue lines) and hypothetical single major paths (yellow lines). . . . .	67
3.35 A single fracture in (a) closed, (b) sheared (off-set) and (c) partially open states; (d)-(f) three possible cases of two intersecting fractures. . . . .	67
3.36 Schematic diagram of the model geometry, boundary conditions and mesh discretization. . . . .	70
3.37 The evolution of fracture reservoir damage during fluid injection (the injection rate is constant at 2.5 kg/s). . . . .	72
3.38 Damage evolution in the rocks after 1 hour of fluid injection under different stress states. . . . .	73
3.39 Damage evolution in the fractured rocks after 0.5 hours of simultaneous fluid injection in two wells . . . . .	74
3.40 Benchmarking idea for 2D plane-strain conditions; upper figures represent M processes, lower figures represent HM processes . . . . .	75
3.41 Geometry and location of Pressure-Exerting Elements (PEEs) and Dynamic-Sealing-Strips (DSSs). . . . .	76
3.42 The results of the strain field for the 2D benchmark exercise M1 are shown, with loading scenarios defined in Table 3.4. It's important to note the distinct strain ranges; the strain value at the sheath is much higher than the visualization range (UFZ-VPF/FEM-OGS6). . . . .	77
3.43 Volumetric strain versus angle for an intact sample (M1) (UFZ-VPF/FEM-OGS6). . . . .	77
3.44 Geometry and location of PEEs and DSSs. . . . .	78
3.45 Strain profile for 2D specimens include two-wings fracture, M3a (UFZ-VPF/FEM-OGS6). . . . .	79
3.46 Strain profile for 2D specimens include one-wing fracture, M3b (UFZ-VPF/FEM-OGS6). . . . .	79
3.47 Volumetric strain versus angle for fractured samples, M3a and M3b (UFZ-VPF/FEM-OGS6). . . . .	80
3.48 Geometry and location of PEEs and DSSs. . . . .	81
3.49 Strain profile for 2D specimens include a pressurised two-wings fracture, HM3a (UFZ-VPF/FEM-OGS6). . . . .	82
3.50 Strain profile for 2D specimens include a pressurised one-wing fracture, HM3b (UFZ-VPF/FEM-OGS6). . . . .	82

3.51	Volumetric strain versus angle for fractured samples, <i>HM3a</i> and <i>HM3b</i> (UFZ-VPF/FEM-OGS6).	83
3.52	Geometry and location of PEEs and DSSs. . . . .	85
3.53	Resulting fields for benchmark HM4 Scenario I, for different time steps (UFZ-VPF/FEM-OGS6).	85
3.54	Resulting fields for benchmark HM4 Scenario II, for different time steps (UFZ-VPF/FEM-OGS6).	86
3.55	Resulting fields for benchmark HM4 Scenario III, for different time steps (UFZ-VPF/FEM-OGS6).	87
3.56	Resulting fields for benchmark HM4 Scenario III, for different time steps (CAS) . . . . .	88
4.1	TUBAF experimental facilities for direct shear tests forming the basis for Task G Step 1 . . . . .	91
4.2	Experimental work concepts for the Constant Normal Load (CNL) and Constant Normal Stiffness (CNS) tests, respectively Nguyen, 2013 . . . . .	92
4.3	CNL test results Frühwirt, Pötschke, and Konietzky, 2021 . . . . .	92
4.4	Point cloud representing the surface of a granite sample from Saxony. The size is 65 mm by 170 mm and the cloud contains approx. 98000 points. . . . .	93
4.5	Comparison of shear stress–shear displacement curves under four normal loading stresses (1, 2.5, 5.0, and 7.5 MPa) between Freiberg shear tests and two-dimensional numerical simulation by CASRock . . . . .	95
4.6	Comparison of shear stress–shear displacement curves under two normal loading stresses (1 and 2.5 MPa) between Freiberg shear tests and three-dimensional numerical simulation via CASRock simulator . . . . .	95
4.7	Comparison of shear stress–shear displacement curves under 1 MPa normal stress loading conditions among different calculation codes and experimental tests . . . . .	96
4.8	Validation of the joint model with shear under constant normal stress tests for Freiberg granite. Solid lines are modelling results; dotted lines are experimental values (Nguyen et al., 2024) . . .	97
5.1	GREAT cell sample and apparatus . . . . .	99
5.2	(a) Overview of model geometry used for McDermott et al., 2018; Fraser-Harris et al., 2020 (b) Vertical fracture plane in cell, generic geometry for prediction of normal and shear stress on fracture plane, (c) Radial hydraulic loading in cell, (d) Actual loading relative to fracture location for prediction of stress distribution in polyaxial stress field within cell. . . . .	100
5.3	Modelling of internal stress tensor under different surface loading conditions . . . . .	100
5.4	Additional information to calculation of displacement results and consideration of two different types of possible boundary condition at the platen sample interface, friction free, and totally restrained. . . . .	102
5.5	Different labelling of PEE’s in raw experimental data. . . . .	103
5.6	GREAT cell samples . . . . .	104
5.7	Experiment types conducted on synthetic samples (polymer and polyester resin) McDermott et al., 2018 . . . . .	105



5.8	The results of the strain field for the 2D/3D benchmark exercise M1 are shown, with loading scenarios defined in Table 5.3. It's important to note the distinct strain ranges; the strain value at the sheath is much higher than the visualization range. . . . .	107
5.9	Comparing volumetric strain at different angles for 2D and 3D cases in the M1 benchmark under true triaxial loading . . . . .	107
5.10	Comparing volumetric strain at different angles for 2D and 3D cases in the M1 benchmark under axi-symmetrical loading . . . . .	108
5.11	A comparison of measured strain in the laboratory and numerical experiments (3D axisymmetric case): Circumferential and Volumetric strains compared. . . . .	110
5.12	A comparison of measured strain in the laboratory and numerical experiments (3D Triaxial Case): Circumferential and volumetric strains compared. . . . .	110
5.13	Analyses of fracture impact on circumferential strain under polyaxial loading (synthetic PMMA sample). To account for the influence of fracture orientation, we replicate this benchmark by rotating the fracture. In the clockwise direction, the fracture orientation is considered clockwise from the positive x-axis. . . . .	111
5.14	Volumetric strain at $(x, y, z) \in \mathbb{R}^3 \mid  x^2 + y^2 - 0.065^2  < 10^{-6} \wedge  z - 0.1  < 10^{-6}$ for different loading scenarios compare with the experimental circumferential strain. The angle is measured clockwise from the positive x-axis (OGS-6.) . . . . .	112
5.15	3DEC model with an internal fracture . . . . .	113
5.16	Volumetric and circumferential strain results obtained from the partially fractured 3DEC model . . . . .	114
5.17	Information of the flow test performed within the GREAT cell (modified from Fraser-Harris et al., 2020) . . . . .	115
5.18	TOUGH-3DEC model for the hydro-mechanical flow tests . . . . .	116
5.19	Effective normal stress and fluid pressure distribution of 3DEC model with 10 GPa/m of fracture normal stiffness under case C . . . . .	116
5.20	Permeability changes by applied normal stress under five different polyaxial stress conditions . . . . .	117
5.21	OGS#LIE model for the hydro-mechanical flow tests. . . . .	118
5.22	OGS#LIE simulation: permeability obtained with different high joint stiffnesses. . . . .	119
5.23	OGS#LIE simulation: Fracture normal stress obtained with two joint stiffnesses. . . . .	120
5.24	OGS#LIE simulation: permeability and normal stress distribution in the fracture. . . . .	120
5.25	OGS#LIE simulation: stress and strain distribution in the matrix. . . . .	120
5.26	Analyses of fracture impact on circumferential strain under polyaxial loading (synthetic PMMA sample).To account for the influence of fracture orientation, we replicate this benchmark by rotating the fracture. In the clockwise direction, the fracture orientation is considered positive, with the zero value starting at 3 o'clock. . . . .	121

5.27	Volumetric strain at $(x, y, z) \in \mathbb{R}^3 \mid  x^2 + y^2 - 0.065^2  < 10^{-6} \wedge  z - 0.1  < 10^{-6}$ for different loading scenarios. The angle is measured clockwise from the positive $x$ -axis (OGS-6.) . . . . .	122
5.28	Left: Representation of vertical fracture (Fraser-Harris et al., 2020, Figure 11); Right: Model representation of domain with fracture. . . . .	124
5.29	HM simulation results for the fully fractured sample . . . . .	125
5.30	Coupled hydro-mechanical modeling results: calculated fracture permeability vs. normal stress. . . . .	125
6.1	Experimental concept. (a)Initial critical stress state (blue half-circle) and expected failure stress state (red half-circle), and (b) Heating boundaries were set in the direction of $\sigma_{\min}$ and thermal stress will be induced in the direction of $\sigma_{\max}$ due to restraints of expansion . . . . .	127
6.2	Experimental procedure . . . . .	128
6.3	Schematic diagrams showing the locations of heaters, clip-on gages, thermocouples, and AE sensors (a) from the full front view and (b) on the six square faces of a cube. On the back side of the specimen, a camera was used to take photos of the back side for DIC analysis, and the fracture slip and shear dilation at the five locations (labeled 1–5) were indirectly measured. . . . .	129
6.4	Asperity distribution (topography) for the bottom surface of (a) SF, and (b) RF . . . . .	130
6.5	Results of temperatures. (a) Evolutions of temperatures at the five measure points of T1–T5 on the specimen surface and their heating rates; (b) Spatial distribution of T1–T5 after heating duration of 6,000 s. The plane in grey represents the location of the fracture surface . . . . .	132
6.6	Evolutions of the maximum principal stress, as well as shear and normal displacements in (a) SF and (b) RF during the heating . . . . .	135
6.7	(a) Working principal of the clip-on displacement transducers used in this study (Clip-on Displacement Transducer   Tokyo Measuring Instruments Laboratory Co., Ltd. (tml.jp)), and (b) the influence of temperature on the displacement measurement by the transducer. . . . .	136
6.8	(a) Photographs of the sheared-off particles and slickensides on the fracture surfaces in SF; (b) the top and bottom surface deformation in RF after thermoshearing test. The red arrows show the shear direction of fractures. . . . .	137
6.9	AE hit amplitude, cumulative absolute energy, and cumulative hit number (a) SF and (b) RF . . . . .	138
6.10	Generation of KICT test case model with a mated rough fracture surface (SSM/DynaFrax). . . . .	139
6.11	Comparison of temperature evolutions (model vs. experiment) and temperature distribution inside the PFC3D model showing biconical pattern (SSM/DynaFrax). . . . .	140
6.12	Comparison of fracture normal and shear displacement evolution between the rough fracture KICT experiment and PFC3D modelling (SSM/DynaFrax). . . . .	141
6.13	Distribution of smooth joint contact dip angle, normal displacement and shear displacement after applying heat (SSM/DynaFrax). . . . .	141
6.14	Generation of FLAC3D model for planar fracture and rough unmated fracture, and temperature distribution (LBNL). . . . .	142

6.15	Temperature evolution comparison: (left) temperature within fracture, (right) temperature on rock/model surface (LBNL) . . . . .	143
6.16	Comparison of fracture normal and shear displacement evolution between the rough fracture KICT experiment and FLAC3D modelling (LBNL). . . . .	143
6.17	Distribution of shear displacement on fracture surface: flat fracture, mated rough fracture, and unmated rough fracture (LBNL). . . . .	144
6.18	Model setup, initial and boundary conditions (CNSC). . . . .	144
6.19	Comparison of fracture normal and shear displacement evolution between the rough fracture KICT experiment and COMSOL modelling (CNSC). . . . .	145
6.20	Distribution of rock displacement at different selected times, and evolution of shear and normal displacement and comparison with experiment monitoring. . . . .	146
6.21	Generation of rough fracture surface model in 3DEC (KIGAM). . . . .	147
6.22	Generation of a mated and an unmated rough fracture model (KIGAM). . . . .	147
6.23	Comparison of experimental and numerical results of surface temperature evolution (KIGAM). . . . .	148
6.24	Comparison of mated fracture normal and shear displacement evolution between the rough fracture KICT experiment and 3DEC modelling (KIGAM). . . . .	148
6.25	Comparison of unmated fracture normal and shear displacement evolution between the rough fracture KICT experiment and 3DEC modelling (KIGAM). . . . .	148
6.26	Planar and rough fracture models and slip distribution on the fracture surface before applying heat (KAERI). . . . .	149
6.27	Evolution of temperature at selected locations in the model and its biconical distribution in the model. . . . .	150
6.28	Comparison of fracture normal and shear displacement evolution between the rough fracture KICT experiment and TOUGH-3DEC modelling (KAERI). . . . .	150
6.29	Comparison of fracture normal and shear displacement evolution between the rough fracture KICT thermal slip experiment and the modelling results from all teams. . . . .	151
7.1	Concept and routes of SAFENET-2 . . . . .	155
B.1	NMM mathematical and physical meshes . . . . .	162
B.2	Flexible choice of local approximation functions: (a) linear function (Wang et al., 2016), (b) a jump junction for a weak discontinuity (Hu, Wang, and Rutqvist, 2015), (c) a discontinuous function for a fracture (Hu, Rutqvist, and Wang, 2016a; Hu, Rutqvist, and Wang, 2017) . . . . .	163
B.3	Geometric representation of an element with one intersection by two fracture . . . . .	164
B.4	Geometric representation of open, bonded and sliding contact states for elements divided by intersecting fractures . . . . .	165
B.5	The components of a FLAC3D zone. . . . .	166

B.6 Interface elements, nodes, and the representative interface area (Itasca Consulting Group, 2020). 167

B.7 The constitutive model of an interface node (Itasca Consulting Group, 2020). . . . . 168

## List of Tables

1.1	Overview of experimental work in Task G	16
2.1	Numerical methods and codes	18
3.1	Rock parameters of granite used in the direct shear tests (Frühwirt, Pötschke, and Konietzky, 2021)	44
3.2	Overview of code/software and capabilities for the benchmark	68
3.3	Material properties of the fractured rock mass, including the matrix, fractures and pore fluid (Norbeck, McClure, and Horne, 2018; Lei, Gholizadeh Doonechaly, and Tsang, 2021)	70
3.3	Material properties of the fractured rock mass, including the matrix, fractures and pore fluid (Norbeck, McClure, and Horne, 2018; Lei, Gholizadeh Doonechaly, and Tsang, 2021)	71
3.4	Loading scenarios for mechanical deformation benchmarks	76
3.5	Material properties	76
3.6	Loading Conditions for Different Angles	78
3.7	Material and Fluid Properties	84
3.8	Loading Conditions for Different Angles	84
4.1	Rock parameters of granite and basalt used in the direct shear tests.	93
4.2	Data overview	93
4.3	CNL experiments (TUBAF)	94
5.1	Overview of material properties for the GREAT cell samples	104
5.2	Material properties	106
5.3	Loading scenarios for mechanical deformation benchmarks	106
5.4	Loading Conditions for partially fractured sample (reference: supplemental materials within McDermott et al., 2018).	112
5.5	Fracture properties for 3DEC model	113
5.6	Loading scenarios for hydro-mechanical simulation in partially fractured sample	115
5.7	Material properties	124
6.1	Material properties	130
6.2	Average JRC values before and after thermoshearing tests, static friction coefficients ( $\mu_s$ ), and the critical stress states for thermoshearing tests of SF and RF	130
6.2	Average JRC values before and after thermoshearing tests, static friction coefficients ( $\mu_s$ ), and the critical stress states for thermoshearing tests of SF and RF	131
6.3	Comparison of measurements of displacements by DIC analysis and stresses in the two fractures	134

6.4	Acoustic emission (AE) signals during thermoshearing, including cumulative energy, hit number, peak hit amplitude, and counts of peak hit amplitude . . . . .	137
6.5	Numerical codes and methods of the research teams adopted for the test case modelling of the KICT thermoslip experiment. . . . .	139
A.1	Nomenclature . . . . .	160